DIPHOSPHINE DIOXIDE CAGES AND HYDROGEN PEROXIDE ADDUCTS OF PHOSPHINE OXIDES: SYNTHESES AND APPLICATIONS IN SURFACE SCIENCE

A Dissertation

by

CASIE RENEE HILLIARD

Submitted to the Office of Graduate and Professional Studies of
Texas A&M University
in partial fulfillment of the requirements for the degree of

DOCTOR OF PHILOSOPHY

Chair of Committee,	Janet Bluemel
Co-Chair of Committee,	John A. Gladysz
Committee Members,	Hongcai Zhou
	David Barondeau
	Hong Liang
Head of Department,	David Russell

December 2013

Major Subject: Chemistry

ABSTRACT

Understanding the adsorption of phosphine oxides on silica surfaces has a threefold incentive. **(a)** Efficiently removing phosphine oxides from reaction mixtures is crucial after many synthetic procedures, for example the Wittig reaction. **(b)** Using the P=O group for probing the surface acidity of oxides. **(c)** Most importantly, getting more insight regarding the nature of the P=O/surface interaction. Hereby, the mobility of the adsorbed species is of fundamental interest. In the classical ^{31}P MAS and in HRMAS NMR spectra the reduction of the originally large CSA, the residual halfwidth, as well as the downfield shift of the signals when adsorbing phosphine oxides on silica surfaces are most indicative. This research provides new insights regarding the strength of the phosphine oxide adsorption on various silica surfaces and the diverse modes of mobility. Furthermore, an oxidation procedure for the synthesis of a variety of phosphine oxides, including the model compounds used for the adsorption studies, has been developed. It yields the well-defined H_2O_2 adducts as key intermediates, which have been fully characterized and methods for their controlled and efficient decomposition are described.

For adsorbed phosphine oxides, the changes of the ^{31}P solid-state NMR signals as compared to the polycrystalline materials can stem from both the translational mobility of the compound across the silica surface and the interaction of the P=O group with the silanol groups of the silica. Molecules containing two phosphine oxide groups, one of them being sterically prevented from interacting with the surface, are target compounds for the adsorption studies. Since the P nuclei are bound within the same molecule, both experience the same translational mobility, but only one P=O group can undergo quaternization by contact with the surface. Therefore, the contribution of each

factor to the CSA reduction upon adsorption can be determined. The diphosphine cages and their dioxides can serve as such probe molecules and their adsorption on silica has been examined.

Since none of these small cages, containing five to twelve methylene groups in each alkyl chain, are presently known in the literature, a new synthetic route to access the diphosphine cage derivatives, namely the dioxide cages, had to be explored. Employing Fe gyroscopes as starting materials and releasing the phosphine oxides from the metal center to form the dioxide cage molecules is most effective and will be highlighted. Having synthesized the diphosphine dioxide cages, their ^{31}P MAS NMR characteristics in the polycrystalline and surface-adsorbed states will be discussed in detail. In summary, the two largest diphosphine dioxide cages adsorbed on silica only show one signal in the ^{31}P solid-state NMR spectra, indicating both sides of each cage are interacting with the support. On the other hand, the smallest cage, containing 10 methylene groups in each alkyl chain, when adsorbed results in two distinct signals in the ^{31}P solid-state NMR spectra, meaning one P=O group is adsorbed on the support while the other is pointing away from the surface, as desired. Examining the different CSA values of the two signals proves that both the translational mobility and partial quaternization effect play a role in the overall CSA reduction for the adsorbed species.

DEDICATION

I dedicate this dissertation to my grandpas. Although you are not here to celebrate, I know you would be proud of me and happy there is a doctor in the family!! I love you!

ACKNOWLEDGEMENTS

I would like to begin by thanking my family whose support and guidance has helped me stay strong even through the most challenging times. I am so glad they have always encouraged my academics and urged me to achieve great things in my life. I know their motivation has helped me complete my Ph.D. and will continue to inspire me in the future. I thank you all, especially Mom, Dad, Eric, Nana, and Grandma Peggy, for your advice and unconditional love.

I also would like to thank both of my co-advisors for all of their support and assistance throughout the years. Dr. Bluemel, thank you for always pushing me to do my best and helping provide direction in my research so I could accomplish my goals. Dr. Gladysz, thanks for your advice and guidance and for always providing the best references to check out.

Furthermore, I want to show my appreciation to my entire committee, Dr. Barondeau, Dr. Zhou, and Dr. Liang. You've provided insightful questions and valuable input about what directions to pursue in my research. Thank you for showing up to my seminars and allowing me the time to present my research to you. Also, thanks to Dr. Shantz for supporting me as a committee member during the beginning of my Ph.D. and my preliminary exam.

Lastly, I must acknowledge my friends both here in College Station and across the US. Thank you for always answering my calls and never letting me give up. Thanks for helping me through the tough times and celebrating with me during the great moments. I appreciate you much more than you know, and I love you all. Thank you!!

TABLE OF CONTENTS

	Page
ABSTRACT	ii
DEDICATION	iv
ACKNOWLEDGEMENTS	v
TABLE OF CONTENTS	vi
LIST OF FIGURES	viii
LIST OF SCHEMES	xiv
LIST OF TABLES	xvi
NOMENCLATURE	xix
CHAPTER I INTRODUCTION	1
Background	1
Specific Aims	6
Approach	7
CHAPTER II SYNTHESIS, PURIFICATION, AND CHARACTERIZATION OF PHOSPHINE OXIDES AND THEIR HYDROGEN PEROXIDE ADDUCTS.	12
Introduction	12
Results and Discussion	15
Conclusion	40
Experimental	41
CHAPTER III ADSORPTION OF PHOSPHINE OXIDES ON SILICA SURFACES: A SOLID-STATE NMR STUDY	55
Introduction	55
Results and Discussion	60
Conclusion	97
Experimental	98

CHAPTER IV IRON GYROSCOPES AS STARTING MATERIALS FOR THE SYNTHESES OF DIPHOSPHINE CAGE DERIVATIVES 114

Introduction 114
Results and Discussion 116
Conclusion 150
Experimental 151

CHAPTER V ADSORPTION OF DIPHOSPHINE DIOXIDE CAGES ON SILICA SURFACES 165

Introduction 165
Results and Discussion 169
Conclusion 183
Experimental 184

CHAPTER VI CONCLUSION 187

REFERENCES 192

APPENDIX A 200

APPENDIX B 214

APPENDIX C 264

APPENDIX D 273

LIST OF FIGURES

FIGURE Page

1.1 ^{31}P CP/MAS (3 kHz) and wideline (0 kHz) NMR spectra of polycrystalline (top two traces) and adsorbed (bottom two spectra) diphosphine cage **1** with $(CH_2)_{14}$ alkyl chains. 4

1.2 Diphosphine cages and their corresponding monoxides and dioxides..... 5

1.3 Model phosphine oxides for adsorption studies 8

2.1 ^{31}P NMR spectra of **3** (bottom trace) and **3a** (top trace) in C_6D_6 17

2.2 Change of the $\delta(^{31}P)$ of $Bu_3P{=}O{\cdot}(H_2O_2)$ (**3a**) with its concentration in C_6D_6..... 18

2.3 Water uptake of $Me_3P{=}O$ (**2**) and $Bu_3P{=}O$ (**3**) in air..... 19

2.4 ^{31}P MAS (top, 4 kHz) and wideline (bottom, 0 kHz) spectra of polycrystalline **6** 20

2.5 ^{31}P MAS (top, 4 kHz) and wideline (bottom, 0 kHz) spectra of polycrystalline **6a** 21

2.6 ^{31}P MAS (top, 4 kHz) and wideline (bottom, 0 kHz) spectra of polycrystalline **5** 22

2.7 ^{31}P MAS (top, 4 kHz) and wideline (bottom, 0 kHz) spectra of polycrystalline **5a** 23

FIGURE Page

2.8 Single crystal X-ray structure of $Bu_3P=O$ (**3**), view from showing the aligned P=O bonds 25

2.9 Single crystal X-ray structure of $Bu_3P=O$ (**3**), view along the P=O bond..... 26

2.10 Single crystal X-ray structure of the dimer of **5a**..... 27

2.11 Additional views of the single crystal X-ray structure of the dimer of **5a**. 28

2.12 IR spectra of neat **3** (bottom), **3a** (top), and **3a** with adsorbed H_2O after partial decomposition of the bound H_2O_2 (middle) 30

2.13 Physical appearance of neat $Bu_3P=O$ (**3**, right) and $Bu_3P=O\cdot(H_2O_2)_x$ (**3a**, left, x = 0.5–1.0) in a vial..... 33

2.14 Evolution of small O_2 bubbles during decomposition of the neat materials $R_3P=O\cdot(H_2O_2)_x$ (x = 0.5–1.0) at the given temperatures (**2a**–**6a**)..... 37

2.15 Molecular sieves placed in a tea bag and suspended in toluene in a round bottom flask for easy removal after the reaction..... 40

3.1 ^{31}P solid-state NMR spectra of polycrystalline $OPPh_3$ (**6**) (top) and $OPPh_3$ adsorbed on silica ($\mathbf{6_{ads}}$) (bottom)..... 62

3.2 ^{31}P MAS NMR spectra of **3** adsorbed on silica ($\mathbf{3_{ads}}$)..... 63

3.3 ^{31}P MAS NMR spectra of polycrystalline $OPCy_3$ (**5**) (top two traces) and $OPCy_3$ adsorbed on silica ($\mathbf{5_{ads}}$) (bottom three spectra)..... 65

FIGURE Page

3.4 Leaching of the phosphine oxides $\mathbf{2_{ads}}$–$\mathbf{6_{ads}}$ from wet silica in different solvents 73

3.5 Leaching of phosphine oxides $\mathbf{2_{ads}}$–$\mathbf{6_{ads}}$ from silica versus polarity index for the given solvents 74

3.6 Surface coverage values of phosphine oxides $\mathbf{3_{ads}}$–$\mathbf{6_{ads}}$ on wet silica pre-treated with different solvents..... 76

3.7 Surface coverage values of phosphine oxide **3** adsorbed on silica pre-treated with different solvents. 77

3.8 ^{31}P HRMAS spectra of phosphine oxide $Bu_3P{=}O$ (**3**) adsorbed on wet silica ($\mathbf{3_{ads}}$) and the halfwidths $\nu_{1/2}$ of the signals 79

3.9 Surface coverages of $Bu_3P{=}O$ (**3**) and Bu_3P (**7**) adsorbed on the silica surface after being applied in a 1 : 1 mixture for the competition experiments 82

3.10 Competition of **3** and **7** adsorbing on the different silica surfaces..... 83

3.11 Dry grinding of **6** with wet silica 86

3.12 Dry grinding of **5** with wet silica 87

3.13 T_1 times of PPh_3 (**8**) adsorbed on silica at various surface loadings 90

3.14 T_1 times of $OPPh_3$ (**6**) adsorbed on silica at various surface loadings 91

3.15 Tetraphosphine tetroxides **9**–**11** for adsorption studies..... 93

FIGURE Page

3.16 ^{31}P MAS NMR spectra of the Sn tetraphosphine tetroxide (**11**) as a polycrystalline powder and adsorbed on wet silica $\mathbf{11_{ads}}$ 95

3.17 ^{31}P MAS NMR spectra of $\mathbf{11_{ads}}$ on wet silica 96

3.18 ^{31}P HRMAS NMR spectrum of $\mathbf{11_{ads}}$ on wet silica 97

4.1 Diphosphine cages (**I**) and their corresponding dioxides (**III**) 115

4.2 Fe phosphine complexes for test reactions 117

4.3 ^{13}C NMR spectrum of complex **13** showing virtual couplings highlighted in red 120

4.4 ^{31}P MAS NMR (top and middle) and wideline spectrum (bottom) of **14** .. 122

4.5 ^{31}P MAS NMR (top) and wideline spectrum (bottom) of **15** 123

4.6 ^{31}P NMR spectra of the products after the reaction of **12** with H_2O_2 (top) and after removal of H_2O_2 (bottom) 126

4.7 ^{31}P NMR spectrum of the reaction mixture after oxidation of **12** in air 129

4.8 ^{31}P NMR spectrum of the reaction mixture after treating **12** with Meerwein's salt 133

4.9 ^{31}P NMR spectrum of the reaction mixture after reaction of **12** with HCl. 136

FIGURE Page

4.10 ^{31}P MAS NMR (top) and wideline spectrum (bottom) of **28** 140

4.11 ^{31}P MAS NMR spectra of **28** after combining it with dry SiO_2 at the indicated rotational frequencies 142

4.12 ^{31}P NMR spectrum of the products from oxidation of gyroscope **28** by H_2O_2 144

4.13 ^{31}P NMR spectrum after the oxidation of **28** with ^{t}BuOOH to give dioxide cage **31** 145

4.14 ^{13}C NMR spectrum of diphosphine dioxide cage **31** 146

4.15 HMBC spectrum of diphosphine dioxide cage **31** 147

4.16 ^{31}P NMR spectrum of diphosphine dioxide cage **32** 149

4.17 ^{31}P NMR spectrum of diphosphine dioxide cage **33** 150

5.1 Diphosphine dioxide cages **31**–**33** for adsorption studies 168

5.2 ^{31}P MAS spectra of **32** at the indicated rotational frequencies 171

5.3 ^{31}P MAS spectra of **33** at the indicated rotational frequencies 173

5.4 ^{31}P MAS NMR of **33** adsorbed on dry silica (**33$_{ads}$**) 175

5.5 ^{31}P MAS spectra of **32** adsorbed on dry silica (**32$_{ads}$**) 177

FIGURE Page

5.6 ^{31}P MAS NMR of **31** adsorbed on dry silica (**31$_{ads}$**)..... 179

5.7 Simulation ^{31}P wideline spectrum of **31** adsorbed on dry silica (**31$_{ads}$**) ... 181

5.8 ^{31}P CP/MAS NMR of **31** adsorbed on dry silica (**31$_{ads}$**) 182

5.9 ^{31}P HRMAS spectrum of **31$_{ads}$** in THF..... 183

LIST OF SCHEMES

SCHEME Page

1.1 Synthesis of diphosphine (**I**) or diphosphine dioxide (**III**) cages from the corresponding Fe gyroscopes... 10

2.1 Representative tertiary phosphine oxides **2**–**6** used in this work 13

2.2 Yields of clean phosphine oxides **2**–**6** with respect to the corresponding phosphines after oxidation with hydrogen peroxide to form **2a**–**6a**, decomposition of attached H_2O_2, and removal of water with molecular sieves (x,y = 0.5–1.0)..... 38

4.1 Synthesis of the Fe phosphine complexes **12**–**15**..... 118

4.2 Overview of reagents tested to remove the Fe center of **12** from the phosphine ligands..... 124

4.3 Oxidation of **12–15** with aqueous H_2O_2. The Fe containing product has not been identified..... 125

4.4 Oxidation of **14** with ^{t}BuOOH. 127

4.5 Oxidation of **12** by exposure to air..... 128

4.6 Attempted ligand exchange with PCl_3 129

4.7 Attempted ligand exchange with PMe_3..... 130

4.8 Synthesis of the borane adduct **18**..... 131

SCHEME Page

4.9 Attempted synthesis of the methylphosphonium salt **19** 132

4.10 Synthesis of the phosphonium salts **20**–**23** 133

4.11 Synthesis of the phosphonium salts **24**–**27** 135

4.12 Attempted decomposition of complex **12** by silica 137

4.13 Attempted decomposition of complex **12** by alumina 138

4.14 Representative synthesis of the Fe complex **30** 139

4.15 Oxidation of **28** to give the diphosphine dioxide **31** 143

4.16 Oxidation of **29** to give the diphosphine dioxide **32** 148

4.17 Oxidation of **30** to give the diphosphine dioxide **33** 148

LIST OF TABLES

TABLE Page

2.1 ^{31}P NMR chemical shifts δ [ppm] of the phosphine oxides **2**–**6** and their corresponding H_2O_2 adducts **2a**–**6a** in C_6D_6 and $CDCl_3$ and the differences $\Delta\delta(^{31}P) = \delta(\text{adduct}) - \delta(\text{phosphine oxide})$ 16

2.2 IR absorptions ν of the phosphine oxides **2**–**6** and their corresponding H_2O_2 adducts **2a**–**6a** and the wavenumber differences $\Delta\nu(P{=}O) = \nu(\text{phosphine oxide}) - \nu(\text{adduct})$ 31

2.3 Melting points and decomposition temperature ranges [°C] of the phosphine oxides **2**–**6** and their corresponding H_2O_2 adducts **2a**–**6a**.... 36

3.1 "Footprints" and maximum coverage values of the phosphine oxides **2**–**6** and the large diphosphine cage **1** on the silica surface..... 68

3.2 Maximum surface coverages (molecules per 100 nm^2) of phosphine oxides **2**–**6** under different conditions..... 70

3.3 ^{31}P T_1 times of $\mathbf{6_{ads}}$ and $\mathbf{8_{ads}}$ at different surface loadings 91

3.4 ^{31}P isotropic chemical shifts and CSA values of **9** and **11** and adsorbed species $\mathbf{9_{ads}}$ and $\mathbf{11_{ads}}$..... 94

3.5 Data for adsorption of **2**–**6** on dry silica at 90 °C 102

3.6 Data for adsorption of **2**–**6** on wet silica at 90 °C..... 102

3.7 Data for adsorption of **2**–**6** on wet silica at RT 103

TABLE Page

3.8 Data for adsorption of **2a**–**6a** on wet silica at RT 103

3.9 Data for adsorption of **2**–**6** on large batches of wet silica for leaching studies 105

3.10 Leaching of **2**–**6** from wet silica in different solvents. 105

3.11 Surface coverages of **3**–**6** on wet silica after pre-treatment with toluene .. 108

3.12 Surface coverages of **3**–**6** on wet silica after pre-treatment with THF 108

3.13 Surface coverages of **3**–**6** on wet silica after pre-treatment with acetone .. 109

3.14 Amounts for dry grinding experiments for **5** and **6** on silica. 111

3.15 Specific Surface Loadings of **6** and **8** for ^{31}P T_1 time measurements. 112

3.16 Surface coverages of **9** and **11** on silica. 113

4.1 ^{31}P NMR chemical shifts and IR data for complexes **12–15** 118

4.2 CSA values [ppm] for polycrystalline **14**. The CSA is given as the span of the wideline signals, $\delta_{11} - \delta_{33}$ 121

4.3 Conditions for the oxidation of **12**–**15** with aqueous H_2O_2 126

TABLE Page

4.4 Chemical shifts and yields of the ethylphosphonium salts **20**–**23** after reaction of **12–15** with Meerwein's salt as determined by ^{31}P NMR spectroscopy 134

4.5 Chemical shifts and yields of the $[R_3PH]^+$ phosphonium salts **24**–**27** after reaction of **12–15** with HCl as determined spectroscopically (^{31}P NMR) by integrating the product peak and the signals of oxidic byproducts 136

4.6 CSA values [ppm] for Fe gyroscope **28** and for **28** combined with SiO_2.. 141

5.1 ^{31}P CSA values [ppm] for the polycrystalline signal of the diphosphine dioxide cages **32** and **33** obtained by simulation of the wideline spectra. The error margin for the values is ± 2 ppm 172

5.2 Amounts for adsorption of diphosphine dioxide cages **31**–**33** on dry silica 174

5.3 CSA values [ppm] for $\mathbf{33_{ads}}$. The error margin for the values is ± 2 ppm. 176

5.4 CSA values [ppm] for $\mathbf{32_{ads}}$. The error margin for the values is ± 2 ppm. 178

5.5 CSA values [ppm] for $\mathbf{31_{ads}}$. The error margin for the values is ± 3 ppm. 181

NOMENCLATURE

δ	chemical shift in ppm
λ	wavelength
^{13}C	carbon nucleus (NMR)
^{1}H	proton (NMR)
^{31}P	phosphorus nucleus (NMR)
$\{^{1}H\}$	proton decoupled
$\{^{31}P\}$	phosphorus decoupled
Å	Ångstrom
Ac	acetyl, $–COCH_3$
ACS	American Chemical Society
ATR	Attenuate Total Reflectance
B3LYP	Becke, three parameter, Lee-Yang-Parr
BDA	benzylideneacetone
BET	Brunauer Emmett Teller
br	broad
Bu	butyl
COSY	COrrelation SpectroscopY (2D NMR)
CP	cross-polarization
CSA	chemical shift anisotropy
Cy	cyclohexyl
d	doublet (NMR), days
DABCO	1,4-diazabicyclo[2.2.2]octane
DD	dipolar dephasing

DFT	density functional theory
DMSO	dimethylsulfoxide
eq	equivalents, equatorial (NMR)
ESI	electron spray ionization
FID	free induction decay (NMR), flame ionization detector
FT	Fourier Transformation
h	hour
HMBC	Heteronuclear Multiple Bond Correlation (2D NMR)
HPLC	high-performance liquid chromatography
HRMAS	high-resolution magic angle spinning
HR-MS	high-resolution mass spectrometry
HSQC	Heteronuclear Single Quantum Coherence (2D NMR)
Hz	Hertz
i	ipso
J	scalar coupling constant
IR	infrared
m	multiplet (NMR), medium (IR)
m	meta
MAS	magic angle spinning
Me	methyl
NMR	nuclear magnetic resonance
o	ortho
Oct	octyl
p	para
Ph	phenyl

ppm	parts per million
R	alkyl group
RT	room temperature
s	singlet (NMR), strong (IR)
t	triplet (NMR)
THF	tetrahydrofuran
TMS	tetramethylsilane
UV	ultraviolet
ν	wavenumber
$\Delta\nu_{1/2}$	signal width at half height
Vis	visible
vs	very strong (IR)
VT	variable temperature
w	weak (IR)

CHAPTER I

INTRODUCTION

BACKGROUND

Adsorption phenomena on oxide surfaces are of huge interest in many fields, spanning from chromatography to the chemistry of sensors, to gas and liquid storage applications, gas purification, and environmental sciences. Therefore, adsorption of various molecules and materials on different supports has been studied for many decades. Due to the wide range of the fields involved, in this project we will consider only the adsorption of molecules on oxide supports, as studied by solid-state NMR spectroscopy. Initial investigations focused on adsorbing small organic molecules, such as olefins and substituted benzenes, on silica or other porous solids.[1] Most commonly, gases have been adsorbed on supports because the complicating influence of solvents can be avoided this way.[2]

These adsorption studies were extended to the adsorption of compounds containing phosphine and phosphine oxide groups. The adsorption of phosphines on silica-alumina surfaces was first studied by Lunsford *et al.*[3] using adsorption from the gas phase as well as by Maciel *et al.*,[4] where phosphines were adsorbed from solution. In all studies the primary goal was to investigate the surface acidity by interacting the basic phosphines with the Brønsted acid sites on zeolites. In ^{31}P MAS NMR, the physisorbed R_3P species were observed, as well as the R_3PH^+ resulting from the protonation of the phosphine due to the acidic sites. This provided an accurate quantification of the Brønsted acid sites on the support, but the Lewis acid sites could not be examined because of the small chemical shift difference between the free and the physisorbed phosphine signals. This result led Maciel and coworkers to explore the interactions of

phosphine oxides with silica-alumina supports.[5] When using the phosphine oxide probes, the Lewis-bound oxide was distinguishable, allowing for quantification of the Lewis acid sites accessible in the zeolite, in addition to the Brønsted acid sites. Furthermore, methods have been developed to measure the distances between the different acid sites on zeolite surfaces using diphosphine probe molecules of distinct sizes.[6]

Further investigations using phosphine and phosphine oxide compounds as probe molecules to gain more insight into the surface acidity of different silica-alumina zeolites have been undertaken over the decades[2,7] and such studies continue to be of high interest in recent years.[8] Although all these studies focused on the surface acidity applications, it is important to note that a significant reduction in the chemical shift anisotropies (CSA) of these phosphine or phosphine oxide signals was always seen in the ^{31}P solid-state NMR spectra for the adsorbed species. This line-narrowing phenomenon is of basic interest because it might lead to better insights into the nature of the adsorption process, and therefore, it deserves further investigation. Javey and coworkers have already explored the interactions of phosphine oxides with silica to determine whether the P=O groups interact with the surface via hydrogen bonding or covalent bonds.[9] These results showed that hydrogen bonding interactions accounted for the majority of phosphine oxide adsorption, but when using triethylphosphine oxide, it appeared that elimination reactions occurred at elevated temperatures to remove an ethyl substituent and form covalent P–O–Si bonds with the silica. The resulting silica materials were only analyzed using washing experiments and XPS measurements, so further insight could be gained by examining these phosphine oxide adsorptions on silica using solid-state NMR, which is an important aspect of the current project.

Previous studies in the Bluemel group regarding the adsorption of phosphines on

silica were carried out to examine the ^{31}P solid-state NMR characteristics and probe the surface interactions.[10] Phosphines, such as triphenylphosphine, were adsorbed on silica, which does not contain highly acidic Brønsted sites and therefore it did not generate protonated phosphonium R_3PH^+ byproducts. In these studies there was consistently a large decrease in the chemical shift anisotropy (CSA) when going from the polycrystalline material to the adsorbed species. The reduction in the CSA is believed to stem from the partial quaternization of the phosphorus atom upon interacting with the support and/or from the increased translational mobility of the phosphine on the silica surface as compared to its fixed position in the crystal lattice.

In order to examine these effects in more detail, a new probe molecule, combining two equivalent phosphine groups within the same molecule, was desired. The diphosphine cages of the Gladysz group[11,12] appear to be good candidates for the adsorption research because they contain two phosphines bound together. If only one phosphine interacts with the silica surface, but both have the same translational surface mobility, the non-adsorbed phosphine group could serve as an intramolecular standard to investigate the key question, whether translational mobility or partial quaternization of the phosphines interacting with the silica surface is responsible for the reduction of their CSA.

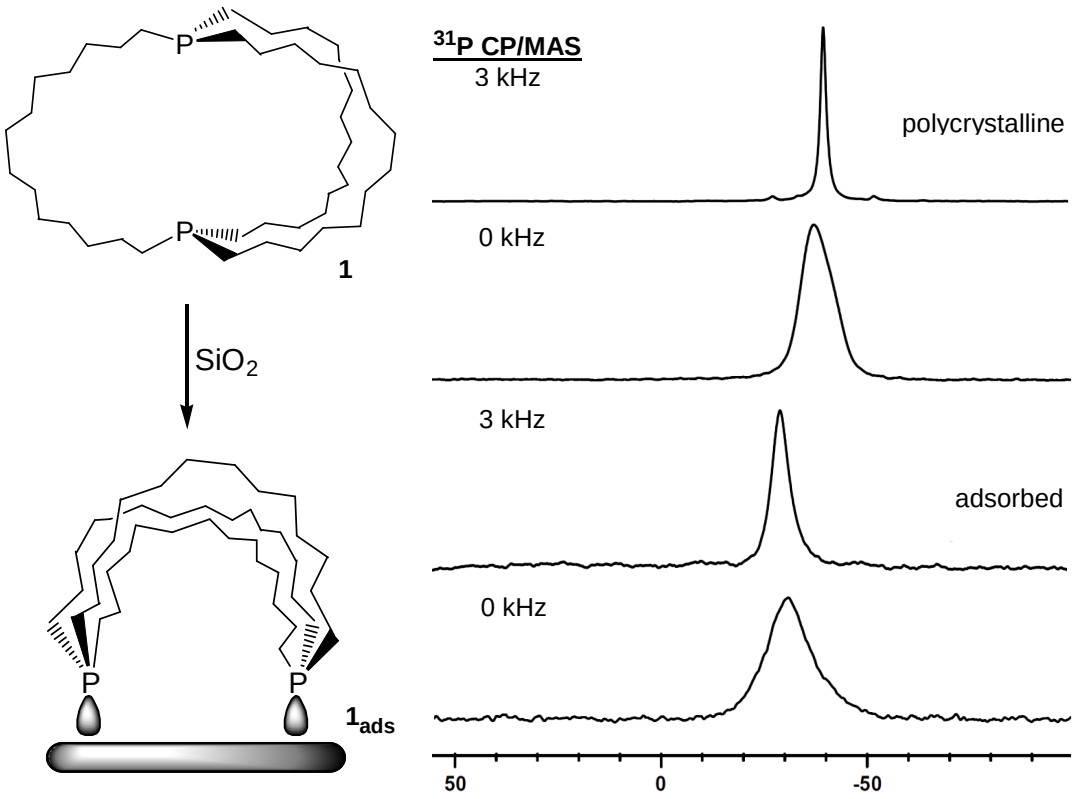

Figure 1.1. ^{31}P CP/MAS (3 kHz) and wideline (0 kHz) NMR spectra of polycrystalline (top two traces) and adsorbed (bottom two spectra) diphosphine cage **1** with $(CH_2)_{14}$ alkyl chains.[10]

The diphosphine cage molecule **1** was studied first, which contained 14 CH_2 groups in each of the three alkyl chains and is comparatively large. This molecule was adsorbed from solution to give $\mathbf{1_{ads}}$ and the resulting material showed only one ^{31}P MAS (Magic Angle Spinning) and wideline (no spinning) NMR signal.[10] The characteristic downfield shift of the signal showed that due to the length of the alkyl chains, both phosphines of the cage were able to reorient themselves to interact with the silica surface, resulting in a parachute-type compound (Figure 1.1).[13] Therefore, a more

rigid system is desired to ensure that only one phosphine group per molecule can access the silica surface at a given time. For studying these adsorption phenomena, the current project is now focused on the synthesis of smaller cages (Figure 1.2), which is described fully in the Specific Aims section of this Introduction.

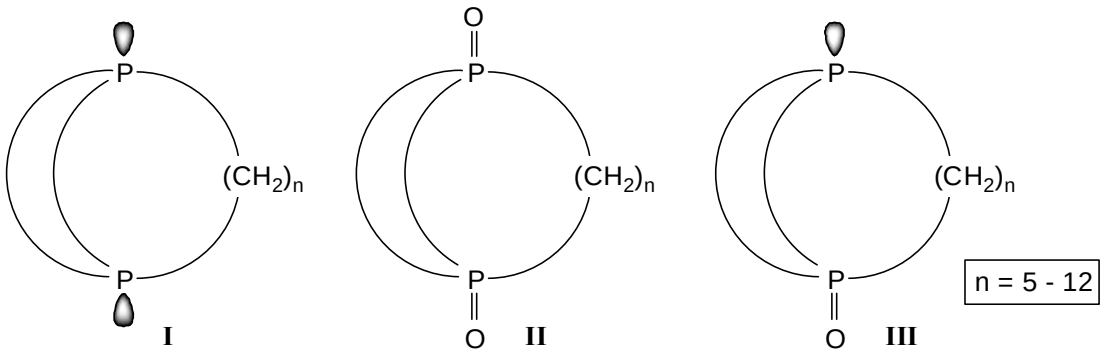

Figure 1.2. Diphosphine cages and their corresponding monoxides and dioxides.

The large cage **1**, previously employed for the initial adsorption study, was obtained by removing the metal center from a Pt-containing gyroscope synthesized by the Gladysz group.[11,14] Derivatives of the diphosphine cages, such as dioxides (**III**), and smaller cages can ideally be generated from metal-containing gyroscopes as well. To access the greatest size range of diphosphine cages **I**, it is advantageous to focus on the Fe gyroscopes, which can have cages ranging from 10 to 14 methylene groups in each alkyl chain.[15] The Fe gyroscopes can also be synthesized in higher yields as compared to the Pt analogs because they achieve a three-fold preorganization of the alkyl chains around the metal center leading to increased efficiency of the subsequent metathesis reaction. The Fe gyroscope series actually has the smallest gyroscope of all the metal complexes, and this is important for our adsorption studies to ensure the cage is rigid

enough and cannot fold to form a parachute on the surface.

In addition, we want to utilize the dioxide cages (**III**) because they incorporate the P=O group with its signals displaying a larger CSA in the solid state. Therefore, a more drastic reduction in the CSA upon adsorption might be observed as well as a greater difference of the chemical shifts of the signals of the polycrystalline material and the adsorbed species. Furthermore, the phosphine oxide group may also increase the rigidity of the cage by slowing any potential homeomorphic isomerization process[11] in which the cages can convert between different *in/out* conformers. In the case of the large phosphine cage **1**, the transformation from the *in/in* isomer to the *out/out* isomer has a low energy barrier ($\Delta G^{\ddagger}$ = 10–12 kcal/mol) allowing for easy conversion at room temperature,[11] which may have contributed to the ability of the cage to fold into a parachute on the silica surface. In the diphosphine dioxide cages (**III**) this process may have a significantly altered energy requirement, which is something that will be investigated for the different cage sizes. Finally, the dioxide cages would require the P=O groups to be pointing to the outside of the cage in order to interact with surface silanols and be adsorbed on the silica support, so the ^{31}P solid-state NMR spectra may provide insights into the P=O group orientations of the cages as well.

SPECIFIC AIMS

The primary goal of this project is to synthesize diphosphine cages and their oxide derivatives (Figure 1.2) for applications in surface science. The disphosphine cages **I**, **II**, and **III** are ideal candidates to further probe the drastic reduction in the CSA of adsorbed species. The cages contain two phosphorus atoms bound within the same molecule, which means both phosphorus nuclei must have the same translational motion across the silica surface. Also, as long as the cage is small enough, only one phosphorus-

containing group should be able to interact with the silica support at a given time. This means for the diphosphine (**I**) and dioxide (**III**) cages, which each contain two chemically equivalent phosphorus atoms, that two different ^{31}P resonances should be visible in the event the adsorbed moiety stays in place long enough so that a rapid intramolecular exchange between adsorbed and not adsorbed moiety ("tumbleweed" scenario) can be excluded. In this case, the differences of the chemical shifts between the adsorbed and not adsorbed phosphorus-containing groups will provide valuable information. Because of the "internal standard nature" of this array, the ^{31}P chemical shifts will be independent of external factors, such as crystal lattice, solvent concentration, or surface coverage of the phosphines. Therefore, any changes in the CSA of only one of the ^{31}P signals can be attributed to the quaternization effect due to interactions with the silica surface and not to the mobility of the whole molecule. If the CSA of both nuclei should remain identical, then its large reduction stems from the increased mobility of adsorbed **I** and **III** on the silica surface. Comparing the systems **I** and **III**, since the CSA is much larger for **III**, its changes may be larger as well and thus easier to monitor.

APPROACH

One major component of this project is the adsorption of the dioxide cages (**III**), and therefore a better understanding of the interactions of phosphine oxides with silica surfaces is necessary for interpreting the results of the solid-state NMR study involving the cages. A selection of representative model phosphine oxides (Figure 1.3) will be adsorbed from solution onto the silica surface and then their ^{31}P solid-state NMR characteristics will be examined. The trialkylphosphine oxides with linear methyl, butyl, and octyl chains are important because they serve as direct model compounds for the

cages. Tricyclohexyl- and triphenylphosphine oxide will be used to probe whether the trends observed in the solid-state NMR spectra are universal and apply to a wide range of phosphine oxides with different steric demands and electronic characteristics. Clean phosphine oxides as starting materials are a prerequisite for these model studies. However, this seemingly simple oxidation reaction is a complex process that can yield a multitude of different products. Therefore, the oxidation of the corresponding phosphines will be investigated in depth. The insight obtained hereby will also allow for the clean oxidation of more complex systems, such as the tetraphosphine linkers previously utilized by the Bluemel group.[16,17] The tetraphosphine oxides (Figure 1.3) constitute another class of target model phosphine oxides for studying the directionality of the P=O adsorption.

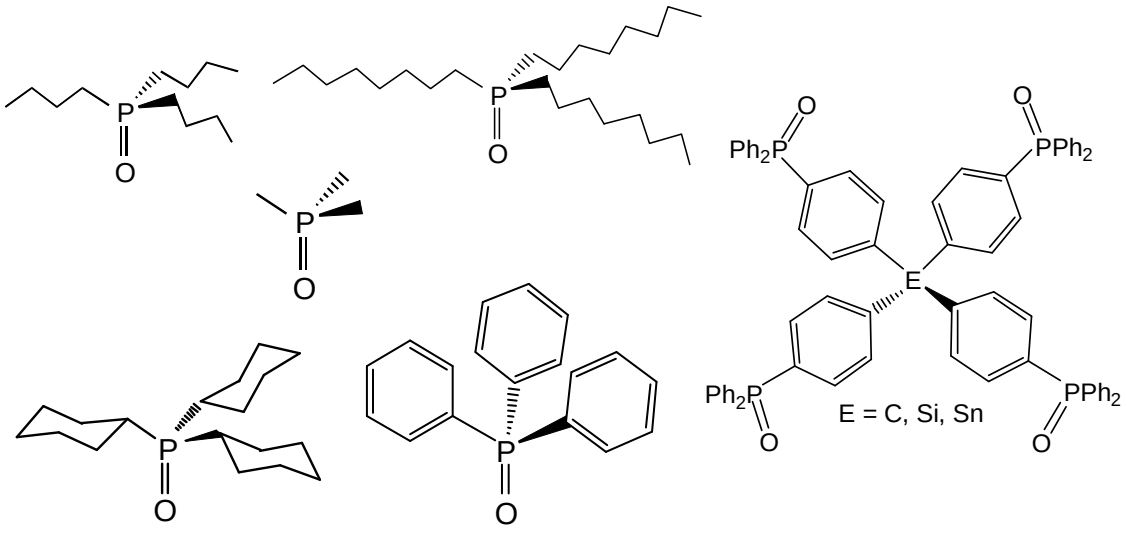

Figure 1.3. Model phosphine oxides for adsorption studies.

In surface coverage studies it will be determined how much material is necessary

to adsorb a monolayer of phosphine oxide molecules on the silica surface and how this correlates with the sizes of the phosphine oxides. These values from molecules with extended alkyl chains can then be compared with those from the adsorption of the cages (**I**–**III**), optimally providing insight into the degree of "deflation" (height) of the cages on the surface. Next, leaching tests will be performed to establish in which solvents the phosphine oxides will remain at the silica surface and in which they will be fully removed. This, in combination with leaching studies of the model compounds, will provide insights into the mechanism of detachment of the phosphine oxides from the surface. For example, the leaching could be propagated by replacement of the phosphine oxides by solvent molecules on the surface, or it could simply be enhanced by the solubility of the molecule in the corresponding solvent. Understanding the leaching process on a molecular level is also very important for future applications of immobilized catalysts, where the monoxide cages could be tethered to the surface, given that the adsorption is strong enough. The surface mobility of the model phosphine oxides in the presence of different solvents will be further investigated using High Resolution Magic Angle Spinning (HRMAS) NMR.

The adsorption of the tetraphosphine oxide (Figure 1.3) is of interest because this system also contains multiple equivalent phosphorus nuclei bound within one molecule, which in turn implies that they will all have the same translational mobility on the silica surface, while maximally three P=O groups can interact with the surface at a given time. The corresponding tetraphosphine cannot be adsorbed on a silica surface, probably because of the rigid nature of the molecule and the resulting unfavorable directions of the lone pairs at the phosphorus atoms.[10] The tetraphosphine oxide with its two lone pairs at the oxygen atoms eases this steric requirement for adsorption, and in case it can be adsorbed, this assumption is corroborated. Finally, due to the rigid tetrahedral

structure of the compound, maximally three of its phosphine oxide groups can be adsorbed on the silica surface at one time, so it will be interesting to observe differences in the ^{31}P chemical shifts and CSA values of the adsorbed and not adsorbed phosphine oxide groups, and to quantify the number of P=O groups per molecule interacting with the surface at one time.

While gaining more insight into the interactions of phosphine oxides with silica surfaces using model compounds, the synthesis of the cages **I**, **II**, and **III** (Figure 1.2) in a variety of sizes is imperative. In the literature no diphosphine cages or related systems containing between 5 to 12 CH_2 groups in their alkyl chains can be found. As discussed above, these cages are, however, ideal candidates for our applications in surface science studies. It should be noted at this point that during the course of this work many organic routes have been conceived and attempted exhaustively for the synthesis of small diphosphine cages and their derivatives **I**–**III**, but there are many challenges to face with multiple substitution reactions and functional group compatibility of the starting materials**.**

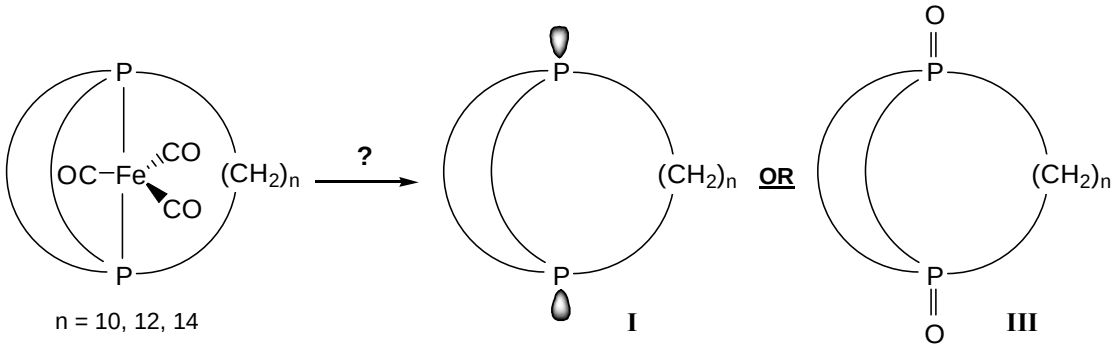

Scheme 1.1. Synthesis of diphosphine (**I**) or diphosphine dioxide (**III**) cages from the corresponding Fe gyroscopes.

Therefore, attention in this dissertation is primarily placed on the synthesis of diphosphine (**I**) and diphosphine dioxide (**III**) cages from the corresponding Fe gyroscope starting materials (Scheme 1.1).[15] Fe gyroscopes are less expensive than their Pt analogs, which had been used to synthesize cage **1**, and with Fe as the center one can access smaller cage sizes as mentioned before. In order to investigate the chemistry of the Fe gyroscopes, several model Fe phosphine complexes will be produced, and methods to remove the $Fe(CO)_3$ fragment from the coordinated ligands will be tested. Different reagents will ideally lead to the uncoordinated phosphines or desired derivatives, such as the phosphine oxides. Once a technique is found to remove the Fe in high yields, the procedure will be applied to remove the Fe cores of the gyroscopes to form the desired cages **I** and **III** in high yields and large amounts.

CHAPTER II

SYNTHESIS, PURIFICATION, AND CHARACTERIZATION OF PHOSPHINE OXIDES AND THEIR HYDROGEN PEROXIDE ADDUCTS*

INTRODUCTION

Phosphines represent one of the most important and ubiquitous classes of substances. Due to their unique properties they play prominent roles as ligands in coordination chemistry and catalysis.[16,18,19] Phosphine oxides are equally important but receive less attention due to various factors. In some cases they are unavoidable stoichiometric side-products. This is, for example, the case for the Wittig reaction and its variations,[20] the Staudinger reaction,[21] or the Appel[22] reaction. Separating the products from the phosphine oxides after these reactions can be rather tedious. In other cases, phosphine oxides might be the sign of insufficient exclusion of oxygen when the phosphine was the actual target molecule of any synthesis or application.

Every chemist working with phosphine ligands has to deal with phosphine oxides to some extent and these, in turn, can be oxidized to form a variety of products.[23] Therefore, it is surprising that they do not receive more attention in the literature. Much of the knowledge about phosphine oxides within research groups working with phosphines is anecdotal. This is in part because they are elusive species regarding their nature and characterization. For example, they form adducts with H_2O,[24] boranes,[25] or H_2O_2.[26] Furthermore, their ^{31}P NMR chemical shifts are very solvent dependent (see below), and the chemical shift range is fairly uncharacteristic. Therefore, they can, for example, easily be confused with phosphonium salts.[27]

---

* Hilliard, C. R.; Bhuvanesh, N.; Gladysz, J. A.; Blümel, J. *Dalton Trans.* **2012**, *41*, 1742–1754. - Reproduced by permission of The Royal Society of Chemistry (RSC). http://pubs.rsc.org/en/content/articlelanding/2012/dt/c1dt11863c

However, recently a systematic and mechanistic study has provided a deeper insight into the oxidation process of phosphines with molecular oxygen.[23a] Phosphine oxides are also becoming increasingly important as probes for the surface acidity of oxide supports, such as silica or alumina, due to their strong interactions with surface hydroxyl groups. Most of these studies have been conducted using trialkyl phosphine oxides such as $Me_3P{=}O$[5,7–9,28] and $Oct_3P{=}O$[8c] as the probes. Additionally, interesting metal complexes have been characterized with one,[29] two,[30] or three[31] oxygen-bound tertiary phosphine oxide ligands. Furthermore, there is a great potential in secondary phosphine oxides as pre-ligands in catalysis.[32]

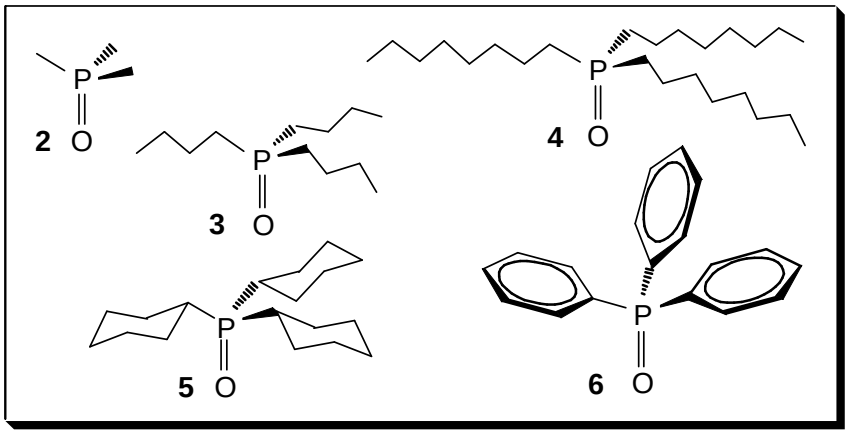

Scheme 2.1. Representative tertiary phosphine oxides **2**–**6** used in this work.

The interest of our group in phosphine oxides is multi-fold. We need clean, adduct-free phosphine oxides with different electronic and steric characteristics for studying adsorption processes on oxide surfaces and the dynamics of the adsorbed species.[33] Many of the strategically important phosphine oxides we require, such as $Sn(p\text{-}C_6H_4P(O)Ph_2)_4$,[33] cannot be purchased and have to be synthesized from the

corresponding phosphines. Furthermore, we have to be able to identify quickly and reliably side-products that can form during the immobilization of phosphine linkers incorporating ethoxysilane groups on oxide surfaces.[27] Therefore, baseline data regarding the NMR and IR spectroscopic characteristics of phosphine oxides and their adducts in solution and in the solid state is essential.

The main focus of this paper is threefold: (i) to explore quick and selective methods for the oxidation of phosphines, (ii) to systematically characterize phosphine oxides in solution and in the solid state by NMR and IR spectroscopy, as well as X-ray crystallography, and distinguish them from their H_2O_2 and H_2O adducts, and (iii) to explore methods that allow the safe, quick, and efficient purification of the phosphine oxides.

The most obvious method to obtain phosphine oxides is the exposure of the corresponding phosphines to air.[23,34] However, this approach is surprisingly limited since many triaryl phosphines, such as triphenylphosphine, even in solution are not efficiently oxidized in air. This phenomenon has recently been described mechanistically by Buchwald.[23a] Another drawback is that the exposure of alkyl phosphines to air can afford numerous products involving insertions of oxygen into phosphorus–carbon bonds (see below).[23] Methods to transfer one single oxygen atom per phosphine have been described,[35] but the necessary reagents are not readily available and would have to be synthesized first.

Therefore, the alternative reaction with aqueous H_2O_2 will also be investigated here. Using a selection of representative alkyl and aryl phosphines, it will be demonstrated that the physical and spectroscopic characteristics of phosphine oxides and their water and hydrogen peroxide adducts are distinctly different from each other. Finally, methods to obtain the adduct-free representative alkyl and aryl

phosphine oxides **2**–**6** (Scheme 2.1) are discussed. Two successful procedures are described, one of which is optimized.

RESULTS AND DISCUSSION

Distinguishing Phosphine Oxides from Their H_2O_2 Adducts

(a) NMR Spectroscopy

Probably the most intriguing part of working with phosphine oxides and their hydrogen peroxide adducts is that the chemical shifts are extremely solvent dependent. In order to obtain accurate chemical shift values with one measurement, we used $ClPPh_2$ as the chemical shift standard in a capillary insert centered in the NMR tubes (details: see Experimental section). Table 2.1 compares the ^{31}P chemical shifts of **2**–**6** and their corresponding H_2O_2 adducts **2a**–**6a** (generated as described below) in benzene and chloroform. For example, when **2** is measured in $CDCl_3$ instead of benzene the signal migrates downfield about 6 ppm. The dependence of $\delta(^{31}P)$ on the solvent is less pronounced for the hydrogen peroxide adducts. Most probably, this reflects the fact that the P=O group is strongly interacting with H_2O_2 by hydrogen bonding and less prone to interactions with solvent molecules. However, even within this class of compounds, the ^{31}P NMR signal of **6a** migrates about 2.6 ppm downfield when changing the solvent from benzene to $CDCl_3$. In general, benzene exerts a shielding effect on the P=O group for both the phosphine oxides and their H_2O_2 adducts (Table 2.1).

Table 2.1. ^{31}P NMR chemical shifts δ [ppm] of the phosphine oxides **2**–**6** and their corresponding H_2O_2 adducts **2a**–**6a** in C_6D_6 and $CDCl_3$ and the differences $\Delta\delta(^{31}P) = \delta(\text{adduct}) - \delta(\text{phosphine oxide})$.

$R_3P=O$ / H_2O_2 adducts	$\delta(^{31}P)$ C_6D_6	$\Delta\delta(^{31}P)$ C_6D_6	$\delta(^{31}P)$ $CDCl_3$	$\Delta\delta(^{31}P)$ $CDCl_3$
2 / **2a**	32.65 / – [a]	– [a]	38.79 / 43.23	4.44
3 / **3a**	43.66 / 51.12	7.46	48.57 / 52.50	3.93
4 / **4a**	43.93 / 48.60	4.67	48.48 / 50.01	1.53
5 / **5a**	46.31 / 50.28	3.97	49.91 / 51.53	1.62
6 / **6a**	25.16 / 27.52	2.36	29.10 / 30.15	1.05

[a] **2a** is not soluble enough in C_6D_6 to observe a signal.

Most significant analytically is the large change of the chemical shift when going from the phosphine oxides to their corresponding H_2O_2 adducts. Figure 2.1 visualizes this dramatic effect for **3** and **3a** in C_6D_6. As it can be read from the values given in Table 2.1, the chemical shift differences can amount to nearly 8 ppm (**3**/**3a**) in benzene. Overall, these shift differences between the substance classes are more pronounced in benzene than in $CDCl_3$. As a general trend, the signals of the H_2O_2 adducts appear downfield from the phosphine oxides. This is in accordance with expectations since the hydrogen bonding of H_2O_2 to the oxygen of the P=O group should lead to a deshielding of the phosphorus nucleus.

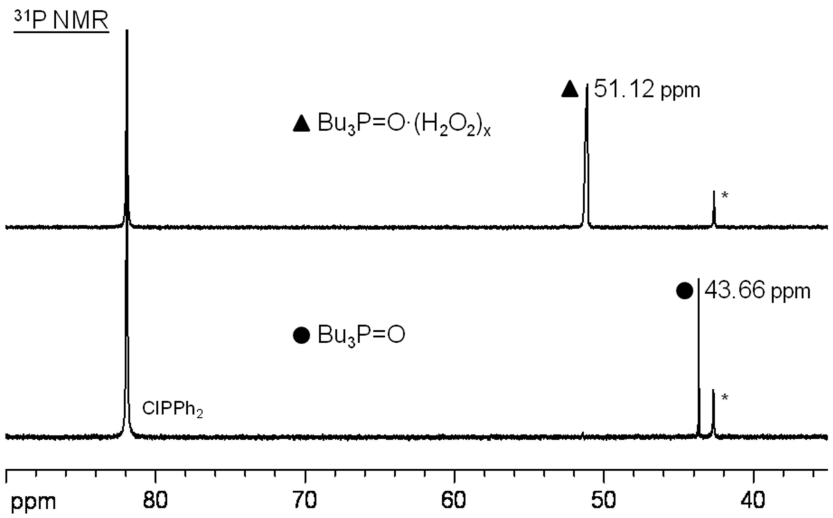

Figure 2.1. ^{31}P NMR spectra of **3** (bottom trace) and **3a** (top trace) in C_6D_6. The asterisks denote traces of $Ph_2ClP{=}O$ in the capillary, which stem from oxidation of the standard Ph_2PCl (see Experimental section).

In addition to the chemical shift issue, the lines of the H_2O_2 adducts are often broad due to the non-stoichiometric interactions of the phosphine oxides with H_2O_2, H_2O, and exchanges with solvent molecules. Furthermore, larger aggregates might form due to the strong intermolecular hydrogen bonding with H_2O_2.

Therefore, we investigated the dependence of $\delta(^{31}P)$ of **3**, **3a**, **6**, and **6a** on their concentration in solution. Benzene has been chosen as the solvent for this quantitative analysis because it leads to the largest $\delta(^{31}P)$ difference between the phosphine oxides and their H_2O_2 adducts (Table 2.1). For **3** and **6**, the ^{31}P chemical shift changes with concentration are minimal. For example, $\delta(^{31}P)$ of **6** varies within a 0.12 ppm range without a clearly distinguishable trend when increasing the concentration from 0.010 to 0.080 mol/L (see Experimental section for stepwise procedure). A concentration change from 0.10 to 0.75 mol/L for **3** results in a chemical shift variation of 0.27 ppm. For both

the H_2O_2 adducts **3a** and **6a**, the changes of $\delta(^{31}P)$ are larger, and characteristic curves are obtained. Figure 2.2 shows the graphical display for **3a**. Overall the chemical shift increases for **3a** (**6a**) by 0.87 (1.25) ppm when the concentration is changed from 0.10 (0.010) to 2.0 (0.080) mol/L. Since at very low concentrations the $\delta(^{31}P)$ for the adducts show a trend towards the phosphine oxides **3** and **6**, we conclude that the solvent is, to some extent, able to break up agglomerated molecules and replace the H_2O_2. However, even with extreme dilution, the very different chemical shifts of the adduct-free phosphine oxides are not reached. Furthermore, the overall chemical shift changes over a dilution range of at least an order of magnitude are noticeable, but far from the $\delta(^{31}P)$ differences between phosphine oxides and their corresponding H_2O_2 adducts.

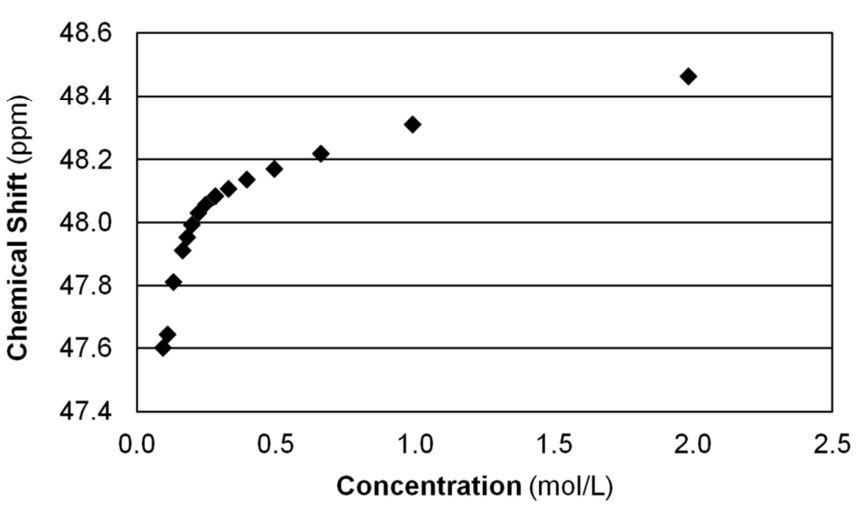

Figure 2.2. Change of the $\delta(^{31}P)$ of $Bu_3P{=}O{\cdot}(H_2O_2)$ (**3a**) with its concentration in C_6D_6.

Since the phosphine oxides $Me_3P{=}O$ (**2**) and $Bu_3P{=}O$ (**3**) are hygroscopic (see below), the dependence of $\delta(^{31}P)$ on the concentration of $\mathbf{3}{\cdot}H_2O$ in C_6D_6 has also

been investigated. The ^{31}P chemical shift of $Bu_3P{=}O{\cdot}H_2O$ changes from 44.35 to 43.60 ppm upon dilution of a 0.36 molar to a 0.05 molar solution, which results again in a noticeable but not crucial overall $\delta(^{31}P)$ change of 0.75 ppm.

In contrast to **2** and **3**, the phosphine oxides **4**–**6** are not hygroscopic. $Me_3P{=}O$ (**2**) is even more hygroscopic than $Bu_3P{=}O$ (**3**),[24] and any exposure to humid air changes the crystalline solid to an oil within less than 5 minutes. Figure 2.3 illustrates the gravimetrically determined uptake of H_2O with time for **2** and **3**. $Me_3P{=}O$ not only absorbs H_2O faster but also a larger amount of it, as compared to **3**. Saturation is reached when the ratio of **2** : H_2O is about 1 : 3.5. On the same timeline, **3** is saturated when the ratio of **3** : H_2O is about 1 : 1.

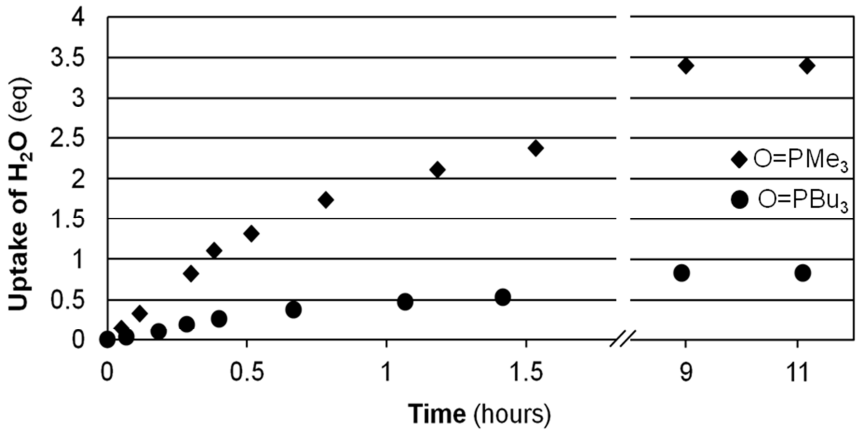

Figure 2.3. Water uptake of $Me_3P{=}O$ (**2**) and $Bu_3P{=}O$ (**3**) in air.

In the previous section we described that with careful chemical shift referencing, it is possible to distinguish the phosphine oxides from their H_2O_2 adducts by ^{31}P NMR in solution. In the solid-state NMR spectra,[36] due to the lack of solvent interactions and exchange equilibria, narrow lines are expected for the

polycrystalline materials. Unfortunately, most of the phosphine oxides **2**–**6** and especially the H_2O_2 adducts **2a**–**6a** are liquids or low-melting solids (see Fig. 2.13 below) that would undergo a phase change under the pressures and elevated temperatures[37] of MAS (Magic Angle Spinning).[36] But for the pairs **5**/**5a** and **6**/**6a**, the CSA (Chemical Shift Anisotropy)[36a] data and ^{31}P MAS spectra could be obtained. Figures 2.4 and 2.5 show, for example, the MAS and wideline spectra of **6** and **6a**. In accordance with our expectation for crystalline material, the residual linewidths of the isotropic peaks in the MAS spectra are only 166 Hz for **6** and 261/268 Hz for the two lines of **6a**. The isotropic lines can easily be determined by varying the rotational speed because in contrast to the rotational sidebands, they are static and do not change their positions.

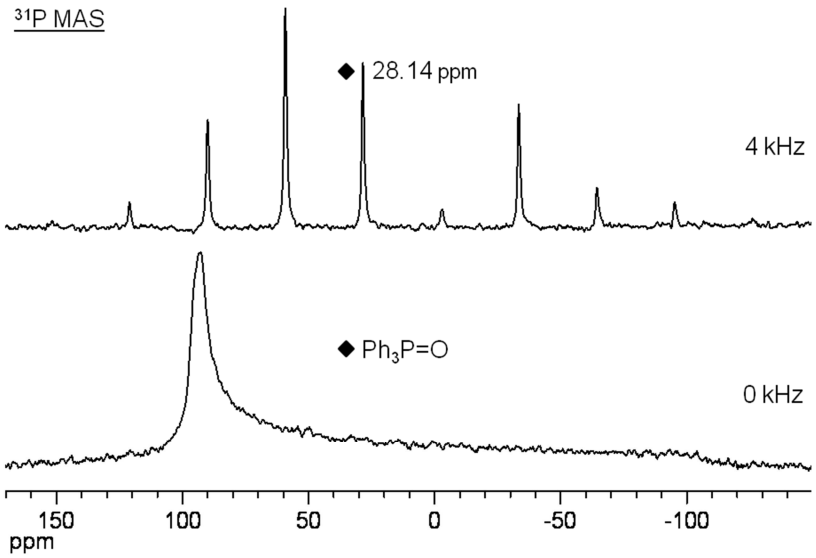

Figure 2.4. ^{31}P MAS (top, 4 kHz) and wideline (bottom, 0 kHz) spectra of polycrystalline **6**. The $\delta(^{31}P)$ value is given for the isotropic chemical shift in the MAS spectrum; the other lines are rotational sidebands.

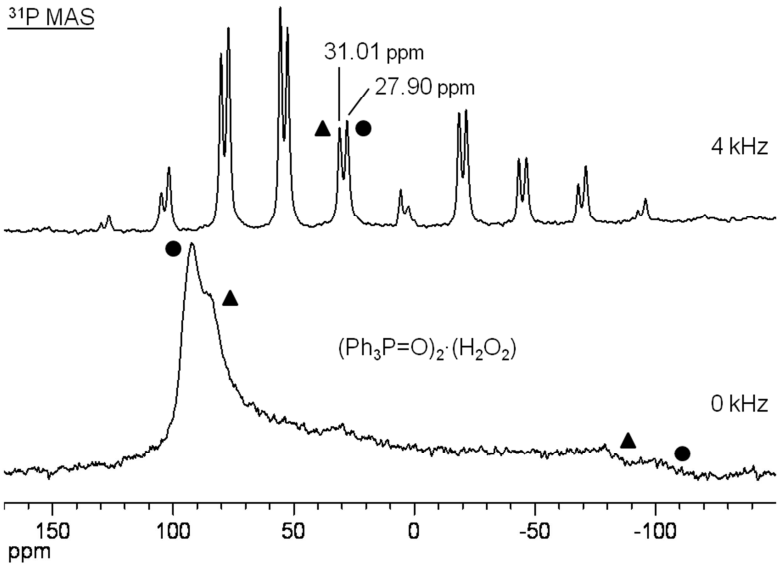

Figure 2.5. ^{31}P MAS (top, 4 kHz) and wideline (bottom, 0 kHz) spectra of polycrystalline **6a**. The $\delta(^{31}P)$ values are given for the two isotropic chemical shifts in the MAS spectrum; the other lines are the rotational sidebands. The symbols represent the δ_{11} and δ_{33} of the two corresponding CSA patterns.

The $\delta(^{31}P)$ of 28.14 ppm for the isotropic line in the solid-state NMR spectrum of **6** (Figure 2.4) lies within the chemical shift ranges found in solution (Table 2.1). There is only one isotropic line for **6**, as expected from earlier results[38] and tri(*p*-tolyl)phosphine oxide.[38c] This is also in accordance with the single crystal X-ray structures of **6**[39] or **3** (see below), which imply that all phosphorus nuclei in the unit cell are magnetically equivalent.

In contrast, the polycrystalline H_2O_2 adduct **6a** displays two isotropic lines in the ^{31}P MAS spectrum (Figure 2.5). The chemical shifts of 31.01 and 27.90 ppm are close to the values found in solution (Table 2.1). Since the intensity ratio of both lines, including the rotational sideband intensities in the integration, is about 1 : 1, the presence of polymorphs is unlikely. The two isotropic lines most probably stem

from two magnetically inequivalent phosphorus nuclei in the unit cell. This is corroborated by the single crystal X-ray structure of the compound $(Ph_3P{=}O)_2{\cdot}(H_2O_2)$,[26c] where one H_2O_2 molecule bridges two $Ph_3P{=}O$ molecules, which leads to two magnetically independent phosphorus nuclei in the unit cell. Additionally, the unit cell of the single crystal of $Cy_3P{=}O{\cdot}(H_2O_2)$ (see below) contains two magnetically inequivalent P nuclei. The splitting of isotropic lines in the ^{31}P MAS spectra of polycrystalline compounds is also often observed for chelate phosphine ligands and metal complexes thereof. For example, $(Ph_2PCH_2)_3SiOEt$ featured three isotropic lines with equal intensities but with a large difference in their chemical shifts.[40] $(Ph_2PCH_2)_2Si(OEt)_2$ and diverse nickel complexes with chelate phosphine ligands[36d,40] always gave two isotropic lines with similar chemical shifts.

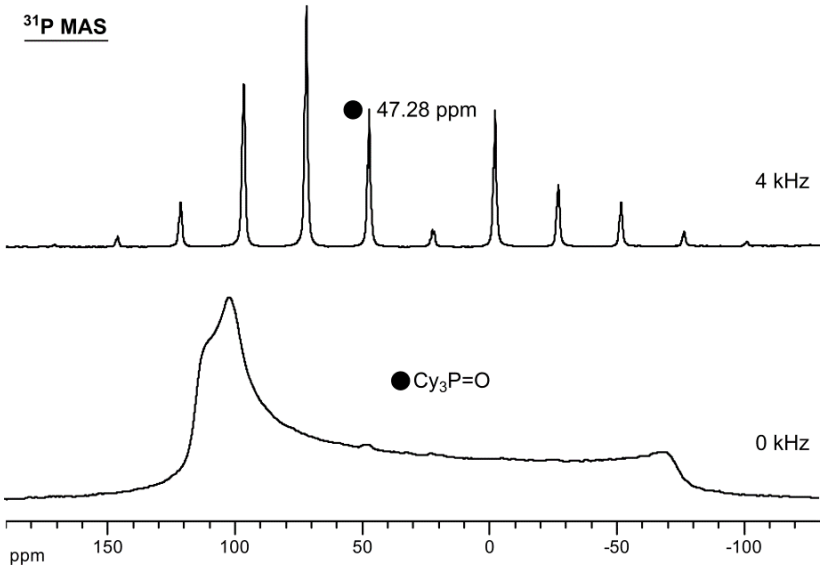

Figure 2.6. ^{31}P MAS (top, 4 kHz) and wideline (bottom, 0 kHz) spectra of polycrystalline **5**. The $\delta(^{31}P)$ value is given for the isotropic chemical shift in the MAS spectrum; the other lines are rotational sidebands.

$Cy_3P{=}O$ (**5**) and its H_2O_2 adduct **5a** exhibit analogous solid-state NMR characteristics as shown in Figures 2.6 and 2.7. The only isotropic signal of **5** has a chemical shift of 47.28 ppm, which lies within the δ ranges found in solution. The residual linewidth is only 158 Hz, so overlapping of two or more isotropic signals is unlikely. Analogous to **6a**, the ^{31}P MAS spectrum of the polycrystalline H_2O_2 adduct **5a** displays two isotropic lines with a 1 : 1 intensity ratio of the signals including the rotational sidebands (Figure 2.7). The chemical shifts of 53.52 and 47.18 ppm are again close to the values found in solution (Table 2.1).

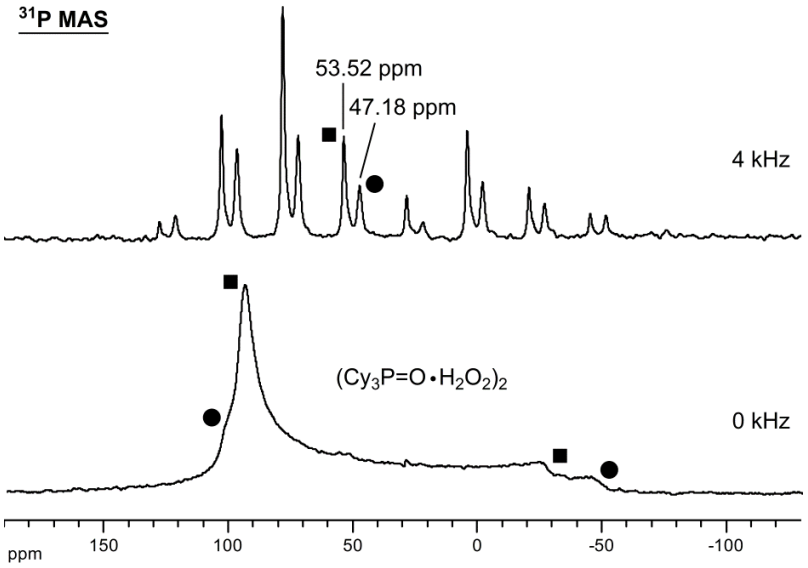

Figure 2.7. ^{31}P MAS (top, 4 kHz) and wideline (bottom, 0 kHz) spectra of polycrystalline **5a**. The $\delta(^{31}P)$ values are given for the two isotropic chemical shifts in the MAS spectrum; the other lines are the rotational sidebands. The symbols represent the δ_{11} and δ_{33} of the two corresponding CSA patterns.

The ^{31}P MAS spectra of the triarylphosphine oxide **6** and its H_2O_2 adduct **6a**

could be obtained with only 64 scans at the moderate spinning speeds of 4 and 5 kHz. Therefore, the wideline spectra without rotation could be recorded as well (Figures 2.4 and 2.5). The Chemical Shift Anisotropy of **6**, defined as the span of the wideline signal,[36a] is about 200 ppm and therewith matches the literature values for **6** (CSA 195–200 ppm),[38] for tri(*p*-tolyl)phosphine oxide (CSA 155 ppm),[38c] or for the trialkylphosphine oxide (n-$C_{14}H_{29})_3P{=}O$ (CSA 190 ppm).[38a] The CSA of the ^{31}P wideline signal of **6a** is substantially smaller with about 170 and 200 ppm for the two ^{31}P wideline signals (Figure 2.5).

The reduction of the CSA on going from a phosphine oxide to its adduct is even more pronounced for the pair **5/5a**. The span of the wideline signal is about 153 ppm for **5** and about 128 and 147 ppm for **5a** (Figures 2.6 and 2.7). In this case, however, the wideline patterns of both signals are not as clearly distinct as for **6a**.

The general CSA reduction on going from the phosphine oxides to their H_2O_2 adducts reflects the fact that with the adduct formation the P=O bond order and its polarity decrease, in accordance with the IR analysis (see below). For example, in the extreme case of decreasing the P=O bond order on going from $Ph_3P{=}O$ to $[Ph_3POEt]BF_4$ the CSA decreases from 195–200 ppm[38a,b] to 74 ppm.[27c] In analogy to H_2O_2 adduct formation, substantial reduction in the CSA is also observed when phosphine oxides are adsorbed on oxide supports, such as silica, as the P=O groups interact with surface silanol groups and undergo partial quaternization.[33]

(b) Crystallography

The crystal structure of a water clathrate of **3** (**3**·$(H_2O)_{34.5}$) has been reported[41] but not the pure substance. Accordingly, suitable crystals of **3** were obtained, X-ray data were collected, and the structure was solved as described in the

Experimental section. This gave the structures displayed in Figures 2.8 and 2.9. The bond lengths and angles about phosphorus (Figure 2.8) were routine. Presumably due to dipole-dipole interactions, a O=P····O=P stacking motif was observed. This has also been found with other crystalline phosphine oxides such as **5**[42] and **6**.[39] These stacking motifs may be relevant for the potential formation of bilayers on silica surfaces.[33] The intermolecular O···P distance, 3.587 Å, exceeds the sum of the van der Waals radii of the oxygen and phosphorus atoms (1.52 and 1.80 Å).[43] The adjacent P=O linkages within a stack are not perfectly aligned, as reflected by intermolecular O–P–O and P–O–P angles of 179.2° and 174.0°.

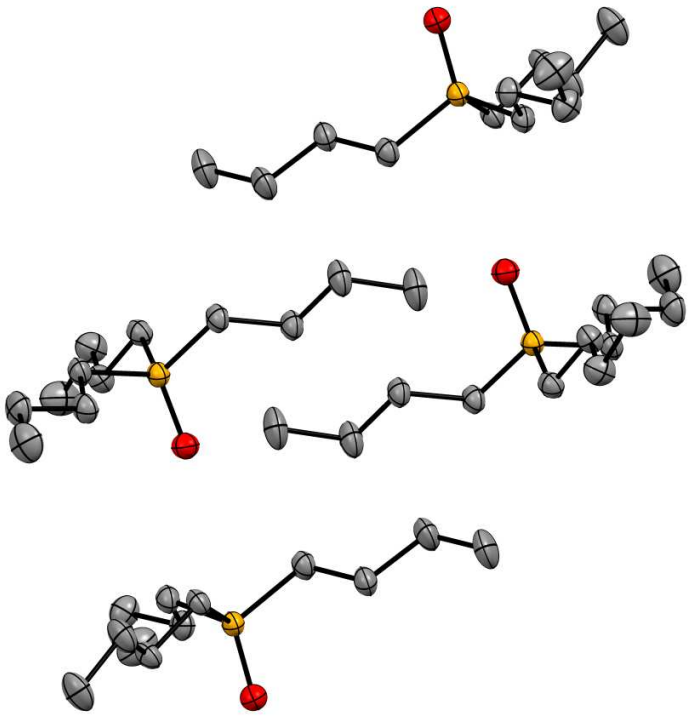

Figure 2.8. Single crystal X-ray structure of $Bu_3P{=}O$ (**3**), view from showing the aligned P=O bonds. Selected bond lengths (Å) and angles (°): P(1)–O(1) 1.489(2), P(1)–C(1) 1.797(3), P(1)–C(5) 1.798(2), P(1)–C(9) 1.798(2), O(1)–P(1)–C(1) 113.10(10), O(1)–P(1)–C(5) 112.90(10), O(1)–P(1)–C(9) 113.11(10).

The butyl groups crystallize in all-anti conformations. Figure 2.7 illustrates that the butyl groups are slightly staggered between adjacent molecules in a stack, as quantified by a C1–P–P–C1 torsion angle of 38.8°. Importantly, the structure does not contradict the finding of only one isotropic line in the MAS spectra of **5** and **6** (see above).

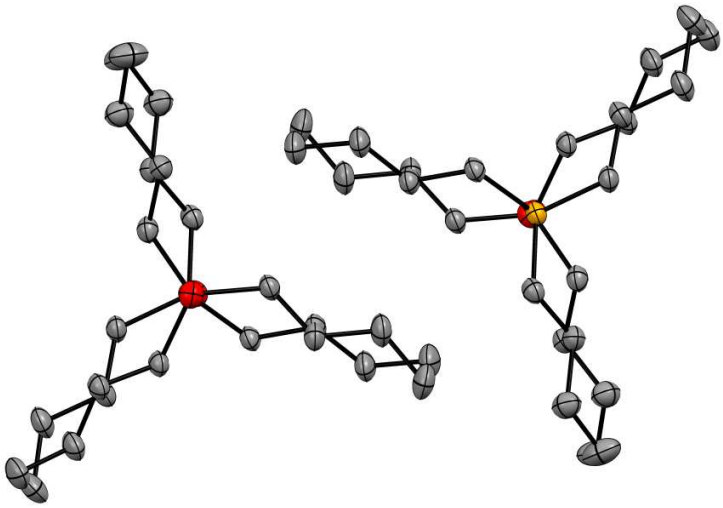

Figure 2.9. Single crystal X-ray structure of $Bu_3P{=}O$ (**3**), view along the P=O bond.

Only one crystal structure of a H_2O_2 adduct of a phosphine oxide, the 2 : 1 complex **6**·HOOH·**6** or $(Ph_3P{=}O)_2{\cdot}(H_2O_2)$, has been previously reported.[26c] Suitable crystals of the 1 : 1 complex **5a** were obtained as described in the Experimental section. X-ray data were collected and the structure was solved in a routine manner that included the location and refinement of the oxygen-bound hydrogen atoms. This gave the cyclic dimeric structure $(Cy_3P{=}O{\cdot}H_2O_2)_2$ or $(\mathbf{5a})_2$ displayed in Figures 2.10 and 2.11. The adduct features two hydrogen bonds to each phosphine oxide oxygen

atom, with an inversion center in the midpoint of the plane formed by the four H_2O_2 oxygen atoms.

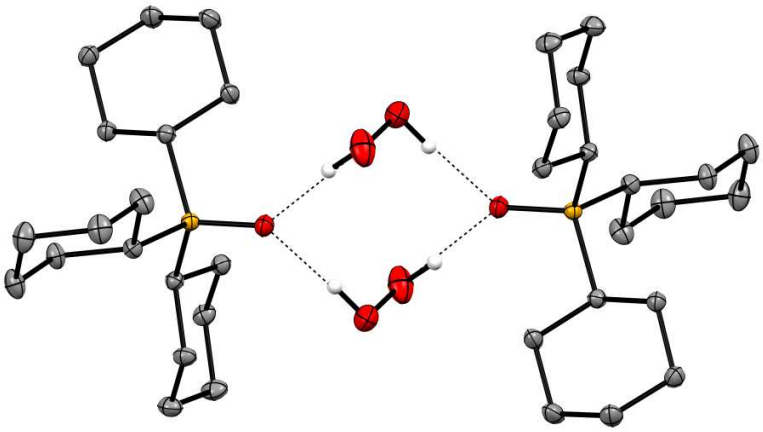

Figure 2.10. Single crystal X-ray structure of the dimer of **5a**. Selected bond lengths (Å) and angles (°): P(1)–O(1) 1.5045(9), P(1)–C(1) 1.8190(12), P(1)–C(7) 1.8209(12), P(1)–C(13) 1.8258(12), O(1)–P(1)–C(1) 111.03(5), O(1)–H(20) 1.876, H(20)–O(20) 0.896, O(20)–O(21) 1.4504(15), O(21)–H(21) 0.895, O(1)–P(1)–C(1) 113.03(5), O(1)–P(1)–C(7) 109.92(5), O(1)–P(1)–C(13) 112.04(5), P(1)–O(1)–H(20) 129.1, O(1)–H(20)–O(20) 176.0, (H20)–O(20)–O(21) 103.2, (O20)–O(21)–H(21) 100.4.

The P=O linkage in $(\mathbf{5a})_2$ proves to be somewhat longer than that in the corresponding phosphine oxide **5**[42] (1.5045(9) vs. 1.490(2) Å). The P=O···H distance (1.876 Å) is in the typical range for hydrogen bonds, and the O···O distance in the P=O···H−O unit (2.743 Å) compares with that in $(Ph_3P{=}O)_2{\cdot}(H_2O_2)$ (2.759 Å), for which the oxygen-bound hydrogen atom could not be located.[26c]

The cyclohexyl rings and the assembly defined by the six oxygen atoms adopt chair conformations. Within the latter, the HO−OH distance is within experimental error of that in crystalline H_2O_2 (1.4504(15) vs. 1.453(7) Å).[44] The dihedral angles

defined by the HO−OH and (P=O)···O−O···(O=P) units (89.54° and 87.10°) are also very close to the dihedral angle in crystalline H_2O_2 (90.2(6)°). Hence, the structure of H_2O_2 is not appreciably affected by bonding to **5**.

Importantly, Figures 2.10 and 2.11 corroborate the finding of two isotropic lines in the ^{31}P solid-state NMR spectra of the H_2O_2 adducts of the phosphine oxides, because there are two magnetically independent phosphorus nuclei in the unit cell.

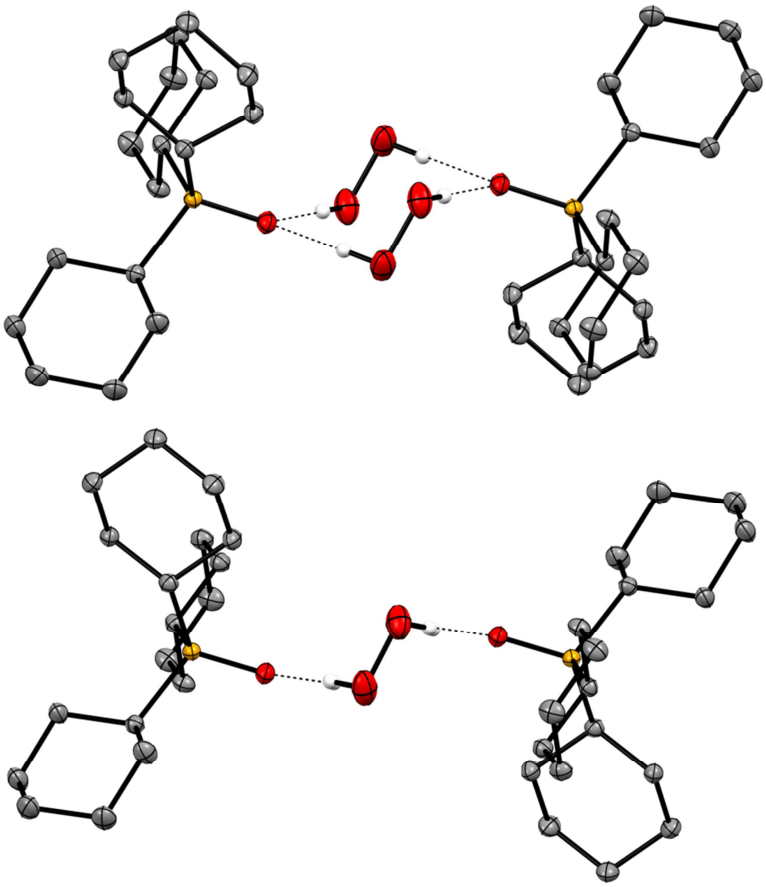

Figure 2.11. Additional views of the single crystal X-ray structure of the dimer of **5a**. Top: tilted side view, bottom: side view.

(c) IR Spectroscopy

IR spectroscopy[45] provides unique insight into the phosphine oxide and H_2O_2 adduct scenario because it probes both the P=O groups[26b,46] and all O–H species[26b] via their stretching vibrations. As in solid-state NMR, the IR spectra can be recorded using the neat liquid or polycrystalline samples, and therefore, the results are independent of any interactions of the functional groups with solvents. Figure 2.12 shows, as a representative case, the IR spectra of **2** (top), **2a** (bottom), and **2a** after partial decomposition of the bound H_2O_2 as described below (middle). Table 2.2 summarizes all IR data.

As the predominant analytical features, the spectrum of **3** (Figure 2.12, bottom) shows only the bands typical for C–H stretching absorptions below 3000 cm^{-1} and the P=O stretching band at 1153 cm^{-1}. All bands are very narrow, indicating that the vibrations within the molecules are well-defined.

In contrast, while the C–H stretching bands are practically unchanged as compared to **3**, the IR spectrum of **3a** (Figure 2.12, top) shows a broad O–H stretching band for the bound H_2O_2 at 3217 cm^{-1}.[26b] The intense P=O band has shifted to the lower wavenumber of 1123 cm^{-1}. This indicates that the P=O bond order has decreased, rendering the corresponding stretching vibration lower in energy. This change goes along with the broadening of the line because of the less well-defined vibrations due to the hydrogen bonding interactions with the H_2O_2 molecules.

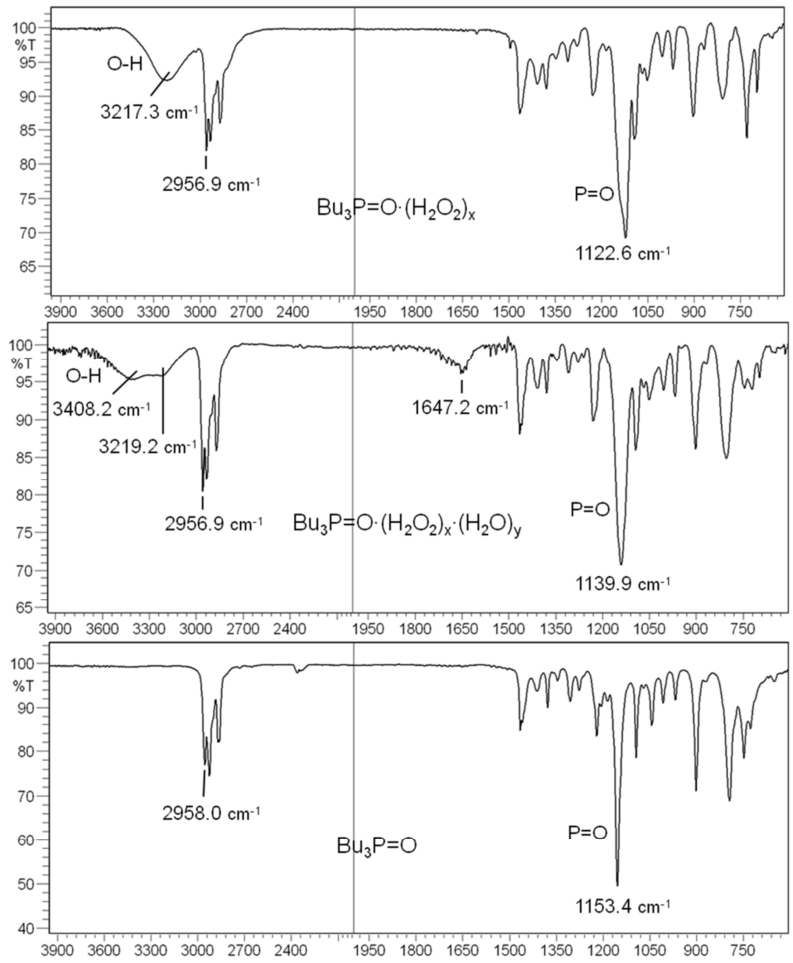

Figure 2.12. IR spectra of neat **3** (bottom), **3a** (top), and **3a** with adsorbed H_2O after partial decomposition of the bound H_2O_2 (middle).

When the H_2O_2 molecule in **3a** is partially decomposed thermally, the H_2O strongly adsorbs to the P=O bond. Its O–H stretching vibration is distinctly different from that of adsorbed H_2O_2, but its band at 3408 cm^{-1} is also broad, as can be seen in the middle spectrum of Figure 2.12. The stretching band of the residual adsorbed H_2O_2 molecules remains practically unchanged at 3219 cm^{-1}. As an additional, analytically useful feature, the overtone of the O–H absorption of the H_2O band

appears at about 1647 cm^{-1}, as described in the literature for adducts of $Ph_3P=O$.[26b] Again, the P=O stretching frequency is broad and found at a lower wavenumber (1140 cm^{-1}) for **3**·$(H_2O_2)_x(H_2O)_y$ (x,y = 0.5–1.0) than for **3**.

Table 2.2. IR absorptions ν of the phosphine oxides **2**–**6** and their corresponding H_2O_2 adducts **2a**–**6a** and the wavenumber differences Δν(P=O) = ν(phosphine oxide) – ν(adduct).

$R_3P=O$ / H_2O_2 adduct	**ν(P=O)** [cm^{-1}]	**Δν(P=O)** [cm^{-1}]	**ν(O–H) of 2a–6a** [cm^{-1}]
2 / 2a	1161 / 1094	67	3217
3 / 3a	1153 / 1123	30	3217
4 / 4a	1144 / 1142	2	3217
5 / 5a	1157 / 1138	19	3264
6 / 6a	1188 / 1174	14	3233

Overall, IR spectroscopy is a powerful tool for quickly analyzing the nature and purity of phosphine oxides and their various adducts, and it was primarily used in the following experiments for characterizing all involved species and optimizing the two most promising procedures for obtaining clean phosphine oxides.

Controlled decomposition of the hydrogen peroxide adducts 2a–6a to give the phosphine oxides 2–6

(a) Syntheses of 2a–6a

When phosphines are oxidized in air, especially trialkylphosphines, an

astonishing multitude of byproducts are possible besides the desired phosphine oxides $R_3P{=}O$. Only Me_3P gives $Me_3P{=}O$ (**2**) in a reasonably clean reaction, most probably due to the fast oxidation process. The same is true for neat Ph_2PH, which forms $Ph_2HP{=}O$ exclusively in a radical oxidation process when exposed to air.[34] The predominant side-reaction is the additional insertion of oxygen atoms into P–C bonds[23] to form mainly phosphinic and phosphonic and occasionally phosphoric acid esters that can be identified by their $\delta(^{31}P)$.[23,27a,26e] For example, when toluene solutions of Bu_3P are exposed to air, a typical ^{31}P NMR spectrum would show the signal of the desired product $Bu_3P{=}O$ (**3**, 43.34 ppm, 44%), as well as resonances for the phosphinic acid ester $Bu_2(BuO)P{=}O$ (53.96 ppm, 45%), the phosphonic acid ester $Bu(BuO)_2P{=}O$ (36.28 ppm, 7%), traces of unidentified oxidation products around 30 ppm and unreacted phosphine (–32.20 ppm). The product ratio does not change with the reaction time, and we could not optimize this reaction to give only, or at least predominantly, **3**. Even if it was feasible to separate the product from the reaction mixture, all the side-products still lead to a diminished yield of phosphine oxide.

As an additional complicating factor, H_2O from the humid air can be adsorbed due to the formation of hydrogen bonds with the P=O group, rendering the analysis of mixtures by ^{31}P NMR difficult (see above). This H_2O uptake takes place preferentially with short alkyl chain substituents R, as discussed above. Triarylphosphines might not be oxidized by air at all.[23a] For example, Ph_3P is not transformed into the oxide **6** when dissolved in a nonpolar solvent and exposed to the ambient atmosphere for months. Taking all these limitations into account, the oxidation of phosphines by simple exposure to air is not a feasible or efficient way to obtain clean tertiary phosphine oxides. This overall scenario might also be responsible for the frustration that researchers can experience when handling

phosphines without carefully excluding air.

In contrast, when H_2O_2 is employed as the oxidant in the synthesis of phosphine oxides, no byproducts are obtained, and the reaction proceeds smoothly at room temperature and in a well-defined manner. However, H_2O_2 molecules form hydrogen bonds to the oxygen of the P=O bond and adducts of the type $R_3P{=}O{\cdot}(H_2O_2)_x$ with x = 0.5 to 1.0 are obtained. Interestingly, although the oxidation with hydrogen peroxide is performed in the presence of water, the latter seems to form weaker adducts and is not competitive, so that only H_2O_2 is bound to the products (Figure 2.12, top spectrum). The single crystal X-ray analysis of **6a** proves that two molecules of **6** are bound to one bridging H_2O_2 molecule.[26c] On the other hand, in the case of a H_2O_2 adduct of $Ph_3As{=}O$, a hydrogen-bonded network with a 1 : 1 ratio of arsine oxide to H_2O_2 has been found.[47] The hydrogen peroxide adducts **2a**–**4a** most likely have a less well-defined H_2O_2 to $R_3P{=}O$ ratio as they have an oily appearance and thus can easily be distinguished from the phosphine oxides **2**–**4**, which are all colorless powders, displayed for **3** and **3a** in Figure 2.13.

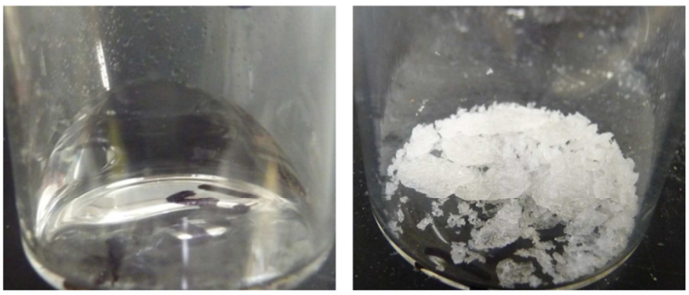

Figure 2.13. Physical appearance of neat $Bu_3P{=}O$ (**3**, right) and $Bu_3P{=}O{\cdot}(H_2O_2)_x$ (**3a**, left, x = 0.5–1.0) in a vial.

(b) Possible methods for decomposing the hydrogen peroxide adducts 2a–6a to give the phosphine oxides 2–6

There are several known approaches for decomposing H_2O_2 attached to phosphine oxides by hydrogen bonds. Bimetallic Pt–Pd surfaces are, for example, known to decompose H_2O_2.[48] Additionally, copper[26a] is reported to achieve the decomposition and also MnO_2.[26a] Furthermore, the adducts can be heated (> 100 ^oC) to release the oxygen from the bound H_2O_2.[26a] However, with the latter method, care has to be taken since the oxygen release can happen quickly, resulting in violent explosions. We tested and evaluated a selection of the known procedures for the decomposition of H_2O_2 attached to phosphine oxides and optimized new methods that also efficiently remove the resulting H_2O quantitatively.

Surprisingly, when we treated **3a** in benzene with freshly cut pieces of a Cu wire, even at higher temperatures and after prolonged exposure, no H_2O_2 decomposition occurred as assayed by IR spectroscopy. However, when **3a** was treated with MnO_2 powder, O_2 evolved immediately and vigorously, and IR spectroscopy confirmed the complete decomposition of H_2O_2. Unfortunately, the H_2O formed during this process remains strongly bound to **3a**. Furthermore, the fine MnO_2 powder could not be removed by standard filtration processes, rendering this process impractical.

Next, we tried silica as a model material for glass with a high surface area because it is generally known that aqueous H_2O_2 decomposes with time at the walls of glass bottles.[26a] Indeed, when stirring **3a** in toluene overnight with a slurry of silica that had not been dried prior to its application ("wet" silica, containing adsorbed H_2O and a maximal number of surface OH groups),[49] H_2O_2 decomposition was complete. However, IR revealed that the formed H_2O was still attached to **3a**,

and it could not be removed by treating the material with Na_2SO_4 or $MgSO_4$.

Since we had so far not found a way to obtain the water-free phosphine oxides from the hydrogen peroxide adducts, we investigated the option of thermal decomposition because then we would at least avoid further product separation steps. Heating **3a** in a toluene solution in order to decompose the attached H_2O_2 to obtain **3a**·$(H_2O)_x$ required 36 h and temperatures of up to 95 °C. Besides still being confronted with the task to remove the bound water, another practical drawback of this method is the time consuming removal of the relatively high-boiling solvents required. Therefore, we studied the decomposition of the neat adducts **2a**–**6a**. We worked on a small scale in melting point tubes behind a safety glass because according to our experience, H_2O_2 adducts of phosphines can lead to explosions when heated in neat form.

Table 2.3 summarizes the data obtained from the neat materials and provides the literature values for comparison. The decomposition of the bound H_2O_2 happens well below the actual boiling point of the corresponding adduct-free phosphine oxide.

Table 2.3 Melting points and decomposition temperature ranges [°C] of the phosphine oxides **2**–**6** and their corresponding H_2O_2 adducts **2a**–**6a**.

$R_3P=O$ / H_2O_2 adduct	**Decomp. temp. of neat H_2O_2 adduct[a]**	**mp of neat $R_3P=O$, obs.**	**mp of neat $R_3P=O^{lit}$**
2 / 2a	63–94	135–139	137.5–138.5[50]
3 / 3a	98–149	59–63	63–64[51]
4 / 4a	88–140	48–52	48–50[52]
5 / 5a	120–134	158–160	155–157[29]
6 / 6a	136–183	155–157	156.5–158[53]

[a] Values based on appearance of small bubbles in capillary during heating, which are attributed to evolution of oxygen from H_2O_2 decomposition.

As illustrated in Figure 2.14, the effervescence indicates the release of O_2 gas as H_2O_2 is broken down. The onset of the decomposition, as well as its temperature range, varies greatly between the adducts (Table 2.3). Naturally, the decomposition process is better visible for the viscous liquids **2a**–**4a** than for the powders **5a** and **6a**. Interestingly, for both **3a** and **4a** we found that around 150 °C there is a sudden onset of the formation of larger bubbles. We assign this phenomenon to the release of bound H_2O because this temperature is still well below the boiling points of **3a** and **4a**.

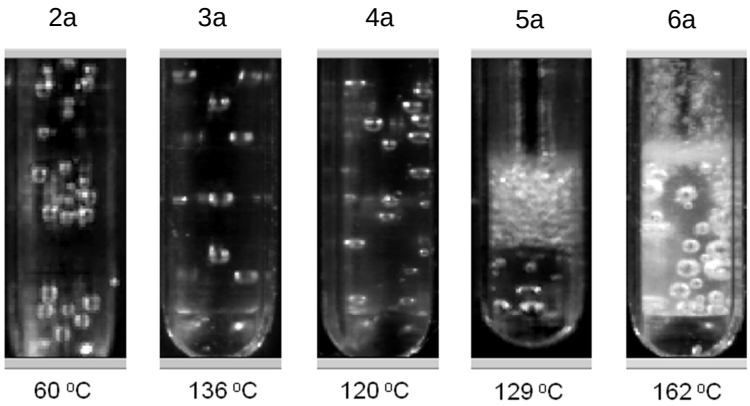

Figure 2.14. Evolution of small O_2 bubbles during decomposition of the neat materials $R_3P{=}O{\cdot}(H_2O_2)_x$ (x = 0.5–1.0) at the given temperatures (**2a**–**6a**).

While the decomposition of the bound H_2O_2 in neat **2a**–**6a** is clearly possible, this method suffers from the fact that water still remains in the samples. Furthermore, high temperatures are needed, and scaling up this process poses a safety risk. Therefore, as described in the following paragraph, we optimized two new methods that can be applied safely in any laboratory and leads to the clean phosphine oxides in a straightforward manner.

(c) Optimized method for decomposing the hydrogen peroxide adducts 2a–6a to give the phosphine oxides 2–6

All methods described in the previous section lead to the water adducts of the phosphine oxides and not the clean species $R_3P{=}O$. One of the safest methods consists of the treatment with silica, which can easily be separated from the supernatant with the product after the reaction. Therefore, instead of using the "wet" silica, we performed the same reaction with silica pre-dried at 200 °C for seven days *in vacuo*. The resulting silica surface should consist largely of siloxane groups with

only a minimal number of residual silanol moieties,[49] which might have the potential to compete with the phosphine oxides for the formed H_2O by adsorbing it. Being less reactive, pre-dried silica is our preferred support material for immobilized catalysts.[19,54] The diminished reactivity of a slurry of pre-dried silica in toluene manifests itself in the prolonged time of about 4 days needed to decompose the H_2O_2 in **3a**. Fortunately, however, IR spectroscopy of the supernatant proves the disappearance of O–H stretching bands for both H_2O_2 and residual water. The adduct-free and clean phosphine oxides can be obtained in this way. The only drawback of using silica is that phosphine oxides are strongly adsorbed at its surface.[33] Therefore, in order to diminish the loss of product, several wash cycles are required to detach the phosphine oxides from the silica surface.

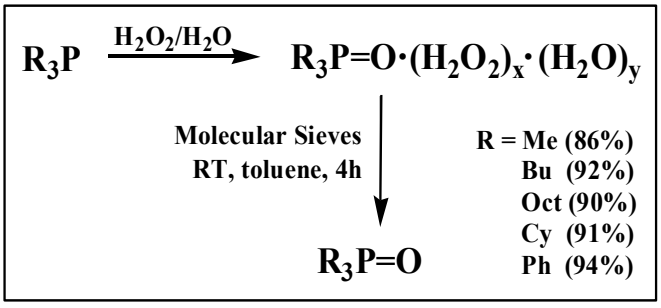

Scheme 2.2 Yields of clean phosphine oxides **2**–**6** with respect to the corresponding phosphines after oxidation with hydrogen peroxide to form **2a**–**6a**, decomposition of attached H_2O_2, and removal of water with molecular sieves (x,y = 0.5–1.0).

Our quest for a material that would decompose the H_2O_2 in **2a**–**6a** and at the same time quickly remove the resulting H_2O while releasing the phosphine oxides **2**–**6** easily after the reaction, led us to molecular sieves. This material seemed

promising to us because it is known to decompose 30% aqueous H_2O_2 at 80 °C.[55] Indeed, pre-dried molecular sieves with 3Å pore diameter allowed us to obtain the clean phosphine oxides from the corresponding phosphines in very high yields of up to 94% (Scheme 2.2). Most of the loss in the yield occurs in the biphasic oxidation step, as this requires the separation of organic and aqueous layers, and some of the H_2O_2 adducts of the phosphine oxides are rather soluble in water. The loss of the phosphine oxide products due to adsorption has been determined by model reactions to be minimal, less than 2 mol% per g of molecular sieves with the amounts and ratios of solids to phosphine oxides given in the Experimental section. The reason for this is that, in contrast to silica,[49] molecular sieves do not have a large number of acidic protons on the surface, which could strongly interact with the free electron pairs of phosphine oxides.

Using the molecular sieves, both for the decomposition of H_2O_2 and the removal of H_2O from the hygroscopic phosphine oxides were complete within 4 hours at room temperature. At the elevated temperature of 60 °C the whole process is complete within 1 h. The molecular sieves are best placed into a tea bag in order to facilitate stirring and their retrieval after the reaction (Figure 2.15). This protocol is safe and can easily be scaled up, and amounts of more than 5 g of molecular sieves pose no problem.

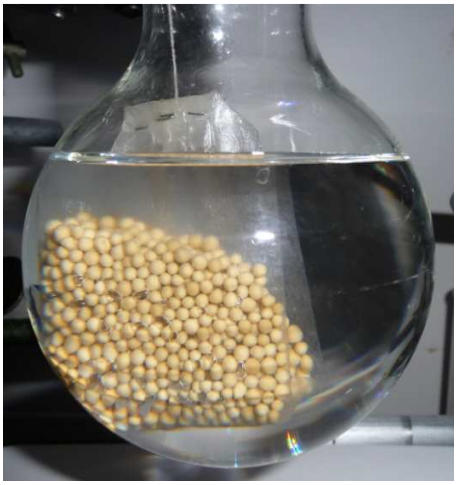

Figure 2.15. Molecular sieves placed in a tea bag and suspended in toluene in a round bottom flask for easy removal after the reaction.

CONCLUSION

It has been demonstrated that the ^{31}P NMR chemical shifts of phosphine oxides and their hydrogen peroxide and water adducts are very different. Furthermore, the ^{31}P solid-state NMR characteristics of the clean phosphine oxides are distinctly different from those of the hydrogen peroxide adducts. IR spectroscopy has been applied to distinguish between the neat phosphine oxides, their hydrogen peroxide adducts, and to detect adsorbed water. Single crystal X-ray structures of $Bu_3P{=}O$ and $Cy_3P{=}O{\cdot}(H_2O_2)$ have been determined, the latter being the first of its type. With IR spectroscopy, a method using molecular sieves could be optimized for the safe and quick decomposition of the bound hydrogen peroxide. The molecular sieves also efficiently and quantitatively remove the water formed in this process. The yields of the clean phosphine oxides are nearly quantitative since phosphine oxides are only weakly adsorbed at the surface of the molecular sieves.

EXPERIMENTAL

(a) General procedures

All reactions involving phosphine starting materials were performed under a purified nitrogen atmosphere. Phosphine oxides were stored under nitrogen. Chemicals were treated as follows: Toluene (Mallinckrodt Chemicals, ACS grade) was distilled from Na/benzophenone and CH_2Cl_2 (Mallinckrodt Chemicals, HPLC grade) was dried in a commercially available solvent purification system (JC Meyer Solvent Systems). C_6D_6 (Cambridge Isotope Laboratories) and $CDCl_3$ (Aldrich) were dried over 3 Å molecular sieves (EMD Chemical Inc.). The latter was also used for obtaining the adduct-free phosphine oxides, and it has the approximate composition (weight percentages): silica gel < 50%, Al_2O_3 < 40%, Na_2O < 30%, K_2O < 15%, MgO < 5%, and quartz < 3%. The molecular sieves were activated by heating in vacuum at 120 °C for 12 h. Bu_3P (Strem Chemicals, 99%), Oct_3P (Alfa Aesar, 90% technical), and Cy_3P (Alfa Aesar) were purified by column chromatography (alumina, elution with CH_2Cl_2). Me_3P (Alfa Aesar, 99%) and $ClPPh_2$ (TCI America, 98%) were used as received but kept in a glove box. H_2O_2 (Acros Organics, 35% aqueous solution) was either used as obtained or diluted and stored at 4 °C. Ph_3P (Aldrich, 99%), MnO_2 (Alfa Aesar, technical, min. 58%), and silica (Merck, 40 Å average pore diameter, 0.063 to 0.2 mm average particle size, specific surface area 750 m^2/g) were used as obtained. In addition to the latter "wet" silica, a "dry" batch was generated by heating the silica for 7 days at 200 °C at the vacuum line.

The ^1H, $^{13}C\{^1H\}$, and $^{31}P\{^1H\}$ NMR spectra of liquids were recorded on a 500 MHz Varian spectrometer at 499.70, 125.66, and 470.17 MHz. The ^1H and ^{13}C chemical shifts were referenced using the solvent signals. For ^1H NMR, the residual protons in the deuterated solvents (C_6D_5H, 7.15 ppm; $CHCl_3$, 7.26 ppm) were used;

for ^{13}C NMR the carbon signals (C_6D_6, 128.02 ppm; $CDCl_3$, 77.00 ppm). For the accuracy of the ^{31}P NMR chemical shifts of solutions, $ClPPh_2$ (neat liquid, $\delta(^{31}P)$ = 81.92 ppm) was used as a chemical shift standard within a capillary centered in the 5 mm sample tubes. The signal assignments were based on previous results[19a,56] and confirmed by 2-dimensional $^{1}H,^{1}H$ COSY and $^{1}H,^{13}C$ COSY NMR correlation spectroscopy experiments. Since the literature data are fragmentary, all ^{1}H, ^{13}C, and ^{31}P NMR data obtained in two different solvents (C_6D_6 and $CDCl_3$) are given below.

The ^{31}P solid-state NMR spectra were recorded on a 400 MHz Bruker Avance widebore NMR spectrometer equipped with a 4 mm broadband probehead and ZrO_2 rotors. The polycrystalline substances were densely packed into the rotors. The chemical shifts were referenced with polycrystalline $(NH_4)H_2PO_4$ (+0.81 ppm) as the external standard. A single pulse program with ^{1}H high-power decoupling was applied, and typically about 3000 scans with a pulse delay of 10 s were sufficient to obtain a good signal-to-noise ratio.

IR data of the neat powders and viscous liquids were recorded on a Shimadzu IRAffinity-1 FTIR instrument using a Pike Technologies MIRacle ATR plate. Melting point videos were obtained in open capillaries with a Stanford Research Instruments MPA100 OptiMelt system.

(b) Synthesis and purification of phosphine oxides

*Representative procedure for the synthesis of the H_2O_2 adducts of the phosphine oxides (**2a**–**6a**)*

For each oxidation the same procedure was applied, except for minor deviations for **2a** and **6a**, which are described below. Representative procedure: Bu_3P (3.552 g, 17.56 mmol) was dissolved in 150 mL of toluene in a Schlenk flask, which was cooled

to 0 °C. Then ten equivalents of concentrated aqueous H_2O_2 solution (35 weight % in H_2O, 17.10 mL, 176.0 mmol H_2O_2) were added dropwise via syringe with vigorous stirring. The reaction mixture was stirred overnight and allowed to slowly warm to room temperature. After 12 h, the toluene layer was transferred into a round bottom flask with a metal cannula. ^{31}P NMR proved that the oxidation process is quantitative. The aqueous layer was washed with toluene (3×20 mL), and all organic phases were combined. The solvent was removed *in vacuo*, and **3a** was obtained as a colorless viscous liquid (3.751 g, 84.7% yield, assuming one H_2O_2 molecule per one phosphine oxide molecules). All H_2O_2 phosphine oxide adducts **2a**–**6a** were characterized by ^{31}P NMR and IR spectroscopy, as well as their melting points (see Tables 2.1–2.3 above). The hydrogen peroxide adducts **2a**–**4a** were colorless oils while **5a** and **6a** were white crystalline solids.

The H_2O_2 adduct **2a** was highly water soluble, so it could not be efficiently extracted into toluene or other polar organic solvents, such as diethyl ether, THF, CH_2Cl_2, and ethyl acetate. Therefore, after the oxidation step, all volatile matter (solvents, excess H_2O_2, H_2O) was removed *in vacuo* at 40 °C. Excess water remained hydrogen-bonded to the adduct **2a** (see Results and Discussion section).

For **6a**, no more than ~2 g of **6** per 150 mL of toluene should be used for the oxidation step because **6a** showed a tendency to precipitate due to its low solubility in toluene. Alternatively, **6a** was be extracted from the aqueous layer with CH_2Cl_2, or the entire synthesis performed using CH_2Cl_2 instead of toluene as the solvent.

*Representative procedure for measuring δ(^{31}P) depending on the concentration of **3**, **3a**, **6**, and **6a***

The H_2O_2 adduct of $Bu_3P{=}O$, **3a** (0.250 g, 0.991 mmol, assuming one molecule of H_2O_2 per one phosphine oxide molecule), was placed into an NMR tube. **3a** was dissolved in 0.5 mL of C_6D_6, and a capillary containing the neat standard $ClPPh_2$ was centered in the NMR tube. The ^{31}P NMR spectrum was recorded applying 32 scans. Subsequently the solution was transferred into a 20 mL vial, and an additional 0.5 mL of C_6D_6 was added. A 0.5 mL aliquot of this solution was placed in the NMR tube and measured as described above. This procedure was repeated ten additional times until a total volume of 6.0 mL was reached. Then 1.5 mL aliquots of C_6D_6 were added three times for greater dilution. The final volume of the mixture was then 10.5 mL.

*Representative procedure for the synthesis of the phosphine oxides **2**–**6** from their H_2O_2 adducts **2a**–**6a** using molecular sieves*

The H_2O_2 adduct **3a** (3.751 g), obtained by treatment of Bu_3P (3.552 g, 17.56 mmol) with aqueous H_2O_2 as described above, was placed into a round bottomed flask and dissolved in 150 mL of toluene. Then, a tea bag (obtained by removing the contents of a commercially available tea bag) was filled with 5 g of activated molecular sieves, closed by stapling and suspended in the middle of the flask and fully immersed in the solvent (Figure 2.15). The solution underneath the tea bag was stirred vigorously at room temperature for 4 h. After retrieving the molecular sieves, the solvent was removed *in vacuo* to give **3** as a colorless powder (3.540 g, 16.21 mmol) in 92.3% yield with respect to the starting phosphine. At 60 °C this reaction is complete after 1 h. All phosphine oxides **2–6** were colorless crystalline solids, and they were characterized by ^{31}P NMR and IR spectroscopy, as well as their melting points (see Tables 2.1–2.3). For the sake of

completeness, and because there are noticeable differences between the data of the phosphine oxides and their H_2O_2 adducts, the ^1H and ^{13}C NMR data are included (see below, (c) in the Experimental section).

*Representative procedure for decomposition of **2a**–**6a** to form **2**–**6** using wet silica*

Toluene (30 mL) was combined with wet silica (0.995 g, no pre-conditioning) and **3a** (0.313 g, 1.240 mmol, assuming one molecule of H_2O_2 per one phosphine oxide molecules), dissolved in 20 mL of toluene, was added to the slurry via pipette with vigorous stirring. The mixture was stirred at RT for 18 h. After the silica had been allowed to settle down for 1 h, the supernatant was decanted. The solvent was removed *in vacuo* to give **3** as a colorless sticky solid (0.146 g, 53.9% yield). The silica was washed with CH_2Cl_2 (2×20 mL) to recover residual surface-adsorbed phosphine oxide **3** (0.089 g, 86.8% combined yield). The decomposition of the adduct **3a** to **3** was confirmed by ^{31}P NMR. The IR spectrum showed a significant amount of water remaining hydrogen-bonded to **3** (see Results and Discussion section).

*Representative procedure for decomposition of **2a**–**6a** to form **2**–**6** using pre-dried silica*

The H_2O_2 adduct of $Bu_3P{=}O$ (**3a**, 0.537 g, 2.128 mmol assuming one molecule of H_2O_2 per one phosphine oxide molecules) was added to a slurry of dry silica (1.356 g) in toluene (30 mL) at RT. The sample was stirred overnight. An IR spectrum showed a significant amount of H_2O_2 remaining in the material. Another 1.027 g of silica was added, and the slurry was stirred for 4 more days. IR analysis proved that all H_2O_2 decomposed, and that the resulting water was quantitatively removed from the phosphine oxide. The supernatant was decanted, and the silica was washed with 20 mL of THF (more wash cycles would improve the yield)[33] to recover residual surface-

adsorbed **3**. The washes were combined and the solvent removed in vacuum to give **3** as a white polycrystalline solid (0.181 g, 39.0% overall yield).

*Representative procedure for the decomposition of H_2O_2 in the adducts **2a–6a** with heating*

The H_2O_2 adduct of $Bu_3P{=}O$ (**3a**, 1.124 g) was placed in a Schlenk flask under nitrogen and dissolved in toluene (100 mL). Then the solution was heated to 90 ^oC for 18 h. After cooling to room temperature an aliquot (20 mL) was removed and placed in a separate Schlenk flask. The solvent was removed from this aliquot in vacuum, and a ^{31}P NMR spectrum showed that the H_2O_2 in the adduct **3a** was not completely decomposed. This result was confirmed by IR, which shows O–H stretching bands for H_2O and H_2O_2 bound to the phosphine oxide **3** (Figure 2.12). The sample was redissolved in 20 mL of toluene and added to the original flask for further heating to 95 ^oC for 18 h. After this round of heating the H_2O_2 was entirely decomposed, but significant amounts of water remained bound to the phosphine oxide **3** by IR. Sodium sulfate (ca. 2 g) was added to the solution, but this was ineffective in removing the residual water.

Representative procedure for decomposition of adducts with MnO_2

The H_2O_2 adduct of $Bu_3P{=}O$ (**3a**, 0.110 g) was placed into a 20 mL vial and dissolved in 5 mL of toluene. When MnO_2 (0.101 g) was added, vigorous bubbling occurs due to the release of oxygen during the decomposition of H_2O_2. The reaction mixture was stirred for 1 h at RT to complete the decomposition process. Then the mixture was filtered through a Pasteur pipette filled with silica gel to remove the MnO_2. The latter was a fine black powder that is not entirely removable by filtration, as indicated by the dark color of the filtrate. The same result was obtained with filter paper

while Celite improved the process slightly. Finally, the toluene was removed *in vacuo*, and the grey product was kept under nitrogen. ^{31}P NMR confirms the decomposition of the H_2O_2 in **3a**, leading to crude **3**·$(H_2O)_x$ (0.167 g).

*Representative procedure for attempted decomposition of H_2O_2 adducts **2a**–**6a** with Cu*

The H_2O_2 adduct of $Bu_3P{=}O$ (**3a**, 0.110 g) was placed into an NMR tube and dissolved in 0.6 mL of C_6D_6. Small copper pieces, cut from a copper wire (ca. 0.1 g overall), were added directly to the NMR tube. The solution was vigorously shaken for 0.5 h, then left at RT for 18 h with occasional shaking. After removal of the copper, the ^{31}P NMR spectrum of the solution showed that no decomposition of the H_2O_2 in **3a** had occurred. The same negative result was obtained when a solution of **3a** was heated to 40 °C for 18 h in the presence of copper pieces or when the mixture was stirred for one week at room temperature.

*Representative procedure for measuring H_2O uptake of the phosphine oxides **2**–**6***

Polycrystalline $Bu_3P{=}O$ (**3**) (1.160 g, 5.313 mmol) was placed on a watch glass and exposed to air. The combined mass of **3** and the watch glass was recorded in intervals of several minutes during the first hour to determine the uptake of H_2O gravimetrically. As H_2O was absorbed by **3**, the crystals became more "wet" in appearance and began to turn into an oil. While the phosphine oxide **3** was exposed to air for 8 more, it completely transformed into the oil $Bu_3P{=}O{\cdot}(H_2O)_{0.84}$ (1.240 g), and no mass increase was noted thereafter.

The result of this experiment is graphically displayed in Figure 2.3, together with the similar data obtained for $Me_3P{=}O$ (**1**). For $Oct_3P{=}O$ (**4**), $Cy_3P{=}O$ (**5**), and $Ph_3P{=}O$ (**6**) no significant mass changes could be observed when they were exposed to humid air.

*Representative procedure quantifying the loss of phosphine oxides **2**–**6** by adsorption on molecular sieves*

The H_2O_2 adduct of $Bu_3P{=}O$ (**3a**, 1.010 g) was placed in a Schlenk flask and dissolved in 50 mL of toluene. A ^{31}P NMR spectrum of the solution (0.5 mL aliquot) was recorded to determine the mole percent of **3** (incorporated in **3a**) with respect to the standard $ClPPh_2$ in a capillary centered in the middle of the NMR tube (12.755 mol%). Molecular sieves (2.206 g) in a tea bag (commercially obtained tea bags are cut open, stripped of their original contents, filled with the molecular sieves and sealed with staples, see Fig. 2.13) were then fully immersed in the solution, and the mixture was stirred at RT for 18 h. A ^{31}P NMR spectrum of the supernatant solution (0.5 mL aliquot) was again recorded, and the amount of **3** was 12.183 mol% as compared to the same standard $ClPPh_2$. Therefore, 4.49 mol% of the phosphine oxide **3** had been lost from the solution by adsorption on the molecular sieves. This corresponded to a loss of 2.03 mol% of **3** per g of molecular sieves. The loss of the phosphine oxides **2** and **4**–**6** due to adsorption on the molecular sieves had been determined to be less than 2 mol% per g of molecular sieves under identical conditions.

(c) NMR data of the phosphine oxides and their H_2O_2 adducts

Trimethylphosphine oxide H_2O_2 adduct (2a)

NMR (δ, $CDCl_3$), $^{31}P\{^1H\}$ 43.23 (s); ^1H 1.57 (d, $^2J(^{31}P–^1H)$ = 13.0 Hz); $^{13}C\{^1H\}$ 17.56 (d, $^1J(^{31}P–^{13}C)$ = 70.1 Hz).

Trimethylphosphine oxide (2)

NMR (δ, C_6D_6), $^{31}P\{^1H\}$ 32.65 (s); ^1H 0.90 (d, $^2J(^{31}P–^1H)$ = 12.8 Hz); $^{13}C\{^1H\}$ 17.99 (d, $^1J(^{31}P–^{13}C)$ = 69.0 Hz).

NMR (δ, $CDCl_3$), $^{31}P\{^1H\}$ 38.79 (s); ^1H 1.51 (d, $^2J(^{31}P–^1H)$ = 12.8 Hz); $^{13}C\{^1H\}$ 18.06 (d, $^1J(^{31}P–^{13}C)$ = 70.0 Hz).

Tributylphosphine oxide H_2O_2 adduct (3a)

NMR (δ, C_6D_6), $^{31}P\{^1H\}$ 51.12 (s); ^1H 1.47–1.34 (m, 12H, PCH_2CH_2), 1.22 (sextet, 6H, $^3J(^1H–^1H)$ = 7.2 Hz, C$H_2$$CH_3$), 0.80 (t, 9H, $^3J(^1H–^1H)$ = 7.3 Hz, CH_3); $^{13}C\{^1H\}$ 27.56 (d, $^1J(^{31}P–^{13}C)$ = 65.1 Hz, P*C*H_2), 24.51 (d, $^3J(^{31}P–^{13}C)$ = 14.0 Hz, *C*$H_2$$CH_3$), 24.00 (d, $^2J(^{31}P–^{13}C)$ = 3.8 Hz, PCH_2*C*H_2), 13.83 (s, *C*H_3).

NMR (δ, $CDCl_3$), $^{31}P\{^1H\}$ 52.50 (s); ^1H 1.64–1.56 (m, 6H, PCH_2), 1.47–1.38 (m, 6H, PCH_2CH_2), 1.32 (sextet, 6H, $^3J(^1H–^1H)$ = 7.2 Hz, C$H_2$$CH_3$), 0.82 (t, 9H, $^3J(^1H–^1H)$ = 7.3 Hz, CH_3); $^{13}C\{^1H\}$ 26.90 (d, $^1J(^{31}P–^{13}C)$ = 65.2 Hz, P*C*H_2), 23.92 (d, $^3J(^{31}P–^{13}C)$ = 14.4 Hz, *C*$H_2$$CH_3$), 23.32 (d, $^2J(^{31}P–^{13}C)$ = 3.9 Hz, PCH_2*C*H_2), 13.29 (s, *C*H_3).

Tributylphosphine oxide (3)

NMR (δ, C_6D_6), $^{31}P\{^1H\}$ 43.66 (s); ^1H 1.49–1.38 (m, 6H, PCH_2CH_2), 1.36–1.29 (m, 6H, PCH_2), 1.23 (sextet, 6H, $^3J(^1H–^1H)$ = 7.3 Hz, C$H_2$$CH_3$), 0.81 (t, 9H, $^3J(^1H–^1H)$ = 7.3 Hz, CH_3); $^{13}C\{^1H\}$ 28.13 (d, $^1J(^{31}P–^{13}C)$ = 65.0 Hz, P*C*H_2), 24.53 (d, $^3J(^{31}P–^{13}C)$ = 13.6 Hz, *C*$H_2$$CH_3$), 24.17 (d, $^2J(^{31}P–^{13}C)$ = 3.8 Hz, PCH_2*C*H_2), 13.82 (s, *C*H_3).

NMR (δ, $CDCl_3$), $^{31}P\{^1H\}$ 48.57 (s); ^1H 1.69–1.64 (m, 6H, PCH_2), 1.57–1.49 (m, 6H, PCH_2CH_2), 1.42 (sextet, 6H, $^3J(^1H–^1H)$ = 7.2 Hz, C$H_2$$CH_3$), 0.92 (t, 9H, $^3J(^1H–^1H)$ = 7.3 Hz, CH_3); $^{13}C\{^1H\}$ 27.63 (d, $^1J(^{31}P–^{13}C)$ = 65.0 Hz, P*C*H_2), 24.28 (d, $^3J(^{31}P–^{13}C)$ = 14.2 Hz, *C*$H_2$$CH_3$), 23.75 (d, $^2J(^{31}P–^{13}C)$ = 3.9 Hz, PCH_2*C*H_2), 13.60 (s, *C*H_3).

Trioctylphosphine oxide H_2O_2 adduct (4a)

NMR (δ, C_6D_6), $^{31}P\{^1H\}$ 48.60 (s); ^1H 1.52–1.37 (m, 12H, PCH_2CH_2), 1.28–1.12 (m, 30H, CH_2CH_3), 0.88 (t, 9H, $^3J(^1H–^1H)$ = 7.2 Hz, CH_3); $^{13}C\{^1H\}$ 32.29 (s, $CH_2CH_2CH_3$), 31.58 (d, $^3J(^{31}P–^{13}C)$ = 13.6 Hz, $P(CH_2)_2CH_2$), 29.62 (s, $P(CH_2)_3CH_2$)*, 29.59 (s, $P(CH_2)_4CH_2$)*, 28.08 (d, $^1J(^{31}P–^{13}C)$ = 64.8 Hz, PCH_2), 23.09 (s, CH_2CH_3), 22.10 (d, $^2J(^{31}P–^{13}C)$ = 3.7 Hz, PCH_2CH_2), 14.36 (s, CH_3).

NMR (δ, $CDCl_3$), $^{31}P\{^1H\}$ 50.01 (s); ^1H 1.71–1.62 (m, 6H, PCH_2), 1.57–1.47 (m, 6H, PCH_2CH_2), 1.41–1.32 (m, 6H, $PCH_2CH_2CH_2$), 1.32–1.28 (m, 24H, $(CH_2)_4CH_3$), 0.86 (t, 9H, $^3J(^1H–^1H)$ = 7.2 Hz, CH_3); $^{13}C\{^1H\}$ 31.61 (s, $CH_2CH_2CH_3$), 30.98 (d, $^3J(^{31}P–^{13}C)$ = 13.8 Hz, $P(CH_2)_2CH_2$), 28.90 (s, $P(CH_2)_3CH_2$)*, 28.88 (s, $P(CH_2)_4CH_2$)*, 27.57 (d, $^1J(^{31}P–^{13}C)$ = 64.6 Hz, PCH_2), 22.44 (s, CH_2CH_3), 21.46 (d, $^2J(^{31}P–^{13}C)$ = 2.7 Hz, PCH_2CH_2), 13.87 (s, CH_3).

* = assignments are interchangeable

Trioctylphosphine oxide (4)

NMR (δ, C_6D_6), $^{31}P\{^1H\}$ 43.93 (s); ^1H 1.57–1.48 (m, 6H, PCH_2CH_2), 1.44–1.37 (m, 6H, PCH_2), 1.33–1.19 (br m, 30H, $(CH_2)_5CH_3$), 0.91 (t, 9H, $^3J(^1H–^1H)$ = 7.1 Hz, CH_3); $^{13}C\{^1H\}$ 32.24 (s, $CH_2CH_2CH_3$), 31.57 (d, $^3J(^{31}P–^{13}C)$ = 13.1 Hz, $P(CH_2)_2CH_2$), 29.58 (s, $P(CH_2)_3CH_2$)*, 29.57 (s, $P(CH_2)_4CH_2$)*, 28.49 (d, $^1J(^{31}P–^{13}C)$ = 64.6 Hz, PCH_2), 23.06 (s, CH_2CH_3), 22.21 (d, $^2J(^{31}P–^{13}C)$ = 3.8 Hz, PCH_2CH_2), 14.35 (s, CH_3).

NMR (δ, $CDCl_3$), $^{31}P\{^1H\}$ 48.48 (s); ^1H 1.67–1.59 (m, 6H, PCH_2), 1.58–1.48 (m, 6H, PCH_2CH_2), 1.40–1.32 (m, 6H, $PCH_2CH_2CH_2$), 1.32–1.18 (br m, 24H, $(CH_2)_4CH_3$), 0.85 (t, 9H, $^3J(^1H–^1H)$ = 7.1 Hz, CH_3); $^{13}C\{^1H\}$ 31.78 (s, $CH_2CH_2CH_3$), 31.39 (d, $^3J(^{31}P–^{13}C)$ = 13.6 Hz, $P(CH_2)_2CH_2$), 29.09 (s, $P(CH_2)_3CH_2$)*, 29.04 (s,

$P(CH_2)_4CH_2$)*, 27.95 (d, $^1J(^{31}P–^{13}C)$ = 65.0 Hz, PCH_2), 22.61 (s, CH_2CH_3), 21.70 (d, $^2J(^{31}P–^{13}C)$ = 3.7 Hz, PCH_2CH_2), 14.06 (s, CH_3).

* = assignments are interchangeable

Tricyclohexylphosphine oxide H_2O_2 adduct (5a)

NMR (δ, C_6D_6), $^{31}P\{^1H\}$ 50.28 (s); ^1H 1.87 (br d, 6H, $^2J(^1H_{eq}–^1H_{ax})$ = 12.8 Hz, PCHCH_{eq}), 1.74 (dtt, 3H, $^2J(^{31}P–^1H_{ax})$ = 11.7 Hz, $^3J(^1H_{ax}–^1H_{ax})$ = 12.6 Hz, $^3J(^1H_{ax}–^1H_{eq})$ = 3.0 Hz, PCH_{ax}), 1.67–1.61 (m, 6H, $PCHCH_2CH_{eq}$), 1.56–1.51 (m, 3H, $PCH(CH_2)_2CH_{eq}$), 1.44–1.33 (m, 6H, PCHCH_{ax}), 1.12–1.00 (m, 9H, $PCHCH_2CH_{ax}CH_{ax}$); $^{13}C\{^1H\}$ 35.41 (d, $^1J(^{31}P–^{13}C)$ = 61.0 Hz, PCH), 27.11 (d, $^3J(^{31}P–^{13}C)$ = 11.9 Hz, $PCHCH_2CH_2$), 26.50 (d, $^2J(^{31}P–^{13}C)$ = 2.9 Hz, $PCHCH_2$), 26.39 (d, $^4J(^{31}P–^{13}C)$ = 1.3 Hz, $PCH(CH_2)_2CH_2$).

NMR (δ, $CDCl_3$), $^{31}P\{^1H\}$ 51.53 (s); ^1H 1.94–1.78 (m, 15H, $PCH_{ax}CH_{eq}CH_{eq}$), 1.74–1.67 (m, 3H, $PCH(CH_2)_2CH_{eq}$), 1.47–1.35 (m, 6H, PCHCH_{ax}), 1.29–1.17 (m, 9H, $PCHCH_2CH_{ax}CH_{ax}$); $^{13}C\{^1H\}$ 35.19 (d, $^1J(^{31}P–^{13}C)$ = 60.8 Hz, PCH), 26.87 (d, $^3J(^{31}P–^{13}C)$ = 11.7 Hz, $PCHCH_2CH_2$), 26.23 (d, $^2J(^{31}P–^{13}C)$ = 2.9 Hz, $PCHCH_2$), 26.08 (d, $^4J(^{31}P–^{13}C)$ = 1.4 Hz, $PCH(CH_2)_2CH_2$).

Tricyclohexylphosphine oxide (5)

NMR (δ, C_6D_6), $^{31}P\{^1H\}$ 46.31 (s); ^1H 1.91 (br d, 6H, $^2J(^1H_{eq}–^1H_{ax})$ = 12.7 Hz, PCHCH_{eq}), 1.73 (dtt, 3H, $^2J(^{31}P–^1H_{ax})$ = 11.5 Hz, $^3J(^1H_{ax}–^1H_{ax})$ = 12.5 Hz, $^3J(^1H_{ax}–^1H_{eq})$ = 3.0 Hz, PCH_{ax}), 1.68–1.62 (m, 6H, $PCHCH_2CH_{eq}$), 1.57–1.52 (m, 3H, $PCH(CH_2)_2CH_{eq}$), 1.46–1.35 (m, 6H, PCHCH_{ax}), 1.13–1.00 (m, 9H, $PCHCH_2CH_{ax}CH_{ax}$); $^{13}C\{^1H\}$ 35.49 (d, $^1J(^{31}P–^{13}C)$ = 61.0 Hz, PCH), 27.13 (d,

$^{3}J(^{31}P–^{13}C)$ = 11.6 Hz, PCHCH$_2$*C*H$_2$), 26.57 (d, $^{2}J(^{31}P–^{13}C)$ = 2.9 Hz, PCH*C*H$_2$), 26.42 (d, $^{4}J(^{31}P–^{13}C)$ = 1.3 Hz, PCH(CH$_2$)$_2$*C*H$_2$).

NMR (δ, $CDCl_3$), $^{31}P\{^{1}H\}$ 49.91 (s); ^{1}H 1.91 (br d, 6H, $^{2}J(^{1}H–^{1}H)$ = 12.8 Hz, PCHCH_{eq}), 1.88–1.79 (m, 9H, PCH_{ax}CH$_2$CH_{eq}), 1.75–1.68 (m, 3H, PCH(CH$_2$)$_2$CH_{eq}), 1.48–1.36 (m, 6H, PCHCH_{ax}), 1.30–1.18 (m, 9H, PCHCH$_2$CH_{ax}CH_{ax}); $^{13}C\{^{1}H\}$ 35.37 (d, $^{1}J(^{31}P–^{13}C)$ = 60.8 Hz, P*C*H), 26.93 (d, $^{3}J(^{31}P–^{13}C)$ = 11.6 Hz, PCHCH$_2$*C*H$_2$), 26.34 (d, $^{2}J(^{31}P–^{13}C)$ = 2.9 Hz, PCH*C*H$_2$), 26.14 (d, $^{4}J(^{31}P–^{13}C)$ = 1.4 Hz, PCH(CH$_2$)$_2$*C*H$_2$).

Triphenylphosphine oxide H_2O_2 adduct (6a)

NMR (δ, C_6D_6), $^{31}P\{^{1}H\}$ 27.52 (s); ^{1}H 7.75–7.69 (m, 6H, H_o), 7.06–6.96 (m, 9H, H_m, H_p); $^{13}C\{^{1}H\}$ 134.12 (d, $^{1}J(^{31}P–^{13}C)$ = 103.0 Hz, C_i), 132.40 (d, $^{2}J(^{31}P–^{13}C)$ = 9.7 Hz, C_o), 131.61 (d, $^{4}J(^{31}P–^{13}C)$ = 2.8 Hz, C_p), 128.55 (d, $^{3}J(^{31}P–^{13}C)$ = 12.1 Hz, C_m).

NMR (δ, $CDCl_3$), $^{31}P\{^{1}H\}$ 30.15 (s); ^{1}H 7.69–7.64 (m, 6H, H_o), 7.57–7.52 (m, 3H, H_p), 7.48–7.44 (m, 6H, H_m); $^{13}C\{^{1}H\}$ 132.31 (d, $^{1}J(^{31}P–^{13}C)$ = 102.8 Hz, C_i), 132.06 (d, $^{2}J(^{31}P–^{13}C)$ = 10.0 Hz, C_o), 131.96 (d, $^{4}J(^{31}P–^{13}C)$ = 2.8 Hz, C_p), 128.49 (d, $^{3}J(^{31}P–^{13}C)$ = 12.3 Hz, C_m).

Triphenylphosphine oxide (6)

NMR (δ, C_6D_6), $^{31}P\{^{1}H\}$ 25.16 (s); ^{1}H 7.77–7.71 (m, 6H, H_o), 7.06–6.96 (m, 9H, H_m, H_p); $^{13}C\{^{1}H\}$ 134.00 (d, $^{1}J(^{31}P–^{13}C)$ = 102.6 Hz, C_i), 132.04 (d, $^{2}J(^{31}P–^{13}C)$ = 9.7 Hz, C_o), 131.17 (d, $^{4}J(^{31}P–^{13}C)$ = 2.7 Hz, C_p), 128.15 (d, $^{3}J(^{31}P–^{13}C)$ = 11.9 Hz, C_m).

NMR (δ, $CDCl_3$), $^{31}P\{^{1}H\}$ 29.10 (s); ^{1}H 7.70–7.64 (m, 6H, H_o), 7.57–7.52 (m, 3H, H_p), 7.49–7.43 (m, 6H, H_m); $^{13}C\{^{1}H\}$ 132.54 (d, $^{1}J(^{31}P–^{13}C)$= 103.4 Hz, C_i), 132.07 (d, $^{2}J(^{31}P–^{13}C)$ = 9.9 Hz, C_o), 131.89 (d, $^{4}J(^{31}P–^{13}C)$ = 2.8 Hz, C_p), 128.46 (d, $^{3}J(^{31}P–$

^{13}C) = 12.1 Hz, C_m).

(d) Crystallography

General procedure

Data were collected using a BRUKER APEX2 X-ray diffractometer. Cell parameters were obtained from 60 frames using a 0.5° scan and refined using the number of reflections given in sections **A** and **B**. Integrated intensity information for each reflection was obtained by reduction of the data frames with the program APEX2.[57] Lorentz, polarization, crystal decay effects, and absorption corrections[58] were applied. The space group was determined from systematic reflection conditions and statistical tests. The structure was solved by direct methods using SHELXTL (SHELXS) and refined (weighted least squares refinement on F^2) using SHELXL-97.[59] Non-hydrogen atoms were refined with anisotropic thermal parameters. The parameters were refined by weighted least squares refinement on F^2 to convergence.[59]

A. A nearly saturated toluene solution of **3** was sealed in a vial under N_2 and kept first in a refrigerator (2 °C, 1 h) and then a freezer (–17 °C, 12 h). The colorless needles were directly mounted from the warmed sample. Hydrogen atoms were placed in idealized positions and were refined using a riding model.

Crystal data: $C_{12}H_{27}OP$, M_r = 218.31, monoclinic, space group $P2_1/c$, T = 150(2) K, a = 9.326(6), b = 15.281(10), c = 10.136(7) Å, α = 90°, β = 100.548(15)°, γ = 90°, V = 1420.1(16) Å^3, Z = 4, D_c = 1.021 g/cm^3, F_{000} = 488, θ range for data collection 2.22° to 27.61º, 15057 reflections collected, independent reflections 3264 (R_{int} = 0.0594). Final *GooF* = 1.062, R indices based on reflections with I > 2σ(I) (refinement on F^2) R_1 = 0.0595, wR_2 = 0.1490, R indices (all data) R_1 = 0.0885, wR_2

= 0.1788.

B. A toluene solution of **5a** was sealed in a vial under N_2 and kept first in a refrigerator (2 °C, 12 h) and then a freezer (–17 °C, 2 d). The colorless blocks, which dissolved upon warming, were directly mounted from the cold sample. Carbon-bound hydrogen atoms were placed in idealized positions. Oxygen-bound hydrogen atoms were located from the difference Fourier map and refined using a riding model.

Crystal data: $C_{18}H_{35}O_3P$, M_r = 330.43, triclinic, space group *P–1*, T = 110(2) K, a = 8.579(2), b = 9.584(3), c = 12.260(3) Å, α = 95.445(3)°, β = 97.065(3)°, γ = 112.824(3)°, V = 910.8(4) Å^3, Z = 2, D_c = 1.205 g/cm^3, F_{000} = 364, θ range for data collection 1.69° to 27.48°, 10409 reflections collected, 4067 independent reflections (R_{int} = 0.0169). Final *GooF* = 1.044, R indices based on reflections with [I > 2σ(I)] (refinement on F^2) R_1 = 0.0327, wR_2 = 0.0843, R indices (all data) R_1 = 0.0376, wR_2 = 0.0880.

CHAPTER III

ADSORPTION OF PHOSPHINE OXIDES ON SILICA SURFACES: A SOLID-STATE NMR STUDY

INTRODUCTION

In the past phosphonates or phosphonic acids have been extensively studied when adsorbed on a variety of solid supports, such as metal oxides or silica, due to their applications in materials chemistry and in catalysis.[60] Phosphine oxides, on the other hand, have not received much attention as adsorbed species. The Bluemel group has previously studied phosphine oxides tethered to ethoxysilane groups covalently bound to the silica support[27a] but until now did not examine in detail the direct interaction of the P=O bond with the silica surface. Phosphine oxidation occurs during the immobilization of a phosphine linker on a solid support, when oxygen is not excluded rigorously. Understanding the key solid-state NMR features of these byproducts and their interaction with the surface is imperative for the proper characterization of the desired phosphine-modified silica.

In recent years, Javey *et al.* investigated the formation of phosphine oxide monolayers on silica surfaces.[9] The authors were able to adsorb $OPEt_3$ and $OPPh_3$ on a silica surface, but bis(2,2,2-trifluoroethyl) methylphosphonate, $CH_3PO(OCH_2CF_3)_2$, would not bind irreversibly to the surface. The authors believed that the electron-withdrawing groups pulled electron density away from the P=O bond, which interfered with the bonding interactions to the SiO_2 surface. The other two phosphine oxides that were adsorbed seemed to exhibit much different packing patterns on the surface as recognized by XPS and AFM. To examine the interactions with the silica surface, the researchers washed the monolayers with DCM, which did not lead to phosphine oxide

detachment. However, when the surfaces were washed with methanol the $OPEt_3$ surface coverage was reduced and eventually the $OPPh_3$ on the silica surface was completely removed. This led Javey and coworkers to propose that the phosphine oxides bind to the silica surface through strong hydrogen bonds between the P=O group and the silanol protons of the silica, and the adsorbed phosphine oxides are replaced by the methanol during the wash cycle.[9]

These results were very surprising because the interactions between phosphine oxides and silica supports had not been examined thoroughly in the past. As mentioned in Chapter I, the adsorption of phosphine oxides on various supports, such as silica and alumina, had only been studied as a means to quantify the acidic sites on the surface.[3–8] More recently, the dynamic motion of phosphines on a support has been noted by Grey and coworkers, and diphosphines were used to measure the distance between different acidic sites on zeolite surfaces.[6,27a] In these publications the authors describe the physisorbed phosphines as mobile while the protonated phosphines are held more tightly by the negative siloxide counteranion on the support. The only evidence for this mobility on the surface is the small linewidth of a signal in the ^{31}P MAS NMR spectra, which is indicative of isotropic motion on the zeolite that significantly reduces the CSA and other anisotropic line broadening effects.[27a]

Despite the simple mentioning that phosphines may have some mobility across an oxide support, no other detailed studies using solid-state NMR have focused on this phenomenon. A deeper insight into the interactions of phosphines with silica is important in our group because many of the linkers for our immobilized catalyst systems employ phosphines to tether the metals to the surface. Understanding how the phosphines interact with silica was the initial motivation that led the Bluemel group to investigate the solid-state NMR characteristics of their adsorption.[10] One previous

project mainly utilized PPh_3 and PCy_3 for the adsorption studies. Both phosphines display a drastic reduction in the chemical shift anisotropy (CSA) when going from the polycrystalline material to the adsorbed species.[10]

In addition to adsorbing the phosphines from solution, Yang in the Bluemel group pioneered the adsorption of phosphines from the solid state onto a silica support. This was accomplished by grinding dry PPh_3 (**7**) with silica and monitoring the progress of the adsorption over time with solid-state NMR.[10] A reduction of the ^{31}P CSA similar to the one observed after impregnation of the silica with a phosphine from solution was observed when going from the polycrystalline solid to the adsorbed material without a solvent. Furthermore, due to the downfield shift of the signal of the adsorbed species, both the adsorbed and polycrystalline materials exist on the surface and can be distinguished in the NMR spectra. This means that the transition from a monolayer to crystalline phosphine is abrupt and no stacking of layers occurs.

The Bluemel group has expanded the concept of using dry grinding to study the adsorption of organometallic complexes on silica as well. A recent publication from the group demonstrated that both ferrocene and chromocene are adsorbed on silica from the solid state by grinding the dry components, polycrystalline metallocene and silica, together.[61] The formation of a mobile surface species is confirmed by a reduction of the CSA and the residual linewidths in the ^1H and ^{13}C MAS NMR spectra. This is the first publication that demonstrates that adsorption by dry grinding causes a reduction in the CSA of the metallocene signals, which indicates that the molecules of the solid must break out of the crystal lattice and "melt" onto the surface to be adsorbed.[61] These dry grinding experiments are very exciting and reveal the surface-adsorbed species must exhibit translational mobility to be able to spread across the silica support. The drastic reduction of the CSA and residual linewidth implies that the metallocene molecules must

be cruising within the pores and simulate an isotropic reorientation similar to the one in solution.[61]

Regarding the phosphines, the chemical shift anisotropy (CSA) originates from the electronic (un)symmetry around the phosphorus nucleus in a polar functional group being measured. Since in polycrystalline material all molecules are oriented randomly with respect to the external magnetic field, the electrons shield each ^{31}P nucleus differently. This gives rise to signals with different chemical shifts which add up to the wideline pattern, which is a spectrum obtained without rotation. The observed CSA reduction upon adsorption of a phosphine can be caused by two main factors: mobility and increased electronic symmetry around the P nucleus due to at least partial quaternization. In the case of the adsorbed phosphines, the translational mobility refers to the phosphines moving across the surface but continually interacting with the support. This results in a decrease in the CSA because the molecules are more mobile than in the crystal lattice and, therefore, exhibit more solution-like isotropic motion. The partial quaternization component is effective at making the electronic environment around the P nucleus more symmetric because it provides four bonding interactions around phosphorus as opposed to three bonds and one lone pair.

This quaternization hypothesis is corroborated by examining the CSA of phosphines (typically 50–70 ppm) versus that of alkylphosphonium salts (15–40 ppm).[27c] In the salts, there are four symmetric P–C bonds around the phosphorus giving rise to a drastically diminished CSA value. After recognizing that each, the translational mobility and partial quaternization, can in principle effect the decrease in the CSA value of the adsorbed species, the goal was to try to disentangle these factors. One way to do this is using a probe molecule with two equivalent phosphorus nuclei bound together but only one being able to access the support at a given time. In this way, both phosphine

groups experience the same mobility, but only one can be quaternized due to sterics. From this concept the idea of using diphosphine cages (**I**) and their oxide derivatives (**II** and **III**) as highlighted in Chapter I (Figure 1.2), for adsorption studies, was envisaged.

Examining the adsorption of monofunctional phosphine oxides on silica was imperative to provide a basic set of data for comparison with the cages **II** and **III** that contain two P=O groups. The importance of understanding the interactions with the surface is especially evident for the diphosphine monoxide cages **I**, which contain both a phosphine and a phosphine oxide group. Previously it was thought that the phosphine oxide may not bind firmly to silica and that the dominant interaction with the surface would occur by the interactions of the lone pair of the free phosphine with silanol groups on the silica surface. However, the new findings by Javey and coworkers[9] demonstrated that phosphine oxides could bind strongly to the support and therefore the nature of these interactions needed to be examined in more detail using solid-state ^{31}P NMR spectroscopy. For this purpose, the adsorption of representative phosphine oxides was tested on "wet" silica, containing a maximal number of surface silanol groups, and dried silica with a minimum number of silanol groups.

Also, in regards to phosphine oxides, the adsorption process may have potential applications in the purification processes after various organic reactions, such as the Wittig,[20] Staudinger,[21] or Appel reactions,[22] all of which generate $OPPh_3$ as a byproduct. Stirring with silica in certain solvents may easily remove phosphine oxides from a reaction mixture, allowing the product to be isolated from the supernatant. New applications involving the adsorption of phosphine oxides on silicon wafers were just highlighted in the literature,[62] and understanding the P=O/surface interaction will help to further improve these systems. This again establishes that the phosphine oxide adsorption study is very relevant for a multitude of applications.

RESULTS AND DISCUSSION

Solid-state NMR Spectra of Asdorbed Phosphine Oxides on Silica

As previously discussed a significant reduction of the CSA is observed for phosphines when adsorbed on different silica supports.[10] Being that polycrystalline phosphine oxides display a much larger CSA (150–200 ppm) in the solid state[63] as compared to the analogous phosphines (50–70 ppm), it was anticipated that the CSA reduction would be even more pronounced. However, a look at the corresponding ethoxyphosphonium salts with CSA values of 70–120 ppm[27c] shows that the expected reduction of the CSA upon adsorption would be in the range of 30–130 ppm which is, however, analytically still significant. As mentioned in Chapter II, the solid-state NMR spectra were only measured for $OPCy_3$ (**5**) and $OPPh_3$ (**6**) because the other model phosphine oxides were melting at too low a temperature and thus were not suitable for MAS measurements.

The adsorption procedure was primarily carried out using toluene. First, the silica was weighed into a Schlenk flask and suspended in toluene to form a slurry. The given phosphine oxides **2**–**6** were weighed into a different Schlenk flask at an excess of approximately 100 molecules per 100 nm^2 of silica, dissolved in toluene, and then added to the silica slurry while stirring overnight. The next day stirring was stopped to allow the silica to settle. Subsequently, the supernatant was transferred into a round bottom flask. One wash of the silica with toluene was performed to remove any polycrystalline solid that might have remained on the support. The supernatant and wash phase were combined, the solvent was remove in vacuo, and the residue was weighed to calculate the amount of phosphine oxide that had been adsorbed and to determine the exact surface coverage.

In all cases, the phosphine oxides adsorbed on silica, $\mathbf{2_{ads}}$–$\mathbf{6_{ads}}$, displayed the

anticipated large reduction of the CSA as compared to the polycrystalline material and also showed a lowfield shift of the isotropic line (Fig. 3.1). The chemical shift change is indicative of possible hydrogen bonding between the oxygen of the P=O group and the hydrogens of the surface silanol groups because a similar change in chemical shift is observed for the phosphine oxide H_2O_2 adducts as a result of hydrogen bonding.[63]

By comparing the ^{31}P MAS NMR spectrum of polycrystalline **6** with that of the adsorbed species $\mathbf{6_{ads}}$, the following interesting features can be observed (Figure 3.1). The isotropic line in the polycrystalline solid **6** is found at 28.1 ppm while the signal for adsorbed material $\mathbf{6_{ads}}$ shifts to 36.4 ppm on wet silica and 35.0 ppm on thoroughly dried silica, an overall change of approximately 8 ppm. Also, one can clearly see that the originally large CSA of **6** with about 200 ppm is significantly reduced to only about 15 ppm, as evidenced by the disappearance of rotational sidebands in the spectrum measured at 4 kHz and the wideline spectrum at 0 kHz (Figure 3.1), when adsorbed on either form of silica. Once again this line-narrowing effect is thought to arise from the mobility of the phosphine oxide across the support surface in addition to the partial quaternization at the P nucleus created by the hydrogen bonding. In this case, the quaternization is referred to as the P=O bond becoming more like a P–OR bond (R = H in the case of hydrogen bonding) when adsorbed. Alkoxyphosphonium salts, such as $[Cy_3POEt]BF_4$ (CSA = 92 ppm), are known to have smaller CSA values in the range of 70–120 ppm[27c] as compared to similar trialkylphosphine oxides (CSA = 200 ppm).[63]

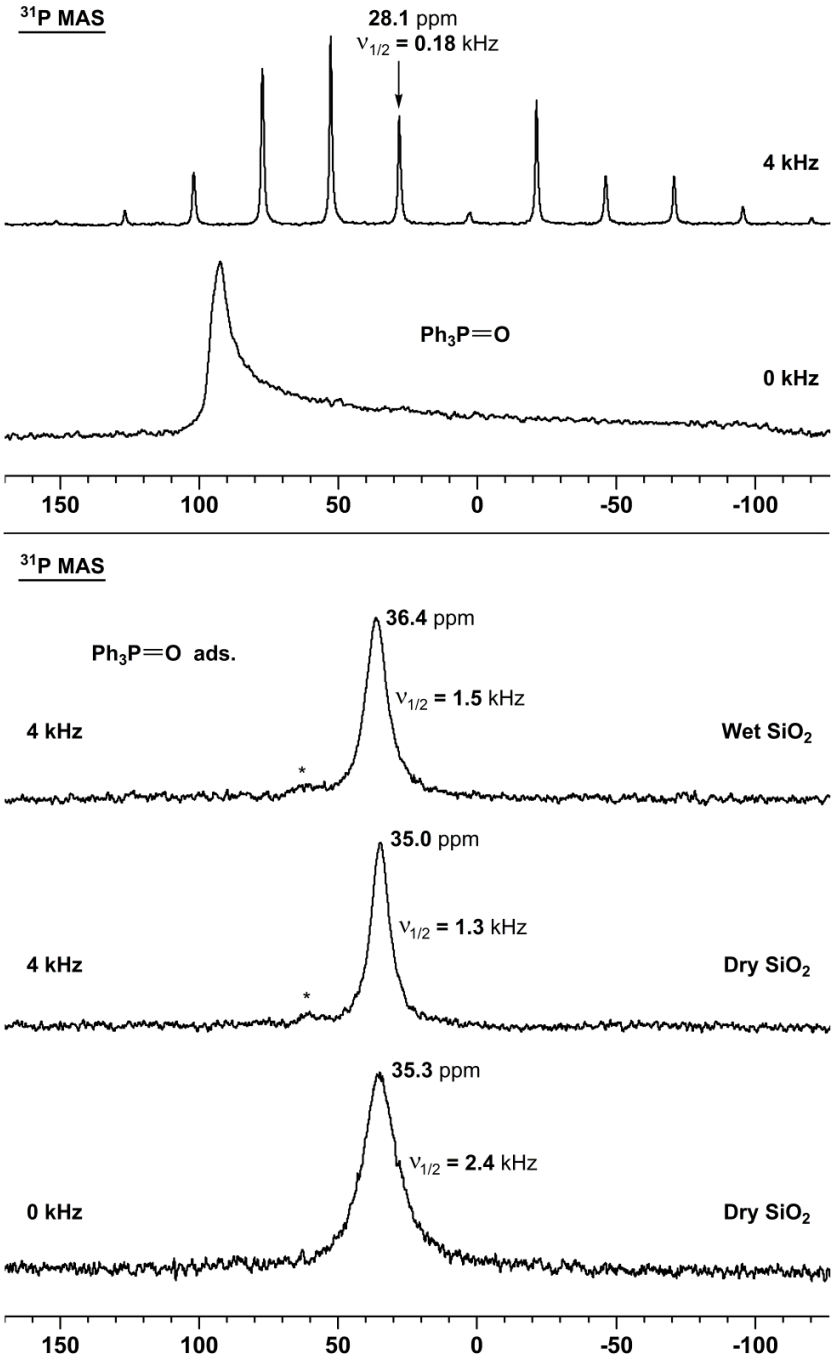

Figure 3.1. ^{31}P solid-state NMR spectra of polycrystalline $OPPh_3$ (**6**) (top) and $OPPh_3$ adsorbed on silica (**6$_{ads}$**) (bottom). Asterisks denote the rotational sidebands in the spectra of the adsorbed materials. In the 4 kHz spectrum of the polycrystalline solid, all signals are rotational sidebands except for the isotropic line indicated by an arrow.

Although the measurements of the polycrystalline materials could not be performed for the low-melting phosphine oxides with linear alkyl chains, **2**–**4**, these compounds were important to serve as trialkylphosphine models for the cage molecules. As seen in the ^{31}P MAS NMR spectra of $OPBu_3$ adsorbed on wet and dry silica ($\mathbf{3_{ads}}$) (Figure 3.2), the material also displays a small CSA of only about 19 ppm as deduced from the halfwidth of the wideline spectrum (Figure 3.2, bottom). Both spectra of $\mathbf{3_{ads}}$ on wet or dry silica are very similar with approximately the same halfwidths and chemical shifts.

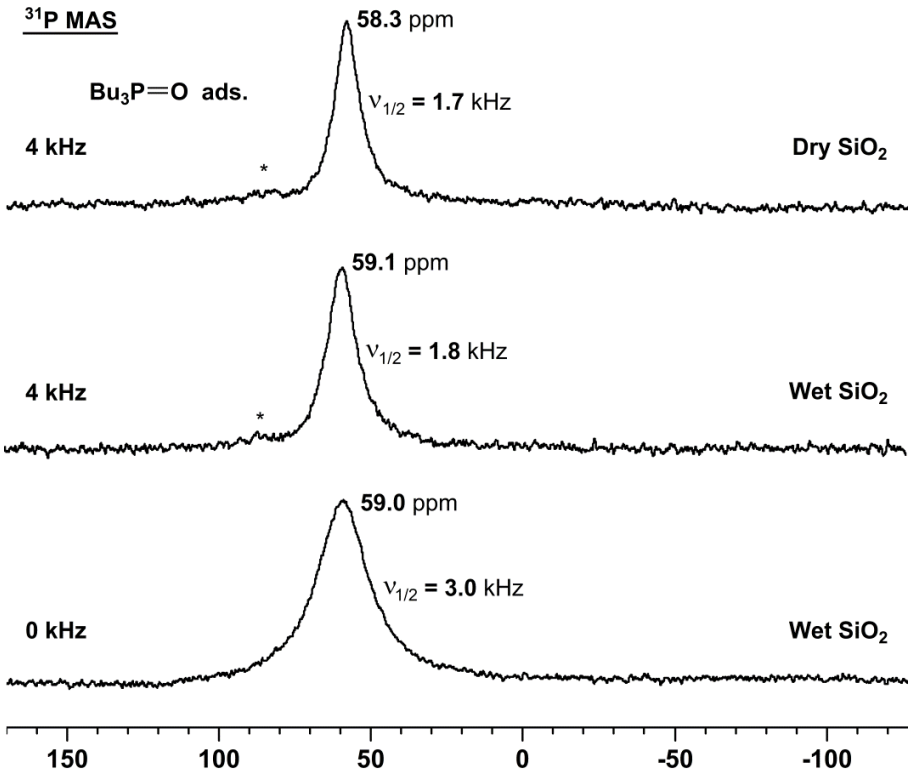

Figure 3.2. ^{31}P MAS NMR spectra of **3** adsorbed on silica ($\mathbf{3_{ads}}$). Asterisks denote the rotational sidebands.

On the other hand, after the adsorption of bulky $OPCy_3$ on silica, the signal of $\mathbf{5_{ads}}$ retains a much larger CSA in the ^{31}P MAS spectra (Figure 3.3). It is hypothesized that the sterically demanding substituents may prohibit the interaction of the P=O group with the silica surface. When comparing the polycrystalline solid **5** to the compound adsorbed on silica, $\mathbf{5_{ads}}$, the isotropic line shifts from 47.6 ppm to 59.1 ppm on wet silica and to 59.2 ppm on dry silica, which confirms that the P=O group is interacting with the support. Polycrystalline material, which would lead to narrow signals on top of the broad resonances, is not observed in the spectra. If the phosphine oxide is hydrogen bonding to the support and completely immobile, then a CSA value close to that of the alkoxyphosphonium salts (CSA = 70–120 ppm)[27c] would be expected, which is slightly less than what is observed experimentally (Figure 3.3). Therefore, this system possibly exhibits a decreased translational mobility due to the stronger hydrogen bonding with the support. The larger change of the chemical shift upon adsorption, about 12 ppm, as compared to the shift change for Ph_3PO of ca. 8 ppm supports this assumption.

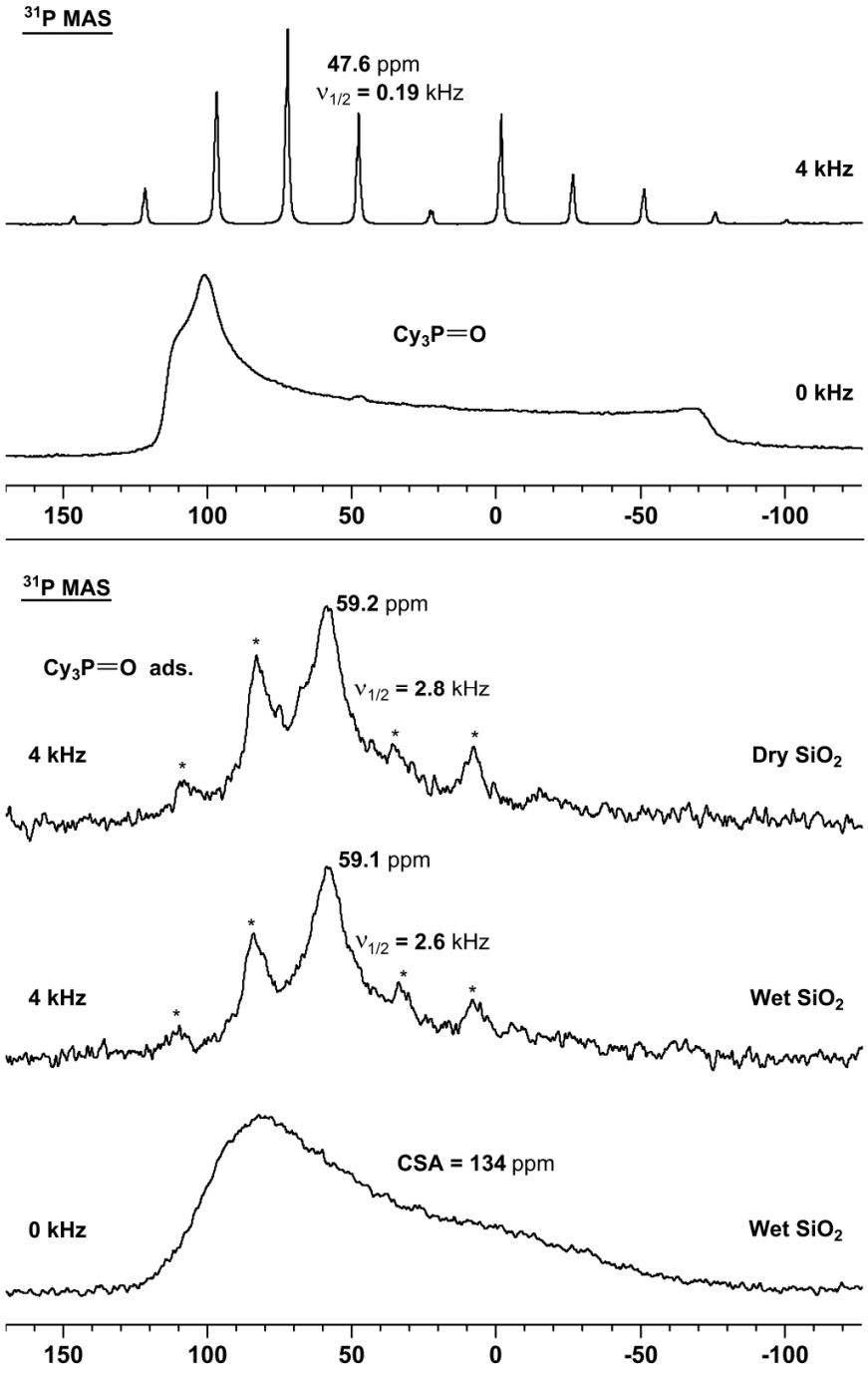

Figure 3.3. ^{31}P MAS NMR spectra of polycrystalline $OPCy_3$ (**5**) (top two traces) and $OPCy_3$ adsorbed on silica ($\mathbf{5_{ads}}$) (bottom three spectra). Asterisks denote the rotational sidebands in the spectra of the adsorbed material. In the 4 kHz spectrum of the polycrystalline solid, all signals are rotational sidebands except for the isotropic line.

Surface Coverages of Phosphine Oxides on Silica Supports

The maximal surface coverage of the adsorbed phosphine oxides had to be determined in order to compare with the values obtained when adsorbing the cage molecules **I**–**III** on silica. The size of the model phosphine oxides can be determined from their crystal structures and then correlated with the surface coverages (see below). In this way the "footprint" of the cage compounds on silica can be estimated by comparing the maximum surface coverage of each cage to that of the model compounds and determining the size range associated with that specific coverage. The comparison will be most effective with the phosphine oxides containing linear alkyl chains as they are most closely related to the cage compounds. Knowing the approximate size of the cages on the support enables one to speculate whether the cages are "standing upright", having a normal round cage structure, or "deflating down", meaning the P nuclei are moving closer together towards the surface causing the alkyl chains to be pushed outward, onto the surface. Also, the cages could form a parachute-like structure[13] on the support in which both phosphines are adsorbed, and this would result in a "footprint" similar to that of the "deflated" cage on the surface.

The standard adsorption procedure described above was utilized for the surface coverage experiments, and one wash with toluene was used to remove any residual polycrystalline solid. The surface loading is determined gravimetrically by collecting the supernatant, removing the solvent, and weighing the remaining residue. By subtracting this amount from the total amount of phosphine oxide used for the adsorption, one can calculate how much phosphine oxide remains on the silica. It is assumed at this coverage a sub-monolayer of phosphine oxide is adsorbed on the surface with all of the P=O groups interacting with the support, as confirmed by one signal in ^{31}P MAS NMR. The values are usually less than the maximum coverage determine from the "footprint" of the

phosphine oxides (Table 3.1) indicating a densely packed monolayer is not formed from the adsorption from solution, but the values are reproducible indicating this is the maximum amount that can be adsorbed from toluene.

The "footprint" of each of the model compounds was calculated from distances measured in the crystal structures of each compound or of complexes containing the phosphine oxides. The average distance between the P nucleus and the outermost H atom of each substituent, e.g. alkyl chain or phenyl ring, was determined for the different phosphine oxides. This distance plus half of the van der Waals radius for H (1.20 Å)[64] was used as the radius for the calculations. It was assumed that each phosphine oxide was like a circle on the silica surface, so the area of the circle is what is defined as the "footprint" of each phosphine oxide (Table 3.1). However, it should be noted that this approach does not account for the interlocking of alkyl chains, which is possible for the large $OPOct_3$ (**4**) and will be discussed below in regards to its surface coverage values. Furthermore, the packing efficiency of circles into a square lattice is only 78.54%, so when looking at the standard 100 nm^2 area of the silica surface, only 78.54 nm^2 is accessible by the packing of the phosphine oxides, again assuming no interlocking or overlapping of the circles. Therefore, the maximum coverage values (Table 3.1) are calculated by dividing the 78.54 nm^2 by the "footprint" of each phosphine oxide.

Table 3.1. "Footprints" and maximum coverage values of the phosphine oxides **2**–**6** and the large diphosphine cage **1** on the silica surface.

Phosphine Oxides	**Avg. Distance from P to Outermost H** (nm)	**Radius** (nm)	**"Footprint"** (nm^2)	**Maximum Coverage** (molecules per 100 nm^2)
$O=PMe_3$ (**2**)	0.235[65]	0.295	0.268	293
$O=PBu_3$ (**3**)	0.612[63]	0.672	1.42	55.4
$O=POct_3$ (**4**)	1.109[66,*a*]	1.169	4.29	18.3
$O=PCy_3$ (**5**)	0.561[63,*b*]	0.621	1.21	64.8
$O=PPh_3$ (**6**)	0.567[67]	0.627	1.24	63.5
Cage **1** "upright"	0.692[11,*c*]	0.752	1.78	44.2
Cage **1** "deflated" or "parachute"	0.895[12,*d*]	0.955	2.86	27.4

[a] $OPOct_3$ is a ligand in a Eu complex structure. [b] Crystal structure of $Cy_3PO \cdot H_2O_2$ adduct (**5a**) was used. [c] Crystal structure of the borane adduct of cage **1** was used. [d] Crystal structure of the gold complex of cage **1** was used.

The "footprint" of the trialkylphosphine oxides **2**–**4** increases as expected with increasing the size of the alkyl chains. Therefore, it would be expected that $OPMe_3$ (**2**) would have the highest surface coverage and $OPOct_3$ (**3**) would have the lowest coverage. As mentioned above, the "footprint" of **4** is most likely overestimated because of the long alkyl chains. It would leave a lot of open space of the silica support if the chains did not intercalate, so most likely surface coverages higher than the theoretical maximum coverage (Table 3.1) should be observed to account for the assumptions made during the calculations. $OPCy_3$ (**5**) and $OPPh_3$ (**6**) are actually very similar in size with **5** having a slightly larger footprint, so similar surface loadings would be expected.

Although both of these phosphine oxides are thought to have bulkier substituents than **3**, their "footprints" are actually smaller than **3**, which has the alkyl chains stretched out around the P center. The size of cage **1** falls in between that of **3** and **4** and varies significantly depending on if the cage is "standing upright" on the surface or is "deflating down" or forming a parachute-like structure on the support.

As expected the overall trend shows that the smaller phosphine oxides, such as $OPMe_3$ (**2**), with a smaller "footprint" have the highest surface loading since they take up less room on the silica surface (Table 3.2). However, only 100 molecules per 100 nm^2 was initially added to the silica, so in the case of **2**, the theoretical maximum surface coverage (Table 3.1) was much higher and could not be achieved from this loading. The largest phosphine oxide, $OPOct_3$ (**4**), with long alkyl chains, then should have the lowest surface coverage, which is, however, not the case under at all reaction conditions (Table 3.2). As the data in the table show, the degree of wetness of the silica plays a dominant role, and also the presence of H_2O_2. The latter can be contemplated as "induced wetness", as the H_2O_2 decomposes on the silica surface to give H_2O.[63] In general, the solubilities of the phosphine oxides in toluene are a factor as well since the solubilities of surface-adsorbed species correlate with their leaching for a given solvent.[19a] As demonstrated below, toluene removes significant amounts of phosphine oxide from the surface but is still one of the solvents that results in the least amount of leaching of the phosphine oxides from the support, making is applicable for these surface coverage studies. The full set of data, including the initial amount of phosphine oxide and silica used, for the surface coverage experiments can be found in the Experimental section in Tables 3.5–3.8.

Table 3.2. Maximum surface coverages (molecules per 100 nm^2) of phosphine oxides **2**–**6** under different conditions. Wet silica corresponds to material as obtained from the vendor, dry silica has been dried in vacuo at 300 °C for three days.

Phosphine Oxides	$R_3P{=}O \cdot (H_2O_2)$ on wet silica at RT	Wet silica at RT	Wet silica at 90 °C	Dry silica at 90 °C
$O{=}PMe_3$ (**2**)	90.0	88.9	65.3	53.2
$O{=}PBu_3$ (**3**)	76.5	62.2	43.4	29.0
$O{=}POct_3$ (**4**)	45.9	47.6	29.4	25.1
$O{=}PCy_3$ (**5**)	52.0	43.3	44.5	37.1
$O{=}PPh_3$ (**6**)	34.0	30.6	32.9	26.2

Besides ambient temperature 90 °C was tested for the adsorption process to further investigate the implications of the reaction temperature on the surface coverage of a given phosphine oxide. The standard adsorption method was applied at room temperature or 90 °C with the workup procedures always being performed at ambient temperature. In this way, leaching effects due to different solubilities of the phosphine oxides at various temperatures were excluded. However, the experiment would show whether a higher temperature helps the phosphine oxides to replace adsorbed solvent molecules from the surface or adsorb at less favorable sites that might not be populated at room temperature. The temperature of 90 °C was chosen because that is the standard temperature used by the Bluemel group for all immobilizations on silica, especially those involving ethoxysilane groups that covalently bind to the silica support under formation of siloxane groups. Another important goal was to probe whether the phosphine oxides were only interacting with the silica surface by hydrogen bonding or whether they could

form covalent bonds at higher temperatures, which had been proposed by other research groups.[9] The heating could provide additional energy for the formation of covalent bonds, but this was never observed. All supernatant liquids of the different adsorption mixtures were analyzed by ^{31}P NMR or TLC to show that only the phosphine oxide was removed from the silica surface and no quaternized species. Even in cases when polar solvents, such as acetone and THF, were used to remove all adsorbed phosphine oxide from the silica, the supernatants showed only the respective phosphine oxide. This is strong evidence that the phosphine oxide remains unaltered on the silica and no covalent Si–O–P bonds are created. If these types of covalent bonds were formed, it would not be possible to detach the phosphine oxide from the surface by simply washing with solvents, so this concept could be discarded. At higher temperatures, there was a pronounced decrease in the overall surface coverage of the phosphine oxides with linear alkyl chains (Table 3.2), possibly due to a shift in the adsorption/desorption equilibrium.

A significant trend found in these surface coverage experiments is that the surface loadings for all phosphine oxides is higher on the wet silica as compared to the silica dried at 300 °C in high vacuum. This result corroborates our belief that the phosphine oxides interact with the silica surface through hydrogen bonding with silanol groups or adsorbed water. Wet silica has many more surface silanol groups that could form hydrogen bonds with the polar P=O groups.

Further evidence for this hydrogen bonding is shown by the room temperature experiments. When using the H_2O_2 adducts of the phosphine oxides as starting materials for the adsorption, the surface coverage was typically higher than in the case of the pure phosphine oxides. Although the H_2O_2 adducts are broken down with the wet silica over time as confirmed by NMR and IR spectra,[63] residual water may still be bound to the phosphine oxides. The water molecules can again facilitate hydrogen bonding with the

silica surface as reflected in the increased surface loadings. The ^{31}P MAS spectrum of the adduct **3a** adsorbed on wet silica at room temperature has a similar chemical shift of 59.8 ppm as compared to the value of the adsorbed phosphine oxide $\mathbf{3_{ads}}$ (δ = 59.1 ppm, Figure 3.2). The same observation is made regarding the linewidths, with 1.9 kHz for adsorbed H_2O_2 adduct **3a** and 1.8 kHz for adsorbed pure phosphine oxide $\mathbf{3_{ads}}$.

Leaching Studies

One potential application of the phosphine oxide adsorption on silica is reaction product purification, and therefore a general understanding of how the adsorbed species interacts with the silica in different solvents is imperative. All phosphine oxides adsorbed on wet silica $\mathbf{2_{ads}}$–$\mathbf{6_{ads}}$ were subjected to a variety of solvents to determine the degree of leaching of the oxide from the support (Figure 3.4). It was expected that some leaching would be observed because the phosphine oxides were only bound through hydrogen bonds to the silica surface, which could easily be disrupted by solvent molecules as shown in previous work.[9]

As seen below (Figure 3.4) there is some leaching in all solvents tested. The minimum amount of phosphine oxide removal from the surface occurs in pentane or toluene. This is why toluene was used for the maximal surface coverage determination experiments. The largest amount of leaching of the phosphine oxides is seen in THF or methanol, which coincides with the results by Javey and coworkers.[9] Due to the small aliquots of material used for each leaching test, there was some inherent error in the measurements as expected from the sensitivity of the balance. With phosphine oxides **3**–**6** the error remained below 3% for all leaching studies, but for $OPMe_3$ (**2**) the error margin was about ± 4%. This may account for some of the variations in the leaching of **2** as compared to the other phosphine oxides. However, it should be noted that **2** is also

much more polar as evidenced by its hygroscopic nature and it is partially soluble in water,[63] so solubility most likely plays a major role as well.

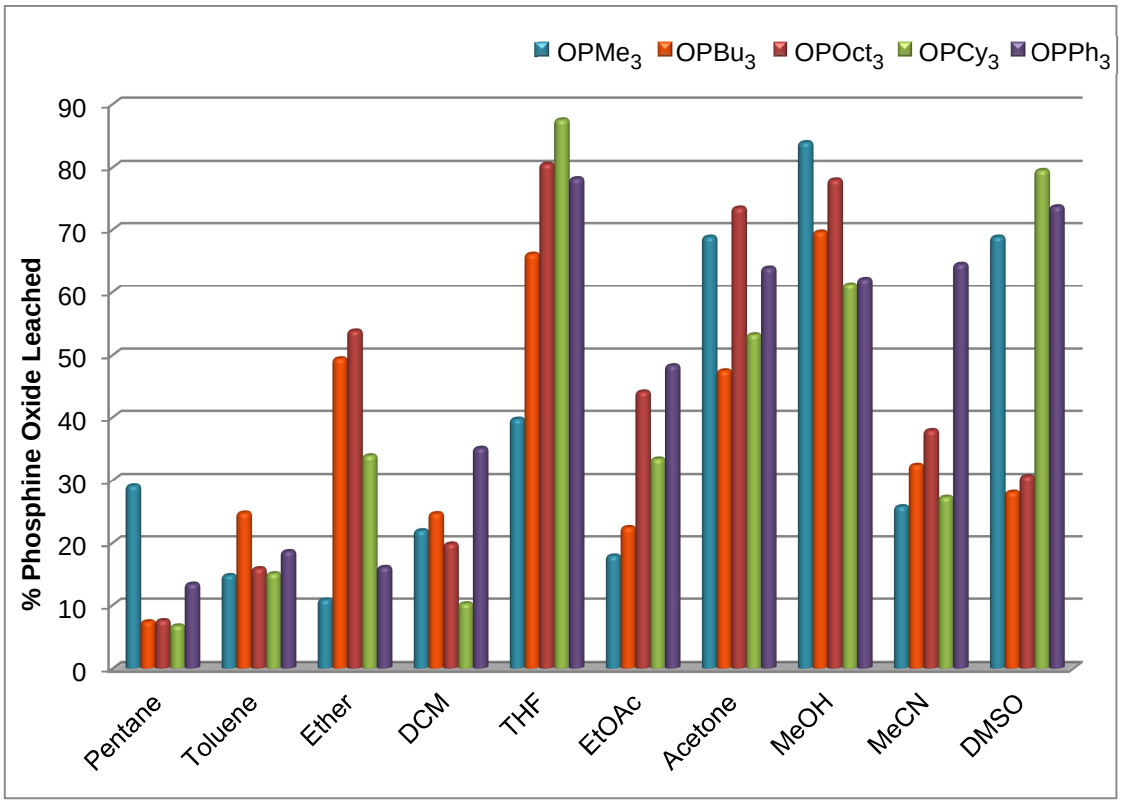

Figure 3.4. Leaching of the phosphine oxides $\mathbf{2_{ads}}$–$\mathbf{6_{ads}}$ from wet silica in different solvents.

The leaching of the phosphine oxides was compared to the polarity of the different solvents (Figure 3.5). Initially it was assumed that the polarity of the solvent had an important influence on the leaching effects, but as shown below there is no clear trend from the data. Although it does appear that some of the more polar solvents cause the phosphine oxides to leach more from the support as opposed to nonpolar solvents, the overall trend does not show the amount of phosphine oxide leached directly increases

as solvent polarity increases for any of the phosphine oxides **2**–**6**. It is also apparent that the protic nature of the solvent does not greatly affect the leaching since both THF and methanol show the greatest leaching effects, while only methanol could form hydrogen bonds with the phosphine oxides. Furthermore, the water content in each solvent should be minimal because either distilled solvents were used or the solvents were thoroughly degassed and dried over activated molecular sieves prior to the leaching tests. Therefore, hydrogen bonding of any water in the solvent with the P=O group is most likely not a contributor to removing the adsorbed phosphine oxide from the silica.

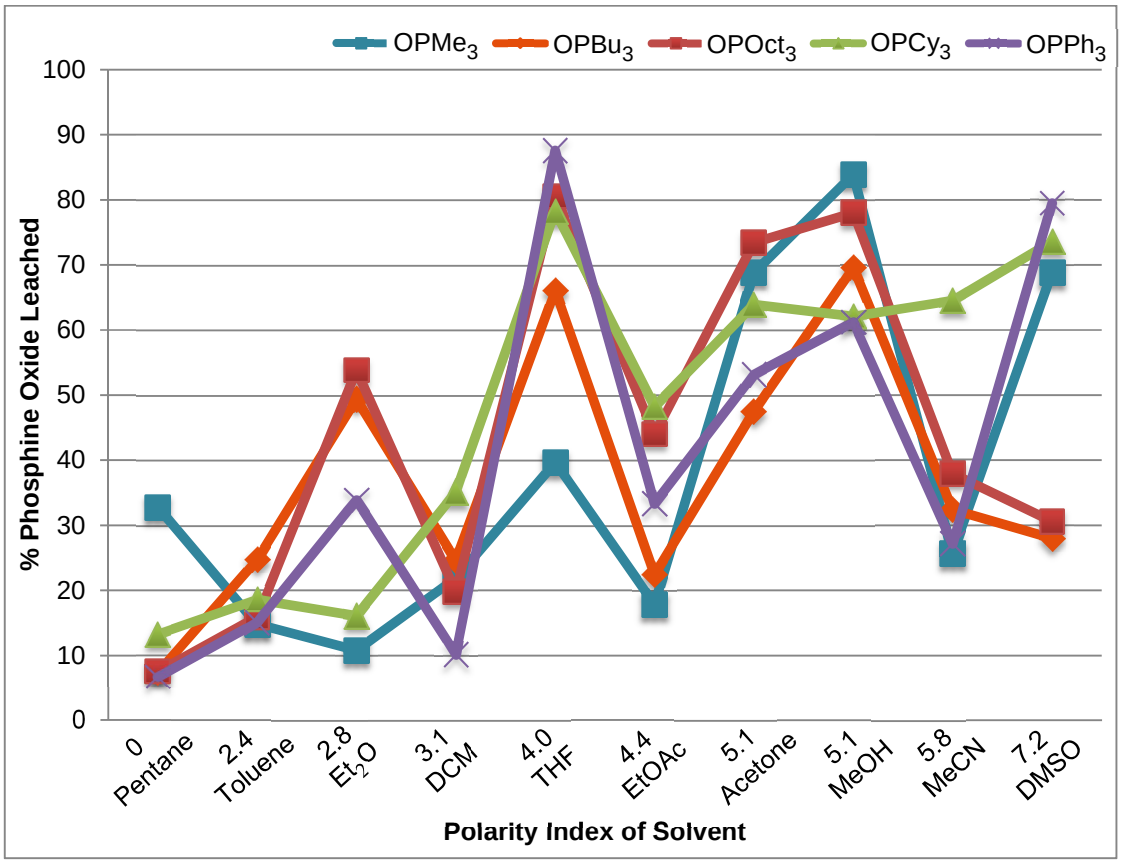

Figure 3.5. Leaching of phosphine oxides $\mathbf{2_{ads}}$–$\mathbf{6_{ads}}$ from silica versus polarity index for the given solvents.

In all, the leaching is probably influenced most by the solubility of each phosphine oxide in a given solvent. This would account for the variations seen for the individual phosphine oxides **2**–**6** in the different solvents. Another factor that may also have an impact on the leaching studies is the ability of the solvent to interact with the silica surface. If the solvent can be adsorbed strongly on silica as well, there may be some competition for the surface sites, which in turn may be why certain solvents are able to remove the phosphine oxides from the support. The exact amounts of materials used for each leaching trial are given in Tables 3.9 and 3.10 in the Experimental section.

Pre-treatment of Silica with Polar Solvents

As a means of assessing the ability of different solvents to strongly interact with the support and prevent the contact of phosphine oxides with the surface, thereby facilitating the leaching process, silica was exposed to selected solvents prior to the adsorption procedure. In these experiments the silica was first stirred overnight with a specific solvent, either toluene, acetone, or THF. Toluene was selected as the standard of comparison since all other adsorption studies of the phosphine oxides on silica, including the surface coverage studies, had been performed using toluene. Acetone and THF were picked because they are polar solvents that had potential to interact with the silica and both caused a high degree of leaching of the phosphine oxides. After the silica was exposed to the solvents overnight, the stirring was stopped so the silica could settle and the supernatant was removed. There was no vacuum applied for drying, so this left the silica slightly damp with the given solvent prior to the adsorption process. The standard adsorption procedure was applied where toluene was added to the silica to form a slurry, and in a separate flask the phosphine oxide was dissolved in toluene and then added to the silica slurry via pipette. The mixture in toluene was stirred overnight to give time for

the adsorption of the phosphine oxide to take place. The following day the supernatant was collected, solvent removed, and the residue weighed to determine the surface coverages shown in Figure 3.6. The amounts of phosphine oxide and silica used for each experiment can be found in the Experimental section in Tables 3.12 and 3.13.

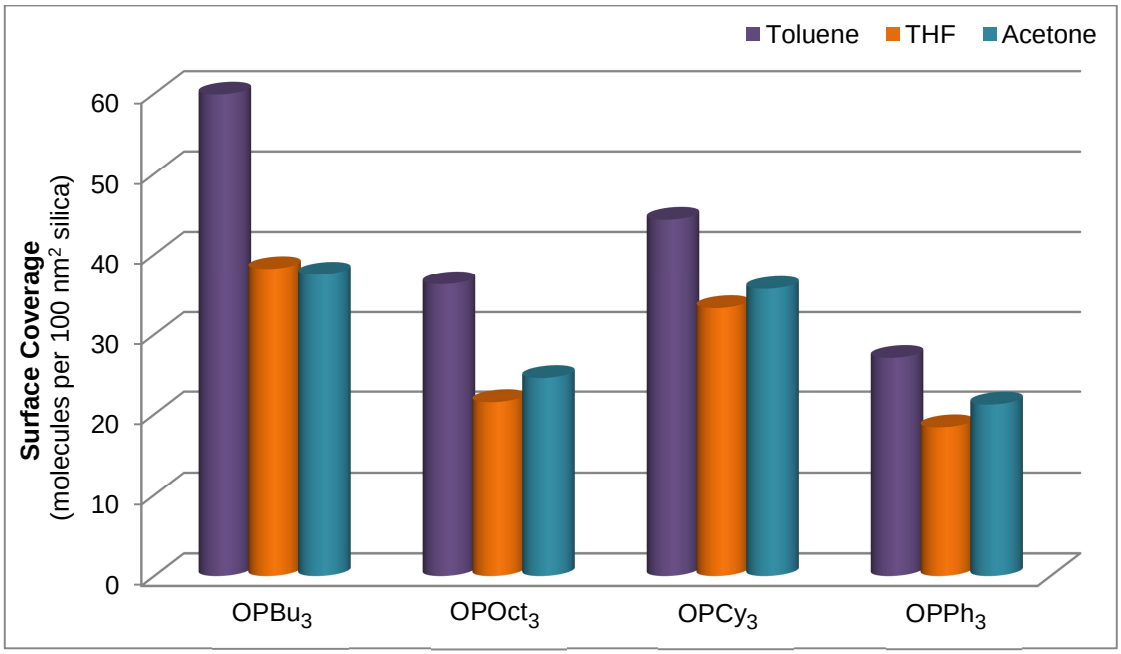

Figure 3.6. Surface coverage values of phosphine oxides $\mathbf{3_{ads}}$–$\mathbf{6_{ads}}$ on wet silica pre-treated with different solvents.

As clearly shown in Figure 3.6, the silica exposed to polar solvents prior to adsorption had a decreased surface loading of every phosphine oxide $\mathbf{3_{ads}}$–$\mathbf{6_{ads}}$ as compared to exposure to toluene. Toluene does not keep the phosphine oxides from adsorbing on silica because the surface coverage is in the range of the maximal surface coverage determined previously (Table 3.2). The results for the polar solvents show that both acetone and THF are able to interact with the silica surface and may be inhibiting

the adsorption of the phosphine oxides.

In order to verify that the polar solvents are actually adsorbing on the silica surface, another set of experiments was conducted in which the same pre-treatment technique was applied but then the resulting silica was dried for several minutes under vacuum before the adsorption of **3**. The silica appeared white and powdery after the drying indicating no liquid solvent could be present, but there could still be several layers of solvent molecules adsorbed on the surface of the silica. The drying of the silica is effective at removing some of this adsorbed solvent from the surface as indicated by a slight increase in the surface coverage using these batches of silica (Figure 3.7). Nevertheless, the surface loadings are still lower than on the silica treated only with toluene, again confirming the polar solvents are adhering to the support and preventing adsorption of the phosphine oxides to some degree.

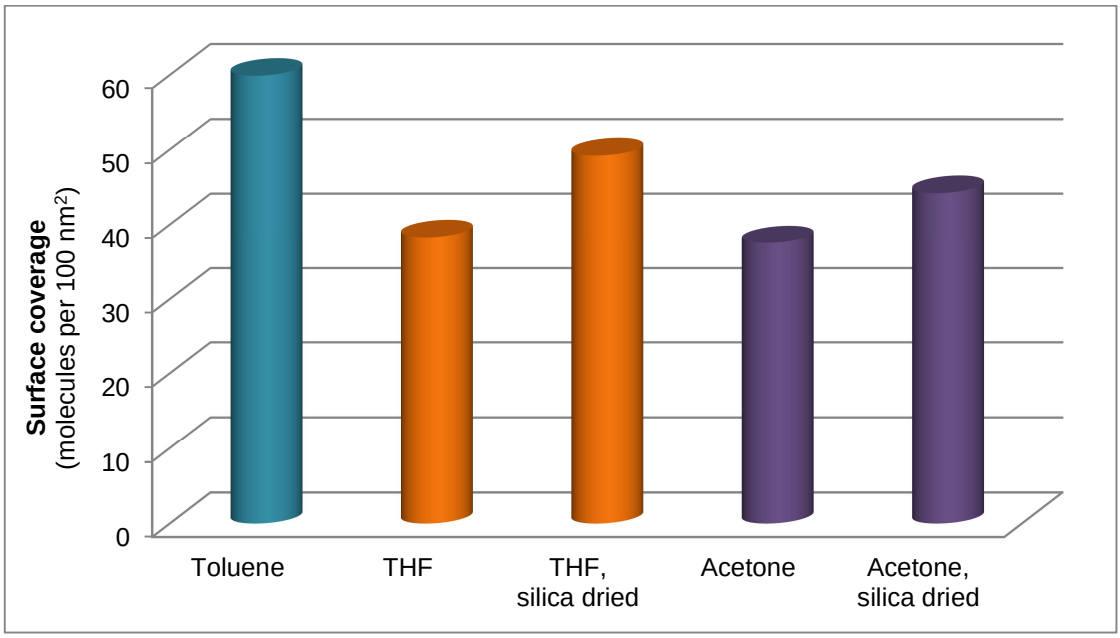

Figure 3.7. Surface coverage values of phosphine oxide **3** adsorbed on silica pre-treated with different solvents.

High-Resolution Magic Angle Spinning (HRMAS) NMR Measurements

HRMAS provides a unique way to obtain narrower signals in solid-state NMR spectra of immobilized species by supplying a few drops of solvent to the silica to form a slurry. All mobile components of the material will give narrower signals, while immobile species will not be visible. A special rotor equipped with an insert to confine the solvent at moderate spinning speeds of up to 2 kHz is required for these measurements. HRMAS is a great technique to mimic reaction conditions and see how compounds tethered to an insoluble support, such as an immobilized linker or catalyst, react in solution, *in situ*. Classic solution or solid-state NMR spectroscopy of the dry material is not applicable in these cases. One of our motives behind studying the adsorption of phosphine oxides was to better characterize byproducts that arise in the synthesis of immobilized catalysts, so better spectral resolution is appreciated.

Furthermore, it is interesting to investigate the strength of the adsorption in various solvents and to probe directly whether the phosphine oxides continue to interact with the silica or whether they are completely washed off the surface in solution. While the leaching experiments described above only distinguish between the phosphine oxides attached to the support and dissolved in the supernatant solution, HRMAS can provide insight about the scenario in the so-called interphase, the boundary region at the interface between solid and liquid.

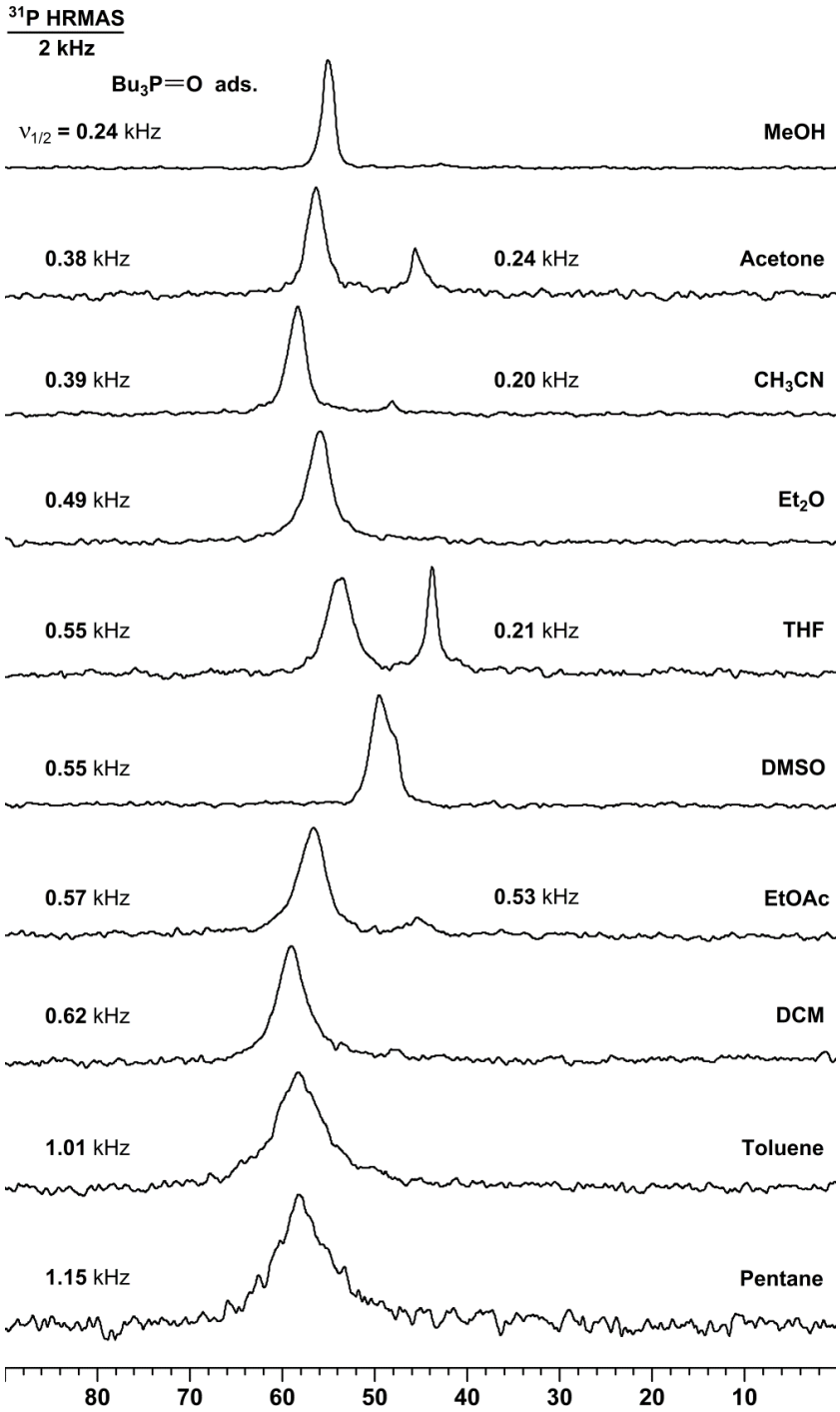

Figure 3.8. ^{31}P HRMAS spectra of phosphine oxide $Bu_3P{=}O$ (**3**) adsorbed on wet silica (**3**$_{\mathbf{ads}}$) and the halfwidths $\nu_{1/2}$ of the signals.

The ^{31}P HRMAS spectra of $\mathbf{3_{ads}}$ in the presence of the indicated solvents are shown in Figure 3.8. They exhibit interesting features for the different solvents. In most of the nonpolar solvents, such as pentane and toluene, only one broad signal is visible at about the same chemical shift as $\mathbf{3_{ads}}$ in the solid state. This indicates that in these cases the phosphine oxide adsorption on silica is strong and that it persists in the presence of the solvent. Therefore, these solvents not disrupt the interactions of the P=O group with the surface silanol groups, which coincides with the leaching data because these solvents did not cause significant amounts of phosphine oxide leaching from the support. Furthermore, although the HRMAS signal is comparatively broad ($\nu_{1/2}$ = 1.01 kHz), the half width is still smaller than that in the ^{31}P MAS NMR spectrum ($\nu_{1/2}$ = 1.80 kHz) showing that the added solvent does have a mobilizing effect, which probably consists of additional wagging and rotational degrees of freedom. An increase of translational mobility is less likely because the solvent molecules, even if they are not strongly adsorbed should still stand in the way of the phosphine oxide and slow its motion down.

On the other hand, polar solvents, such as THF and acetone, which were shown to cause large amounts of phosphine oxide to leach from the silica, display two separate signals in the HRMAS spectra. The signal around 55 ppm in THF, for example, stems from the adsorbed phosphine oxide $\mathbf{3_{ads}}$ still residing at the silica surface while the signal shifted upfield to about 43 ppm corresponds to phosphine oxide **3** that has leached from the surface. It might be dissolved in the solvent. However, the linewidth of more than 200 Hz speaks for a lower mobility. Fully dissolved small molecules typically exhibit linewidths of 20 to 50 Hz when measured in a rotor. Thus, even in solvents where the phosphine oxides are known to leach off the support, some portion of the oxide remains at the silica surface, potentially in equilibrium with the strongly adsorbed molecules. Overall, in practical terms these results demonstrate that multiple wash cycles

are necessary to remove all adsorbed phosphine oxide from the surface. For all other phosphine oxides **2** and **4**–**6**, very similar data was obtained from the HRMAS NMR spectra with slight variations in regards to which solvents caused leaching of each oxide into solution.

Competition Studies

As noted in the introduction of this chapter, the predominant adsorption pathway for the diphosphine monoxide cage **I** was originally believed to be via the phosphine moiety adsorbing on silica. Now, having studied the adsorption of the model phosphine oxides and realizing the strength of their interaction with the support is stronger than expected, some competition experiments had to be conducted. The adsorption of $OPBu_3$ (**3**) was tested against the corresponding PBu_3 (**7**) on various types of silica. In all experiments a 1 : 1 mixture of **3** and **7** in toluene was applied to the silica and the mixture was stirred overnight. The silica was subsequently allowed to settle, and the supernatant was transferred to another flask, the solvent was removed in vacuo, and the residue was weighed. ^{31}P NMR spectroscopy was used to analyze the amounts of **3** and **7** in the supernatant and reveal how much of each component was adsorbed on silica. The surface coverages of both compounds on the different silica supports are shown in Figure 3.9. Dry silica 1 refers to the silica that is dried *in vacuo* at 300 °C for about 7 days and stored in a large Schlenk flask for use by the group. This is the standard dried silica used for the previous adsorption experiments. For investigating the effect of the dryness of the silica on the competition experiments, a small batch of this pre-dried silica was dried even more rigorously by heating it *in vacuo* with a heat gun (~150 °C, 3 cycles, 10 mins. each) yielding dry silica 2.

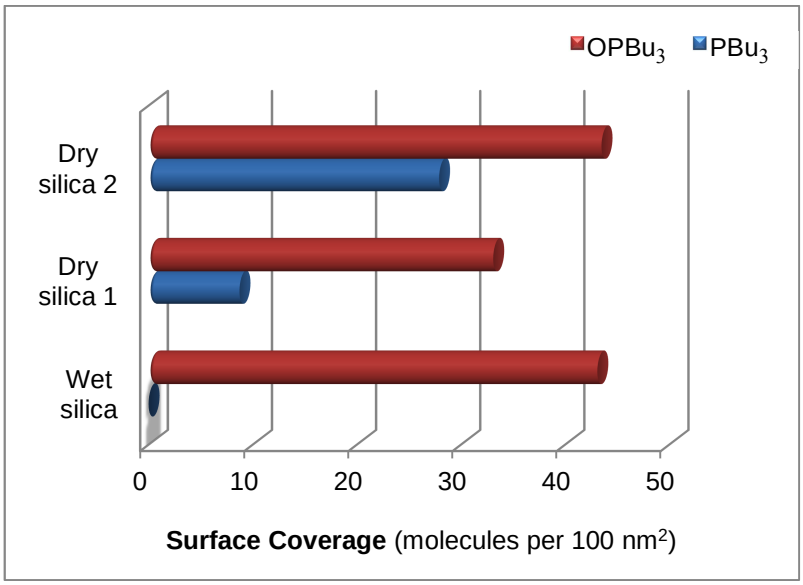

Figure 3.9. Surface coverages of $Bu_3P{=}O$ (**3**) and Bu_3P (**7**) adsorbed on the silica surface after being applied in a 1 : 1 mixture for the competition experiments.

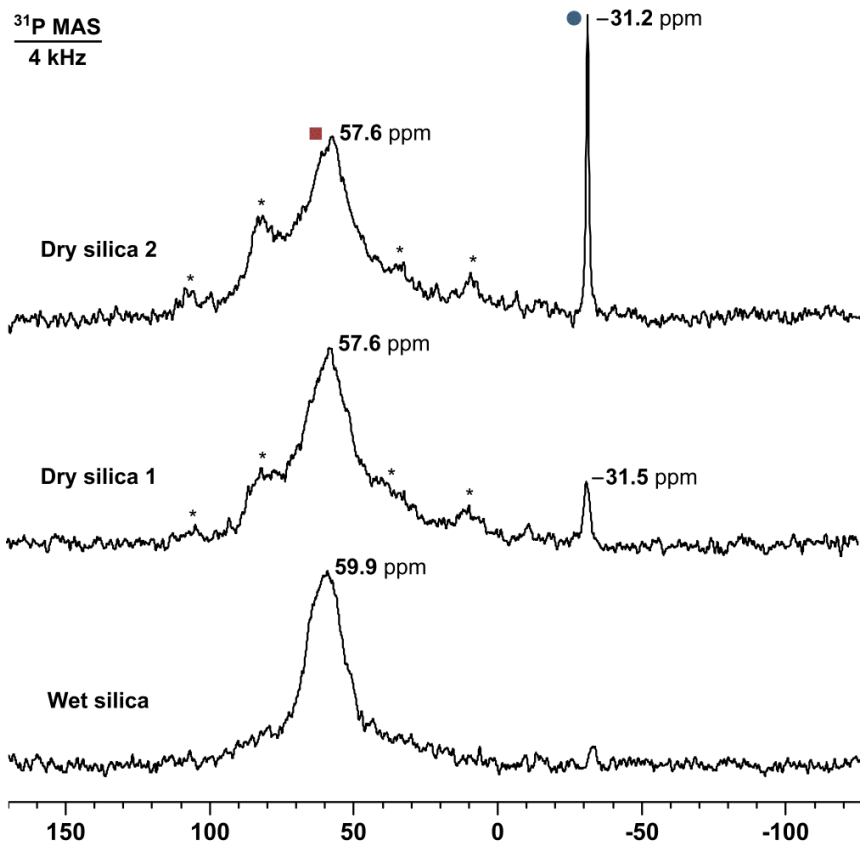

Figure 3.10. Competition of **3** and **7** adsorbing on the different silica surfaces.

On each type of silica it is evident that the phosphine oxide **3** adsorbs more strongly than the phosphine **7** (Figures 3.9 and 3.10). Practically no phosphine was adsorbed onto the wet silica as seen in Figure 3.9 and this was confirmed by ^{31}P NMR analysis of the supernatant solution and weighing the residue after solvent removal. The wet silica is known to have many more surface silanol groups which could form hydrogen bonds with the phosphine oxide leading to a much higher loading of **3** on this type of silica. On the dried silica many of the surface silanols are condensed to form siloxane groups on the surface. In this case there are fewer sites for the phosphine oxide **3** to hydrogen bond with the support, so its surface coverage decreases. Being that all

surface sites are not occupied with phosphine oxide, there is some room for phosphine **7** to be adsorbed as well but still in lower quantities than the oxide. When the silica is dried more thoroughly as in the case of dried silica 2 (Figure 3.10), the preference for the phosphine oxide to be adsorbed over the phosphine diminishes even more and there is about a 1.6 : 1.0 ratio of **3** : **7** on the silica. Overall, for the adsorption of the monoxide cage **I** the phosphine oxide group will most likely be more strongly adsorbed but on the dry silica there is the possibility that either side of the cage could interact with the support.

The overall insight of this experiment is that phosphine oxides preferentially interact with surface silanol groups by hydrogen bonding. Phosphines, on the other hand, interact with Lewis acidic sites using their lone pair but can also potentially bond with the surface silanol groups since the surface coverages of the phosphines were approximately the same on both wet and dry silica.[10]

Dry Grinding Experiments

All adsorption experiments discussed thus far dealt with the adsorption of the phosphine oxide from solution onto silica. During Dr. Yang's dissertation on phosphines in the Bluemel group, it had also been discovered that phosphines undergo adsorption from the solid state onto the silica surface.[10] This was an unprecedented result for phosphines with high melting points, and it confirmed that the phosphines must be translationally mobile across the silica surface, allowing them to break out of the crystal lattice and while being adsorbed to slowly migrate away from the crystal. It was also discovered that the phosphines reproducibly formed only a monolayer on the surface and the excess phosphine remained polycrystalline in nature, displaying a large CSA in the ^{31}P MAS spectra.

Therefore, this experiment was repeated here using the phosphine oxides. Special emphasis was placed on the comparison of the time required for the adsorption starting with dry polycrystalline phosphine oxides. Only $OPCy_3$ (**5**) and $OPPh_3$ (**6**) were solids with high melting points and thus suitable for the dry grinding experiments. First, **6** was ground with wet silica in the glove box and the ^{31}P MAS NMR spectra were recorded over time (Figure 3.11). The materials were only ground together once, but the adsorption continued to progress over a 4 day period. The amounts of phosphine oxide and silica used for each trial can be found in the Experimental section in Table 3.14. The adsorption process is very quick and adsorbed phosphine oxide $\mathbf{6_{ads}}$ can be seen initially after only 15 minutes. The chemical shift of the signal for $\mathbf{6_{ads}}$ (δ = 35–36 ppm) matches well with the one observed from the adsorption performed using toluene (δ = 36.5 ppm). Also, the excess polycrystalline material has a chemical shift of 28.1 ppm, again matching what was seen for the ^{31}P MAS NMR of the pure polycrystalline **6**. At 4 days the two signals seem to merge and shift to 33.6, which is in between the chemical shifts of the adsorbed species and the polycrystalline solid. Even after 24 days, the ^{31}P MAS NMR showed the same signal shape. An excess of 100 molecules per 100 nm^2 was applied to the silica which is approximately 1.5 times the amount needed to form a densely packed monolayer (63.5 molecules per 100 nm^2, Table 3.1) on the silica surface. Possibly the phosphine oxides are able to stack on the silica surface, which has been observed in some phosphine oxide crystal structures,[63] and form bilayers or multiple layers on the silica creating this new signal. This is just speculative, but the grinding experiments of $OPBu_3$ (**3**) showed similar results with the adsorbed signal overlapping with the signal of any remaining polycrystalline solid. In the case of **3**, much more than the maximal surface coverage, as determined from solution (Table 3.2), was adsorbed again indicating multiple layers may have formed.

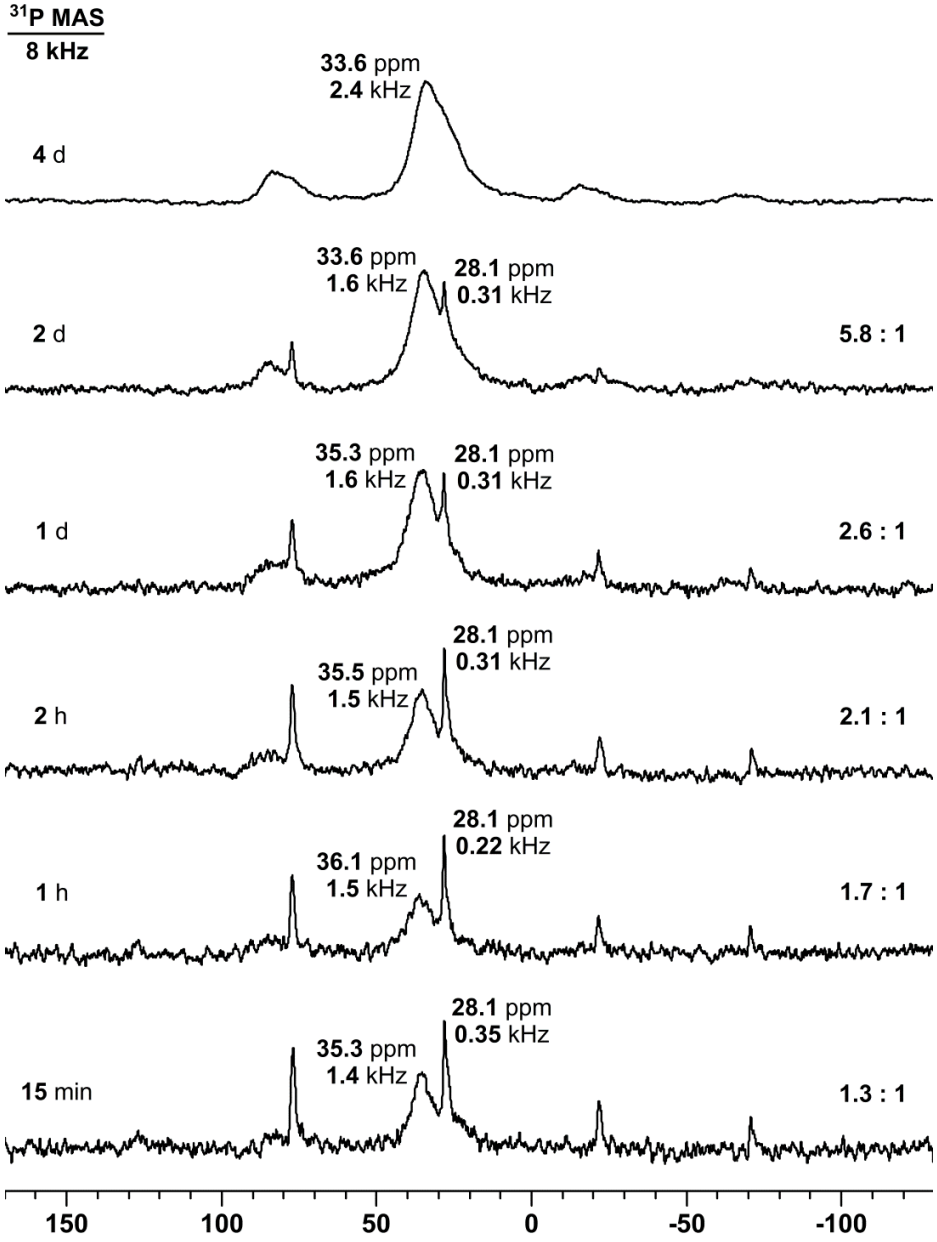

Figure 3.11. Dry grinding of **6** with wet silica. The $\mathbf{6_{ads}}$: $\mathbf{6_{cryst}}$ ratio is given on the right side of each spectrum.

For phosphine oxide **5** the ^{31}P MAS NMR spectra display a similar trend. The amount of adsorbed phosphine oxide $\mathbf{5_{ads}}$ increases over time (Figure 3.12). In this case,

the signal of $\mathbf{5_{ads}}$ is at ~58 ppm while the polycrystalline **5** has a chemical shift of 47.8 ppm. The difference of over 10 ppm between the two signals allows them to be more easily distinguished than in the case of **6** and $\mathbf{6_{ads}}$. This is important when deconvoluting the spectrum to integrate how much of each species exists on the surface.

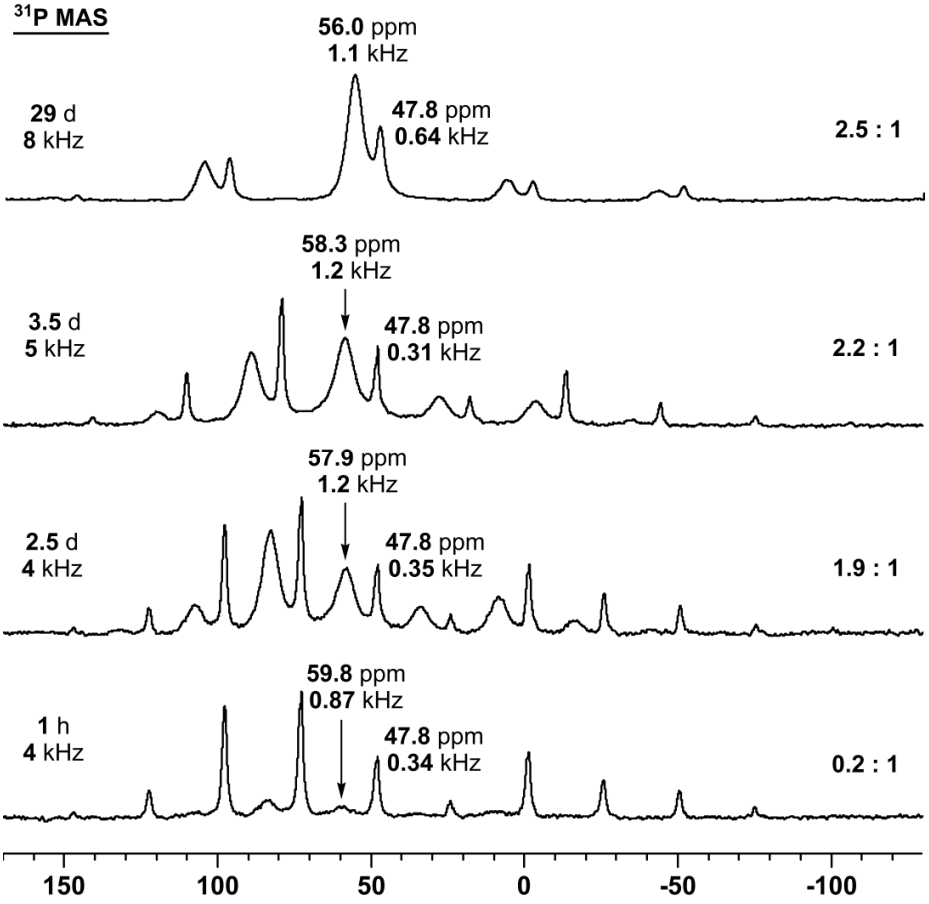

Figure 3.12. Dry grinding of **5** with wet silica. The $\mathbf{5_{ads}}$: $\mathbf{5_{cryst}}$ ratio is given on the right side of each spectrum.

Also, the adsorption of **5** on silica is clearly a much slower process than for **6** because there is barely any $\mathbf{5_{ads}}$ visible in the spectrum after 1 hour. A decreased

translational mobility of **5** on the surface, as a result of its bulky substituents or due to electronic effects, which cause it to hydrogen bond strongly to the support and remain immobile, would explain this observation and would further clarify why $\mathbf{5_{ads}}$ does not have as large of a reduction of the CSA when on silica as evidenced by its many rotational sidebands (Figure 3.3). Another factor distinguishing the adsorption of **5** versus **6** would be its aromatic substituents, which can aid in the adsorption process because they also are known to interact with silica and can help the compound slide across the surface.[61] The sample was measured again after 29 d to see how much of **5** was adsorbed once the system reached an equilibrium point, and a ratio of 2.45 : 1 was observed for $\mathbf{5_{ads}}$: $\mathbf{5_{cryst}}$.

Lastly, the solid-state adsorption experiments were also conducted with dry silica and similar results were obtained. For **6** the adsorption seemed to occur at a similar rate using the dry silica, and once again after 3 days the signals merged maybe indicating bilayer formation on the support. On the other hand, for **5** the adsorption was much slower using the dry silica and even after 5 days not nearly as much adsorbed phosphine oxide $\mathbf{5_{ads}}$ could be seen in the spectrum. For **5** it seems the surface silanol groups and hydrogen bonding interactions with the P=O group are vital to accelerate the adsorption from the solid state.

^{31}P T_1 Relaxation Time Measurements of Adsorbed Phosphine Oxides

The ^{31}P T_1 (spin-lattice) relaxation time values obtained from solid-state NMR measurements can give an indication about the mobility of substances on a support. Typically, molecules that are more mobile will give a shorter T_1 time than those that are less mobile.[68] The polycrystalline solids should have very long T_1 times because the molecules are locked in the crystal lattice and therefore are not very mobile beyond

vibrations. For example, the T_1 times of solid organometallic complexes containing PPh_3 ligands, such as Wilkinson's catalyst, are several minutes.[69] Even in solution the T_1 times remain rather long for these compounds and have been calculated to be 30.8 s for PPh_3 and 19.8 s for $OPPh_3$ at room temperature in $CDCl_3$.[70] The goal of the measurements presented here was to compare the T_1 times of adsorbed phosphines with those of adsorbed phosphine oxides and to investigate how the surface coverages may affect the mobilities and in turn the T_1 times. Therefore, $OPPh_3$ (**6**) and its corresponding phosphine PPh_3 (**8**) were both adsorbed on silica with different surface loadings (amounts given in the Experimental section in Table 3.15). The monolayer amount (~206 molecules per 100 nm^2) was the value determined from the dry grinding experiments by Dr. Yang for **8**[10] because this was the surface loading at which only one signal of adsorbed PPh_3 ($\mathbf{8_{ads}}$) could be observed and at higher loading a signal for $\mathbf{8_{cryst}}$ was seen as well. The sub-monolayer was slightly more than one tenth that coverage and the excess was almost three times the monolayer amount.

The pulse programs used to measure the T_1 times was a saturation recovery experiment. During the saturation recovery method a series of pulses transfer the magnetization to the *x*,*y*-plane and allow it to dephase resulting in no net magnetization in any direction. Since the magnetization is saturated, no signal seen in the NMR spectrum. Then, a delay is added to allow the magnetization to relax back to the *z*-plane, and by increasing this delay, a signal emerges in the spectra and increases in intensity. The peak intensity of the isotropic signal of the adsorbed species, either $\mathbf{6_{ads}}$ or $\mathbf{8_{ads}}$, was determined by using the Data Analysis function to calculate the intensities, which are the signal-to-noise values for the selected peak. All of these values were then normalized by dividing by the largest peak intensity, which was typically found in the spectrum with the longest delay, and subtracting the values from 1 to give the

exponential decay graphs (Figures 3.13 and 3.14). By fitting the curves with an exponential decay function, the T_1 times could be found from the resulting equations and are reported in Table 3.3.

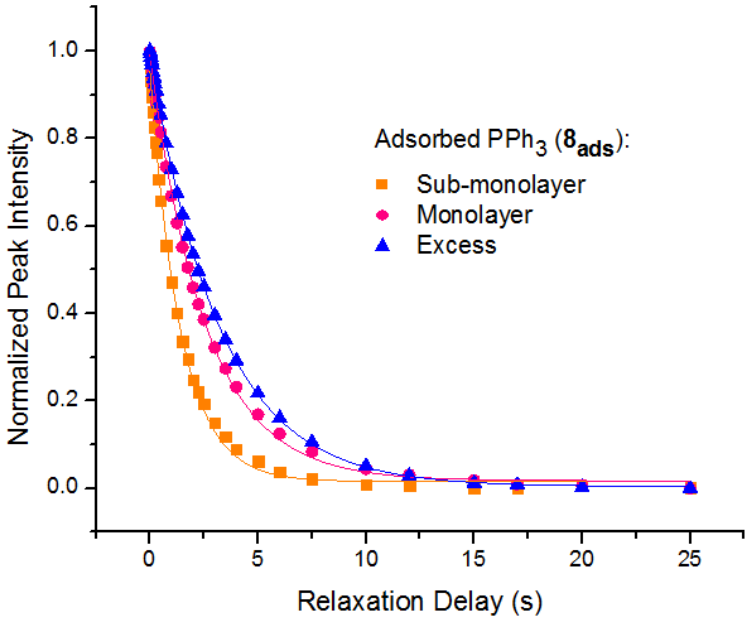

Figure 3.13. ^{31}P T_1 times of PPh_3 (**8**) adsorbed on silica at various surface loadings.

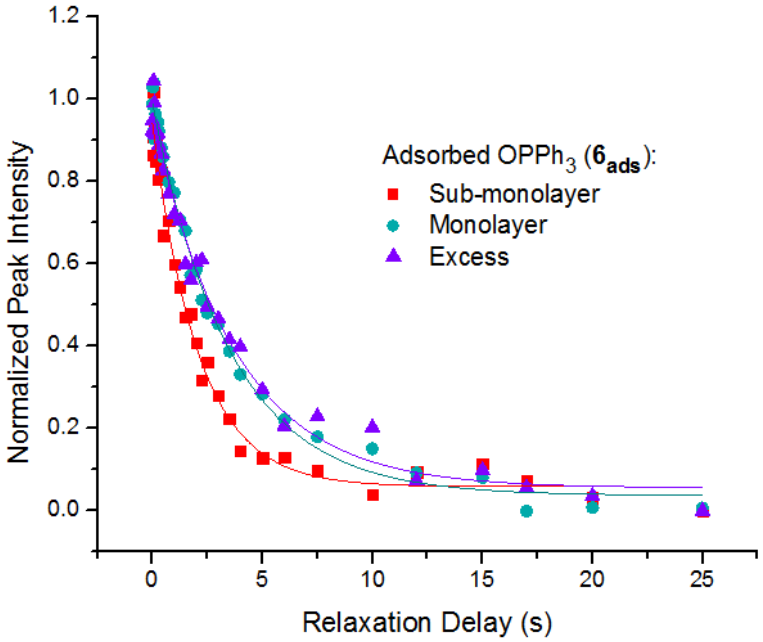

Figure 3.14. ^{31}P T_1 times of $OPPh_3$ (**6**) adsorbed on silica at various surface loadings.

Table 3.3. ^{31}P T_1 times of $\mathbf{6_{ads}}$ and $\mathbf{8_{ads}}$ at different surface loadings.

	T_1 Times [s]	
Coverages	**Adsorbed PPh_3 (8_{ads})** (molecules per nm^2)	**Adsorbed $OPPh_3$ (6_{ads})** (molecules per nm^2)
Sub-monolayer	**1.4** (26.6)	**2.1** (27.1)
Monolayer	**2.6** (206)	**3.5** (206)
Excess	**3.2** (591) (2.6 : 1)[a]	**3.9** (590) (2.8 : 1)[a]

[a] The additional value is the ratio of adsorbed to polycrystalline material on the surface, meaning $\mathbf{8_{ads}}$: $\mathbf{8_{cryst}}$ or $\mathbf{6_{ads}}$: $\mathbf{6_{cryst}}$.

As shown in Table 3.3, the adsorbed phosphine $\mathbf{8_{ads}}$ consistently shows a shorter T_1 times at a given surface coverage than the adsorbed phosphine oxide $\mathbf{6_{ads}}$. This implies that **6** has less mobility on the silica surface, which can be supported by the idea that hydrogen bonding may hold the phosphine oxides more strongly at the surface silanol groups leading to a decreased translational mobility. Furthermore, as the surface coverage of either compound increases the T_1 time increases as well indicating at higher loadings the compounds are less mobile on the support. The excess polycrystalline material on the silica may inhibit the motion of the adsorbed species resulting in less translational mobility at the higher surface coverages. At low loadings the substances have plenty of room on the silica surface and can be more mobile resulting in a shorter T_1 time.

Adsorption of Tetraphosphine Tetroxide

The Bluemel group has used a rigid tetraphosphine scaffold as a linker to generate many immobilized catalysts.[16] The tetraphosphine linker has four equivalent phosphine groups in one molecule, therefore it represents another good candidate for the adsorption studies. Maximally three of the four phosphines can be adsorbed on silica at a given time due to steric reasons. Therefore, this compound can also serve as an intramolecular standard for translational mobility studies and probe how this contributes to the CSA reduction.

Dr. Yang of the Bluemel group attempted to adsorb the C tetraphosphine on silica, but the orientation of the lone pairs was not favorable for the compound to interact with the silica surface.[10] The ^{31}P MAS NMR spectra of the adsorbed species appeared exactly the same as that of the polycrystalline material, which indicated no adsorption occurred.

The series of tetraphosphine tetroxides **9–11** (Figure 3.15) were all synthesized, but only the adsorption of **9** and **11** on silica were performed to compare with Dr. Yang's data. It was assumed that the P=O groups may be able to hydrogen bond to the silica via the oxygen lone pairs and be adsorbed. The tetroxides were adsorbed on silica with a loading of approximately 5 molecules per 100 nm^2, which is the amount typically used for the immobilization of this linker system in the formation of immobilized catalysts.[16] The exact amounts of tetroxides and silica used for each experiment are in Table 5.16 in the Experimental section.

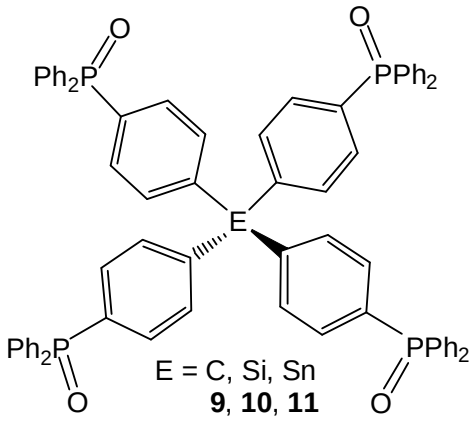

Figure 3.15. Tetraphosphine tetroxides **9**–**11** for adsorption studies.

The ^{31}P MAS and wideline NMR of each of the adsorbed tetraphosphine oxides showed two signals indicating that adsorption at the surface via the P=O occurred (Figure 3.16 and Appendix). Furthermore, the chemical shift of the isotropic line changed from 26.0 ppm for the polycrystalline solid to 35.8 ppm for the adsorbed material, again proving that adsorption took place. The CSA is reduced drastically by 22 ppm (Figure 3.15) when comparing the one of **11** (178 ppm) with the largest CSA value

of **11$_{ads}$** (156 ppm).

Table 3.4. ^{31}P isotropic chemical shifts and CSA values of **9** and **11** and adsorbed species **9$_{ads}$** and **11$_{ads}$**.

Tetroxide	**Silica**	**δ_{iso}(^{31}P)** (ppm)	**CSA** (ppm)
9	–	29.4	193
9$_{ads}$	wet	36.4	154
9$_{ads}$	dry	32.5	165
11	–	26.0	178
11$_{ads}$	wet	35.8	156
11$_{ads}$	dry	34.5	156

However, the wideline spectrum shows that there is at least one second species which leads to the bump at about 38.2 ppm (Figure 3.16, bottom). This most likely happens because only maximally three of the P=O groups can interact with the support and the P=O groups pointing away from the silica experience only the overall translational mobility, but not any line-narrowing effect due to formation of [$R_3PO\cdots HO^-$]. However, if three of the P=O groups are interacting with the silica, the translational mobility is significantly reduced because all the groups would have to move together in the same direction across the support, which is highly unlikely. Therefore, it should be mostly the rotational mobility that is responsible for the reduction in the CSA upon adsorption. Rotations of the tetraphosphine tetroxide scaffold are always possible if one P=O group stays fixed in one place and acts as a pivot point, while the other three

are detached from the surface and free to rotate.

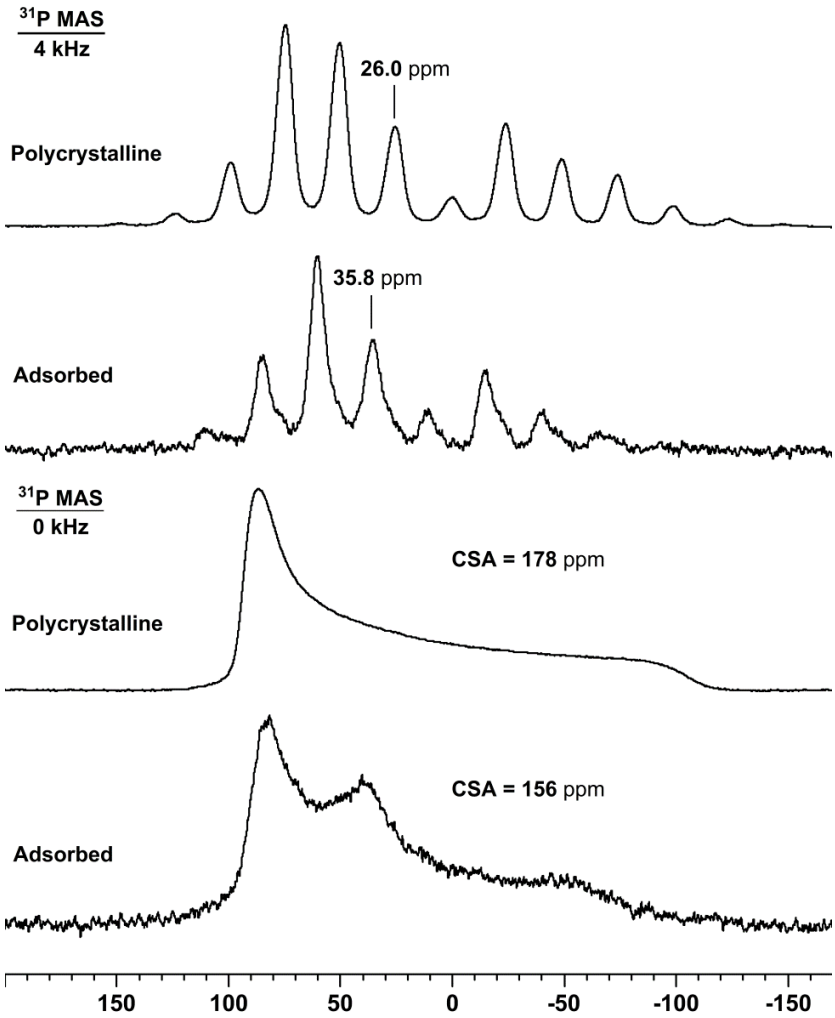

Figure 3.16. ^{31}P MAS NMR spectra of the Sn tetraphosphine tetroxide (**11**) as a polycrystalline powder and adsorbed on wet silica $\mathbf{11_{ads}}$.

Unfortunately, since there are four phosphine oxides in the molecule and either one, two, or three can be interacting with the silica at a given time, the signal of the adsorbed P=O groups could not be separated from that of the not adsorbed P=O group

even at higher spinning speeds up to 13 kHz (Figure 3.17). There is clearly a small shoulder upfield from the major peak, which would be close to the chemical shift of the polycrystalline material, but the two signals are overlapping too much to allow an analysis of the differences in the CSA.

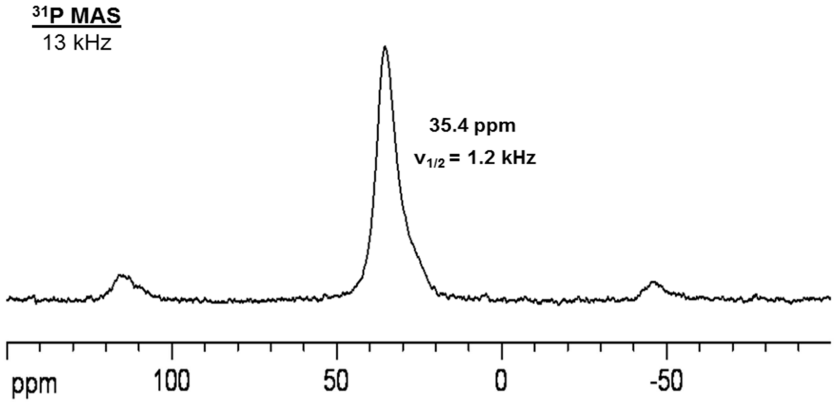

Figure 3.17. ^{31}P MAS NMR spectrum of $\mathbf{11_{ads}}$ on wet silica.

HRMAS NMR can also be used to analyze the tetraphosphine tetroxides adsorbed on silica (Figure 3.18), but the presence of a solvent complicates the scenario because THF can cause some leaching of the phosphine oxides from the silica. There are definitely two signals in a 1 : 1 in the HRMAS spectrum. One stems from the adsorbed P=O groups and one from the P=O groups pointing away from the surface and potentially the P=O groups of molecules that have leached from the support and are no longer interacting with the silica. Unfortunately, the CSA completely collapses when the THF slurry is measured with HRMAS (Figure 3.18), so no information about the CSA of the adsorbed versus not adsorbed P=O groups can be determined from the spectrum. However, the mere presence of two different signals at 27.9 and 23.7 ppm with the

halfwidths of about 780 and 370 ppm, respectively, implies that a substantial number of P=O groups are adsorbed on the silica surface. Based on the downfield shift and the larger chemical shift value one can attribute the signal at 27.9 ppm to the adsorbed P=O groups.

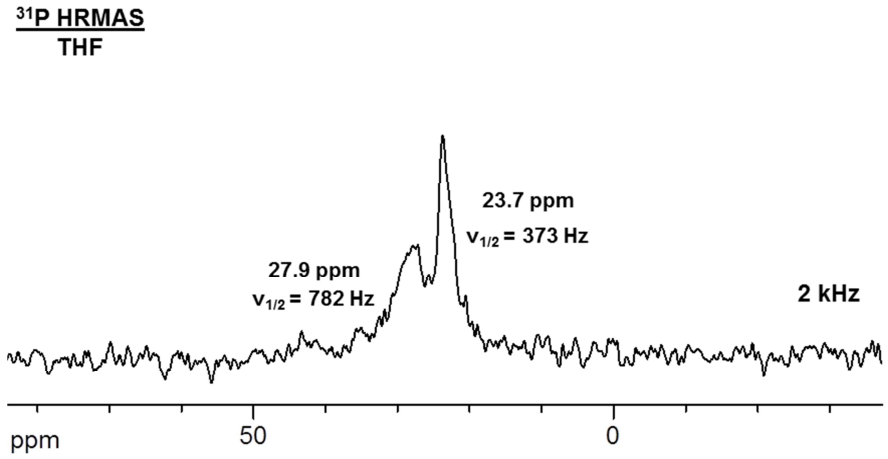

Figure 3.18. ^{31}P HRMAS NMR spectrum of $\mathbf{11_{ads}}$ on wet silica.

CONCLUSION

A series of model phosphine oxides **2**–**6** were adsorbed on wet and dry silica surfaces, and in all cases there was a drastic reduction in the CSA of the adsorbed species $\mathbf{2_{ads}}$–$\mathbf{6_{ads}}$ as well as a downfield shift of the isotropic line. The surface coverages of each oxide on silica was determined and in general related to the size of the compound. The ^{31}P NMR spectra of the adsorbed phosphine oxides $\mathbf{2_{ads}}$–$\mathbf{6_{ads}}$ in various solvents were examined using HRMAS spectroscopy. Quantitative leaching experiments were undertaken. Polar solvents, such as acetone and THF, were shown to interact with the silica support leading to a decrease in the surface coverages and also contributing to

the leaching effects of these solvents. Phosphine oxides were also proven to adsorb stronger than phosphines on silica by competition studies. Furthermore, phosphine oxides can be adsorbed not only from solution but from the solid state by dry grinding together with the silica. This result confirms that the phosphine oxides have translational mobility on silica allowing them to spread across the surface and be adsorbed. The mobility was further probed using T_1 relaxation time measurements, which showed that phosphines are, at a given surface coverage, more mobile on the support than phosphine oxides. Lastly, the tetraphosphine tetroxides **9** and **11** have been adsorbed on silica. They both display two signals in the ^{31}P MAS NMR spectra for the adsorbed and not adsorbed P=O groups.

EXPERIMENTAL

(a) General procedures

All reactions involving phosphine starting materials were performed under a purified nitrogen atmosphere. Phosphine oxides were stored under nitrogen. Chemicals were treated as follows: Toluene (Mallinckrodt Chemicals, ACS grade), THF (Macron, ACS grade), Et_2O (J.T.Baker, ACS grade), and pentane (J.T.Baker) were distilled from Na/benzophenone and CH_2Cl_2 (Mallinckrodt Chemicals, HPLC grade) was dried in a commercially available solvent purification system (JC Meyer Solvent Systems). EtOAc (Macron, ACS grade), CH_3CN (EMD, HPLC grade), MeOH (Aldrich, ACS grade), acetone (Mallinckrodt, ACS grade), and DMSO (Aldrich, ACS grade) were all degassed by five cycles vacuum/N_2 and dried over 3 Å molecular sieves. C_6D_6 (Cambridge Isotope Laboratories) and $CDCl_3$ (Aldrich) were dried over 3 Å molecular sieves (EMD Chemical Inc.). The latter was also used for obtaining the adduct-free phosphine oxides, and it has the approximate composition (weight percentages): silica gel < 50%, Al_2O_3 <

40%, Na_2O < 30%, K_2O < 15%, MgO < 5%, and quartz < 3%. The molecular sieves were activated by heating in vacuum at 120 °C for 12 h. Bu_3P (Strem Chemicals, 99%), Oct_3P (Alfa Aesar, 90% technical), and Cy_3P (Alfa Aesar) were purified by column chromatography (alumina, elution with CH_2Cl_2). Me_3P (Alfa Aesar, 99%) and $ClPPh_2$ (TCI America, 98%) were used as received but kept in a glove box. H_2O_2 (Acros Organics, 35% aqueous solution) was either used as obtained or diluted and stored at 4 °C. Ph_3P (Aldrich, 99%), MnO_2 (Alfa Aesar, technical, min. 58%), and silica (Merck, 40 Å average pore diameter, 0.063 to 0.2 mm average particle size, specific surface area 750 m^2/g) were used as obtained. In addition to the latter "wet" silica, a "dry" batch was generated by heating the silica for 7 days at 300 °C at the vacuum line.

The ^1H, $^{13}C\{^1H\}$, and $^{31}P\{^1H\}$ NMR spectra of liquids were recorded on a 500 MHz Varian spectrometer at 499.70, 125.66, and 470.17 MHz. The ^1H and ^{13}C chemical shifts were referenced using the solvent signals. For ^1H NMR, the residual protons in the deuterated solvents (C_6D_5H, 7.15 ppm; $CHCl_3$, 7.26 ppm) were used; for ^{13}C NMR the carbon signals (C_6D_6, 128.02 ppm; $CDCl_3$, 77.00 ppm). For the accuracy of the ^{31}P NMR chemical shifts of solutions, $ClPPh_2$ (neat liquid, $\delta(^{31}P)$ = 81.92 ppm) was used as a chemical shift standard within a capillary centered in the 5 mm sample tubes.

The ^{31}P solid-state NMR spectra were recorded on a 400 MHz Bruker Avance widebore NMR spectrometer equipped with a 4 mm or 7 mm broadband probehead and ZrO_2 rotors. The polycrystalline substances were densely packed into the rotors. The chemical shifts were referenced with polycrystalline $(NH_4)H_2PO_4$ (+0.81 ppm) as the external standard. A single pulse program with ^1H high-power decoupling was applied, and typically about 64 scans with a pulse delay of 10 s were sufficient to obtain a signal while more scans, about 3000, generated a good signal-to-noise ratio.

HRMAS measurments were performed by adding several drops of solvent to the silica in the 4 mm suspension NMR rotors with inserts. The HRMAS spectra were recorded using a single pulse program with ^{1}H high-power decoupling and typically about 64 scans. However, with the tetroxides **9** and **11** more scans from 128–1000 scans were used for the HRMAS measurements. The pulse length was 2.5 μs at 6.60 dB power level, and the recycle delay was 5 s. The T_1 time measurements were performed using a saturation recovery pulse program, and the delay was incremented from 0.075–25 s. The intensity of the signal for the adsorbed species was determined in MestRec using the Data Analysis function and normalized as described above to give the exponential decay graphs (Figures 3.13 and 3.14).

(b) Procedures for different adsorption studies:

*Representative procedure for the adsorption of the phosphine oxides **2**–**6** on silica*

The wet silica (1.003 g) is placed in a Schlenk flask and degassed (three cycles vacuum then N_2) on the vacuum line. Toluene (30 mL) is added to form a slurry. The phosphine oxide **3** (0.151 g, 0.692 mmol, ~50 molecules/100 nm^2) is weighed quickly in air into a separate Schlenk flask, and toluene (20 mL) is added to dissolve **3**. The solution of **3** is transferred to the silica slurry via a cannula. The reaction mixture is stirred at 400 rpm overnight at 90 °C in a closed Schlenk flask. The following day the stirring is stopped, the reaction flask is cooled and the mixture is left to settle for 1 h. The supernatant is transferred into a pre-weighed round bottom flask via pipette, and the solvent is removed using the rotary evaporator. The silica is washed once with toluene (20 mL) by stirring for 30 min. Again the stirring is stopped, the mixture is allowed to settle for 1 h, and the supernatant is added to the same round bottom flask as before. After removing the solvent, the round bottom flask is weighed giving a residue of 0.041

g (0.19 mmol of crude **3**, 27% recovered). Some silica is present in the supernatant as evidenced by a slightly cloudy and opaque supernatant solution, so the material is redissolved in toluene (2 x 10 mL) and filtered through a short plug of Celite (1 cm x 3 cm) into a new pre-weighed round bottom flask. After thorough drying, the round bottom flask is weighed giving a residue of **3** of 0.033 g (0.15 mmol of **3,** 21% recovered **3**). ^{31}P and ^{1}H NMR spectroscopy confirmed only **3** was present in the supernatant. By subtracting the mass of **3** recovered from the supernatant from the total mass of **3** applied to the silica, the surface coverage is 0.118 g **3** per g (0.540 mmol **3** per g silica) of silica or 43.4 molecules **3** per 100 nm^2 silica surface. The silica $\mathbf{3_{ads}}$ is dried at the vacuum line at approximately 35 °C for 3–4 h prior to being measured by solid-state NMR spectroscopy.

For the phosphine oxides **3**–**6**, the same excess of 50 molecules per 100 nm^2 is initially applied to the surface. This value has been determined as a sufficient excess from earlier adsorption studies that had used more intensive wash cycles and different solvents, such as pentane, for washing the silica. In those experiments the same conditions were applied, but an excess of 100 molecules per 100 nm^2 was initially added to the silica. Two wash cycles with toluene and one wash cycle with pentane were used to remove excess phosphine oxide on the support. These earlier experiments consistently showed surface coverages of about 40 molecules per 100 nm^2 or less for the larger phosphine oxides. For **2**, an excess of 100 molecules per 100 nm^2 is always used.

Also, as noted in the surface coverage section above, in certain experiments the adsorption is performed at room temperature, so no cooling of the silica is needed after stirring overnight.

Table 3.5. Data for adsorption of **2**–**6** on dry silica at 90 °C.

Phos-phine Oxide	**Mass of Silica** (g)	**Mass of Oxide** (g)	**Oxide in super-natant** (g)	**Oxide on Silica** (g)	**Surface Coverage** (g oxide / g SiO_2)	**Surface Coverage** (mmol oxide / 100 nm^2 SiO_2)	**Surface Coverage** (molecules oxide / 100 nm^2 SiO_2)
2	0.999	0.082	0.021	0.061	0.061	0.662	53.2
3	1.005	0.133	0.054	0.079	0.079	0.362	29.0
4	0.999	0.248	0.127	0.121	0.121	0.313	25.1
5	1.003	0.185	0.048	0.137	0.137	0.462	37.1
6	1.005	0.172	0.081	0.091	0.091	0.327	26.2

Table 3.6. Data for adsorption of **2**–**6** on wet silica at 90 °C.

Phos-phine Oxide	**Mass of Silica** (g)	**Mass of Oxide** (g)	**Oxide in super-natant** (g)	**Oxide on Silica** (g)	**Surface Coverage** (g oxide / g SiO_2)	**Surface Coverage** (mmol oxide / 100 nm^2 SiO_2)	**Surface Coverage** (molecules oxide / 100 nm^2 SiO_2)
2	1.005	0.084	0.009	0.075	0.075	0.815	43.4
3	1.003	0.151	0.033	0.118	0.118	0.540	65.3
4	1.002	0.246	0.104	0.142	0.142	0.367	29.4
5	1.004	0.186	0.021	0.165	0.164	0.553	44.5
6	1.007	0.175	0.057	0.115	0.114	0.410	32.9

Table 3.7. Data for adsorption of **2**–**6** on wet silica at RT.

Phosphine Oxide	Mass of Silica (g)	Mass of Oxide (g)	Oxide in supernatant (g)	Oxide on Silica (g)	Surface Coverage (g oxide / g SiO_2)	Surface Coverage (mmol oxide / 100 nm^2 SiO_2)	Surface Coverage (molecules oxide / 100 nm^2 SiO_2)
2	0.999	0.117	0.015	0.102	0.102	1.110	88.9
3	1.005	0.277	0.107	0.170	0.169	0.774	62.2
4	1.007	0.482	0.251	0.231	0.229	0.592	47.6
5	1.006	0.369	0.187	0.182	0.181	0.611	49.0
6	1.000	0.346	0.240	0.106	0.106	0.381	30.6

Table 3.8. Data for adsorption of **2a**–**6a** on wet silica at RT.

Phosphine Oxide	Mass of Silica (g)	Mass of Oxide (g)	Oxide in supernatant (g)	Oxide on Silica (g)	Surface Coverage (g oxide / g SiO_2)	Surface Coverage[b] (mmol oxide / 100 nm^2 SiO_2)	Surface Coverage[b] (molecules oxide / 100 nm^2 SiO_2)
2	1.009	0.115[a]	0.017	0.141	0.140	1.11	89.1
3	1.005	0.320	0.111	0.209	0.208	0.824	76.5
4	1.005	0.528	0.306	0.222	0.220	0.523	45.9
5	1.002	0.412	0.198	0.214	0.214	0.648	52.0
6	1.004	0.327	0.240	0.106	0.106	0.339	34.0

[a] $Me_3PO{\cdot}H_2O_2$ (**2a**) was generated *in situ* by adding 0.121 mL of H_2O_2 to **2**. [b] The molar masses were determined by adding the mass of H_2O_2 (34.014 g/mol) to the mass of each phosphine oxide because it was assumed that each adduct had a 1 : 1 ratio of phosphine oxide : H_2O_2.

*Representative procedure for the leaching tests of the phosphine oxides **2–6** from silica*

The same adsorption procedure described above is applied to a larger amount of wet silica (3.997 g). 120 mL of toluene was added to the silica to form a slurry and 80 mL to the phosphine oxide **3** to dissolve the compound. The phosphine oxide **3** (0.473 g, 2.167 mmol) is stirred with the silica in toluene at 90 °C overnight. The following day the mixture is left to settle, and the supernatant is transferred into a round bottom flask, dried, and weighed (0.072 g, 0.33 mmol, 15% of **3** recovered). The surface coverage is calculated to be 36.8 molecules **3** per 100 nm^2 silica (0.401 g, 1.84 mmol, 0.100 g **3** per g silica). The silica is then divided into 10 Schlenk flasks with each aliquot weighing 0.4 g.

In one experiment for $\mathbf{3_{ads}}$ the silica (0.407 g) is stirred with THF (8 mL) overnight at room temperature. The next day the stirring is stopped, the mixture is left to settle for 30 min, and the supernatant is filtered through filter paper into a pre-weighed round bottom flask. The silica is rinsed quickly (2 x 4 mL) with THF to collect all of the THF between the silica particles and remaining in the pores that may have dissolved phosphine oxide in it. Again the supernatant is added to the same round bottom flask. The solvent is removed with a rotary evaporator, and after thorough drying on the vacuum line at 30 °C, the supernatant is found to weigh 0.027 g, which shows 66% of **3** leached from the silica in THF.

Table 3.9. Data for adsorption of **2**–**6** on large batches of wet silica for leaching studies.

Phos-phine Oxide	Mass of Silica (g)	Mass of Oxide (g)	Oxide in super-natant (g)	Oxide on Silica (g)	Surface Coverage (g oxide / g SiO_2)	Surface Coverage (mmol oxide / 100 nm^2 SiO_2)	Surface Coverage (molecules oxide / 100 nm^2 SiO_2)
2	4.002	0.300	0.027	0.273	0.0682	0.741	56.8
3	3.997	0.473	0.072	0.401	0.100	0.458	36.8
4	4.003	0.575	0.078	0.497	0.124	0.321	25.8
5	4.004	0.654	0.066	0.588	0.147	0.496	39.8
6	4.000	0.469	0.108	0.370	0.0925	0.332	26.7

Table 3.10. Leaching of **2**–**6** from wet silica in different solvents.

Phosphine Oxide	Solvent	Mass of Silica (g)	Amount on Silica (g)	Mass of Oxide in Supernatant (g)	Amount of Oxide Leached (%)
2	CH_3CN	0.399	0.0272	0.007	26
3		0.400	0.0401	0.013	32
4		0.404	0.0502	0.019	38
5		0.400	0.0587	0.016	27
6		0.402	0.0372	0.024	65
2	MeOH	0.402	0.0274	0.023	84
3		0.401	0.0402	0.028	70
4		0.516	0.0641	0.050	78
5		0.612	0.0898	0.055	61
6		0.400	0.0370	0.023	62
2	Acetone	0.405	0.0276	0.019	69
3		0.399	0.0400	0.019	48
4		0.406	0.0504	0.037	73
5		0.397	0.0583	0.031	53
6		0.406	0.0376	0.024	64
2	Et_2O	0.406	0.0277	0.003	11
3		0.404	0.0405	0.020	49
4		0.404	0.0502	0.027	54
5		0.402	0.0590	0.020	34
6		0.402	0.0372	0.006	16

Table 3.10. Continued.

Phosphine Oxide	Solvent	Mass of Silica (g)	Amount on Silica (g)	Mass of Oxide in Supernatant (g)	Amount of Oxide Leached (%)
2		0.409	0.0279	0.005	18
3		0.400	0.0401	0.009	22
4	EtOAc	0.403	0.0501	0.022	44
5		0.408	0.0599	0.020	33
6		0.403	0.0373	0.018	48
2		0.397	0.0271	0.004	15
3		0.403	0.0404	0.010	25
4	Toluene	0.404	0.0502	0.008	16
5		0.405	0.0595	0.009	15
6		0.406	0.0376	0.007	19
2		0.402	0.0274	0.006	22
3		0.404	0.0405	0.010	25
4	CH_2Cl_2	0.407	0.0506	0.010	20
5		0.402	0.0590	0.006	10
6		0.400	0.0370	0.013	35
2		0.403	0.0275	0.009	33
3		0.406	0.0407	0.003	7.4
4	Pentane	0.405	0.0503	0.004	7.5
5		0.406	0.0596	0.004	6.7
6		0.406	0.0376	0.005	13
2		0.406	0.0277	0.011	40
3		0.407	0.0408	0.027	66
4	THF	0.400	0.0497	0.040	81
5		0.397	0.0583	0.051	88
6		0.401	0.0371	0.029	78
2		0.405	0.0276	0.019	69
3		0.642	0.0644	0.018	28
4	DMSO	0.631	0.0784	0.024	31
5		0.617	0.0906	0.072	80
6		0.646	0.0598	0.044	74

Representative procedure for the polar solvent pre-treatment of the silica

In these experiments the silica is first stirred with a given solvent, either toluene, THF, or acetone, overnight, and then the typical adsorption procedure, as outlined above, was applied. For one representative experiment, wet silica (1.008 g) is stirred with THF (20 mL) overnight. The following day the stirring is stopped, and the THF is removed via pipette leaving the silica slightly damp. Toluene (30 mL) is then added to the silica to form a slurry. The phosphine oxide **3** (0.190 g, 0.870 mmol) is weighed into a Schlenk flask and toluene is added (20 mL) to dissolve the compound. The mixture is stirred at room temperature overnight, the silica is left to settle for 1 h, and the supernatant is filtered through filter paper into a round bottom flask. The silica is washed once with toluene (20 mL) for 30 min, and this supernatant is added to the round bottom as well. The mass of the supernatant after drying is found to be 0.085 g (0.39 mmol, 45% of **3** recovered) giving a surface coverage of 0.104 g per g silica or 38.3 molecules **3** per 100 nm^2 silica.

In the experiments where the silica is dried to remove some more of the polar solvent, new samples with THF or acetone pre-treatment were obtained by stirring in the given solvent overnight. The next day the supernatant was removed via pipette as described above, but in these cases the silica was dried in the vacuum line for about 10 minutes to give a white powder that was no longer damp. The standard adsorption procedure to obtain maximum surface coverages, which is given as the first representative procedure in the Experimental section, was then applied using toluene as the solvent for the adsorption.

Table 3.11. Surface coverages of **3**–**6** on wet silica after pre-treatment with toluene.

Phos-phine Oxide	Mass of Silica (g)	Mass of Oxide (g)	Oxide in super-natant (g)	Oxide on Silica (g)	Surface Coverage (g oxide / g SiO_2)	Surface Coverage (mmol oxide / 100 nm^2 SiO_2)	Surface Coverage (molecules oxide / 100 nm^2 SiO_2)
3	0.024	0.164	0.024	0.164	0.163	0.747	59.9
4	0.077	0.176	0.077	0.176	0.174	0.450	36.2
5	0.038	0.164	0.038	0.164	0.164	0.553	44.3
6	0.024	0.094	0.024	0.094	0.094	0.338	27.1

Table 3.12. Surface coverages of **3**–**6** on wet silica after pre-treatment with THF.

Phos-phine Oxide	Mass of Silica (g)	Mass of Oxide (g)	Oxide in super-natant (g)	Oxide on Silica (g)	Surface Coverage (g oxide / g SiO_2)	Surface Coverage (mmol oxide / 100 nm^2 SiO_2)	Surface Coverage (molecules oxide / 100 nm^2 SiO_2)
3	1.008	0.190	0.085	0.105	0.104	0.476	38.3
3, dried[a]	0.998	0.187	0.054	0.134	0.134	0.614	49.2
4	1.006	0.254	0.150	0.104	0.103	0.266	21.5
5	1.000	0.199	0.076	0.123	0.123	0.415	33.3
6	1.007	0.118	0.054	0.064	0.064	0.230	18.4

[a] In this experiment the silica was dried quickly *in vacuo* after pre-treatment with THF leaving the silica as a dry powder prior to the adsorption procedure.

Table 3.13. Surface coverages of **3**–**6** on wet silica after pre-treatment with acetone.

Phos-phine Oxide	Mass of Silica (g)	Mass of Oxide (g)	Oxide in super-natant (g)	Oxide on Silica (g)	Surface Coverage (g oxide / g SiO_2)	Surface Coverage (mmol oxide / 100 nm^2 SiO_2)	Surface Coverage (molecules oxide / 100 nm^2 SiO_2)
3	1.000	0.188	0.086	0.102	0.102	0.467	37.5
3, dried[a]	1.005	0.188	0.067	0.121	0.120	0.550	44.2
4	1.003	0.258	0.139	0.119	0.119	0.308	24.6
5	1.009	0.203	0.070	0.133	0.132	0.445	35.7
6	1.009	0.119	0.045	0.074	0.073	0.262	21.2

[a] In this experiment the silica was dried quickly *in vacuo* after pre-treatment with acetone leaving the silica as a dry powder prior to the adsorption procedure.

*Representative procedure for the competition of $OPBu_3$ (**3**) versus PBu_3 (**7**) adsorbed on silica*

The adsorption procedure is applied as described above, but a 1 : 1 ratio of **3** : **7** is used in these experiments. Dry silica (1.004 g) is weighed into a Schlenk flask and degassed at the vacuum line, and toluene (30 mL) is added to form a slurry. $OPBu_3$ (**3**) (0.122 g, 5.59 mmol) is weighed into a Schlenk flask, which is then transferred into the glove box. PBu_3 (**7**) (0.112 g, 5.54 mmol) is weighed into the same Schlenk flask in the glove box. After being placed under N_2, toluene (20 mL) is added to dissolve the compounds, and the mixture is transferred to the silica slurry via cannula. The adsorption is performed at 90 °C in toluene overnight. The following day the supernatant is removed, but no wash cycles are applied. The supernatant is collected in a Schlenk flask, which is weighed to give a mass of 0.131 g. The ^{31}P NMR spectrum of the supernatant shows only 24% is **3** and the remainder

is the phosphine **7**. There are some trace impurities from the oxidation of the phosphine **7**, but these are in small amounts less than 5%. By calculating the respective surface coverages, the loading of **3** is 0.096 g per g silica () or 35.1 molecules per 100 nm^2 and the loading of **7** is only 0.012 g per g silica () or 4.8 molecules per 100 nm^2.

The second batch of dry silica (dry silica 2) is dried under vacuum in three additional cycles for 5 min each while heating with the heat gun at high temperatures (~150 °C).

*Representative procedure for dry grinding of phosphine oxides **5** and **6** with silica*

The dry silica (0.503 g) is weighed into a Schlenk flask and transferred into the glove box. $OPPh_3$ (**6**) (0.179 g, 6.43 mmol, theoretically 100 molecules per 100 nm^2, corresponding to an excess of 380% with respect to the maximal surface coverage of 26.2 molecules per 100 nm^2 (Table 3.2)) is weighed into a vial and transferred into the glove box. In the glove box, both solids are combined in a mortar and ground together for 15 minutes using a pestle. The mixture was then packed into a 4 mm rotor and measured by ^{31}P solid-state NMR spectroscopy using a simple high-power decoupling pulse sequence. The time of the measurements is determined from t = 0 being immediately after the grinding process is finished. The solids are left as a mixture in the glove box and measured periodically over the next week to watch the progression of the adsorption.

Table 3.14. Amounts for dry grinding experiments for **5** and **6** on silica.

Phos-phine Oxide	Type of Silica	Mass of Silica (g)	Mass of Oxide (g)	Oxide on Silica[a] (g oxide / g SiO_2)	Oxide on Silica[a] (mmol oxide / 100 nm^2 SiO_2)	Theoretical Surface Coverage[a] (molecules oxide / 100 nm^2 SiO_2)
5	wet	1.001	0.384	0.384	1.30	104
6		1.009	0.357	0.354	1.27	102
5	dry	0.509	0.188	0.369	1.24	100
6		0.503	0.179	0.356	1.28	103

[a] These values give the combined amounts of adsorbed and polycrystalline material present on the surface.

Representative procedure for adsorption at specific surface coverages for T_1 measurements

The standard adsorption procedure, which is the first representative procedure in the Experimental section, is applied using dry silica (1.103 g) and PPh_3 (**7**) (0.742 g, 2.83 mmol, about 200 molecules per 100 nm^2). The surface loading matches the coverage for a densely packed monolayer as determined by Dr. Yang.[10] This was the maximum loading where only adsorbed phosphine was observed in the ^{31}P MAS spectrum with no resdiual polycrystalline solid on the surface. In these experiments, pentane was used as the main solvent to coincide with the work done by Dr. Yang and because the solvent would all be removed *in vacuo*, which would be easier to do with a low boiling point solvent. The phosphine **8** was dissolved in pentane (20 mL) and added to a slurry of the silica in pentane (30 mL). The mixture was left stirring overnight at 400 rpm, and after 18 h all of the solvent was removed at the vacuum line to give the specfic surface coverages desired with all the material remaining on

the support. In the case of excess **8** on silica, Et_2O (5 mL) had to be used to dissolve all of the polycrystalline material before adding it to silica. With the phosphine oxide **6**, Et_2O (10–20 mL) instead of pentane had to be used for each batch to dissolve all of the solid before adding it to the silica slurry which was in pentane (30 mL).

Table 3.15. Specific Surface Loadings of **6** and **8** for ^{31}P T_1 time measurements.

Phosphine Oxide and Coverage[a]	**Mass of Silica** (g)	**Mass of Oxide** (g)	**Oxide on Silica**[b] (g oxide / g SiO_2)	**Oxide on Silica**[b] (mmol oxide / 100 nm^2 SiO_2)	**Theoretical Surface Coverage**[b] (molecules oxide / 100 nm^2 SiO_2)
6 s	1.063	0.100	0.0941	0.338	27.1
6 m	1.035	0.740	0.715	0.257	206
6 e	0.430	0.879	2.044	7.345	590
8 s	1.160	0.101	0.0871	0.332	26.6
8 m	1.103	0.742	0.673	0.257	206
8 e	1.052	2.033	1.933	7.368	591

[a] Sub-monolayer (s), monolayer (m), and excess (e) of compound on the surface as determined from grinding experiments by Dr. Yang that showed a monolayer of PPh_3 to be 206 molecules per 100 nm^2 (Yang thesis, Table 3-3).[10] [b] These values give the total amount of oxide present on the surface. In the case of the excess loadings both adsorbed species and polycrystalline material exist on the silica.

*Representative procedure for adsorption of the tetraphosphine oxides **9–11***

The standard adsorption procedure is applied using wet silica (0.994 g) and Sn tetraphosphine oxide **11** (0.075 g, 6.11 mmol, only 5 molecules per 100 nm^2). The surface loading matches the coverages of the tetraphosphine linkers bound to the silica during the synthesis of immobilized catalysts. In these experiments, however,

the tetraphosphine oxides are not soluble in toluene alone, so THF (15 mL) is used in addition to toluene (5 mL) to dissolve the oxide **11**, which is then transferred into the flask with the silica slurry in toluene (30 mL). Also, with a low loading initially applied to the surface, the supernatant is simply removed in vacuum to ensure all of the tetraphosphine oxide **11** will remain on the silica support. The sample is then analyzed by ^{31}P MAS and HRMAS NMR spectroscopy to determine if adsorption occurred as described above in the results and discussion section.

Table 3.16. Surface coverages of **9** and **11** on silica.

Phos-phine Oxide	**Type of Silica**	**Mass of Silica** (g)	**Mass of Oxide** (g)	**Surface Coverage** (g oxide / g SiO_2)	**Surface Coverage** (mmol oxide / 100 nm^2 SiO_2)	**Surface Coverage** (molecules oxide / 100 nm^2 SiO_2)
9	wet	0.997	0.070	0.070	0.062	5.0
11		0.994	0.075	0.075	0.061	4.9
9	dry	0.998	0.062	0.062	0.055	4.4
11		1.001	0.079	0.079	0.064	5.2

CHAPTER IV

IRON GYROSCOPES AS STARTING MATERIALS FOR THE SYNTHESES OF DIPHOSPHINE CAGE DERIVATIVES

INTRODUCTION

Gyroscopes with Pt and Fe centers have been synthesized previously in the Gladysz group,[13,14] and removal of the metal fragment could generate the cage compounds needed for our adsorption studies. The large diphosphine cage **1** discussed in the Introduction had been generated by removing the $PtCl_2$ core from the corresponding Pt gyroscope.[11] Although this procedure afforded the cage, a stoichiometric amount of expensive Pt was wasted. Furthermore, the smallest cage size possible for the platinum gyroscopes contains 12 CH_2 groups in each alkyl chain, which is very similar in size to the large C_{14} diphosphine cage used above. With the Fe gyroscopes, a smaller cage with only 10 CH_2 groups per alkyl chain is accessible in good yields due to the favorable preorganization of the alkyl chains during the metathesis reaction.[14] This selectivity-enhancing effect also leads to substantially higher yields for the Fe gyroscopes as compared to their Pt analogs of equal size. Therefore, the goal of the current project is to synthesize Fe gyroscopes with 10, 12, and 14 CH_2 groups in each alkyl chain and then to find a method for removing the $Fe(CO)_3$ moieties to give the empty diphosphine cages (**I**) and/or one of its derivatives, such as the diphosphine dioxide cages (**III**) (Figure 4.1).

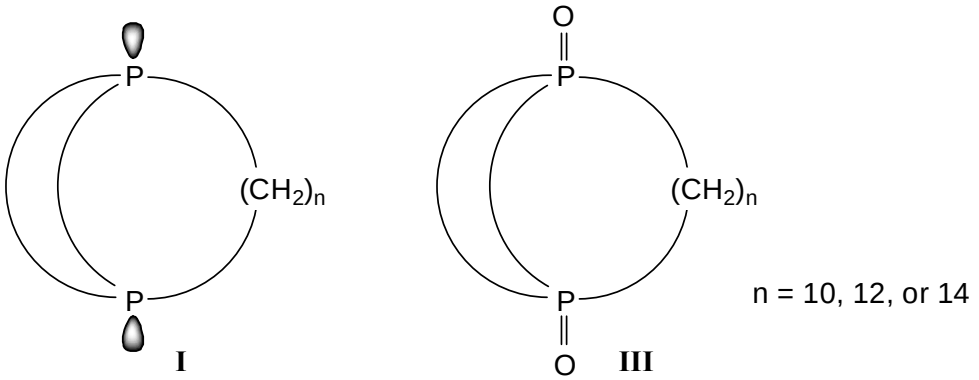

Figure 4.1. Diphosphine cages (**I**) and their corresponding dioxides (**III**). The monoxide cage **II** was mentioned in Chapter I but is not a direct target of the syntheses using Fe gyroscopes as starting materials.

Many trialkylphosphine Fe carbonyl complexes are known in the literature,[71,72] and methods for their decomposition have been researched to some extent. Photochemical reactions have been attempted with Fe carbonyl complexes, but irradiation always led to the removal of the CO groups and not the release of the phosphine ligands. Also, in one study after the CO group was liberated the phosphine substituent on a neighboring molecule interacted with the electron deficient metal center and formed dimers, so this technique will not be viable in generating the cages from the Fe gyroscope.[73] Electrochemical oxidation has been performed for some iron phosphine complexes as well, and the iron center can be oxidized to form the monocationic species, which is stable in some solvents and the reduction is even reversible when using a Hg electrode.[74] However, further oxidation will generate the Fe^{3+} core causing the release of the phosphines and thereby forming the cage compounds. Furthermore, by supplying an oxidant that can transfer oxygen to the Fe center, the vacant sites around the metal will be occupied aiding in the phosphine liberation. The only other methods investigated with this type of Fe complexes is protonating the phosphines. One study probed how the

basicity of the phosphine ligands affected the metal center basicity, which is an indicator of the electron density at the Fe center. Angelici and coworkers discovered that there was a direct correlation between the phosphine and iron complex basicity values, but the complex was always protonated at the Fe center leading to Fe hydride formation when using triflic acid (pKa ~ –15).[75] Another study also showed that with fluoroboric acid the Fe will be protonated.[76] Therefore, an excess of a strong acid will ideally first protonate the Fe but then lead to the protonation of the phosphine ligands to remove them from the metal center and form the corresponding P–H phosphonium salts.

Being that the reactivity of the Fe phosphine complexes has not been explored extensively, a wide range of reagents were selected for the transformation reactions. In many cases phosphine derivatives that are easy to handle and purify are ideal candidates. Some possible techniques to remove the Fe center have been considered and are grouped by their reactivity as shown below:

- For attack at phosphorus: oxidants, like H_2O_2, O_2, and ^{t}BuOOH, alkylating agents, such as Meerwein's salt and MeI, borane, and acids, e.g. HCl
- For attack at the Fe center: oxidants, SiO_2, Al_2O_3
- For exchange of the phosphine ligands: PCl_3, PMe_3

Various attempts using all these reagents will be discussed in detail in the Results and Discussion section, and the successful methods that generated the desired phosphine derivatives will be highlighted.

RESULTS AND DISCUSSION

Synthesis and Characterization of Model Fe Phosphine Complexes

Several Fe phosphine complexes have been synthesized to test various chemical reagents for removing the $Fe(CO)_3$ moiety before applying these methods to the

gyroscopes for generating the desired diphosphine cage compounds **I** and **III**. To begin, four representative Fe complexes with different phosphine ligands, PBu_3 (**12**), $POct_3$ (**13**), PCy_3 (**14**), and PPh_3 (**15**) (Figure 4.2), were synthesized. The Fe complexes **12** and **13** are studied because their alkyl chains make them very similar to the Fe gyroscopes. Compounds **14** and **15** are used to investigate steric effects of the phosphine ligands and to determine the scope of the reactions for both alkyl and aryl systems.

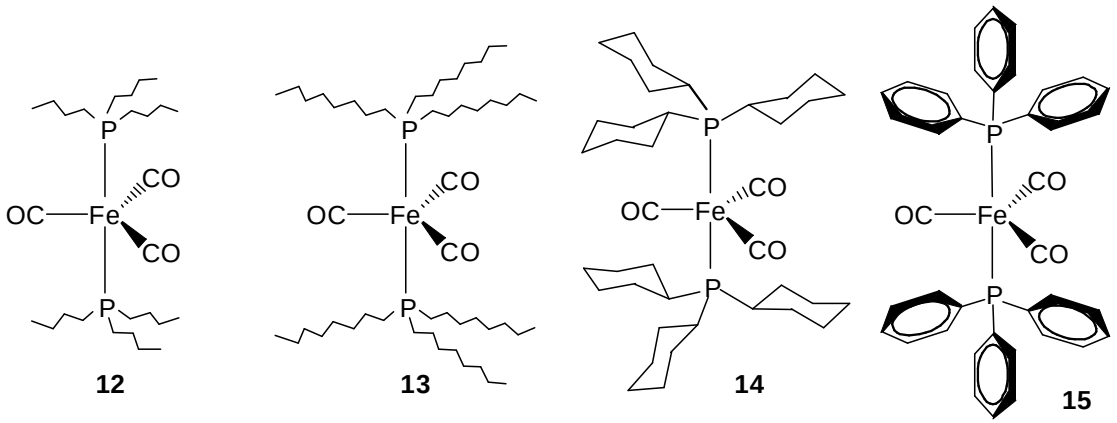

Figure 4.2. Fe phosphine complexes for test reactions.

The synthesis of these compounds was carried out according to literature procedures (Scheme 4.1) using the same technique employed for synthesizing the gyroscope starting materials.[14,76] Complexes **12**, **14**, and **15** had been previously reported, and their ^{31}P NMR chemical shifts and IR data matched the data given in previous publications (Table 4.1 and Experimental section). Complex **13** is a new compound, so its full characterization by ^{31}P, ^{1}H, and ^{13}C NMR including signal assignments as well as IR data are detailed in the Experimental section of this chapter.

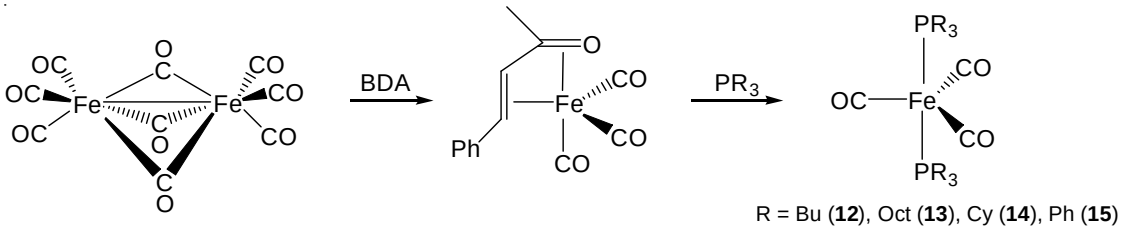

R = Bu (**12**), Oct (**13**), Cy (**14**), Ph (**15**)

Scheme 4.1. Synthesis of the Fe phosphine complexes **12**–**15**.

The ^{31}P NMR chemical shifts (Table 4.1) vary significantly for the complexes giving some indication about the shielding around the phosphorus nuclei. For the Fe complexes with more sterically demanding phosphines, PCy_3 (**14**) and PPh_3 (**15**), the chemical shift values are around 82–86 ppm while for the phosphines with linear alkyl chains, PBu_3 (**12**) and $POct_3$ (**13**), the chemical shifts are between 62 and 65 ppm (Table 4.1). Furthermore, the different cone angles around phosphorus due to the different substituents will affect the coordination at the Fe center and in turn the observed chemical shifts.

Table 4.1. ^{31}P NMR chemical shifts and IR data for complexes **12–15**.

	^{31}P NMR [ppm]		**IR** [cm^{-1}]	
Compound	δ^{expt}	$\Delta^{72,b}$	$\nu_{CO}{}^{expt,c}$	$\nu_{CO}{}^{71,d}$
12	62.26[a]	64.4	1854	1854
13	62.75[a]	–	1858	–
14	85.65[b]	85.9	1842	1842
15	82.34[b]	82.6	1867	1881

[a] NMR spectra recorded in C_6D_6. [b] NMR spectra recorded in $CDCl_3$. [c] IR spectra of neat samples. [d] Solution IR spectra using $CHCl_3$ as solvent.

The IR data for the carbonyl groups provide interesting information about the overall stability of the compounds. One study examining this class of Fe phosphine complexes showed that as the wavenumber for the IR stretching band of the CO ligand gets smaller the lability of the phosphine ligands decreases.[77] This is in agreement with the classical studies by Tolman that used the $Ni(CO)_4$ unit as a probe to monitor the carbonyl IR stretching frequency and correlate it to the phosphine donor strength.[78] This proves for the model compounds **12**–**15**, that the PCy_3 ligands in **14** are bound more strongly to Fe than the other phosphines.

All complexes were also characterized by ^{13}C NMR spectra, which displayed the interesting phenomenon of virtual couplings. Virtual couplings can be seen in the spectra of organometallic compounds with a rigid structure regarding the phosphine ligands, and they have been described in detail in the literature.[79] In the case of **13** (Figure 4.3), the ^{13}C NMR spectrum shows two *pseudo*-triplets for the α- and γ-carbons because they are coupling with the two seemingly "equivalent" phosphorus nuclei in the molecule. The transition from virtual couplings to normal ones is gradual, and for the signal of the α-carbon the formation of a regular double doublet at higher measurement frequencies can be anticipated.

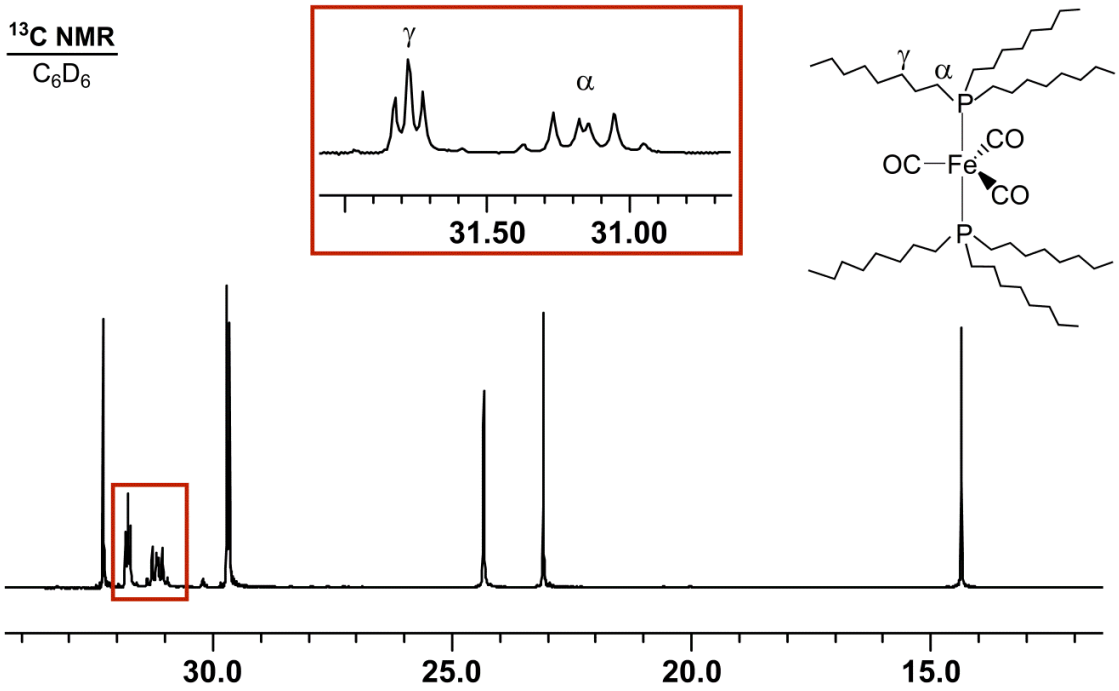

Figure 4.3. ^{13}C NMR spectrum of complex **13** showing virtual couplings highlighted in red.

Furthermore, two of the complexes, **14** and **15**, were characterized by ^{31}P solid-state NMR spectroscopy. Complex **12** has a melting point of 54–56 °C[77] and complex **13** exists as an oil at room temperature, so neither of these compounds were suitable for MAS NMR measurements. As seen in the 13 kHz ^{31}P MAS spectrum of **14** (Figure 4.4, top), there are two isotropic lines indicating that there are at least two magnetically inequivalent phosphorus nuclei in the unit cell of the crystal lattice. The two inequivalent phosphine substituents must have different orientations in the crystal with respect to the external magnetic field giving rise to two unique chemical shifts in the solid state. Unfortunately, the crystal structure of this compound is not known, and attempts to grow X-ray quality single crystals have been unsuccessful. From the span of the wideline pattern the combined chemical shift anisotropy (CSA) of the two signals was found to be

170 ppm (Figure 4.4). By simulating the spectrum of the sample rotated with 4 kHz, the CSA values of the individual signals are found to be 170 ppm for the signal at 88.8 ppm and 169 ppm for the signal more upfield at 83.2 ppm. The δ_{11}, δ_{22}, and δ_{33} values are given for the two signals in Table 4.2. Since the CSA values for the two signals are very similar one can assume that indeed their origin is the different orientation of the phosphine ligands in the unit cell, and not, for example, the presence of polymorphs. The δ_{22} value as taken from the highest point in the wideline spectrum (Figure 4.4, bottom) is around 134 ppm and therefore matches best δ_{22} of the signal at 83.2 ppm, but it is evident that the δ_{11} and δ_{33} values cannot be obtained from the wideline pattern because of the two overlapping signals. The tiny bump at ca. 48 ppm on top of the wideline signal stems from phosphine oxide that formed in the rotor during the prolonged measurement time of the spectrum.

Table 4.2. CSA values [ppm] for polycrystalline **14**. The CSA is given as the span of the wideline signals, $\boldsymbol{\delta_{11} - \delta_{33}}$.[36a] The error margin of the CSA values is ± 3 ppm.

$\boldsymbol{\delta_{iso}(^{31}P)}$	$\boldsymbol{\delta_{11}}$	$\boldsymbol{\delta_{22}}$	$\boldsymbol{\delta_{33}}$	**CSA**
88.8	148	139	–22	170
83.2	142	134	–27	169

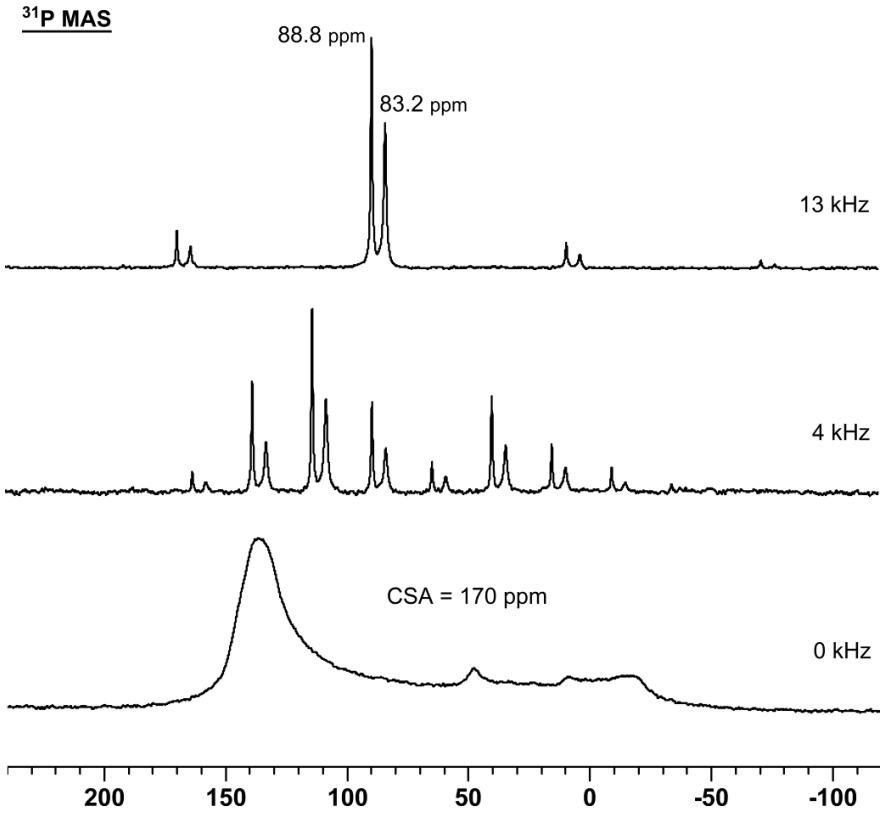

Figure 4.4. ^{31}P MAS NMR (top and middle) and wideline spectrum (bottom) of **14**.

Similarly, with the triphenylphosphine complex **15** the 13 kHz ^{31}P MAS spectrum shows three isotropic lines (Figure 4.5). Being that the solution ^{31}P NMR spectrum showed only one singlet at 82.3 ppm, the additional signals in the solid state are again probably due to multiple molecules in the unit cell of the single crystal. Since the signals are not well resolved the presence of polymorphs in the sample cannot be excluded. The overall CSA of **15** was found to be 190 ppm, which is about 20 ppm larger than that of the analog **14**.

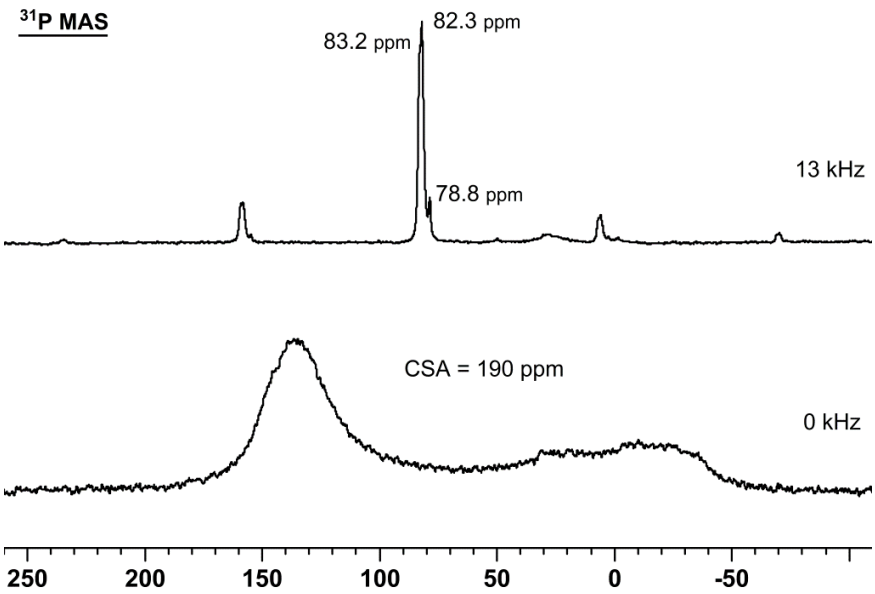

Figure 4.5. ^{31}P MAS NMR (top) and wideline spectrum (bottom) of **15**.

Reactivity of Iron Phosphine Complexes

After the characterization of the compounds **12**–**15**, various methods were tested to remove the $Fe(CO)_3$ core and release the phosphines or phosphine derivatives, for example, phosphine oxides or phosphonium salts. Different reagents were chosen based on their ability to form phosphine derivatives that could be easily converted back to the desired phosphines, so in the case of the gyroscopes they could be used to make the diphosphine (**I**) or diphosphine dioxide (**III**) cages. Scheme 4.2 shows an overview of the reagents tested for removing the Fe from the complexes. Compound **12** was employed as the primary model for these reactions because the tributylphosphine substituents resemble the trialkylphosphine ligands of the cage compounds. The reactions outlined in red were not successful and mainly starting material was recovered. The reactions in blue worked to a moderate degree but required harsher conditions, such as higher temperatures or longer reaction times, to reach completion. The reactions in

green boxes were very productive and gave the desired products in high yields overnight under mild conditions. These important reactions will be discussed in detail below.

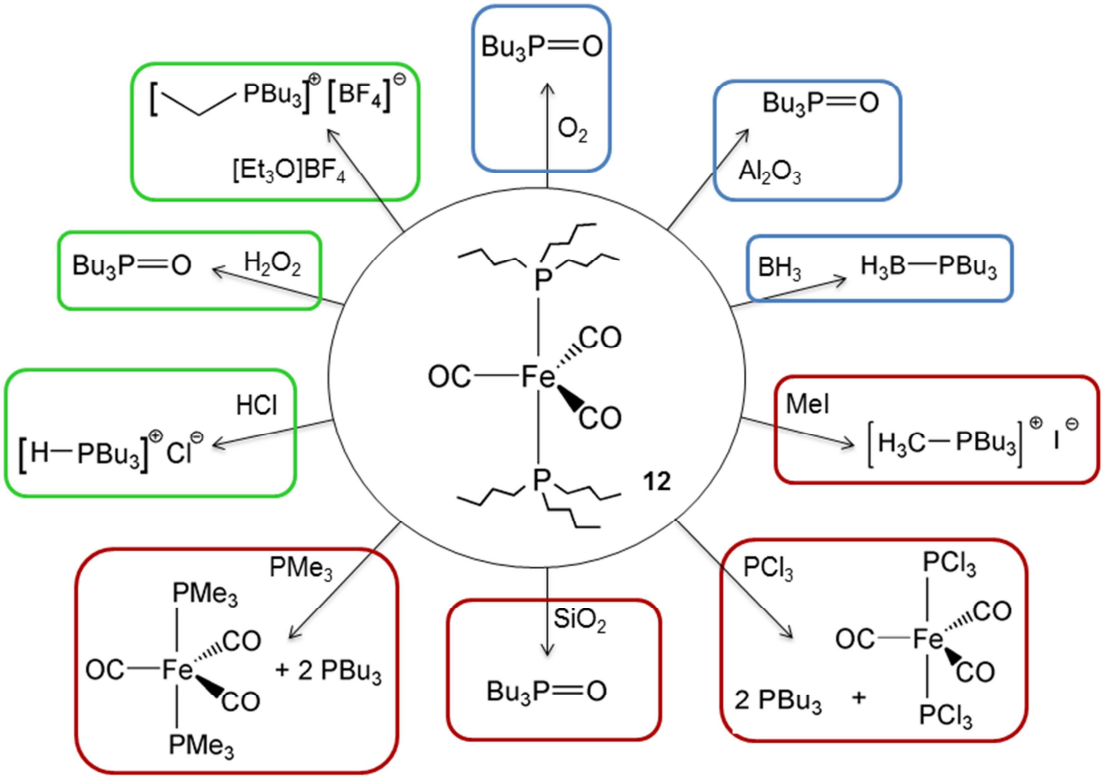

Scheme 4.2. Overview of reagents tested to remove the Fe center of **12** from the phosphine ligands.

All complexes **12**–**15** contained Fe(0), so oxidation was the first reaction run, which would then result in the formation of the corresponding phosphine oxides and oxidized Fe^{3+} species as byproducts that have not been identified.

Initially, oxidation using hydrogen peroxide was attempted with complex **12** in toluene (Scheme 4.3). Overnight the starting material was quantitatively converted to the hydrogen peroxide adduct of the phosphine oxide as identified by ^{31}P NMR (Figure 4.6)

and IR spectroscopy. The formation of these H_2O_2 adducts occurs because of strong hydrogen bonding interactions between the hydrogen atoms of the peroxide molecules and the oxygen of the P=O bond.[63] The adducts are then easily decomposed by molecular sieves to give pure phosphine oxides.[63] Both compounds **12** and **13** can be converted to the oxides **14** and **15** overnight at room temperature using a slight excess of hydrogen peroxide in toluene.

The reactions of complexes **14** and **15** proceed more slowly, most likely due to steric hindrance around the Fe center, and therefore, required a larger excess of hydrogen peroxide (1000 eq., conc. 35%) to go to completion under the same conditions. The biphasic nature of this reaction allows most of the Fe byproduct to be separated into the aqueous phase after the first reaction step, and the rest can either be adsorbed on the molecular sieves or simply filtered off at the end to give the clean phosphine oxides. Overall, the oxidation with hydrogen peroxide was successful for all compounds **12**–**15**, and the yields of **3**–**6** are given in Table 4.2. The yield after the oxidation of **12** was moderately lower, but this is due to the fact that tributylphosphine oxide (**3**) is slightly soluble in the aqueous phase and may have been lost during the workup.

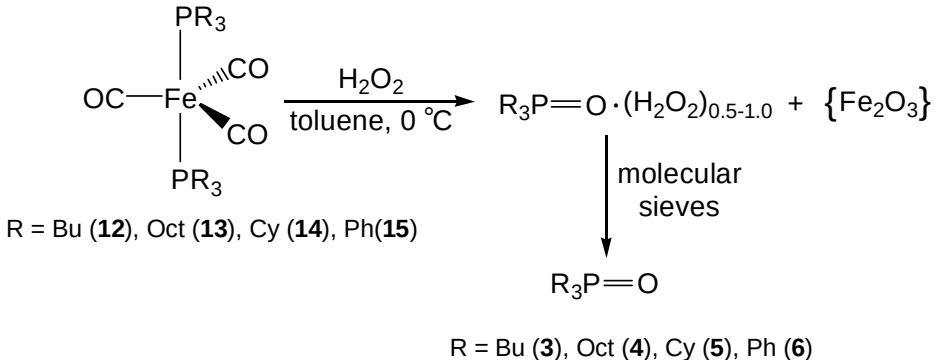

R = Bu (**12**), Oct (**13**), Cy (**14**), Ph(**15**)

R = Bu (**3**), Oct (**4**), Cy (**5**), Ph (**6**)

Scheme 4.3. Oxidation of **12**–**15** with aqueous hydrogen peroxide. The Fe containing product has not been identified.

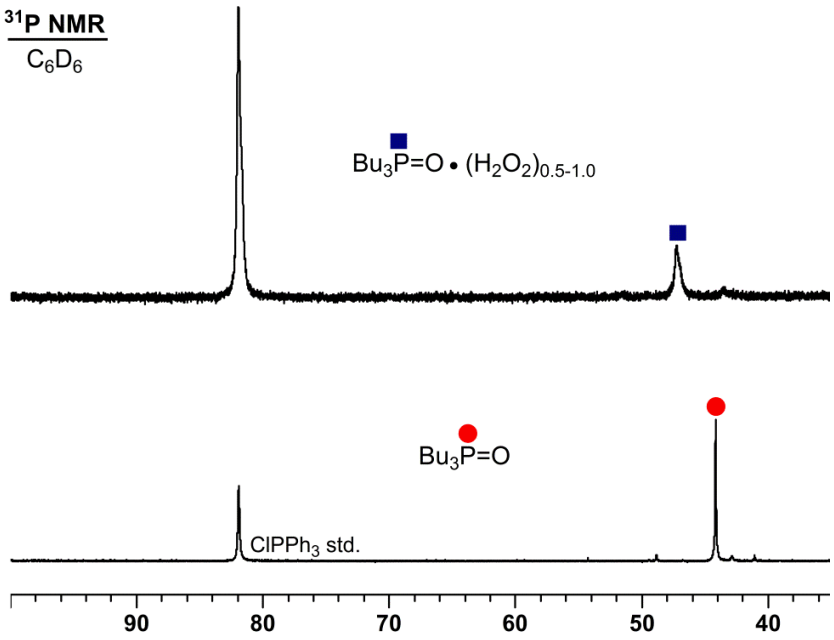

Figure 4.6. ^{31}P NMR spectra of the products after the reaction of **12** with H_2O_2 (top) and after removal of H_2O_2 (bottom).

Table 4.3. Conditions for the oxidation of **12**–**15** with aqueous H_2O_2.

	Excess H_2O_2			
Product	**Concentration** (%)	**Equivalents**	**Time** (d)	**Yield** (%)
3	17.5	10	1	46.9
4	17.5	10	1	90.6
5	35.0	200	3	76.5
6	35.0	200	3	73.5

Oxidation using a stronger oxidizing reagent, ^{t}BuOOH, was also investigated for compound **14** (Scheme 4.4) because the H_2O_2 method had proceeded slowly for this

complex, which coincides with the IR data showing that out of the model compound series PCy_3 is the phosphine binding the strongest to Fe. An excess (20 eq.) of aqueous 17.5% ^{t}BuOOH was added to **14** dropwise at 0 °C in dichloromethane. The Fe phosphine complex was quantitatively converted to the phosphine oxide **5** overnight (72.8% yield). This procedure is clearly more effective for oxidizing compounds whose Fe centers are more shielded by bulky ligands and, hence, ^{t}BuOOH has been used for oxidizing the Fe gyroscope complexes.

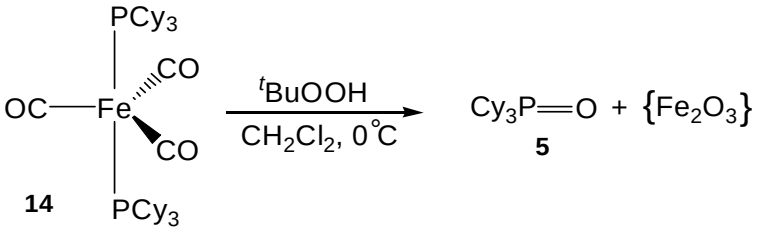

Scheme 4.4. Oxidation of **14** with ^{t}BuOOH.

Having studied several strong oxidizing agents, further probing of the stability of these complexes was performed by exposing them to air to test how they would react with O_2 (Scheme 4.5). Typically, oxidizing a phosphine directly in air creates multiple side products due to the radical nature of the reaction leading to insertion of oxygen into the P–C bonds.[63] Therefore, it would be interesting to test if these byproducts would still be generated when starting from a metal complex or if the presence of a metal may inhibit these side reactions.

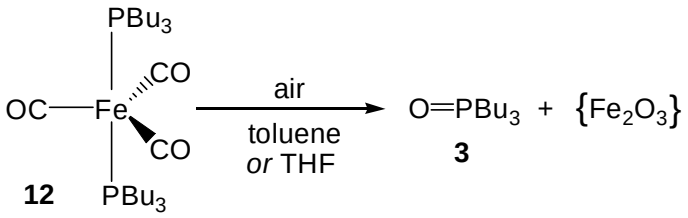

Scheme 4.5. Oxidation of **12** by exposure to air.

Complex **12**, dissolved in toluene, was stirred in air at room temperature and then at 60 °C for several days, but no reaction was observed by ^{31}P NMR. Upon heating at 100 °C for three days, the starting material **12** was completely transformed to the desired phosphine oxide **3**. None of the byproducts could be seen in the ^{31}P NMR spectrum (Figure 4.7). However, since **3** was exposed to air, water adducts might have formed, which explains the more than 3 ppm deviation of the ^{31}P chemical shift from the value reported in the literature for pure Bu_3PO.[63] Additionally, the Fe byproducts might have affected the noticeable downfield shift. Nevertheless, the presence of only one resonance indicates that the Fe center was effective at impeding the oxygen insertion into the P–C bond. THF was used to examine if a more polar solvent may facilitate the oxidation process although it is known to have a lower solubility of O_2 as compared to toluene.[80] The reaction mixture was heated at 50 °C, but the oxidation still required three days to reach completion. Though oxidation in air did work successfully to give clean phosphine oxide as the product (85.4% yield), the reaction needed higher temperatures and longer reaction times as compared to the hydrogen peroxide oxidation. Although this approach is less expensive and safer than the method using H_2O_2 and no adducts or phosphorus-containing byproducts form, it is also noteworthy that the separation of the Fe oxide impurities proved to be more challenging.

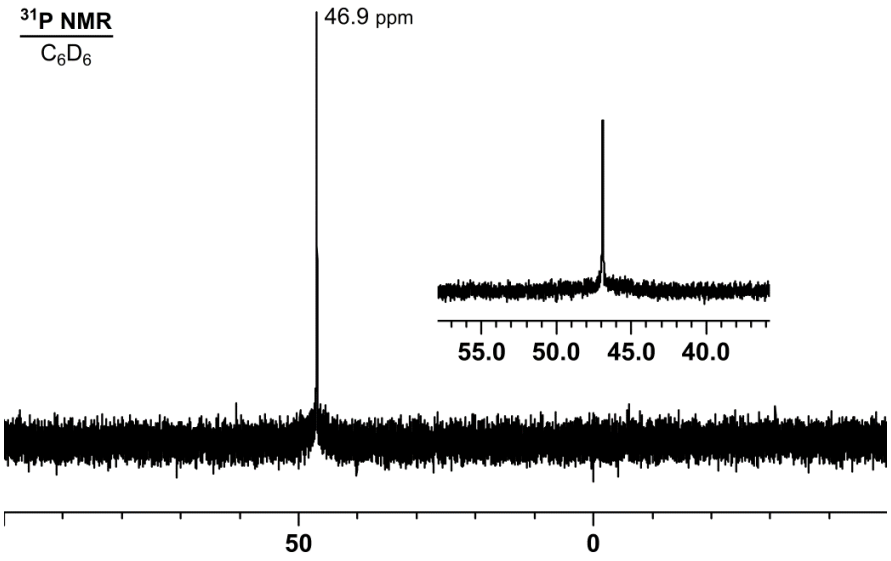

Figure 4.7. ^{31}P NMR spectrum of the reaction mixture after oxidation of **12** in air.

In hopes of discovering a method that would directly lead to the diphosphine cages (**I**), phosphine substitution was attempted using both PCl_3 (Scheme 4.6) and PMe_3 (Scheme 4.7). The reaction of **12** with PCl_3 was tried in toluene at room temperature. No reaction was observed overnight or even after stirring for several days. Being that the chlorines are electron-withdrawing from the phosphorus, a more basic phosphine, such as PMe_3, was tested for the ligand exchange, while the reaction with PCl_3 was not investigated any further.

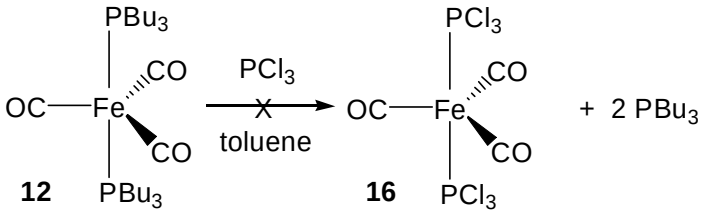

Scheme 4.6. Attempted ligand exchange with PCl_3.

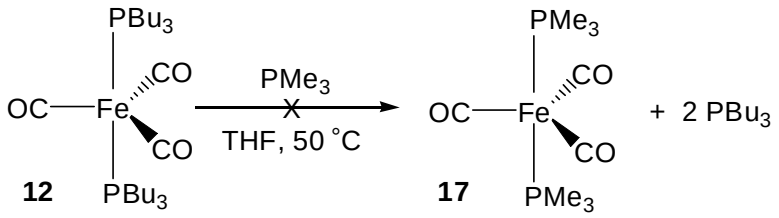

Scheme 4.7. Attempted ligand exchange with PMe_3.

Complex **12** was combined with a slight excess (2.1 eq.) of PMe_3 in toluene and stirred overnight at room temperature, but no reaction occurred. Using larger amounts (10 eq.) of PMe_3, longer reaction times, and higher temperatures did not drive the reaction forward. In the meantime, a paper was found that detailed the enthalpies of phosphine substitution reactions in *trans*-phosphine complexes of Fe.[77] The authors showed that **15** easily underwent phosphine substitution with PMe_3 in THF at 50 °C to give the expected complex **17** (Scheme 4.7). Using their data, Nolan *et al.* calculated this reaction to have an enthalpy of –12 kcal/mol, which they attribute to the lability of the PPh_3 ligand that has a lower basicity and in turn weaker bonding to Fe as compared to trialkylphosphines.[77] Performing the same calculation for the substitution of PBu_3 with PMe_3 as shown in Scheme 4.7 leads to an enthalpy value of +2.8 kcal/mol, meaning the reaction will require a greater energy input and therefore, will not proceed under mild conditions. Just for confirmation of this result, the reaction was executed once more mimicking the conditions used for the PPh_3 substitution because it was thought that THF, being a coordinating solvent, could possibly stabilize some intermediate species. However, even when using a larger excess (20 eq.) of PMe_3 with complex **12** in THF at 50 °C, no reaction took place even for extended time periods of up to one week.

Understanding the difficulty in displacing the phosphines from the Fe center, the focus was shifted to the synthesis of a phosphine borane, which could then be easily converted back to the desired phosphine by deprotecting with a base, such as DABCO. The borane-THF adduct was stirred with **12** overnight at room temperature (Scheme 4.8), but no reaction was seen by ^{31}P NMR. However, after concentrating the mixture, a dark green solid formed in the flask after one day. The ^{31}P NMR spectrum of this mixture revealed about 9% of the starting material had been converted to the expected phosphine borane **18**, and when leaving this concentrated reaction mixture for an additional week, all of the starting material appeared to be transformed into the desired product. Unfortunately, Fe impurities in the sample decreased the signal-to-noise ratio of the ^{31}P NMR spectrum significantly, rendering it difficult to interpret. Nonetheless, the reaction was attempted again under more concentrated conditions in THF, but only 1% of product formation was observed after one day. Being that this reaction requires longer reaction times as compared to the oxidation, it was not viable for the cage synthesis.

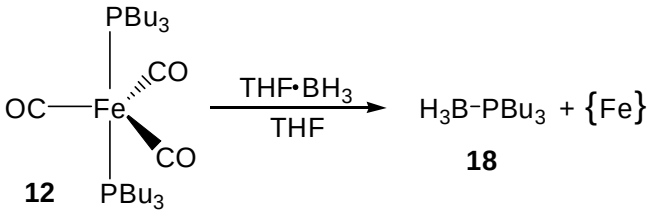

Scheme 4.8. Synthesis of the borane adduct **18**.

Another method to detach the phosphorus ligands from the metal center is to transform the phosphines into phosphonium salts. Alkylating reagents, such as MeI and Meerwein's salt, can be used to produce the alkylphosphonium salts, but these species cannot easily be converted back to the desired phosphines because cleavage of the P–C

bond would not be selective for a specific alkyl substituent. Complex **12** was mixed with a slight excess (2.2 eq.) of MeI in toluene to generate the methylphosphonium salt **19** (Scheme 4.9), but only about 1% of the starting material was converted to the product even after several days.

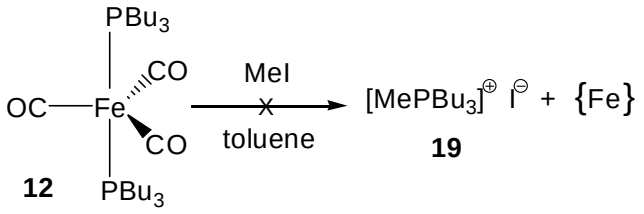

Scheme 4.9. Attempted synthesis of the methylphosphonium salt **19**.

Next, a stronger alkylating agent, $[Et_3O][BF_4]$ or Meerwein's salt, was employed. Complex **12** was reacted with a slight excess (2.2 eq.) of Meerwein's salt in dichloromethane to form the ethylphosphonium salt **20** (Scheme 4.10). At room temperature overnight there was complete conversion of **12** to the anticipated product **20** as seen by ^{31}P NMR spectroscopy (Figure 4.8). A small amount of byproduct, identified as the $[HPR_3]^+$ phosphonium salt, exists in the mixture because of acid present in Meerwein's salt upon receipt from the vendor. This impurity led to slightly less than quantitative yields (Table 4.4) as determined by the ^{31}P NMR spectra of the concentrated reaction mixtures. The crude product can be stirred with water to convert $[HPR_3]^+$ into the phosphine and subsequent extraction with pentane gives the clean ethylphosphonium salt. The reaction with Meerwein's salt was effective for quantitatively converting all compounds **12**–**15** to the desired products and could be a procedure tested on the gyroscope complexes in the future.

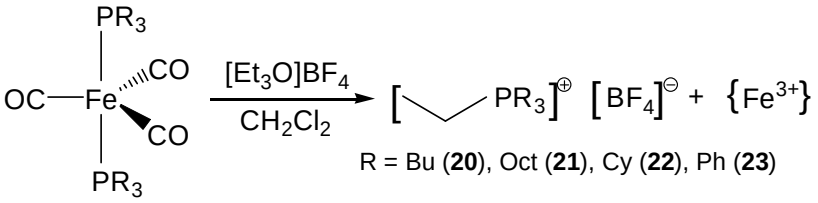

R = Bu (**12**), Oct (**13**), Cy (**14**), Ph (**15**)

R = Bu (**20**), Oct (**21**), Cy (**22**), Ph (**23**)

Scheme 4.10. Synthesis of the phosphonium salts **20**–**23**.

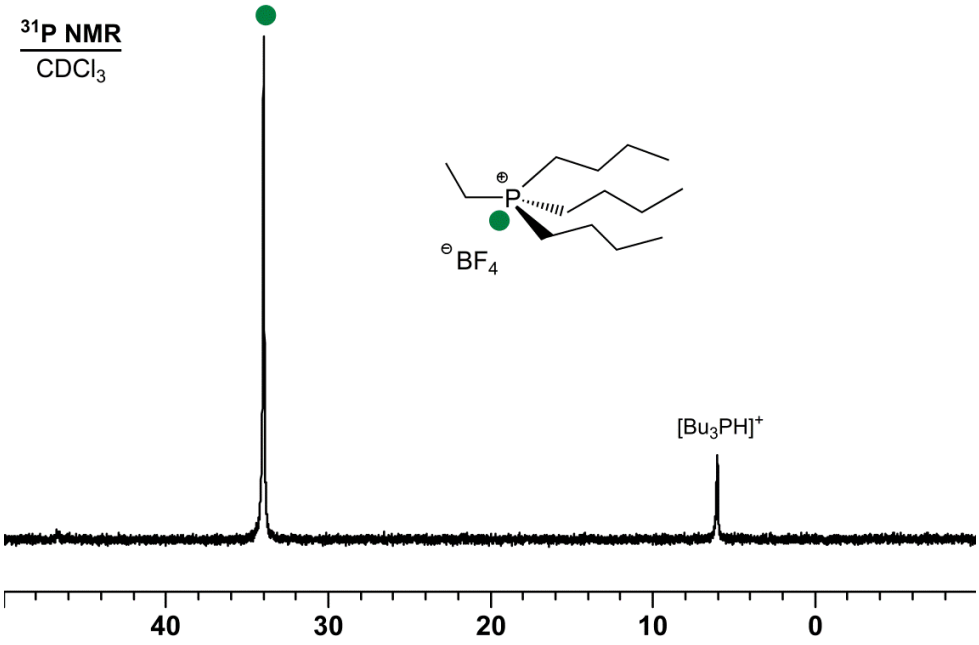

Figure 4.8. ^{31}P NMR spectrum of the reaction mixture after treating **12** with Meerwein's salt.

Table 4.4. Chemical shifts and yields of the ethylphosphonium salts **20**–**23** after reaction of **12–15** with Meerwein's salt as determined by ^{31}P NMR spectroscopy ($CDCl_3$).

Product	**δ(^{31}P)** (ppm)	**Yields** (%)
20	33.99	84.7
21	41.68	93.9
22	68.35	91.7
23	55.94	93.5

Applying strong acids is another option to make phosphonium salts as noted by the formation of the byproduct above (Figure 4.8). The advantage of the $[HPR_3]^+$ phosphonium salts is that they are easily deprotonated to give the corresponding phosphines by stirring them with water or a weak base. Compound **12** is converted readily into the corresponding phosphonium salt **24** (Scheme 4.11) with a slight excess (10 eq.) of 6.05 M HCl in THF (Figure 4.9). However, complexes **13**, **14**, and **15** did not react as easily with HCl and required a greater excess (1000 eq.) of more concentrated 12 M HCl to drive the reactions to completion. All model compounds were fully converted into their corresponding $[HPR_3]^+$ phosphonium salts and byproducts (Table 4.5), as determined by ^{31}P NMR spectroscopy. The byproducts were oxidation products, as seen e.g. in Figure 4.9 at 38.2 ppm, caused by exposure to O_2, because the aqueous acid solution had not been degassed.

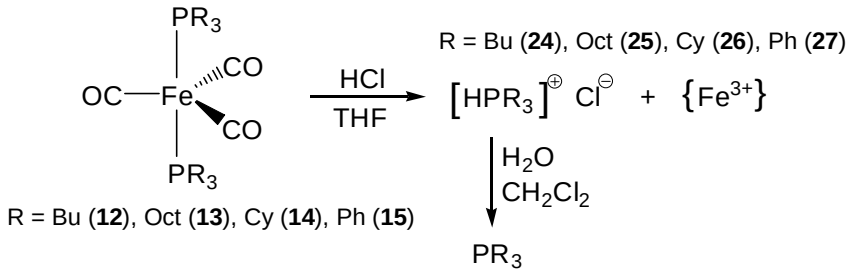

Scheme 4.11. Synthesis of the phosphonium salts **24**–**27**.

After concentrating the mixtures and adding dichloromethane and degassed water, the phosphines could be collected in the organic layer while the Fe salts were removed with the aqueous layer. Separation of the desired phosphines from the oxidation byproducts can be accomplished with column chromatography (Al_2O_3, eluting with CH_2Cl_2) under an inert atmosphere. However, thorough degassing of the water is necessary to ensure that no further oxidation byproducts are generated during the extraction process, which was a major difficulty encountered in the workup attempts. Also, for the arylphosphine complex **15** the phosphonium salt **27** is more acidic, so a large amount of PPh_3 was formed directly from the reaction. The phosphonium salt **27** was not observed by ^{31}P NMR spectroscopy, so the yield of PPh_3 was determined instead since the phosphine is the desired final product (Table 4.5).

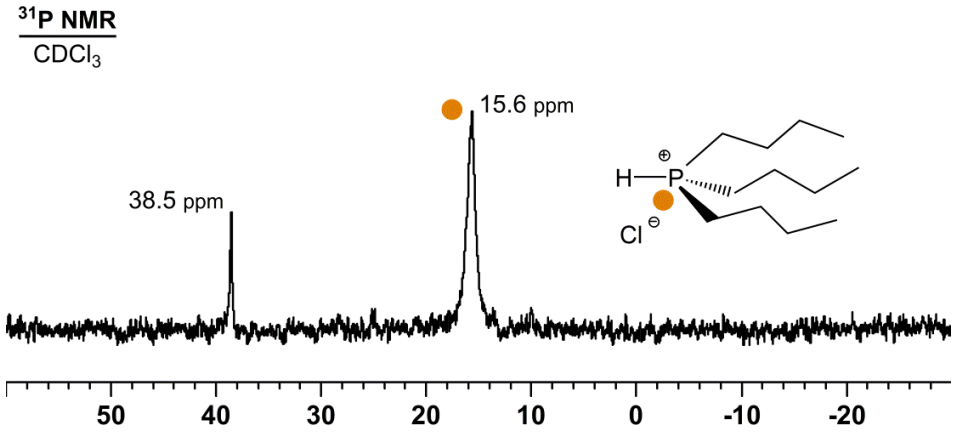

Figure 4.9. ^{31}P NMR spectrum of the reaction mixture after reaction of **12** with HCl.

Table 4.5. Chemical shifts and yields of the $[R_3PH]^+$ phosphonium salts **24**–**27** after reaction of **12–15** with HCl as determined spectroscopically (^{31}P NMR) by integrating the product peak and the signals of oxidic byproducts.

Product	**δ(^{31}P)^{expt}** (ppm)[a]	**δ(^{31}P)^{ref}** (ppm)	**Yields** (%) of $[R_3PH]^+$
24	15.6	13.7[81]	89.2
25	14.9	13.0[81]	60.2
26	36.7	32.7[81] 33.8 (Cl^-)[82]	39.8
27	–5.9 (PPh_3)	6.8 ($[HPPh_3]^+$)[81]	62.1 (PPh_3)

[a] NMR spectra recorded in DCM.

Lastly, some attempts were made to decompose the complexes by possibly generating Fe metal or nanoparticles and releasing the phosphines. It is known from earlier work in the Bluemel group and from a parallel project that Ni carbonyl complexes with phosphine ligands, e.g. $(CO)_2Ni(PPh_3)_2$, can form nanoparticles on oxide supports.[54c,83] Therefore, both silica and alumina were tested to see if the metal in the Fe model complexes could be deposited on the support and the phosphine-containing

supernatant could then be decanted. When combining complex **12** with SiO_2 in toluene (Scheme 4.12) and stirring at room temperature for several days, no reaction took place and only starting material was observed by ^{31}P NMR spectroscopy.

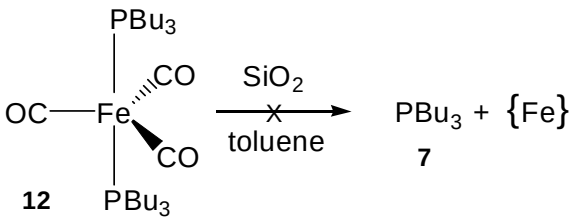

Scheme 4.12. Attempted decomposition of complex **12** by silica.

Alumina has a more acidic surface, depending on its brand, which may assist in the protonation of the phosphine ligands. Complex **12** was combined with neutral Al_2O_3 in toluene (Scheme 4.13) and was allowed to stir at room temperature for three days. Again, when analyzing the supernatant only a minimal amount (~ 1%) of starting material was converted, and instead of the desired phosphine, only phosphine oxide was seen in the ^{31}P NMR spectrum. More exhaustive degassing procedures would need to be applied to the alumina to ensure phosphine oxide cannot be generated. Also, harsher conditions, like high temperatures, might be necessary to achieve full conversion, so this procedure was not investigated in any more detail.

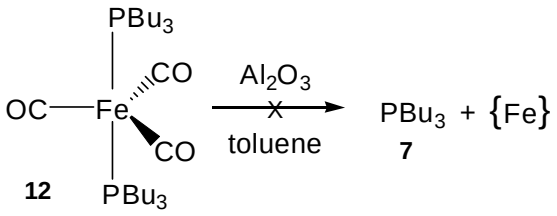

Scheme 4.13. Attempted decomposition of complex **12** by alumina.

Of all the reactions from Scheme 4.2 tested with the various iron phosphine complexes **12**–**15**, oxidation, alkylation, and protonation to form the phosphonium salts were the most effective. These transformations occurred in high yields at room temperature overnight, and the workup was straightforward in many cases. The most convenient for the following adsorption studies is oxidation to directly yield the diphosphine dioxide cages (**III**), which can be adsorbed on the silica support without strict exclusion of oxygen. The protonation will be useful in a future project for obtaining the diphosphine cages (**I**) if proper care is taken during the deprotonation of the phosphonium salts and purification of the air-sensitive phosphines. However, a large excess of strong acid was required to fully decompose the iron complexes **13**–**15**, which may mean the gyroscopes will also require very strong acids or long reaction times. The alkylation is another interesting option to form the phosphonium salts of the cage compounds, but this method will not allow us to generate the diphosphine cages (**I**) because the removal of the ethyl group would not be selective. The oxidation will be the first procedure applied to the iron gyroscopes.

Synthesis of Iron Gyroscopes

As previously mentioned, the Gladysz group has pioneered the synthesis of numerous molecular gyroscopes containing a variety of transition metals in the core

surrounded by diphosphine cages.[13,14] The synthesis of the three Fe gyroscopes containing 10 (**28**), 12 (**29**), and 14 (**30**) CH_2 groups in each of their alkyl chains was accomplished by following literature procedures previously published by the Gladysz group (Scheme 4.13).[14] The complexes **28**–**30** were characterized by NMR and IR spectroscopy, and the data matched the literature values. Methods to remove the $Fe(CO)_3$ moiety, indicated by a "?" in Scheme 4.14, will be applied to these Fe gyroscopes of various sizes to give the desired cage compounds, such as the diphosphine cages (**I**).

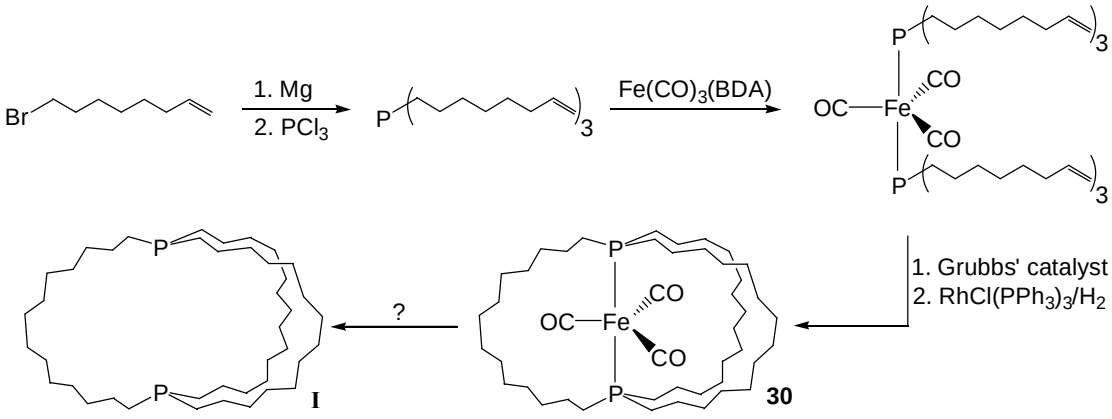

Scheme 4.14. Representative synthesis of the Fe complex **30**.

In addition, the gyroscopes were also characterized by ^{31}P MAS NMR to examine their chemical shifts and CSA values in the solid state. In the 13 kHz spectrum (Figure 4.10, top), it can be seen that the smallest gyroscope, **28**, containing 10 CH_2 groups, has one isotropic line at 73.7 ppm. The CSA is found to be 145 ppm as calculated from the span of the wideline spectrum (Figure 4.10, bottom). It will be

interesting to compare the CSA values of the empty cages of types **I** and **III** with those of the gyroscope once they are synthesized in large enough quantities.

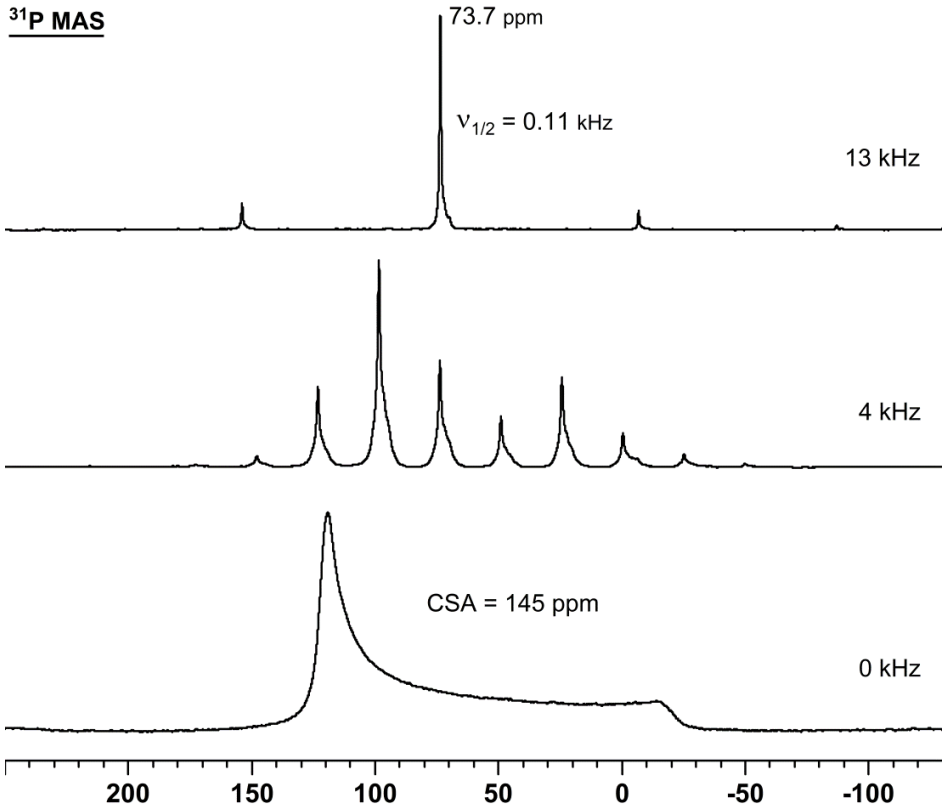

Figure 4.10. ^{31}P MAS NMR (top) and wideline spectrum (bottom) of **28**. The 4 kHz spectrum was taken of a different batch of **28** containing an impurity from incomplete hydrogenation of the double bonds.

The adsorption of the gyroscopes on silica was also investigated. Gyroscope **28** was combined with silica in the solid state by grinding their dry mixture for 15 minutes and in solution by dissolving the gyroscope and adding it to a slurry of silica in toluene. Both experiments led to the same results. There was an increase in the halfwidth of the isotropic line from 0.11 kHz to 0.82 kHz (Fig. 4.11, top). For the polycrystalline sample

28, the simulated spectrum of the measurement at 4 kHz gave a CSA of about 145 ppm (Table 4.6), which can be confirmed by examining the wideline pattern. For the gyroscope **28** on SiO_2, the CSA was ca. 144 ppm as determined from the simulated 4 kHz spectrum. There was no significant change in the CSA pattern of **28** when treated with silica, and only a small change of 0.4 ppm in the chemical shift as compared to the polycrystalline material (Figure 4.11), which indicates that the interactions taking place with the silica do not lead to a chemical reaction or increased mobility of the gyroscope on the silica surface. The larger residual linewidth, however, indicates that the material is no longer crystalline but rather amorphous in the presence of silica. Longer reaction times or elevated temperatures may cause the complex **28** to decompose and allow the free lone pairs of the diphosphine cage **I** to be adsorbed, but this option has not been explored.

Table 4.6. CSA values [ppm] for Fe gyroscope **28** and for **28** combined with SiO_2. The error margin for the values is ± 2 ppm.

	$\delta_{iso}(^{31}P)$	δ_{11}	δ_{22}	δ_{33}	CSA
Polycrystalline 28	73.7	123	119	–22	145
28 with SiO_2	73.3	123	117	–21	144

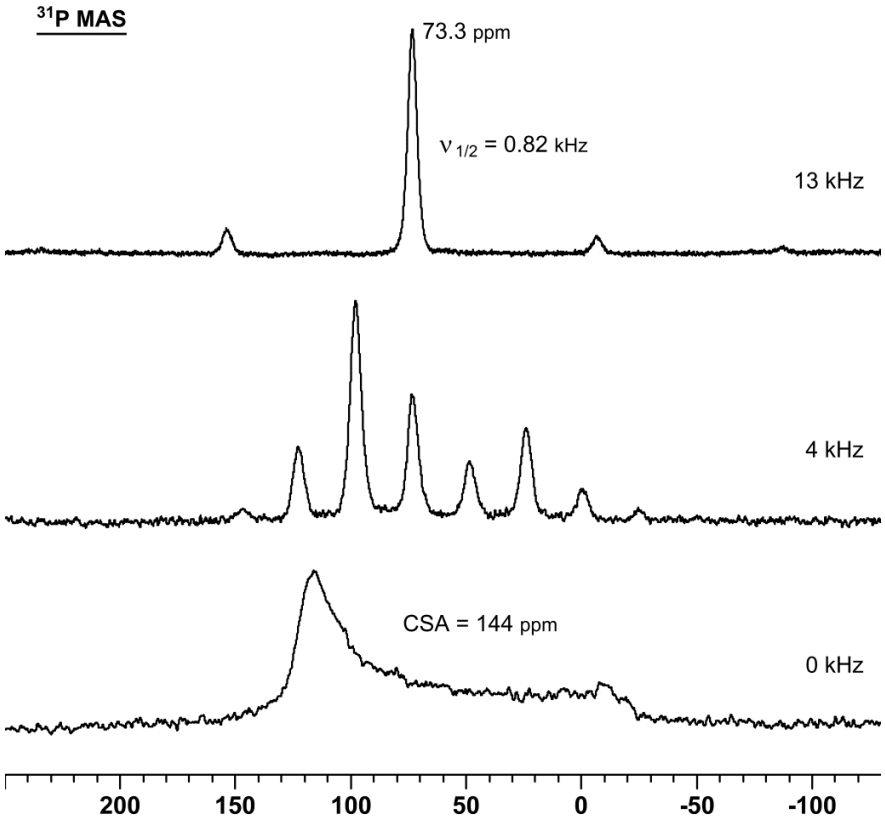

Figure 4.11. ^{31}P MAS NMR spectra of **28** after combining it with dry SiO_2 at the indicated rotational frequencies.

Oxidation of the Iron Gyroscopes

Once the gyroscopes were synthesized and fully characterized, oxidation was the first method tested to try to remove the Fe center and release the dioxide cage (**III**) (Scheme 4.15). Since the more robust Fe model compounds, e.g. **14**, had required a very strong oxidizing reagent to fully decompose the complexes, both H_2O_2 and ^{t}BuOOH were investigated as oxidants for the gyroscopes. The initial reactions were carried out with the smallest gyroscope **28** because it was thought that the shorter alkyl chains may be more effective at shielding the Fe core from attack making it more difficult to oxidize.

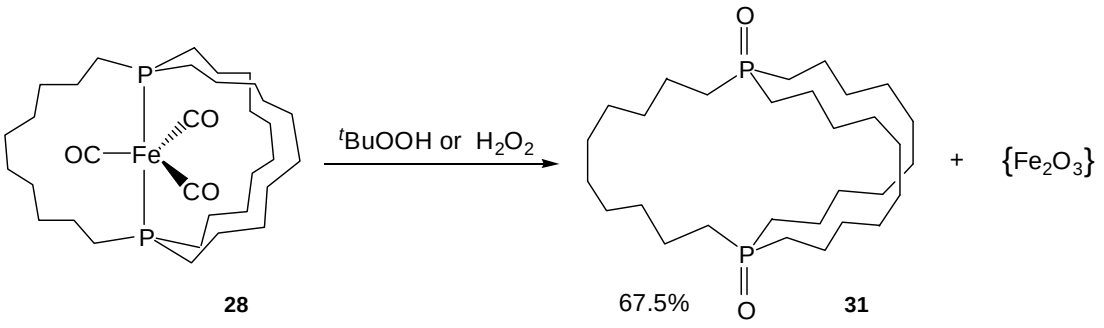

Scheme 4.15. Oxidation of **28** to give the diphosphine dioxide **31**.

Gyroscope **28** was reacted with an excess (200 eq.) of 35% H_2O_2 in toluene at room temperature overnight, but no reaction occurred according to the ^{31}P NMR spectrum. A greater excess (2000 eq.) of concentrated (35%) H_2O_2 and the use of THF as the solvent were necessary to push the reaction to completion. A broad signal around 55 ppm, similar to that of previously reported phosphine oxide H_2O_2 adducts,[63] and another sharp signal around 50 ppm were present. So, formation of the H_2O_2 adduct of the phosphine oxide took place, as expected, and therefore the reaction mixture was stirred with molecular sieves to generate the dioxide cage **31**. Surprisingly, two species are observed in ^{31}P NMR spectrum after the adduct decomposition (Figure 4.12). One of the signals remained unchanged at around 50 ppm, but the other shifts drastically (about 7 ppm) to 48.1 ppm showing clearly decomposition of the H_2O_2 adduct. These different signals could arise from the different orientations of the P=O groups with respect to the cage, such as *out/out* or *in/out* conformations, which differ by about 2.5 ppm in the case of the large diphosphine cage **1**.[11] Also, perhaps some of the H_2O_2 is still interacting with the P=O bonds, especially if pointing inside the cage molecule, and was not decomposed by the molecular sieves. In any case, currently this reaction has been performed on a larger scale to see if the two products can be isolated. Crystallization of

these different species would give confirmation of the actual structure of the dioxide cage **31** formed from oxidation with H_2O_2.

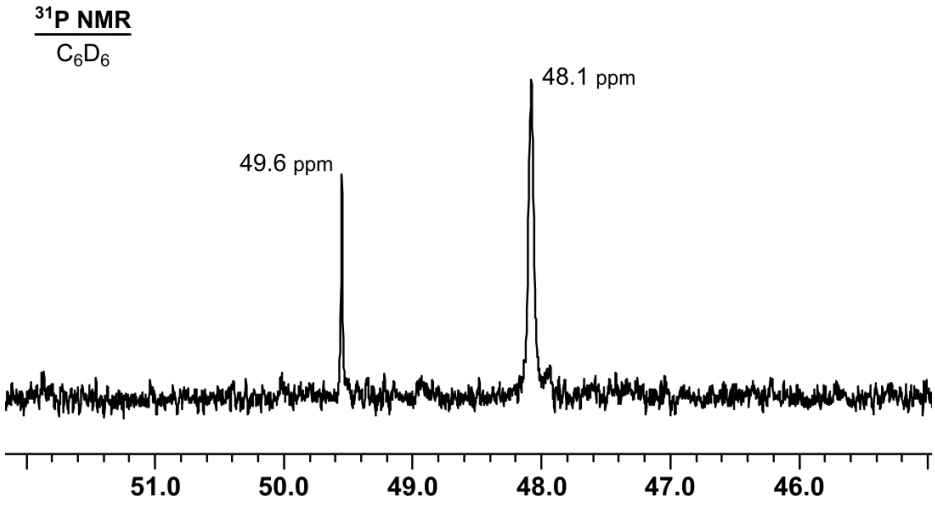

Figure 4.12. ^{31}P NMR spectrum of the products from oxidation of gyroscope **28** by H_2O_2.

As anticipated, the oxidation with H_2O_2 proved to be rather challenging due to the alkyl chains of the gyroscope shielding the Fe center from the oxidizing agent. Therefore, ^{t}BuOOH was tested since it is a stronger oxidant and was able to effectively oxidize **14**. Gyroscope **28**, dissolved in dichloromethane, was mixed with an excess of 35% ^{t}BuOOH (200 eq.) at room temperature, and full conversion was achieved overnight. Fe byproducts were easily removed into the aqueous layer of the reaction mixture, and the dioxide cage **31** could be purified in a straightforward manner. The formation of a peroxide adduct or residual peroxide or *t*-butanol was noted by ^1H NMR and IR, so the mixture was stirred with molecular sieves in hopes of removing residual ^{t}BuOOH and water. The ^{31}P NMR spectrum of the final product displayed only one

signal (Figure 4.13), showing the ^{t}BuOOH oxidation is overall a cleaner oxidation reaction than the reaction with H_2O_2.

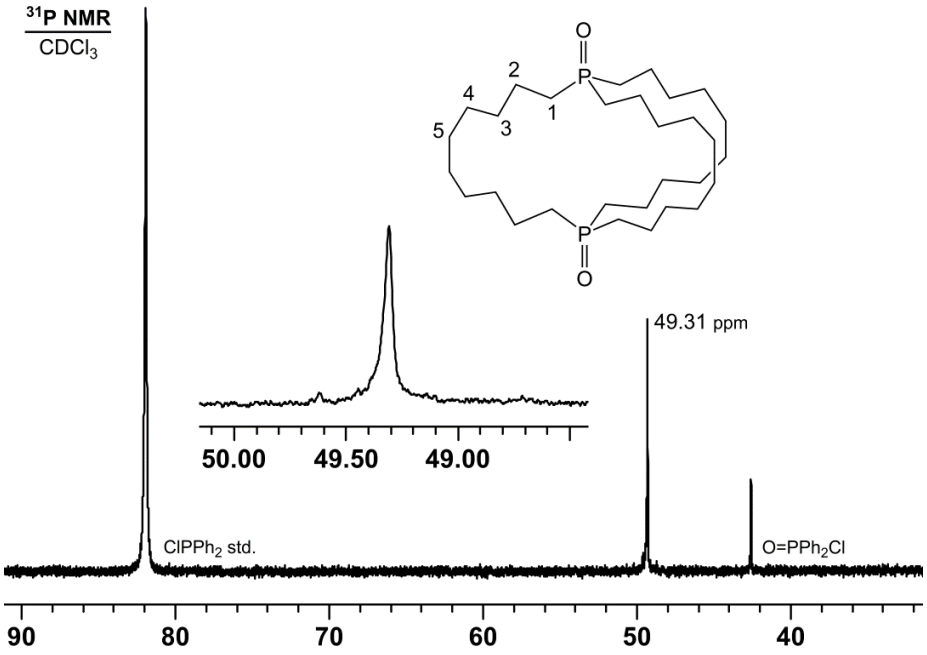

Figure 4.13. ^{31}P NMR spectrum after the oxidation of **28** with ^{t}BuOOH to give dioxide cage **31**.

The final diphosphine dioxide cage **31** was fully characterized by NMR, IR, and mass spectrometry (see Experimental section). 2D NMR techniques, namely ^{1}H,^{1}H COSY, ^{1}H,^{13}C HSQC, and ^{1}H,^{13}C HMBC, were used to fully assign all ^{1}H and ^{13}C signals of the cage **31**. As one can see in the ^{13}C NMR spectrum (Figure 4.14), there are five signals because the cage molecule is symmetric. The coupling constants for carbons in the α [$^{1}J(^{31}\text{P}–^{13}\text{C})$ = 64.4 Hz], β [$^{2}J(^{31}\text{P}–^{13}\text{C})$ = 4.0 Hz], and γ [$^{3}J(^{31}\text{P}–^{13}\text{C})$ = 7.9 Hz] positions with respect to the phosphorus nucleus are similar to what is observed in other trialkylphosphine oxides,[63] allowing these signals to be easily assigned. These

assignments were confirmed by $^{1}H,^{1}H$ COSY and $^{1}H,^{13}C$ HSQC spectra.

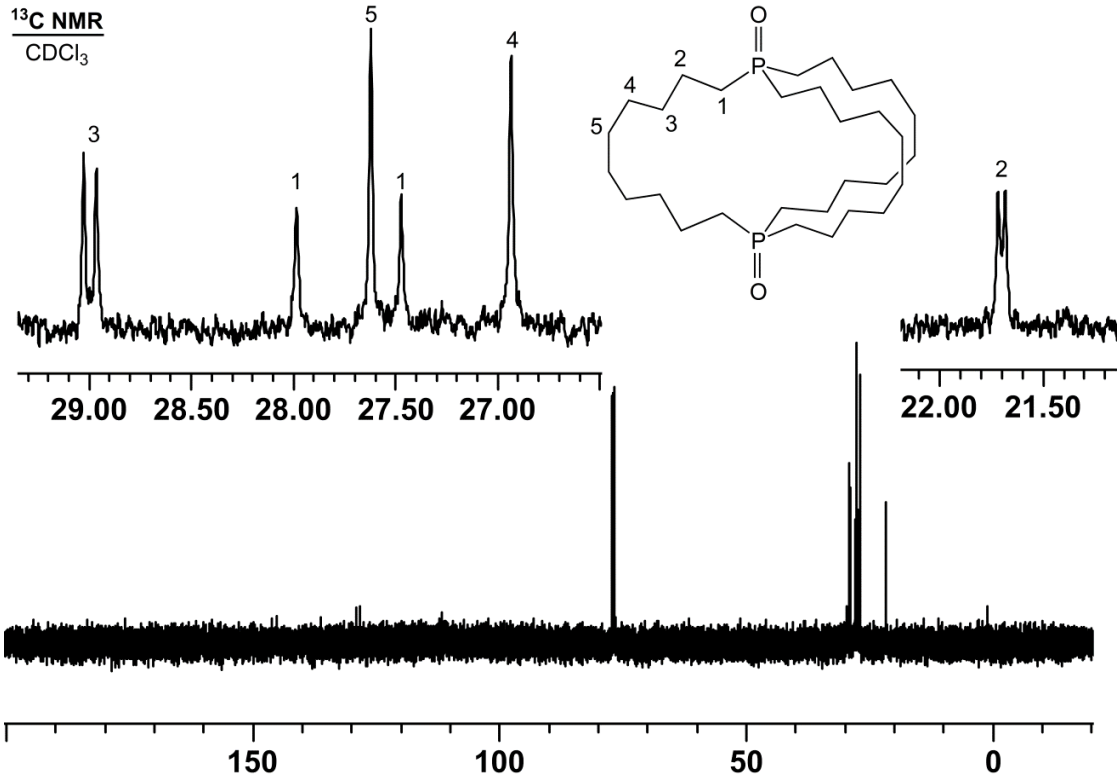

Figure 4.14. ^{13}C NMR spectrum of diphosphine dioxide cage **31**.

In order to determine the assignment of carbons 4 and 5, a $^{1}H,^{13}C$ HMBC spectrum has been recorded. In the HMBC spectrum cross peaks should arise primarily for $^{2}J(^{13}C–^{1}H)$ and ^{3}J but not for ^{1}J. As shown in the HMBC NMR spectrum of **31** (Figure 4.15), there is a distinct cross peak for the protons bound to carbon 3 and the carbon signal at 26.9 ppm (circled in blue), which confirms that this is the signal for carbon 4. On the other hand, the signal at 27.6 ppm does not have a cross peak with the protons at carbon 3 indicating a weaker correlation, which again is in agreement with

this being the signal for carbon 5.

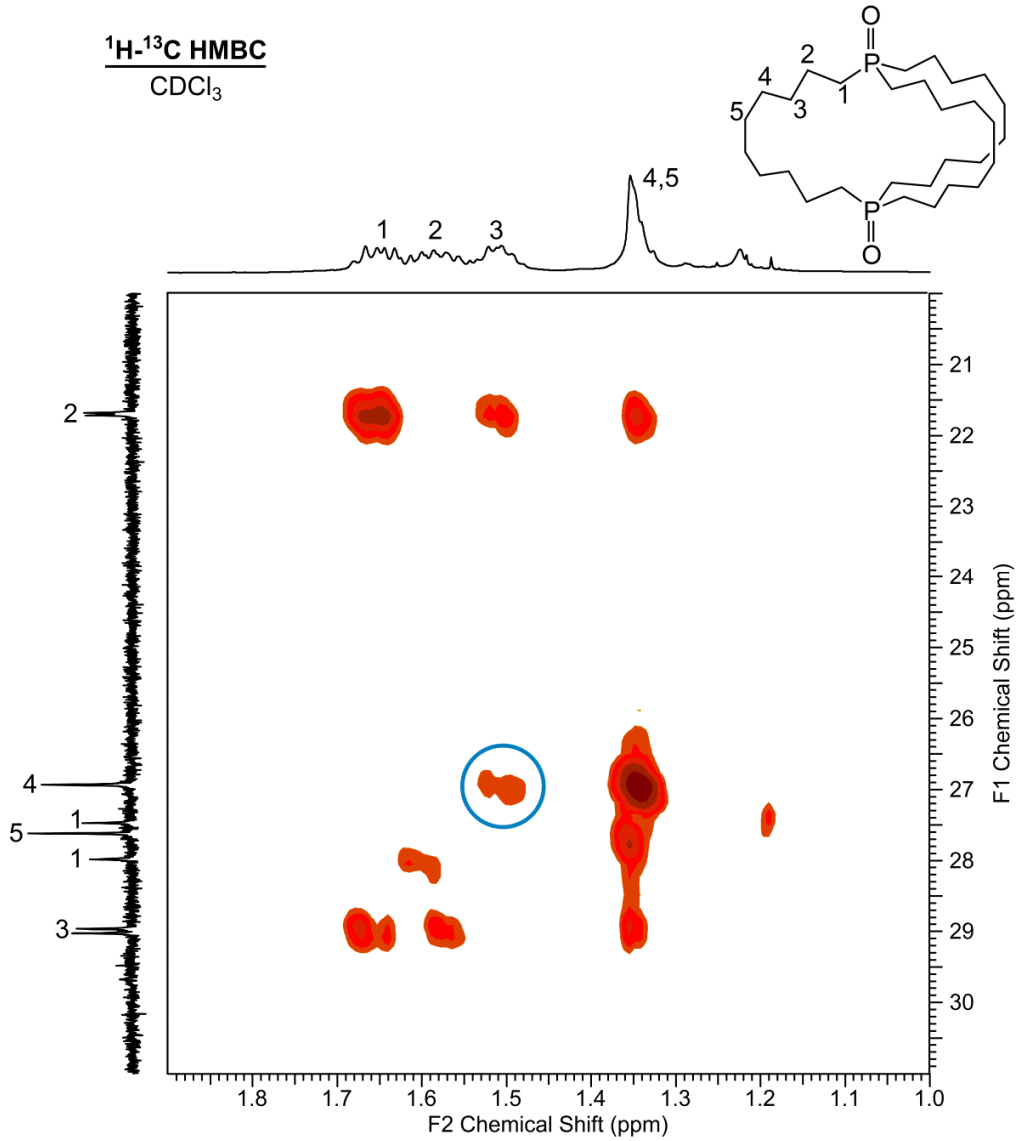

Figure 4.15. HMBC spectrum of diphosphine dioxide cage **31**.

Using ^{t}BuOOH for the oxidation of gyroscope **29** and **30** resulted in the formation of the corresponding diphosphine dioxide cages **32** and **33** (Schemes 4.16 and

4.17) in good yields.

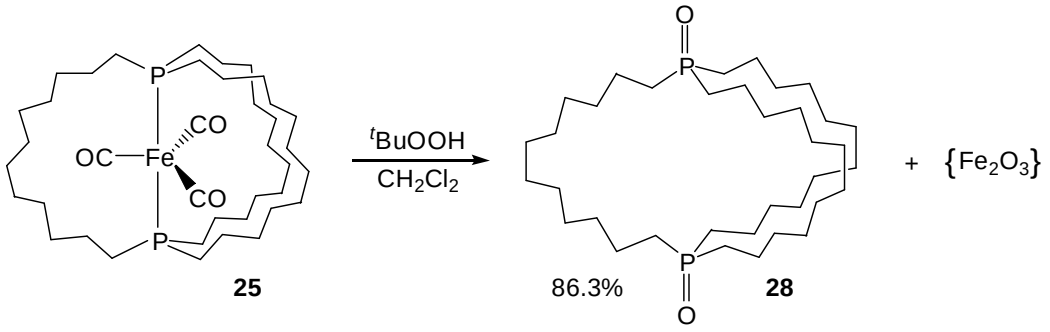

Scheme 4.16. Oxidation of **29** to give the diphosphine dioxide **32**.

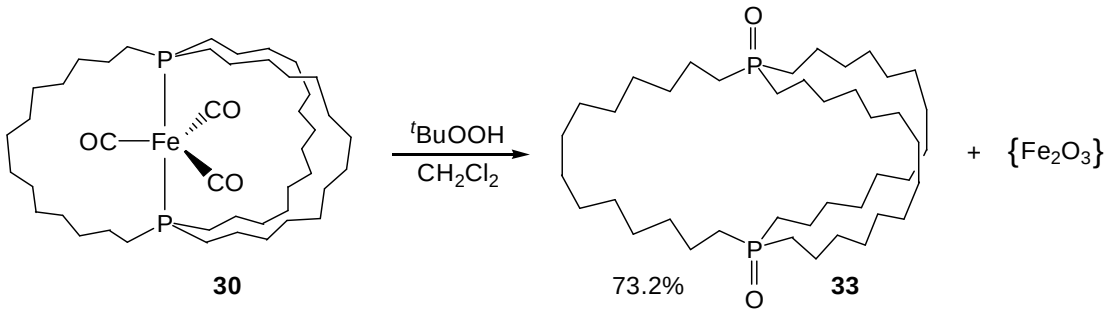

Scheme 4.17. Oxidation of **30** to give the diphosphine dioxide **33**.

The use of an excess of the stronger oxidant, ^{t}BuOOH, proved to be important in the formation of only one product as evidenced by ^{31}P NMR spectroscopy. In some cases in which less equivalents or more dilute ^{t}BuOOH was employed, two signals would arise in the ^{31}P NMR spectrum of the crude product. Once again this phenomenon could be due to some sort of adduct formation or from different isomers of the cage structure being generated. The isomerization of the large diphosphine cage **1** has been explored in detail,[11] and similar studies about the homeomorphic isomerization of these

dioxide cages may be investigated in the future. The clean diphosphine dioxide cages **32** and **33** were synthesized and fully characterized (see Experimental section). The ^{31}P NMR spectra clearly show only one product in each case (Figure 4.16 and 4.17).

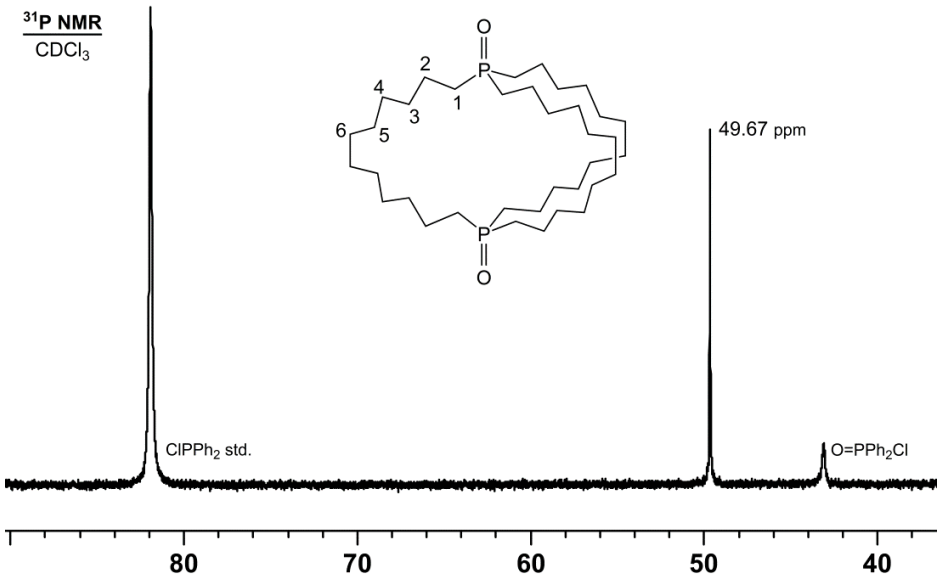

Figure 4.16. ^{31}P NMR spectrum of diphosphine dioxide cage **32**.

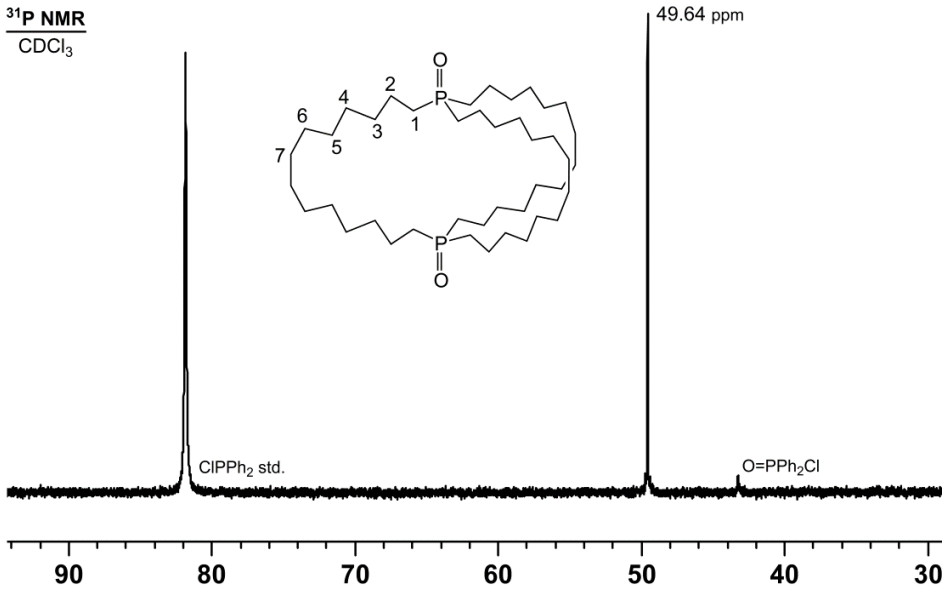

Figure 4.17. ^{31}P NMR spectrum of diphosphine dioxide cage **33**.

CONCLUSION

A goal of this research project was to synthesize the diphosphine dioxide cages **I** and **III** from the Fe gyroscopes pioneered by the Gladysz group. The cage sizes accessible when using these Fe complexes have 10, 12, or 14 CH_2 units in each of the three alkyl chains. In order to determine an efficient method to remove the $Fe(CO)_3$ core from the gyroscope complexes, a series of Fe phosphine model compounds **12**–**15** have been developed. The reactivity of this class of Fe complexes has been extensively tested using the model compounds to probe which reagents released the phosphines from the Fe center and generated useful phosphine derivatives, such as phosphonium salts or phosphine oxides. The most useful method to transform the Fe phosphine complexes is oxidation with a strong oxidant, namely ^{t}BuOOH, which in turn creates the corresponding phosphine oxides as the primary products in high yields. Alkylating agents and acids also have proven to be effective

at releasing the phosphines from Fe model compounds while forming phosphonium salts. The oxidation technique was the most successful, and therefore this procedure has been applied to the Fe gyroscopes to form the diphosphine dioxide cages **31**–**33**. The solid-state NMR characteristics of these dioxide cages **III** and their adsorption on silica will be studied in detail and reported in Chapter V.

EXPERIMENTAL

(a) General procedures

All reactions involving phosphines or Fe phosphine complexes as starting materials are performed under a nitrogen atmosphere. All reactions to synthesize the Fe gyroscopes **28**–**30** follow the procedures outlined by the Gladysz group.[15] Similarly, the Fe phosphine model compounds **12**–**15** are also synthesized in the same manner as the Fe gyroscope starting materials. Some of these model compounds have been previously reported in the literature, and the references are noted in Table 4.1. All intermediate iron complexes are stored under nitrogen. Tricarbonyl (benzylideneacetone)iron, [Fe(BDA)$(CO)_3$], is prepared from a literature procedure by Howell *et al.*,[84] which is differs from that referenced by the Gladysz group. Chemicals are treated as follows: Toluene (Mallinckrodt Chemicals, ACS grade), THF (Aldrich, ACS grade 99+%), and Et_2O (JT Baker, Anhydrous, ACS grade) are distilled from Na/benzophenone; CH_2Cl_2 (Mallinckrodt Chemicals, HPLC grade) and hexanes (Fisher Scientific, HPLC grade) are obtained from a solvent purification system (JC Meyer Solvent Systems); C_6D_6 (Cambridge Isotope Laboratories) and $CDCl_3$ (Aldrich) are dried over molecular sieves; 3 Å molecular sieves (composition of Na_2O, K_2O, MgO, SiO_2, and Al_2O_3, EMD Chemical Inc.) are activated by heating in vacuum at 150 °C for 6 hours; PBu_3 (Strem Chemicals, 99%) and PCy_3 (Alfa Aesar) are purified by filtration through alumina

(elution with CH_2Cl_2); H_2O_2 (Acros Organics, 35 % aqueous) and ^tBuOOH (Alfa Aesar, 70% aqueous) are stored at 4 °C and either used as obtained or diluted; PCl_3 (Aldrich, 99%), $Fe_2(CO)_9$ (Strem, 99%), $POct_3$ (Strem, 97%), PMe_3 (Alfa Aesar, 99%), Grubbs' first generation catalyst (Aldrich), and Grubbs' second generation catalyst (Aldrich) are used as received but stored in the glove box; PPh_3 (Aldrich, 99%), 7-bromo-1-heptene (Gelest), 6-bromo-1-hexene (Aldrich, 95%), benzylideneacetone (BDA) (Alfa Aesar, 98%), $ClPPh_2$ (TCI America, 98%), $CHCl_3$ (EMD, ACS grade), Na_2SO_4 (EMD Chemicals Inc., anhydrous), silica gel (EMD, 60 Å), alumina (Alfa Aesar, neutral), and filter paper (Whatman) are used as received.

The ^1H, $^{13}C\{^1H\}$, and $^{31}P\{^1H\}$ NMR spectra of liquids are recorded on a 500 MHz Varian spectrometer at 499.70, 125.66, and 202.28 MHz and referenced as follows: ^1H NMR, residual C_6D_5H (7.15 ppm) and $CHCl_3$ (7.26 ppm); ^{13}C NMR, internal C_6D_6 (128.02 ppm) and $CDCl_3$ (77.00 ppm); ^{31}P NMR, capillary filled with $ClPPh_2$ (81.92 ppm) centered in the NMR tube. The ^{31}P solid-state NMR spectra were recorded on a 400 MHz Bruker Avance widebore NMR spectrometer equipped with a 4 mm broadband probehead and ZrO_2 rotors. The polycrystalline substances were densely packed into the rotors. The chemical shifts were referenced with polycrystalline $(NH_4)H_2PO_4$ (+0.81 ppm) as the external standard. A single pulse program with ^1H high-power decoupling was applied, and typically about 64 scans with a pulse delay of 10 s were sufficient to obtain a signal while more scans, about 3000–10000, generated a good signal-to-noise ratio. Simulations of the solid-state NMR spectra were performed using WSolids, a program by K. Eichele. Typically using the Herzfeld-Berger method, the rotational speed, δ_{iso}, estimated CSA span, and estimated skew are entered into the program and a simlated spectrum is generated. Then by changing the CSA span the intensity of the simulated spectrum will match

better with the experimental spectrum, and once good overlap is achieved the δ_{11}, δ_{22}, and δ_{33} values can be determined by changing to the Standard mode. These values are compared with the experimental wideline spectrum to ensure there is a good fit. Also, the δ values can be applied to simulate the wideline pattern or another spectrum at a different rotational frequency to confirm the simulation is valid.

IR data were recorded on a Shimadzu IRAffinity-1 FTIR using a Pike Technologies MIRacle ATR plate (Diamond/ZnSe). Mass spectrometry was performed using electron spray ionization (ESI) in the positive mode. The samples were dissolved in dilute solutions of DCM, MeOH, and 1% acetic acid. The flow rate was 7 μL/min and the applied voltage was 4500 V. All of the peaks assigned to 100% were the most intense peaks of the isotope envelope.

(b) Model Iron Phosphine Complexes

Representative procedure for the synthesis of diphosphine iron carbonyl complexes **12–15***:*

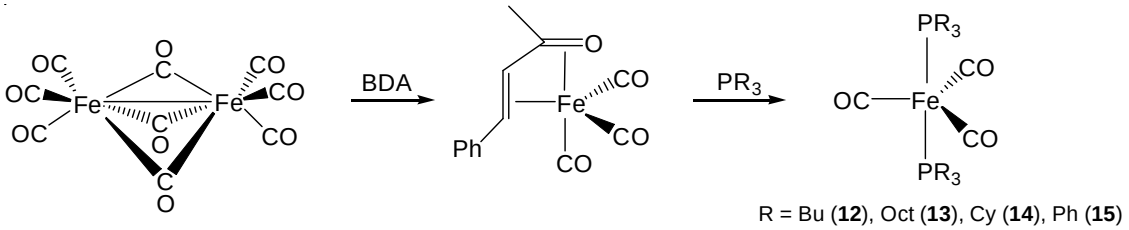

R = Bu (**12**), Oct (**13**), Cy (**14**), Ph (**15**)

*Synthesis of $Fe(CO)_3(POct_3)_2$ **(13)***

(Benzylideneacetone)iron tricarbonyl (0.250 g, 0.874 mmol) and $POct_3$ (0.681 g, 1.837 mmol) are weighed into two separate Schlenk flasks in the glove box. THF is added to both flasks to dissolve $(BDA)Fe(CO)_3$ (20 mL) and $POct_3$ (10 mL). The phosphine solution is transferred to the reaction flask with the metal complex via a metal cannula. The reaction mixture is left stirring at room temperature for 12 h and turns from

red to yellow/green overnight. The solvent is removed *in vacuo*, and the residue is redissolved in hexanes and filtered in the glove box through a column (neutral alumina, 2.5 x 5 cm) using hexanes to remove impurities and a mixture of hexanes and CH_2Cl_2 (2:1) to afford the pure compound **13** (0.629 g, 0.714 mmol, 81.7%) as a light yellow oil.

Bis(tributylphosphine)iron tricarbonyl (12)

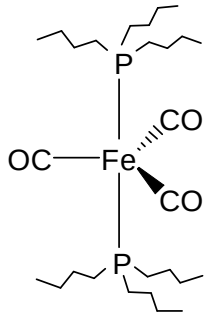

$C_{27}H_{54}O_3P_2Fe$

Mol. Wt. = 544.5181 g/mol

light yellow oil, 75.3% yield

$^{31}P\{^1H\}$ NMR (C_6D_6, 202.28 MHz) δ (ppm): 62.29 (s).

^1H NMR (C_6D_6, 499.70 MHz) δ (ppm): 1.96–1.84 (br m, 12 H, PCH_2), 1.82–1.69 (br m, 12 H, PCH$_2$CH_2), 1.43 (sextet, $^3J(^1H–^1H)$ = 7.2 Hz, 12 H, CH_2CH$_3$), 1.00 (br t, 18 H, CH_3).

$^{13}C\{^1H\}$ NMR (C_6D_6, 125.66 MHz) δ (ppm): 216.15 (t, $^2J(^{31}P–^{13}C)$ = 28.2 Hz, *C*O), 31.68 (virtual dd, span of outer lines = 27.3 Hz, P*C*H$_2$), 26.32 (s, PCH$_2$*C*H$_2$), 24.69 (virtual t, span of outer lines = 13.1 Hz, P(CH$_2$)$_2$*C*H$_2$), 13.98 (s, *C*H$_3$).

Bis(trioctylphosphine)iron tricarbonyl (13)

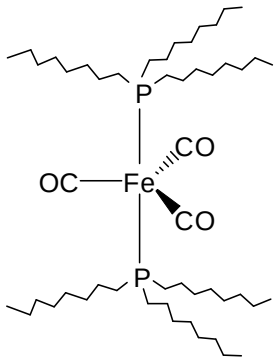

$C_{51}H_{102}O_3P_2Fe$

Mol. Wt. = 881.1463 g/mol

light yellow oil, 81.7% yield

$^{31}P\{^{1}H\}$ NMR (C_6D_6, 202.28 MHz) δ (ppm): 62.75 (s).

^{1}H NMR (C_6D_6, 499.70 MHz) δ (ppm): 1.86–1.73 (br m, 12 H, PCH_2), 1.72–1.59 (br m, 12 H, PCH_2CH_2), 1.30–1.09 (br m, 60 H, overlapping $PCH_2CH_2(CH_2)_5$), 0.91 (br t, 18 H, CH_3).

$^{13}C\{^{1}H\}$ NMR (C_6D_6, 125.66 MHz) δ (ppm): 216.24 (t, $^{2}J(^{31}P–^{13}C)$ = 27.9 Hz, *C*O), 32.30 (s, $CH_2CH_2CH_3$), 31.77 (virtual t, span of outer lines = 12.7 Hz, $P(CH_2)_2CH_2$), 31.11 (virtual dd, span of outer lines = 27.6 Hz, PCH_2), 29.71 (s, $P(CH_2)_3CH_2$)*, 29.67 (s, $CH_2(CH_2)_2CH_3$)*, 24.33 (s, PCH_2CH_2), 23.11 (s, CH_2CH_3), 14.38 (s, CH_3).

* = assignments are interchangeable

IR (cm^{-1}, oil film): 2954 (w), 2922 (w), 2852 (w), 1857 (s, ν_{CO}), 1456 (w), 1412 (w), 1029 (w), 756 (w), 721 (w), 642 (m).

Bis(tricyclohexylphosphine)iron tricarbonyl (14)

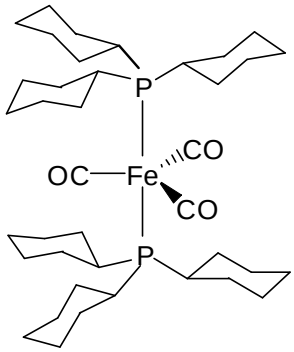

$C_{39}H_{66}O_3P_2Fe$

Mol. Wt. = 700.7449 g/mol

light yellow powder, 54.4% yield

$^{31}P\{^{1}H\}$ NMR ($CDCl_3$, 202.28 MHz) δ (ppm): 85.60 (s).

^{1}H NMR ($CDCl_3$, 499.70 MHz) δ (ppm): 2.25–2.00 (br m, 18 H, PC*H*CH_{eq}) 1.99–1.80 (br m, 12 H, PCHCH$_2$CH_{eq}), 1.80–1.65 (br m, 6 H, PCH(CH$_2$)$_2$CH_{eq}), 1.64–1.42 (br m, 12 H, PCHCH_{ax}), 1.41–1.19 (br m, 18 H, PCHCH$_2$CH_{ax}CH_{ax}).

$^{13}C\{^{1}H\}$ NMR ($CDCl_3$, 125.66 MHz) δ (ppm): 216.83 (t, $^{2}J(^{31}P–^{13}C)$ = 28.2 Hz, *C*O), 38.30 (virtual dd, span of outer lines = 20.5 Hz, P*C*H), 29.51 (s, PCH*C*H$_2$), (virtual t, span of outer lines = 9.8 Hz, PCHCH$_2$*C*H$_2$), 26.23 (s, PCH(CH$_2$)$_2$*C*H$_2$).

Bis(triphenylphosphine)iron tricarbonyl (15)

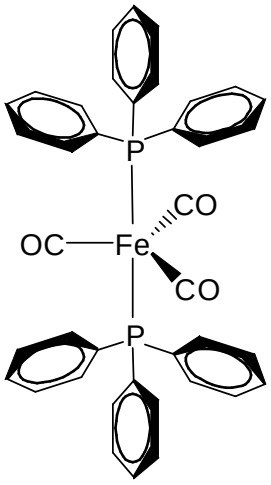

$C_{39}H_{30}O_3P_2Fe$

Mol. Wt. = 664.4605 g/mol

light yellow powder, 76.5% yield

$^{31}P\{^{1}H\}$ NMR ($CDCl_3$, 202.28 MHz) δ (ppm): 82.34 (s).

^{1}H NMR ($CDCl_3$, 499.70 MHz) δ (ppm): 7.59–7.42 (br m, 12 H, H_o), 7.38–7.22 (br m, 18 H_m,H_p).

$^{13}C\{^{1}H\}$ NMR ($CDCl_3$, 125.66 MHz) δ (ppm): 214.24 (t, $^{2}J(^{31}P–^{13}C)$ = 29.0 Hz, *C*O), 136.52 (virtual dd, span of outer lines = 46.2 Hz, C_i), 133.30 (virtual t, span of outer lines = 10.3 Hz, C_o), 129.86 (s, C_p), 128.17 (virtual t, span of outer lines = 9.1 Hz, C_m).

(c) Reactivity of Iron Phosphine Model Compounds

Representative procedure for oxidation reactions with H_2O_2:

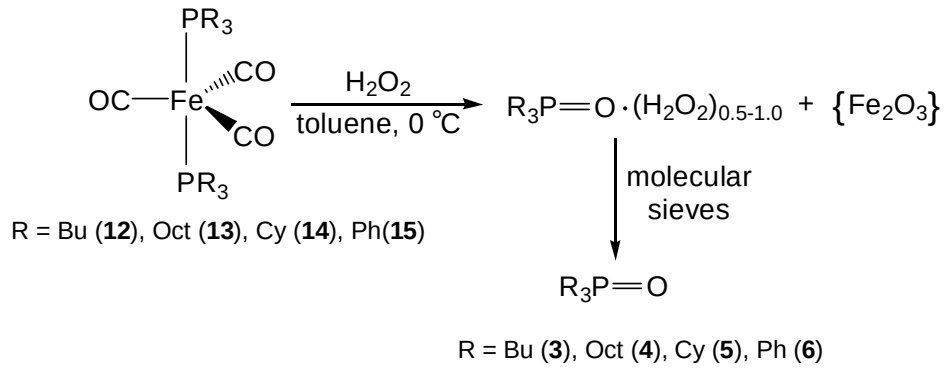

R = Bu (**12**), Oct (**13**), Cy (**14**), Ph(**15**)

R = Bu (**3**), Oct (**4**), Cy (**5**), Ph (**6**)

Bis(tributylphosphine)iron tricarbonyl (**12**) (0.051 g, 0.161 mmol) is weighed into a Schlenk flask in the glove box. Toluene (5 mL) is added to dissolve the starting material. H_2O_2 (17.5%) (0.64 mL, 3.29 mmol) is added dropwise via syringe to the reaction flask at 0 °C. The reaction mixture is allowed to warm to room temperature and stirred for 15 h. The slightly orange organic layer is filtered through filter paper into a round bottom flask to remove the iron-containing impurities, and the aqueous layer is washed with toluene (2 x 10 mL). The solvent is removed from the combined organic phases with a rotary evaporator to give a yellow oil which is identified as the hydrogen peroxide adduct of the phosphine oxide by NMR and IR spectroscopy.[63] Toluene (40 mL) and molecular sieves suspended in a tea bag are added to the flask, and the solution is stirred at room temperature for 15 h. Removal of the solvent on the rotary evaporator results in a slightly beige powder of **3** (0.033 g, 0.15 mmol, 47%). When this reaction is repeated on a larger scale, the yield increases to 57%.

Representative procedure for reactions with Meerwein's salt:

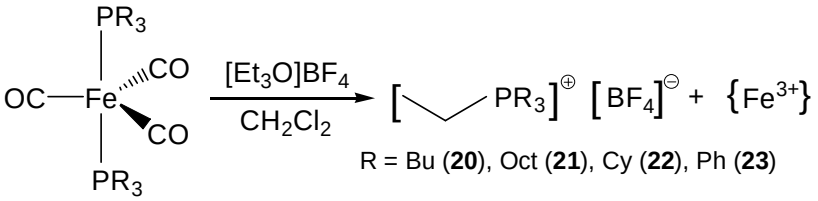

R = Bu (**12**), Oct (**13**), Cy (**14**), Ph (**15**)

R = Bu (**20**), Oct (**21**), Cy (**22**), Ph (**23**)

Bis(tributylphosphine)iron tricarbonyl (**12**) (0.051 g, 0.161 mmol) is weighed into a Schlenk flask in the glove box. CH_2Cl_2 (5 mL) is added to dissolve all starting material. A solution of $[Et_3O][BF_4]$ (1.0 M in CH_2Cl_2, 0.40 mL, 0.40 mmol) is added dropwise via syringe to the reaction flask, and the reaction mixture is stirred for 15 h. Removal of the solvent by oil pump vacuum gives the crude product as a beige powder (84.7% by ^{31}P NMR). After the addition of degassed deionized H_2O (10 mL) and extraction with pentane (3 x 10 mL) yields **20** as the pure white powder (0.085 g, 82.3%).

Representative procedure for protonation reactions with HCl:

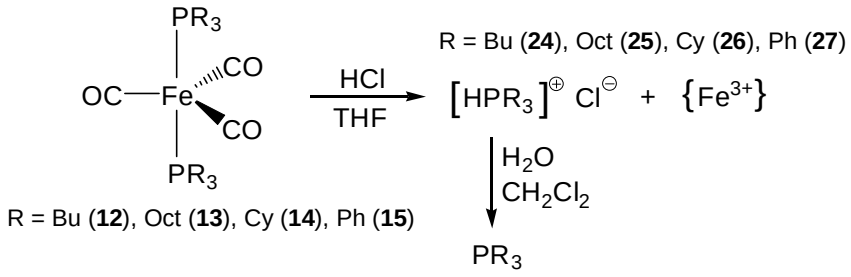

R = Bu (**12**), Oct (**13**), Cy (**14**), Ph (**15**)

R = Bu (**24**), Oct (**25**), Cy (**26**), Ph (**27**)

Bis(tributylphosphine)iron tricarbonyl (**12**) (0.079 g, 0.250 mmol) is weighed into a Schlenk flask in the glove box. THF (15 mL) is used to dissolve all starting material. HCl (6.05 M, 0.42 mL, 2.51 mmol) is added dropwise via syringe to the

reaction flask. The reaction mixture is allowed to stir at room temperature for 15 h. *In situ* ^{31}P NMR confirms that the $[HPR_3]^+$ phosphonium salt **24** is produced. The reaction mixture is concentrated to half its volume, and CH_2Cl_2 (10 mL) and oxygen-containing water (10 mL) are added. The mixture is stirred overnight at room temperature. Separation of the organic layer by transferring it into another Schlenk flask via cannula and washing of the aqueous layer with CH_2Cl_2 (2 x 5 mL) resulted mainly in tributylphosphine oxide as a white powder (0.045 g, 41.2%) with some slight impurities from the insertion of O_2 into the P–C bonds..

For protonation reactions with **13**–**15**, higher concentrations of 12.1 M HCl and prolonged reaction times of up to 72 h are necessary to give quantitative conversions. When using higher concentrations of HCl, ether is employed as the solvent because THF reacts to some extent with HCl to give 4-chlorobutanol.

(d) Diphosphine dioxide cages

*Representative procedure for the synthesis of diphosphine dioxide cages **31**–**33** from the iron gyroscopes **28**–**30**:*

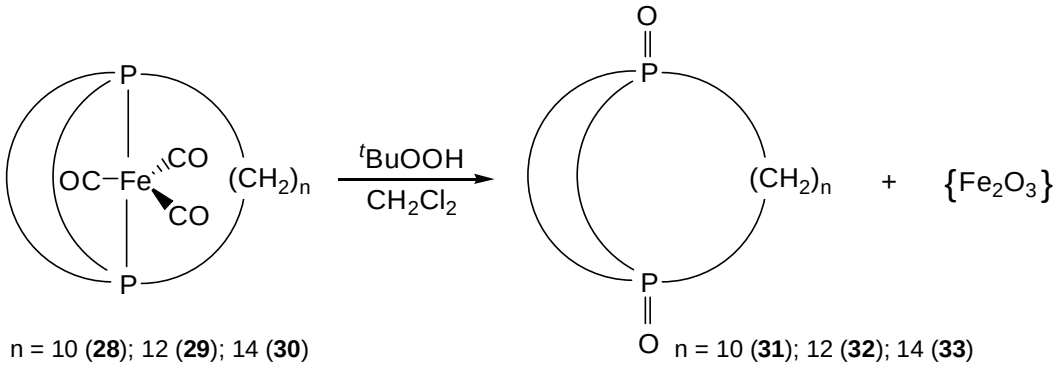

n = 10 (**28**); 12 (**29**); 14 (**30**)

n = 10 (**31**); 12 (**32**); 14 (**33**)

*Synthesis of diphosphine dioxide cage **31**:*

Iron gyroscope **28** (0.045 g, 0.0723 mmol) is weighed into a round bottom flask in air, and CH_2Cl_2 (50 mL) is added to dissolve the solid. The head space of the flask is flushed with nitrogen and is sealed by a rubber septum. The solution is cooled to 0 °C in an ice/water bath. ^{t}BuOOH (9.3 mL, 36.14 mmol, diluted to 35% w/w by 4.65 mL of deionized water) is measured into an Erlenmeyer flask and is added dropwise to the reaction mixture via a plastic syringe. The reaction mixture is left stirring overnight and slowly warms to room temperature. The solution changes from colorless to a light reddish brown overnight. Stirring is stopped and the two solvent layers separate while leaving some brown solid material suspended at the phase boundary. The CH_2Cl_2 phase is transferred into a separate round bottom flask via pipette. The aqueous phase is washed with CH_2Cl_2 (3 x 20 mL). The organic layers are combined, and the solvent is removed using the rotary evaporator to yield the crude product. The light brown solid is then dissolved in $CHCl_3$ (150 mL), and the solution is washed with deionized water (3 x 100 mL). Subsequently, the organic fractions are combined, dried over sodium sulfate, and after evaporation of the solvent, the diphosphine dioxide cage **31** is obtained as a white crystalline solid (0.037 g, 0.0719 mmol, 99.4% crude yield). The crude product is dissolved in toluene and activated molecular sieves in a tea bag are suspended in the mixture, which is left stirring overnight. The next day the mixture is filtered through a pipette with a glass wool plug into a Schlenk flask, and the solvent is removed *in vacuo*. The residue is washed with dry hexane, the solution is transferred to a separate Schlenk flask, and the solvent is removed to give cage **31** as a white powder (0.025 g, 0.0486 mmol, 67.5% yield).

Diphosphine dioxide cage 31:

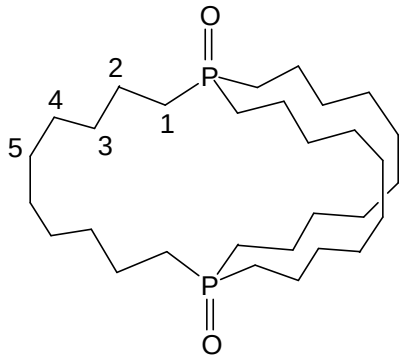

$C_{30}H_{60}O_2P_2$

Mol. Wt. = 514.7413 g/mol

White polycrystalline solid, 67.5% yield

$^{31}P\{^{1}H\}$ NMR ($CDCl_3$, 202.28 MHz) δ (ppm): 49.31 (s).

^{1}H NMR ($CDCl_3$, 499.70 MHz) δ (ppm): 1.72–1.64 (m, 12 H, PCH_2), 1.64–1.57 (m, 12 H, PCH_2CH_2), 1.56–1.48 (m, 12 H, $P(CH_2)_2CH_2$), 1.41–1.32 (br m, 24 H, $P(CH_2)_3CH_2CH_2$).

$^{13}C\{^{1}H\}$ NMR ($CDCl_3$, 125.66 MHz) δ (ppm): 28.99 (d, $^{3}J(^{31}P–^{13}C)$ = 7.9 Hz, $P(CH_2)_2CH_2$), 27.72 (d, $^{1}J(^{31}P–^{13}C)$ = 64.4 Hz, PCH_2), 27.62 (s, $P(CH_2)_4CH_2$), 26.94 (s, $P(CH_2)_3CH_2$), 21.70 (d, $^{2}J(^{31}P–^{13}C)$ = 4.0 Hz, PCH_2CH_2).

IR (cm^{-1}, oil film): 2924 (s), 2855 (m), 1354 (w), 1277 (s), 1159 (w), 1126 (s, ν_{PO}).

MS (positive ESI): 515 ([**31**+H]$^+$, 100%), 516 (impurity, 46%).[a]

[a] In contrast to cages **32** and **33**, the smallest dioxide cage **31** showed an impurity in about 46% in the isotope envelope at 516 m/z. Although the peak would correspond to [**31**+2H]$^+$, this would be expected to be a dication that would appear at 258 m/z, which is not observed in the spectrum.

Diphosphine dioxide cage 32:

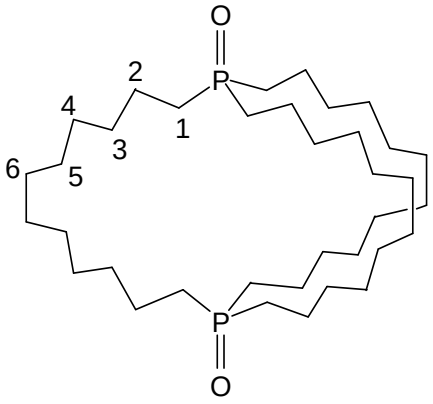

$C_{36}H_{72}O_2P_2$

Mol. Wt. = 598.9032 g/mol

White polycrystalline solid, 86.3% yield

$^{31}P\{^{1}H\}$ NMR ($CDCl_3$, 202.28 MHz) δ (ppm): 49.67 (s).

^{1}H NMR ($CDCl_3$, 499.70 MHz) δ (ppm): 1.73–1.60 (m, 12 H, PCH_2), 1.58–1.47 (m, 12 H, PCH_2CH_2), 1.43–1.34 (m, 12 H, $P(CH_2)_2CH_2$), 1.33–1.22 (br m, 36 H, $P(CH_2)_3CH_2CH_2CH_2$).

$^{13}C\{^{1}H\}$ NMR ($CDCl_3$, 125.66 MHz) δ (ppm): 30.06 (d, $^{3}J(^{31}P–^{13}C)$ = 13.7 Hz, $P(CH_2)_2CH_2$), 28.66 (s, $P(CH_2)_5CH_2$), 28.25 (s, $P(CH_2)_4CH_2$), 27.84 (s, $P(CH_2)_3CH_2$), 27.24 (d, $^{1}J(^{31}P–^{13}C)$ = 64.6 Hz, PCH_2), 21.05 (d, $^{2}J(^{31}P–^{13}C)$ = 3.3 Hz, PCH_2CH_2).

IR (cm^{-1}, oil film): 2957 (w), 2924 (m), 2857 (w), 1728 (s), 1462 (w), 1261 (m), 1121 (m, ν_{PO}), 1072 (m), 1016 (m), 798 (m).

MS (positive ESI): 600 ([**32**+H]$^{+}$, 100%).

Diphosphine dioxide cage 33:

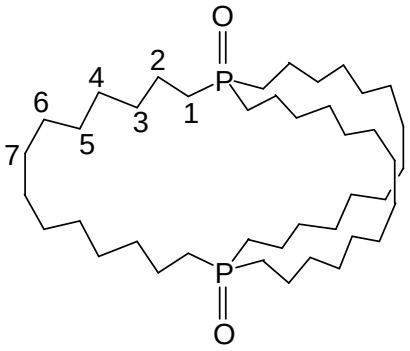

$C_{42}H_{84}O_2P_2$

Mol. Wt. = 683.0627 g/mol

White polycrystalline solid, 73.2% yield

$^{31}P\{^{1}H\}$ NMR ($CDCl_3$, 202.28 MHz) δ (ppm): 50.02 (s).

^{1}H NMR ($CDCl_3$, 499.70 MHz) δ (ppm): 1.70–1.60 (m, 12 H, PCH_2), 1.56–1.45 (m, 12 H, PCH$_2$CH_2), 1.42–1.33 (m, 12 H, P(CH$_2$)$_2$CH_2), 1.31–1.19 (br m, 48 H, P(CH$_2$)$_3$CH_2CH_2CH_2CH_2).

$^{13}C\{^{1}H\}$ NMR ($CDCl_3$, 125.66 MHz) δ (ppm): 30.48 (d, $^{3}J(^{31}P–^{13}C)$ = 14.2 Hz, P(CH$_2$)$_2$*C*H$_2$), 29.21 (s, P(CH$_2$)$_6$*C*H$_2$)*, 29.19 (s, P(CH$_2$)$_5$*C*H$_2$)*, 28.85 (s, P(CH$_2$)$_4$*C*H$_2$), 28.43 (s, P(CH$_2$)$_3$*C*H$_2$), 27.40 (d, $^{1}J(^{31}P–^{13}C)$ = 64.7 Hz, P*C*H$_2$), 21.34 (d, $^{2}J(^{31}P–^{13}C)$ = 3.5 Hz, PCH$_2$*C*H$_2$). * = assignments are interchangeable

IR (cm^{-1}, oil film): 3402 (br w, ν_{OH} of H_2O), 2918 (s), 2851 (m), 1128 (m, ν_{PO}).

MS (positive ESI): 684 ([**33**+H]$^{+}$, 100%).

CHAPTER V

ADSORPTION OF DIPHOSPHINE DIOXIDE CAGES ON SILICA SURFACES

INTRODUCTION

One of the major goals of this research project was to synthesize cage-type compounds, such as **I**–**III**, to adsorb on silica and to examine their solid-state ^{31}P NMR characteristics. As evidenced in Chapter III, the adsorption of phosphines[10] or phosphine oxides on silica leads to a drastic reduction of the CSA of the ^{31}P solid-state NMR signals of the adsorbed material as compared to that of the polycrystalline solid. This phenomenon can originate from two factors, (1) the partial quaternization effect and (2) the quasi isotropic mobility of the substance across the silica surface within its pores.[61]

In the case of phosphines, the formation of weak P···HOSi or P···Si$^{\delta+}$ interactions between the lone pair at P and the surface functional groups would lead to a partial quaternization at the P nucleus. It is known that the CSA of phosphonium salts, such as $[Ph_4P]^+[BF_4]^-$ (CSA = 29 ppm),[27c] is in the range of 15–40 ppm while for the analogous phosphines, e.g. PPh_3 (CSA = 60 ppm), the CSA usually spans from 50–70 ppm.[10] These values confirm that partial quaternization can in principle contribute to the CSA reduction of the adsorbed species. Phosphine oxides display a much larger CSA in ^{31}P MAS NMR of 150–200 ppm, like for $OPPh_3$ (CSA = 200 ppm),[63] but when comparing this to the corresponding alkoxyphosphonium salts the CSA decreases to the range of 70–120 ppm, as seen for $[EtOPPh_3]^+[BF_4]^-$ (CSA = 74 ppm).[27c] Therefore, even for adsorbed phosphine oxides the partial quaternization effect can play a role in the CSA reduction and it might be envisioned as hydrogen bonding of the P=O groups with surface silanol protons to form P=O···HOSi assemblies. In other systems where the

O atom of a phosphine oxide is hydrogen bonding to H_2O_2, it is known that the bond order decreases, as confirmed by IR spectroscopy,[63] indicating the environment around the P nucleus is becoming "more quaternized".

The translational mobility across the surface inside the pores of the silica would be expected to have a significant role in the CSA reduction because it leads to a nearly isotropic motion. In case this motion is fast enough, it reduces the CSA by averaging out the different chemical shifts obtained from immobile solid samples. The mobility of substances on silica has been proven by multiple dry grinding experiments. A recent publication from the Bluemel group showed that ferrocene and chromocene were both able to adsorb onto the support from the solid state by just grinding the metallocenes with silica.[61] The only way for the adsorption to take place without a solvent is for the solids to "melt" onto the surface with the molecules moving away from the crystallite site and into the pores, hereby getting evenly distributed on the silica and forming a monolayer. For these adsorbed metallocenes there was also a reduction of the CSA in ^{1}H and ^{13}C MAS NMR signals, which occurs because of the fast, isotropic mobility of the compounds on the silica surface.[61] Furthermore, the adsorption of phosphines[10] and phosphine oxides (see Chapter III) onto silica by dry grinding has been performed as well. In both cases there was the same reduction in the CSA that was seen by the impregnation method, indicating these compounds must exhibit mobility on silica to move across the support and be adsorbed. In addition, HRMAS measurements (Chapter III) show that solvent is able to mobilize the adsorbed species and lead to an even further CSA reduction. However, since the phosphine oxides keep interacting with the support as seen by the ^{31}P MAS NMR chemical shift, they must be displaying increased translational mobility on the surface.

To examine the contributions of partial quaternization and translational mobility

to the CSA reduction, a molecule bearing multiple phosphine substituents is desired. Hereby, at least one of the P containing groups should not be able to attach to a surface, due to geometry restraints. In this way the P nuclei are all held together in one molecule, so the translational mobility on silica will be the same for all P containing groups. Therefore, the different appearance of their ^{31}P MAS NMR signals should only be due to the different degree of quaternization. Only the phosphine groups that are able to interact with the support will potentially undergo some degree of quaternization. Therefore, by comparing the CSA values of the different signals one can determine how much of the CSA reduction occurs due to quaternization by interacting with the silica surface. This approach had first been applied in the adsorption of bidentate phosphines, such as $Ph_2P(CH_2)_2PPh_2$, on silica, but unfortunately both phosphine groups could be adsorbed giving rise to only one ^{31}P MAS signal.[6] Even when employing more rigid spacers between the phosphines, like in the case of $Ph_2P(p\text{-}C_6H_4)PPh_2$, the molecule could lay flat on the surface leading to adsorption of both P nuclei.[10]

The adsorption of tetraphosphine scaffolds with tetraphenylelement cores, the phosphine analogs of the phosphine oxides **9–11**, was then attempted because their tetrahedral geometry and rigid nature ensured that not all of the four phosphine groups could be adsorbed at the same time. However, the rigid scaffold did not provide the necessary geometry for the lone pairs on P to interact with the silica surface.[10] On the other hand, the phosphine oxides **9** and **11** were able to be adsorbed and showed two distinct signals as anticipated in the ^{31}P MAS spectra. One signal was attributed to the adsorbed phosphine oxide groups, the other to the group pointing away from the surface (Chapter III). There was a noticeable overall reduction of the CSA of both signals as compared to that of the polycrystalline material, but the two different CSA parameter sets could not be obtained because the signals overlapped. Without being able to

deconvolute the spectra and determine the CSA values for the individual signals, unfortunately no quantitative information about the contributions to the CSA reduction could be accessed (Chapter III).

The cage compounds **I**–**III** only have two P nuclei in each molecule, so the separation of the ^{31}P MAS signals from the adsorbed and not adsorbed phosphine oxide groups may be more facile. As described in Chapter I, the large diphosphine cage **1** with 14 CH_2 groups in each alkyl chain has already been adsorbed on silica. In this case due to the large size of the cage, the molecule was able to reorient on the silica surface resulting in the adsorption of both phosphine groups in a parachute-type manner.[10] The double adsorption was evident by a single signal at –29.6 ppm in the ^{31}P MAS spectrum, which is shifted downfield from that of the polycrystalline material (δ = –38.6 ppm).[10] At this point it is also important to note that the CSA was not reduced when going from the polycrystalline material (CSA = 10 ppm) to the adsorbed species (CSA = 12 ppm). The reason for this is that the starting CSA of the polycrystalline material was already rather small, and the loss of crystallinity upon adsorption increased the residual linewidth.

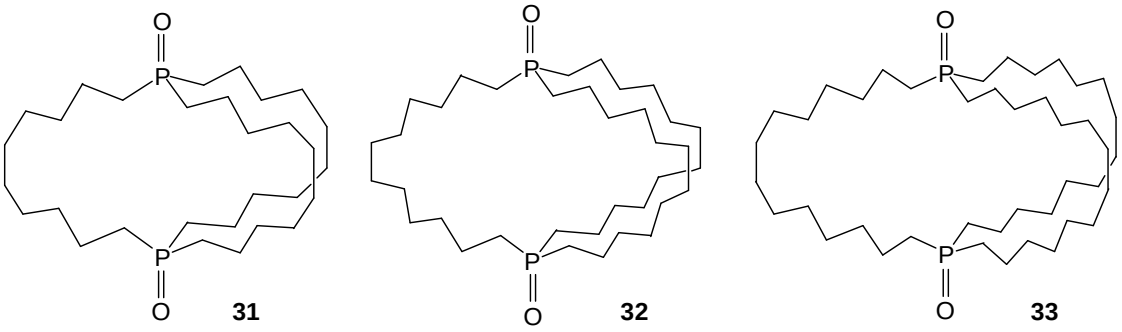

Figure 5.1. Diphosphine dioxide cages **31**–**33** for adsorption studies.

Ideally, cages of a smaller size would be more applicable for the adsorption experiments because they would not be able to rearrange on the silica and form a parachute-type compound. This was our original motivation in utilizing the Fe gyroscopes to form diphosphine cages **I** or diphosphine dioxide cages **III** with 10, 12, and 14 CH_2 groups in each of the alkyl chains (see Chapter IV). The synthesis of this class of diphosphine dioxide cages was successful for the cages **31**–**33** (Figure 5.1) as described in Chapter IV. The adsorption of these cages on silica has been studied extensively with ^{31}P MAS NMR spectroscopy, and the results are reported in the following section.

RESULTS AND DISCUSSION

Measurements of Polycrystalline Material

In order to determine the chemical shifts and the CSA values of the diphosphine dioxides, the ^{31}P MAS spectra of the polycrystalline materials had to be measured. Unfortunately, the smallest cage with 10 CH_2 groups in each alkyl chain (**31**) was a waxy solid. Although it has formed very small crystals from solvent evaporation, when scrapping the material off the glass to pack a rotor it became very sticky and was not a powdery solid with a melting point around 100 °C as desired for the MAS measurements. Multiple batches of the same type of material were obtained, so maybe the compound had incorporated some residual water, although it had been dried with molecular sieves,[63] or other small amounts of impurities. The compound might also have an intrinsically low melting point, like other diphosphine dioxides synthesized in the Gladysz group.[85] Furthermore, the larger cages could be washed with pentane to remove grease and organic impurities because they had very limited solubility in pentane. In the case of **31** the cage was more soluble in pentane,

and this cleaning procedure could not be applied. All of the compound was used for the adsorption experiments so as of now the measurement of the polycrystalline **31** has not been obtained, but it would be expected to display a CSA similar to that of other phosphine oxides in the range of 150–200 ppm.[63] Furthermore, the measurements of the other polycrystalline cage compounds will give us some insight about the shape of the CSA patterns and the chemical shifts of the solids.

The larger cages **32** and **33** were both polycrystalline and suitable for MAS measurements, and the ^{31}P MAS NMR spectra look similar for the two compounds. In the spectra of **32** (Figure 5.2) it is evident that there are two different species since there are clearly two distinct signals. The signal at 56.6 ppm is very narrow with a halfwidth of 0.13 kHz and a CSA of 156 ppm. All CSA values are given in Table 5.1. This signal closely resembles the CSA pattern observed for other polycrystalline phosphine oxides, such as $OPPh_3$ and $OPCy_3$,[63] and the narrow linewidth indicates that it is crystalline in nature. However, the chemical shift value is higher than typical phosphine oxides in the solid state, like $OPCy_3$ (δ = 47.3 ppm) (Chapter II), which could suggest it was some sort of H_2O or ^{t}BuO adduct. In the case of an in/out scenario, there could also be a stacking of the P=O groups, with the formation of intramolecular P=O···P=O moieties. In the Fe gyroscope **30** with the large diphosphine cage containing 14 CH_2 groups in each spoke, the P···P distance across the Fe is 4.411 Å.[15] If one of the P=O groups is pointing inward with a bond length of 1.50 Å, then the Van der Waals radii of O (1.55 Å) and P (1.95 Å) are large enough to allow for an interaction in the given space. In other words, the cage is able to rearrange and "deflate" enough to allow for the P=O···P=O group stacking in the in/out isomer of the cage. The second peak at 48.0 ppm is closer to the expected chemical shift of the phosphine oxide, but the signal is broader with a halfwidth of

0.37 kHz and it does not display any rotational sidebands signifying a drastically diminished CSA. The wideline pattern deconvolution revealed that the broad signal had a CSA of approximately 18 ppm. Due to the broad linewidth and decreased CSA, this species seems to be amorphous and it might be the water adduct of the compound.

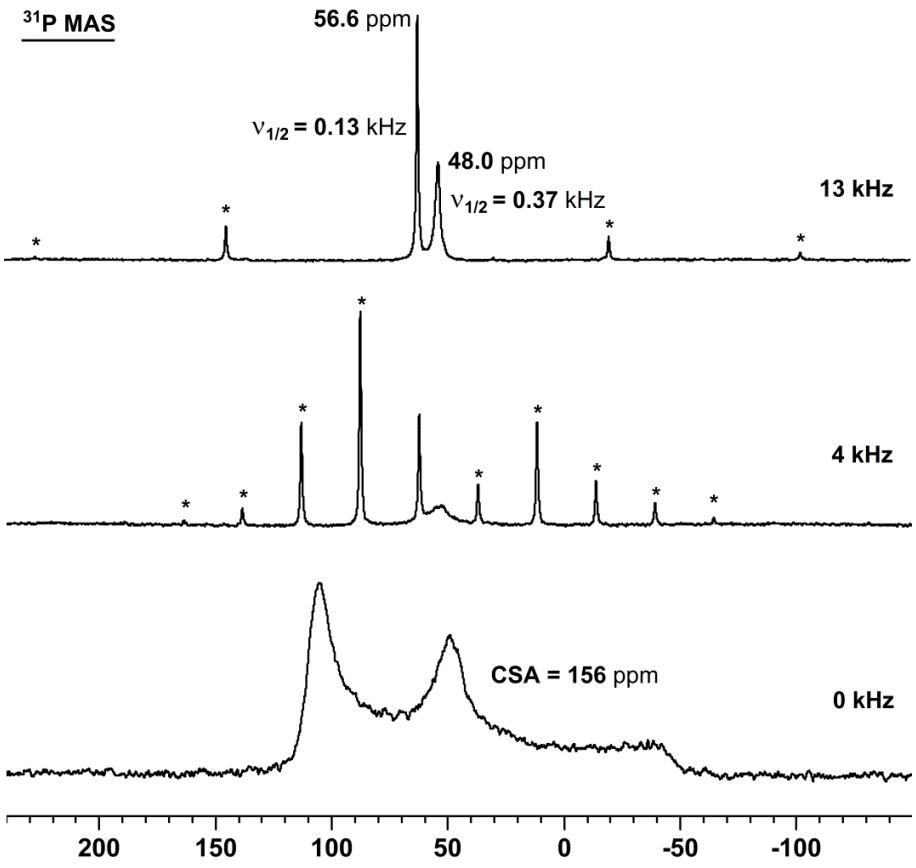

Figure 5.2. ^{31}P MAS spectra of **32** at the indicated rotational frequencies. Asteriks denote the rotational sidebands for the signal at 56.6 ppm and the CSA value corresponds to this signal.

Table 5.1. ^{31}P CSA values [ppm] for the polycrystalline signal of the diphosphine dioxide cages **32** and **33** obtained by simulation of the wideline spectra. The error margin for the values is ± 2 ppm.

Compounds	$\delta_{iso}(^{31}P)$	δ_{11}	δ_{22}	δ_{33}	CSA
32	56.6	111	104	–45	156
33	57.2	114	99	–42	156
	47.0	104	88	–51	155

The larger cage with 14 CH_2 groups in each alkyl chain (**33**) exhibited very similar features to those of **32** in the ^{31}P MAS spectra. However, there are clearly three distinguishable signals in the 4 kHz spectrum (Figure 5.3). In the 13 kHz spectrum a large signal can be seen at 57.2 ppm with a narrow halfwidth of 0.14 kHz. This polycrystalline species exhibits a large CSA of 156 ppm in the solid state. The other two signals are overlapping in the 13 kHz spectrum, but there is clearly a shoulder on the right side of the signal and at least one of the signals has a large CSA, too, because of its manifold of rotational sidebands. Spinning at a slower rate of 4 kHz allows for the two signals to be separated revealing a sharp signal at 47.0 ppm and a broad signal underneath. The signal a 47.0 ppm must be another polycrystalline component because it displays a CSA of 155 ppm. The two signals could represent two different molecules in the unit cell of the crystal lattice that have slightly different orientations giving rise to different chemical shifts. Such a large chemical shift difference is unusual, but it has precedence for cases of two magnetically inequivalent phosphine groups within one molecule.[40,83] The broad signal is again some amorphous material in the sample that could arise from water being present and hydrogen bonding to the P=O bond to form an adduct.

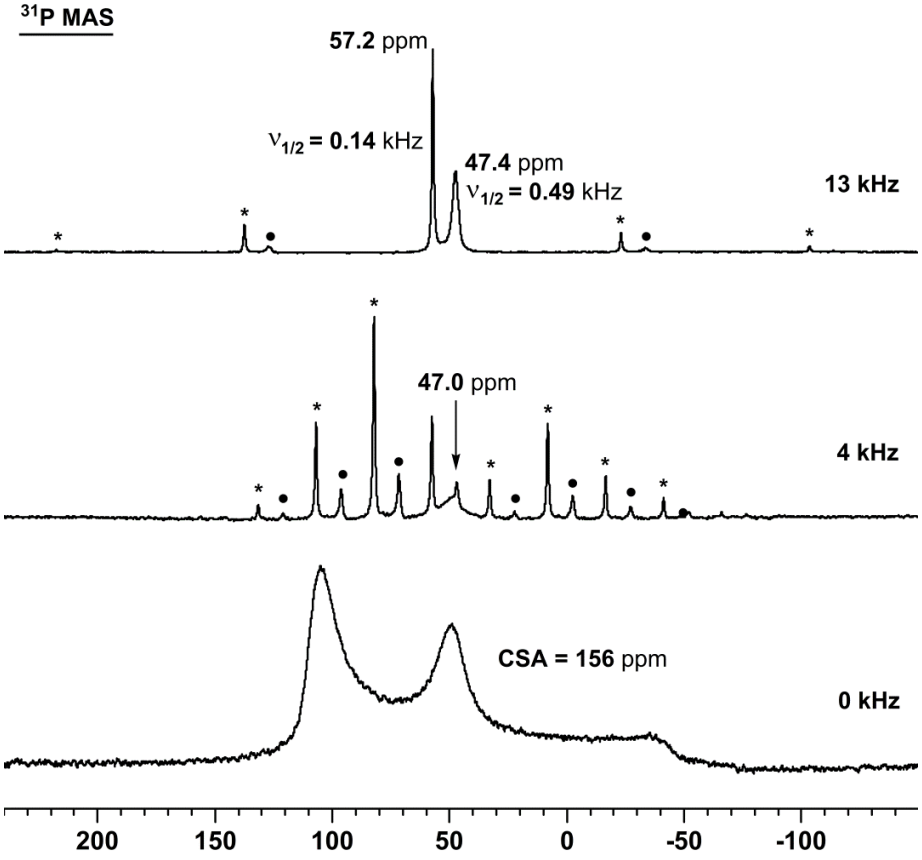

Figure 5.3. ^{31}P MAS spectra of **33** at the indicated rotational frequencies. Asteriks denote the rotational sidebands for the signal at 57.2 ppm and circles denote sidebands for signal at 47.0 ppm.

Diphosphine Dioxide Cages Adsorbed on Silica

The standard adsorption procedure described in Chapter IV was applied using toluene to dissolve the cages and then adding the solution to a slurry of dry silica in toluene. Since only small quantities of the cages **31**–**33** were available for the adsorption experiments, small amounts of silica were used but in each case it was enough material to fill a 4 mm suspension rotor for the ^{31}P MAS measurements. Dry silica was used to ensure no excess water could form adducts with the phosphine oxides and result in new signals in the ^{31}P MAS NMR spectra. Also, the dry silica can hopefully act as a

desiccant and remove any residual water around the P=O bonds, which may have contributed to the broad signal of the amorphous species in the measurements of polycrystalline materials shown above (Figure 5.2 and 5.3). The exact quantities are given in Table 5.2.

Table 5.2. Amounts for adsorption of diphosphine dioxide cages **31**–**33** on dry silica.

Dioxide Cage	**Mass of Silica** (g)	**Mass of Oxide** (g)	**Surface Coverage** (g oxide / g SiO_2)	**Surface Coverage** (mmols oxide / 100 nm^2 SiO_2)	**Surface Coverage** (molecules oxide / 100 nm^2 SiO_2)
31	0.049	0.014	0.29	0.56	45
32	0.051	0.014	0.27	0.45	36
33	0.051	0.014	0.27	0.40	32

First, the adsorption of the largest dioxide cage **33** on silica was studied because this could be compared to the adsorption of the diphosphine cage **1** described in Chapter I.[10] For cage **1** the long alkyl chains with 14 CH_2 groups were flexible and allowed the cage to reorient on the surface and form a parachute-like structure with both phosphines adsorbed on the silica. Therefore, this may be possible with the same size dioxide cage **33**.

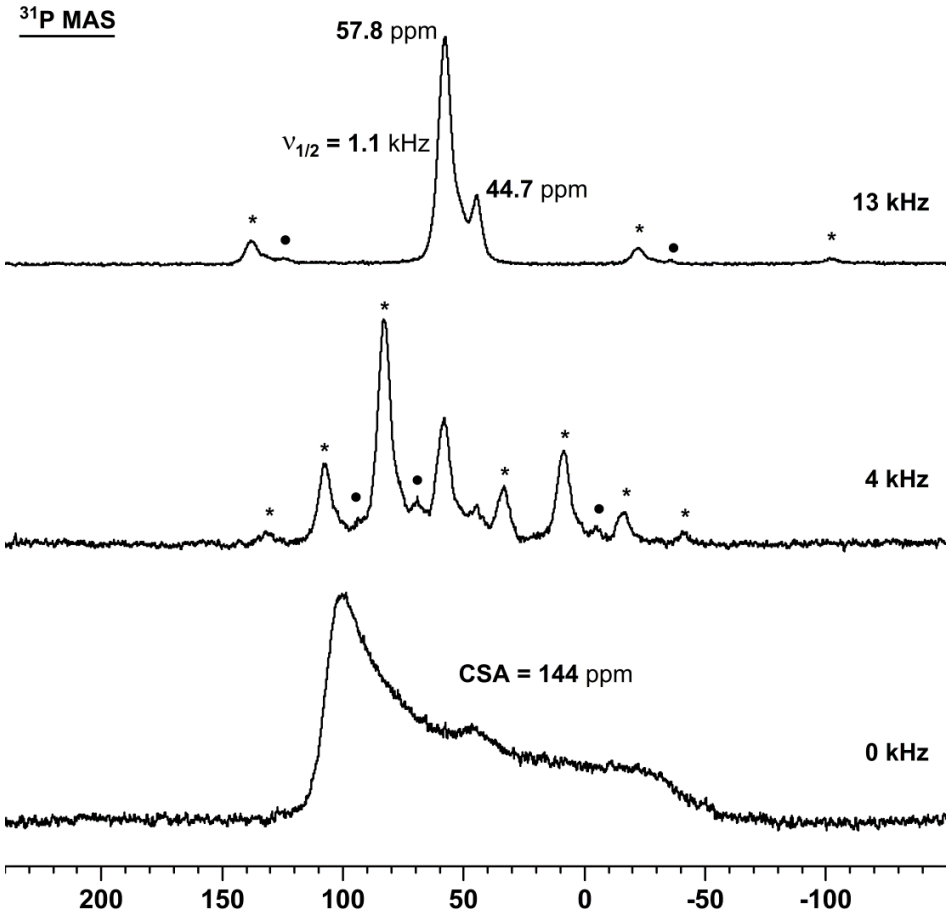

Figure 5.4. ^{31}P MAS NMR of **33** adsorbed on dry silica (**33$_{ads}$**). Asteriks denote the rotational sidebands for the signal at 57.8 ppm and circles denote sidebands for signal at 44.7 ppm.

As seen in Figure 5.4 there are two distinct signals that remain in the ^{31}P MAS spectra of **33$_{ads}$**. The larger signal at 57.8 ppm is only slightly shifted from that of the polycrystalline material (δ = 57.2 ppm), but this is in the range where one would expect the isotropic line for adsorbed trialkylphosphine oxides (see Chapter III). Therefore, it is possible that this signal stems from the dioxide cage **33** adsorbed on the surface. The signal is also broadened with a halfwidth of 1.1 kHz, so this would correspond to the adsorbed P=O groups. The other signal at 44.7 ppm is shifted upfield from the

polycrystalline substance (δ = 47.4 ppm), which is not indicative of adsorption. This chemical shift change may be because the third broad signal has significantly diminished in the spectra of the adsorbed species. The broad signal is still visible in the wideline spectrum as seen by a small bump on top of the spectrum at ca. 45 ppm (Figure 5.4), but it is present in a much smaller amount. Therefore, the adsorption method was successful at removing or transforming the amorphous material, which could be explained by the water being removed and transported into the pores if it was an adduct originally. The CSA values of both signals are approximately 144 ppm (Table 5.3), which is less than that observed for the polycrystalline compound. It appears that both P=O groups were adsorbed on the silica, similar to the adsorption of the diphosphine cage **1**, and maybe some residual polycrystalline substance is on the silica support as well.

Table 5.3. CSA values [ppm] for $\mathbf{33_{ads}}$. The error margin for the values is ± 2 ppm.

$\delta_{iso}(^{31}P)$	δ_{11}	δ_{22}	δ_{33}	CSA
57.8	111	96	–33	144
44.7	100	79	–45	145

Since it appears that both sides of the large cage **33** were adsorbed, the next smallest dioxide cage **32** was adsorbed on silica ($\mathbf{32_{ads}}$) and examined by ^{31}P MAS NMR (Figure 5.5). In this case there was only one signal for $\mathbf{32_{ads}}$ at 57.9 ppm, which was shifted downfield 1.3 ppm from the polycrystalline material (δ = 56.6 ppm). Although this was only a small change in the chemical shift, the value is in expected range for adsorbed phosphine oxides (see Chapter III). The linewidth has increased from

0.13 kHz for the polycrystalline compound to 1.0 kHz for the adsorbed species, and the CSA has decreased slightly to 142 ppm, which is similar to the CSA observed for **33$_{ads}$**. The broad signal of the amorphous material seen in the measurements of the polycrystalline compound (Figure 5.2) is no longer visible in the spectra of **32$_{ads}$**, maybe due to the large residual linewidth of the dominant signal. Since only one signal is observed, both phosphine oxide groups must have been able to interact with the silica and be adsorbed.

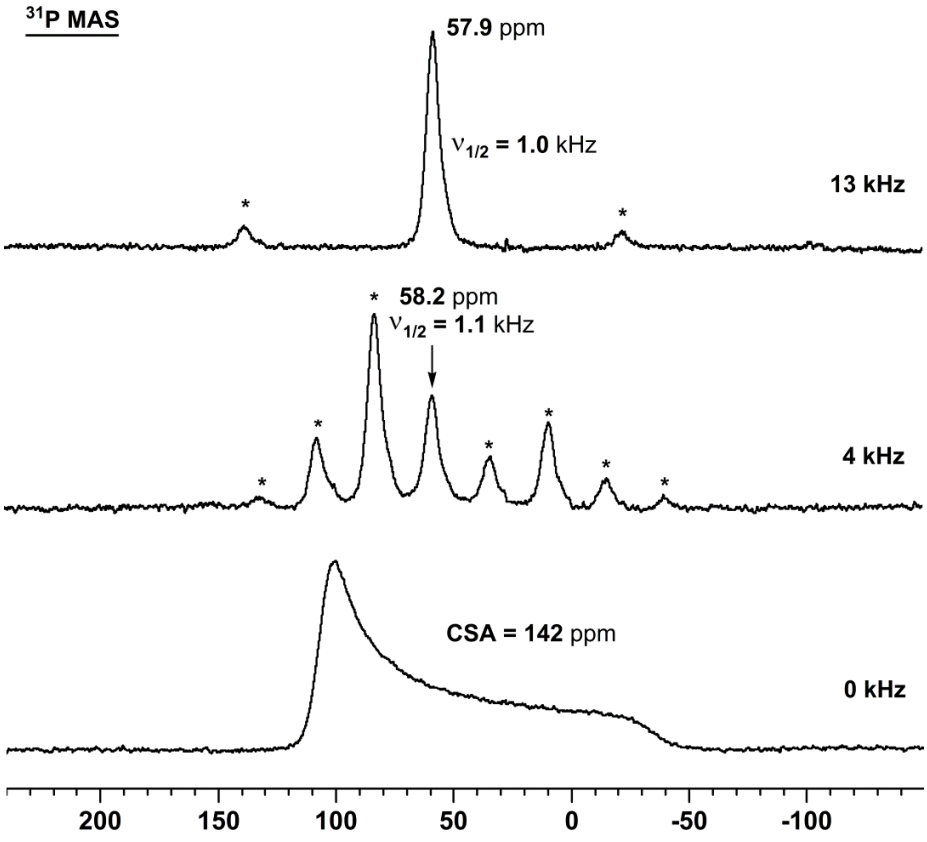

Figure 5.5. ^{31}P MAS spectra of **32** adsorbed on dry silica (**32$_{ads}$**). Asteriks denote the rotational sidebands.

Table 5.4. CSA values [ppm] for $\mathbf{32_{ads}}$. The error margin for the values is ± 2 ppm.

$\delta_{iso}(^{31}P)$	δ_{11}	δ_{22}	δ_{33}	CSA
57.9	108	101	–34	142

With both P=O groups adsorbing on the surface, it was necessary to study a smaller cage size. Adsorption of the smallest available diphosphine dioxide cage **31** was performed using dry silica to obtain $\mathbf{31_{ads}}$, and in this case some very interesting features were seen in the ^{31}P MAS spectra (Figure 5.6). There is only one signal at 56.0 ppm observed in the spectrum measured at 13 kHz, but it is much broader ($\nu_{1/2}$ = 1.7 kHz) than for the other adsorbed cages, $\mathbf{32_{ads}}$ and $\mathbf{33_{ads}}$. This could be an indication that two different signals are overlapping with the isotropic lines having approximately the same chemical shifts. The spectrum of the sample rotated at 4 kHz shows a signal with a large CSA, but this is still significantly smaller than the CSA observed for the other two adsorbed cages. Furthermore, the CSA pattern is much different with the isotropic line being the highest peak in the spectrum (Figure 5.6). This would again indicate two signals were overlapping, one with a CSA pattern similar to other phosphine oxides and one with a pattern like that of the adsorbed monodentate phosphine oxides (see Chapter III).

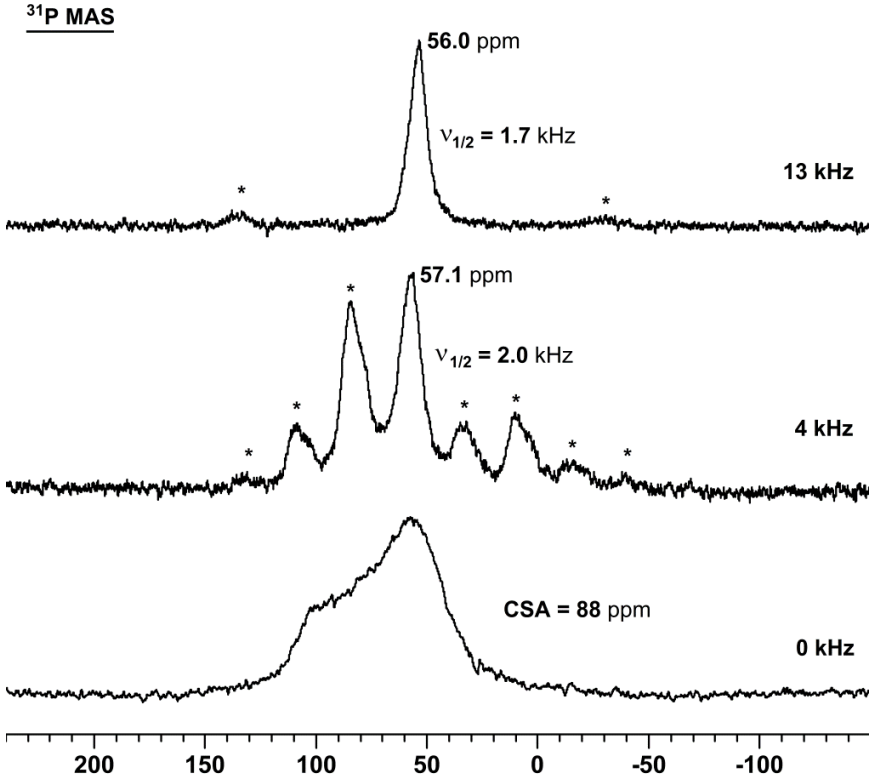

Figure 5.6. ^{31}P MAS NMR of **31** adsorbed on dry silica (**31**$_{ads}$). Asteriks denote the rotational sidebands.

The largest CSA value that can be calculated from the wideline spectrum at 0 kHz is approximately 88 ppm (Table 5.5). This is much less than typical polycrystalline phosphine oxides (CSA = ~200 ppm, Chapter II) and less than the other adsorbed dioxide cages **32**$_{ads}$ and **33**$_{ads}$ (142–145 ppm). This signal with the largest CSA for **31**$_{ads}$ (Figure 5.6) stems from the P=O group that is pointing upward and not interacting with the silica surface because it only displays reduction in the CSA due to translational mobility on the support. Being that there is no data from the measurement of the polycrystalline cage **31**, we must compare to the CSA values of the other dioxide cages **32** and **33**, which were both approximately 156 ppm. Therefore, for **31**$_{ads}$ the CSA

reduction for the P=O group pointing away from silica is 68 ppm, which again is due to the translational mobility component. If only one side of the cage is adsorbed, it would be assumed that the mobility is similar to that of monodentate phosphine oxides (Chapter III) on silica. This is evidenced by a much smaller CSA for the more mobile $\mathbf{3_{ads}}$ on the surface, as compared to the CSA of the other adsorbed cages, which allow for much less mobility due to the two P=O groups potentially pulling in opposite directions.

The second signal for $\mathbf{31_{ads}}$ in Figure 5.6 has an even smaller CSA, and this signal can be assigned to the P=O group interacting with the silica surface. In that case, the larger CSA reduction is due to both translational mobility and to the partial quaternization effect. It is unfortunately difficult to determine the CSA of the other signal because both signals overlap in the spectra at different rotational frequencies and cannot easily be deconvoluted in the wideline spectrum. Line fitting analysis (Figure 5.7), assuming the second signal appears symmetric around the isotropic line and is therefore the highest peak of the wideline pattern, reveals the CSA of this signal to be approximately 32 ppm (Table 5.5). This would mean the CSA of the second signal is reduced overall by about 124 ppm from the CSA values of the polycrystalline cages (156 ppm). It is also reduced 36 ppm more than the other signal of $\mathbf{31_{ads}}$. This additional 36 ppm reduction in the CSA is attributed to the partial quaternization effect because this P=O group is interacting with the support and has the same translational mobility, hence the same CSA reduction due to mobility (68 ppm), as the other P=O group of the cage.

The signals of the other two adsorbed cages, $\mathbf{32_{ads}}$ and $\mathbf{33_{ads}}$, showed only minor CSA reductions (12–14 ppm) due to the partial quaternization effect, which is less than what was observed for $\mathbf{31_{ads}}$. However, these results coincide with the findings for the adsorption of the large diphosphine cage **1** which actually showed an increase in the CSA of 4 ppm when both phosphines of the cage were adsorbed on the silica surface.[10]

For the larger cages, having both P=O groups adsorbed leads to decreased translational mobility because both adsorbed P=O moieties of the molecule might hinder each other's progress on the surface.

Table 5.5. CSA values [ppm] for $\mathbf{31_{ads}}$. The error margin for the values is ± 3 ppm.

$\delta_{iso}(^{31}P)$	δ_{11}	δ_{22}	δ_{33}	CSA
56.0	112	102	26	88
57.9	71	56	39	32

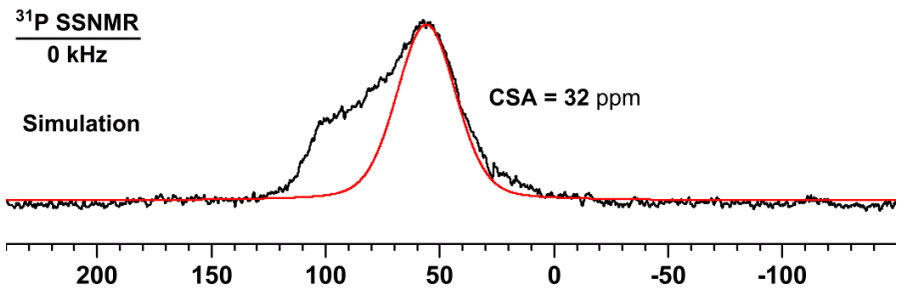

Figure 5.7. Simulation ^{31}P wideline spectrum of **31** adsorbed on dry silica ($\mathbf{31_{ads}}$).

To investigate $\mathbf{31_{ads}}$ in more detail, the ^{31}P CP/MAS NMR was measured as well. The cross-polarization method for signal enhancement works by transferring the magnetization of the surrounding protons to the nucleus being measured, thereby giving rise to a more intense signal. However, for the magnetization transfer to be effective, the compound must be static, so mobile species are not observed in the CP/MAS NMR spectrum. For $\mathbf{31_{ads}}$, the ^{31}P CP/MAS NMR shows only one signal at 59.5 ppm (Figure

5.8), which is shifted downfield from the signal of $\mathbf{31_{ads}}$ seen in the 4 kHz MAS spectrum (57.1 ppm, Figure 5.6). More importantly, the signal shape is much different for the CP/MAS NMR indicating it is only a measurement of the less mobile species and proving there are two signals overlapping in the ^{31}P MAS spectra in Figure 5.6.

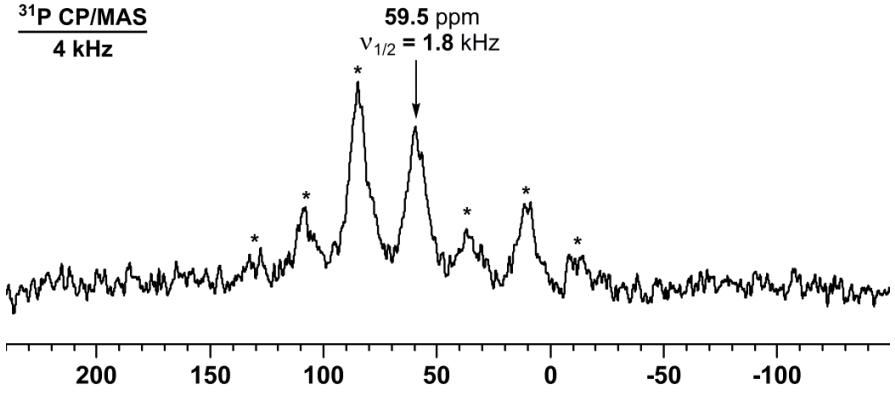

Figure 5.8. ^{31}P CP/MAS NMR of **31** adsorbed on dry silica ($\mathbf{31_{ads}}$).

To confirm adsorption was taking place, the ^{31}P HRMAS NMR spectrum of $\mathbf{31_{ads}}$ was measured with THF as the solvent (Figure 5.9). There were two signals present similar to what was seen for the adsorbed tetraphosphine tetroxide with the tetraphenylstannane core (Chapter III). The signal at 52.5 ppm most likely stems from the adsorbed species while the signal at 49.3 ppm can be attributed to the leached diphosphine dioxide cage **31**. THF will cause slight changes in the chemical shift values, which is why the adsorbed component has a lower $\delta(^{31}P)$ value than in the MAS spectrum. Unfortunately, due to the mobilizing effect of the solvent no CSA information can be obtained from the HRMAS spectrum, but it does indeed confirm that the diphosphine dioxide cage **31** is adsorbed on silica.

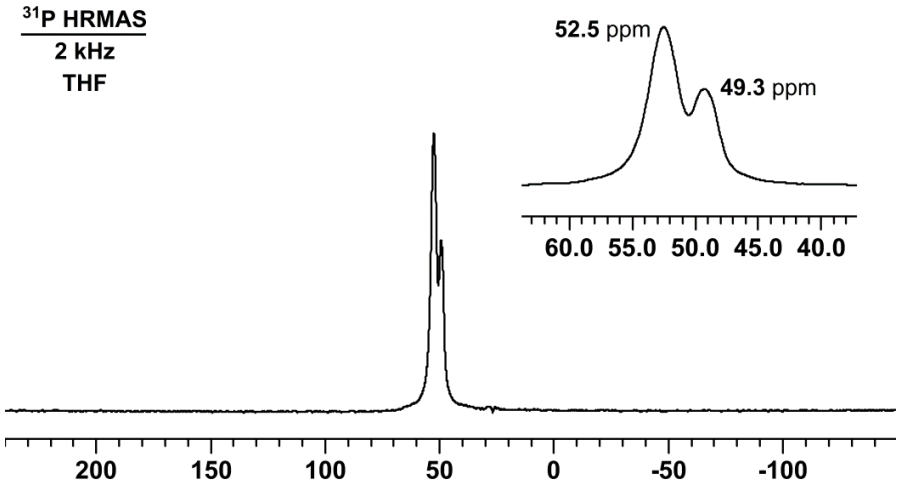

Figure 5.9. ^{31}P HRMAS spectrum of $\mathbf{31}_{\mathbf{ads}}$ in THF.

CONCLUSION

The adsorption of the diphosphine dioxide cages **31**–**33** was carried out in toluene using dry silica. The larger cages **32** and **33** showed predominantly one signal indicating both sides of the cages were interacting with the silica surface. This led to a minor reduction of the CSA values of 12–14 ppm when going from the polycrystalline material to the adsorbed species. The smallest cage **31** on silica showed two overlapping signals with unique sets of CSA values. The larger CSA of 88 ppm was assigned to the signal of the P=O group pointing away from the support, so the CSA reduction with respect to the polycrystalline compound (CSA = ~156 ppm) was solely due to the translational mobility of the cage across the silica surface. The other signal had a CSA of approximately 32 ppm, so this additional reduction of 36 ppm can then only be due to the partial quaternization effect. The smallest cage was successful at displaying two different signals for the adsorbed and not adsorbed P=O groups, and studies of even smaller cages will be interesting to confirm these results.

EXPERIMENTAL

(a) General procedures

All diphosphine dioxide cages **31**–**33** were synthesized according to the procedures discussed in the Experimental section of Chapter IV. The dioxide cages were dried with molecular sieves and stored under nitrogen, but the transfer of the compounds into the reaction vessels for the adsorption experiments was undertaken in air. Chemicals are treated as follows: Toluene (Mallinckrodt Chemicals, ACS grade) and THF (Aldrich, ACS grade 99+%) are distilled from Na/benzophenone; CH_2Cl_2 (Mallinckrodt Chemicals, HPLC grade); C_6D_6 (Cambridge Isotope Laboratories) and $CDCl_3$ (Aldrich) are dried over molecular sieves; 3 Å molecular sieves (composition of Na_2O, K_2O, MgO, SiO_2, and Al_2O_3, EMD Chemical Inc.) are activated by heating in vacuum at 150 °C for 6 hours; silica gel (EMD, 60 Å) and filter paper (Whatman) are used as received. The dry silica gel (Merck, 40 Å) was dried at 300 °C for 6 days

The ^1H, $^{13}C\{^1H\}$, and $^{31}P\{^1H\}$ NMR spectra of liquids are recorded on a 500 MHz Varian spectrometer at 499.70, 125.66, and 202.28 MHz and referenced as follows: ^1H NMR, residual C_6D_5H (7.15 ppm) and $CHCl_3$ (7.26 ppm); ^{13}C NMR, internal C_6D_6 (128.02 ppm) and $CDCl_3$ (77.00 ppm); ^{31}P NMR, capillary filled with $ClPPh_2$ (81.92 ppm) centered in the NMR tube. The ^{31}P solid-state NMR spectra were recorded on a 400 MHz Bruker Avance widebore NMR spectrometer equipped with a 4 mm broadband probehead and ZrO_2 rotors. The polycrystalline substances were densely packed into the rotors. The chemical shifts were referenced with polycrystalline $(NH_4)H_2PO_4$ (+0.81 ppm) as the external standard. A single pulse program with ^1H high-power decoupling was applied, and typically about 3000 scans with a pulse delay of 10 s were sufficient to obtain a signal while more scans, about 10000–20000, generated a good signal-to-noise ratio. The pulse length was 2.5 μs at a power

level of 6.60 dB. Simulations of the solid-state NMR spectra were performed using WSolids, a program by K. Eichele. Typically using the Herzfeld-Berger method, the rotational speed, δ_{iso}, estimated CSA span, and estimated skew are entered into the program and a simlated spectrum is generated. Then by changing the CSA span the intensity of the simulated spectrum will match better with the experimental spectrum, and once good overlap is achieved the δ_{11}, δ_{22}, and δ_{33} values can be determined by changing to the standard mode. These values are compared with the experimental wideline spectrum to ensure there is a good fit. Also, the δ values can be applied to simulate the wideline pattern or another spectrum at a different rotational frequency to confirm the simulation is valid. Additional line fitting analysis was performed using MestRec and the halfwidth of the signal was adjusted to match the experimental spectrum.

(b) Procedures for the adsorption studies

*Representative procedure for adsorption of the diphosphine dioxide cages **31–33***

The standard adsorption procedure is applied using dry silica (0.049 g) and the small dioxide cage **31** (0.014 g, 0.027 mmol). The surface loading is maximized by using the smallest quantity of silica needed to fill a 4 mm suspension rotor. The cage **31** is dissolved in toluene (5 mL) in a glass vial. This solution is transferred to a Schlenk flask containing a slurry of silica in toluene (5 mL). The vial in rinsed (2 x 2 mL) with toluene and this is added to the Schlenk flask via pipette. The mixture is stirred at room temperature for 12 h to facilitate the adsorption process. With a low loading initially applied to the surface, the solvent is simply removed *in vacuo* to ensure all of the diphosphine dioxide cage **31** will remain on the silica support. The sample is then analyzed by ^{31}P MAS and HRMAS NMR spectroscopy to determine

if adsorption occurred as described above in the Results and Discussion section. The surface loadings of all of the cages **31**–**33** are given in Table 5.2.

CHAPTER VI

CONCLUSION

The primary goal of this research is to investigate surface science phenomena and adsorption processes. The adsorption of phosphines and phosphine oxides on oxide supports has been studied for decades in relation to probing surface acidity, but in the Bluemel group the adsorption of phosphines led to some unique observations in the solid-state ^{31}P NMR spectra. Namely, the signals of adsorbed phosphines displayed a significant reduction in the CSA as compared to those of the polycrystalline materials. This reduction is attributed to the interplay of two main factors, the translational mobility of the compound across the silica surface and the partial quaternization of the phosphine due to interactions with the support. In order to understand how much each factor contributes to the reduction of the CSA, a new probe molecule containing two equivalent P nuclei has been targeted. Being that the P nuclei would be bound within the same molecule, they would exhibit the same translational mobility and in turn, the same reduction in the CSA due to the mobility influence. Furthermore, assuming only one of the phosphine groups in the molecule could interact with the support at a given time, any further reduction in the CSA would be a result of the partial quaternization effect. Therefore, diphosphine cages (**I**) and their phosphine oxides (**II**–**III**) are ideal candidates for the adsorption studies.

Prior to adsorbing the cage compounds, the adsorption of phosphine oxides needed to be studied in detail to quantify the CSA reduction and gain a better understanding of the interaction of the P=O group with the silica support. To synthesize phosphine oxides for these model studies, a novel oxidation procedure has been developed as described in Chapter II. This technique employs H_2O_2 to oxidize the

phosphines quantitatively, but this results in the formation of H_2O_2 adducts of the phosphine oxides, in which the H_2O_2 is attached to the oxygen atom of the P=O bond by hydrogen bonds. The decomposition of these adducts has been explored extensively, and a unique method of using activated molecular sieves to break down the H_2O_2, remove the residual water, and thus yielding the clean phosphine oxides has been pioneered in this work. Full characterization of the $R_3P \cdot (H_2O_2)_x$ (R = Me, Bu, Oct, Cy, Ph, x = 0.5–1.0) adducts and their corresponding phosphine oxides by ^{31}P MAS and solution NMR, IR spectroscopy, melting point videos, and X-ray crystallography is described in Chapter II.

Having synthesized a variety of phosphine oxides, the adsorption of these model compounds on silica could be performed and this study is detailed in Chapter III. The polycrystalline phosphine oxides show a much larger CSA of approximately 200 ppm in the solid state as compared to similar phosphines (CSA = 50–70 ppm), and upon adsorption on silica the CSA of each phosphine oxide is also drastically reduced. For most of the adsorbed phosphine oxides the CSA ranges from 15–20 ppm, but for tricyclohexylphosphine oxide (**5**) the CSA remains large at 134 ppm. The monolayer surface coverages of all phosphine oxides on both wet and dry silica and under different reaction conditions have been determined. There is a correlation between the size of the compound and the amount adsorbed from solution. Leaching tests have been performed with different solvents in order to see in which solvents the phosphine oxides would remain at the silica surface and in which solvents they would wash off into solution. There is some degree of leaching in all solvents tested, including nonpolar solvents, such as toluene or pentane, but the highest degree of leaching is seen for polar solvents, such as acetone and THF. It is assumed that these solvents interact with the silica surface as well leading to a competition for adsorption sites on the surface. Pre-treatment studies of

the silica with acetone and THF have been conducted and they lead to a decrease in the surface coverages of the adsorbed phosphine oxides. Next, HRMAS NMR has been used to analyze the phosphine oxides adsorbed on silica and it shows that even in the presence of a solvent the phosphine oxides stay close to the surface and continue to interact with the support. Furthermore, in solvents that induce leaching, the HRMAS spectra show two signals, one for the adsorbed, and one for the leached phosphine oxide in the supernatant. Competition studies investigating the adsorption of phosphines versus the corresponding phosphine oxides on silica with varying degrees of dryness have been carried out. The result is a higher loading of the phosphine oxides in all cases, proving that the phosphine oxides entertain a stronger interaction with the silica surface. Furthermore, the adsorption of phosphine oxides onto silica can take place by simply grinding the dry materials together without any solvent, which demonstrates that they must have a high degree of translational mobility that allows them to "melt" onto the surface and move into the pores. Lastly, the ^{31}P T_1 times of the adsorbed phosphine oxides and phosphines have been investigated to give more insight about their mobility on silica.

The desired cage compounds **I–III** are not literature known, so they needed to be synthesized in large enough quantities to perform the adsorption studies. The most direct route is to generate the diphosphine cages (**I**) and their dioxide derivatives (**III**) from the gyroscope complexes of the Gladysz group. The large diphosphine cage **1** has been previously synthesized from a Pt gyroscope, but with the Fe gyroscope smaller cage sizes can be obtained. Therefore, a method has been developed to remove the Fe center from the gyroscope and release the empty cage. Prior to testing a variety of reactions directly on the Fe gyroscopes, several model Fe phosphine complexes have been synthesized and characterized to probe their reactivities, and this is highlighted in

Chapter IV. Suitable reagents have been combined with the Fe model compounds to determine which would yield desirable phosphine derivatives, such as the phosphine oxide, and from these experiments, three main reactions have been found to be very effective. First, oxidation with a strong oxidant, such as H_2O_2 or ^{t}BuOOH, easily converts the Fe compounds into the corresponding phosphine oxides or H_2O_2 adducts, which are easily transformed into the oxide (Chapter II). Next, protonation with a concentrated acid, like HCl, turns the Fe compounds into the $[HPR_3]^+$ phosphonium salts, which can be changed into the desired phosphines by stirring them with water and extracting the resulting phosphines with an organic solvent. Lastly, alkylation of the Fe complexes with Meerwein's salt yields the ethylphosphonium salts, but these products cannot be converted into the phosphines. Overall, the oxidation method is found to be the most successful and therefore it has been applied to the Fe gyroscopes to synthesize three diphosphine dioxide cages (**31**–**33**) in good yields.

With the cages available, their adsorption on silica could be studied. First, the ^{31}P solid-state NMR measurements of the polycrystalline materials were conducted for the two largest cages **32** and **33** to determine their chemical shifts and CSA information. The CSA of each cage is approximately 156 ppm, and the chemical shifts are around 57 ppm, which is more downfield than most other trialkylphosphine oxides. There are other signals present in the spectra of both cages around 47 ppm. For the smaller cage **32** this broad signal is some amorphous material with a small CSA, but for the larger cage **33** they are two signals in this region. One is some amorphous material, like for **32**, but the other retains a large CSA of 155 ppm, meaning it must arise from some byproduct present in the compound. The adsorption of all cages on dry silica has been performed and analyzed with ^{31}P MAS NMR. For the largest dioxide cage **33**, there are two signals present in the spectra of the adsorbed species, and both have CSA values of

approximately 144 ppm. The CSA has decreased slightly, so it is believed that both sides of the cage were able to adsorb due to its large size allowing for it to reorient on the surface and form a parachute-type structure. The next cage **32** adsorbed on silica only displays one broad signal in the ^{31}P MAS NMR with a CSA of 142 ppm, which again is indicative of both sides of the cages adsorbing on the silica. Interestingly, the smallest cage **31** shows two signals in the ^{31}P MAS NMR when adsorbed on silica, which reveals that only one side of the cage is adsorbed and the other is pointing away from the support as desired. One signal with a CSA of 88 ppm is assigned to the P=O group pointing away from the silica, and the other with a CSA of 32 ppm is for the P=O group interacting with the support. The CSA reduction for the P=O group pointing away from the surface is 68 ppm (polycrystalline CSA = ~156 ppm for other cages), and this reduction is solely due to translational mobility on the silica. The reduction in the CSA of the other signal is 56 ppm greater, corresponding to an overall reduction of 124 ppm with respect to the CSA of the polycrystalline cages, and this can be attributed to the partial quaternization effect. In future projects, these results will be compared to the data for the adsorption of smaller diphosphine and disphosphine dioxide cages with less than 10 methylene groups in their alkyl chains, and this will give more insight into how the translational mobility and partial quaternization affect the CSA.

REFERENCES

1 Pfeifer, H.; Meiler, W.; Deininger, D., NMR of Adsorbed Organic Compounds. In *Annual Reports on NMR Spectroscopy*; 1983; Vol. 15, pp 291–356.

2 (a) Hu, B.; Gay, I. D. *Langmuir* **1995**, *11*, 3845–3847. (b) Morrow, B. A.; Gay, I. D. Infrared and NMR Characterization of the Silica Surface. In *Adsorption on Silica Surfaces*; Papirer, E., Ed.; M. Dekker Inc.: New York, 2000; pp 9–33.

3 (a) Rothwell, W. P.; Shen, W. X.; Lunsford, J. H. *J. Am. Chem. Soc.* **1983**, *106*, 2452–2453. (b) Lunsford, J. H.; Rothwell, W. P.; Shen, W. *J. Am. Chem. Soc.* **1985**, *107*, 1540–1547.

4 Baltusis, L.; Frye, J. S.; Maciel, G. E. *J. Am. Chem. Soc.* **1987**, *109*, 40–46.

5 Baltusis, L.; Frye, J. S.; Maciel, G. E. *J. Am. Chem. Soc.* **1986**, *108*, 7119–7120.

6 Peng, L.; Grey C. P. *Microporous Mesoporous Mater.* **2008**, *116*, 277–283.

7 Alonso, B.; Klur, I.; Massiot, D. *Chem. Commun.* **2002**, 804–805.

8 (a) Seo, Y.; Cho, K.; Jung, Y.; Ryoo, R. *ACS Catal.* **2013**, *3*, 713–720. (b) Chu, Y.; Yu, Z.; Zheng, A.; Fang, H.; Zhang, H.; Huang, S.-J.; Lui, S.-B.; Deng, F. *J. Phys. Chem. C* **2011**, *115*, 7660–7667. (c) Kříž, J.; Dybal, J.; Makrlík, E.; Budka, J.; Vaňura, P. *J. Phys. Chem. A* **2009**, *113*, 5896–5905. (d) Hayashi, S. *Chem. Lett.* **2009**, *38*, 960–961.

9 Yerushalmi, R.; Ho, J. C.; Fan, Z.; Javey, A. *Angew. Chem. Int. Ed.* **2008**, *47*, 4440–4442.

10 Yang, Y. *Dissertation Thesis*, University of Heidelberg, **2007**.

11 Stollenz, M.; Barbasiewicz, M.; Nawara–Hultzsch, A. J.; Fiedler, T.; Laddusaw, R. M.; Bhuvanesh, N.; Gladysz, J. A. *Angew. Chem. Int. Ed*. **2011**, *50*, 6647–

6651.

12 Stollenz, M.; Bhuvanesh, N.; Reibenspies, J. H.; Gladysz, J. A. *Organometallics* **2011**, *30*, 6510–6513.

13 Skopek, K.; Barbasiewicz, M.; Hampel, F.; Gladysz, J. A. *Inorg. Chem.* **2008**, *47*, 3474–3476.

14 Nawara, A. J.; Shima, T.; Hampel, F.; Gladysz, J. A. *J. Am. Chem. Soc.* **2006**, *128*, 4962–4963.

15 Shima, T.; Hampel, F.; Gladysz, J. A. *Angew. Chem. Int. Ed.* **2004**, *43*, 5537–5540.

16 Beele, B.; Guenther, J.; Perera, M.; Stach, M.; Oeser, T.; Blümel, J. *New J. Chem*. **2010**, *34*, 2729–2731.

17 Stach, M. *Diploma Thesis*, University of Heidelberg, **2009**.

18 (a) Gladysz, J. A., Ed. *Recoverable Catalysts and Reagents*, Special Issue of *Chem. Rev*. **2002**, *102*. (b) Blümel, J. *Coord. Chem. Rev*. **2008**, *252*, 2410–2423. (c) Hartley, F. R. *Supported Metal Complexes*; D. Reidel Publ. Co.: Dordrecht, The Netherlands, **1985**. (d) DeVos, D. E.; Vankelecom, I. F. J.; Jacobs, P. A., Eds. *Chiral Catalyst Immobilization and Recycling*; Wiley-VCH: Weinheim, Germany, **2000**. (e) Rothenberg, G. *Catalysis: Concepts and Green Applications*; Wiley-VCH: Weinheim, Germany, **2008**. (f) Barbaro, P.; Liguori, F., Eds. *Heterogenized Homogeneous Catalysts for Fine Chemicals Production*; Springer Science and Business Media: Heidelberg, Germany, **2010**.

19 (a) Guenther, J.; Reibenspies, J.; Blümel, J. *Adv. Synth. Catal*. **2011**, *353*, 443–460. (b) Posset, T.; Guenther, J.; Pope, J.; Oeser, T.; Blümel, J. *Chem. Commun*. **2011**, *47*, 2059–2061.

20 (a) Boutagy, J.; Thomas, R. *Chem. Rev*. **1974**, *74*, 87–99. (b) O'Brien, C. J.; Tellez, J. L.; Nixon, Z. S.; Kang, L. J.; Carter, A. L.; Kunkel, S. R.; Przeworski, K. C.; Chass, G. A. *Angew. Chem. Int. Ed*. **2009**, *48*, 6836–6839.

21 (a) Staudinger, H.; Meyer, J. *Helv. Chim. Acta* **1919**, *2*, 635–646. (b) Gololobov, Y. G.; Zhmurova, I. N.; Kasukhin, L. F. *Tetrahedron* **1981**, *37*, 437–472.

22 Appel, R. *Angew. Chem. Int. Ed.* **1975**, *14*, 801–811.

23 (a) Barder, T. E.; Buchwald, S. L. *J. Am. Chem. Soc.* **2007**, *129*, 5096–5101. (b) Buckler, S. A. *J. Am. Chem. Soc*. **1962**, *84*, 3093–3097. (c) Burkett, H. D.; Hill, W. E.; Worley, S. D. *Phosphorus, Sulfur and Silicon Relat. Elem.* **1984**, *20*, 169–172.

24 Hayashi, S. *Anal. Sci.* **2009**, *25*, 133–136.

25 Beckett, M. A.; Brassington, D. S.; Light, M. E.; Hursthouse, M. B. *Dalton Trans.* **2001**, 1768–1772.

26 (a) Temple, R. D.; Tsuno, Y.; Leffler, J. E. *J. Org. Chem.* **1963**, *28*, 2495. (b) Copley, D. B.; Fairbrother, F.; Miller, J. R.; Thompson, A. *Proc. Chem. Soc.* **1964**, 300–301. (c) Thierbach, D.; Huber, F.; Preut, H. *Acta Crystallogr., Sect. B: Struct. Crystallogr. Cryst. Chem.* **1980**, *B36*, 974–977. (d) Kende, A. S.; Delair, P.; Blass, B. E. *Tetrahedron Lett.* **1994**, *35*, 8123–8126.

27 (a) Blümel, J. *Inorg. Chem*. **1994**, *33*, 5050–5058. (b) Yang, Y.; Beele, B.; Blümel, J. *J. Am. Chem. Soc*. **2008**, *130*, 3771–3773. (c) Sommer, J.; Yang, Y.; Rambow, D.; Blümel, J. *Inorg. Chem*. **2004**, *43*, 7561–7563. (d) Posset, T.; Rominger, F.; Blümel, J. *Chem. Mater*. **2005**, *17*, 586–595.

28 Kao, H.-M.; Chang, P.-C.; Liao, Y.-W.; Lee, L.-P.; Chien, C.-H. *Microporous Mesoporous Mater*. **2008**, *114*, 352–364.

29 (a) Ng, V. W. L.; Taylor, M. K.; Hill, L. M. R.; White, J. M.; Young, C. G. *Eur. J. Inorg. Chem.* **2010**, 3261–3269. (b) Tsai, W.; Liu, Y.-H.; Peng, S.-M.; Liu, S.-T. *J. Organomet. Chem.* **2005**, *690*, 415–421.

30 (a) Li, L.; Wang, Z.; Song, X.; Sun, S. *Spectrochim. Acta, Part A* **2009**, *72*, 816–818. (b) Ben Dhia, M. T.; Sanhoury, M. A. M. K.; Owono Owono, L. C.; Khaddar, M. R. *J. Mol. Struct.* **2008**, *892*, 103–109. (c) Tolis, E. I.; Vallianatou, K. A.; Andreadaki, F. A.; Kostas, I. D. *Appl. Organomet. Chem.* **2006**, *20*, 335–337.

31 (a) Popovici, C.; Fernandez, I.; Ona-Burgos, P.; Roces, L.; Garcia-Granda, S.; Ortiz, F. L. *Dalton Trans.* **2011**, *40*, 6691–6703. (b) Miyata, K.; Hasegawa, Y.; Kuramochi, Y.; Nakagawa, T.; Yokoo, T.; Kawai, T. *Eur. J. Inorg. Chem.* **2009**, 4777–4785.

32 (a) Ackermann, L.; Barfüßer, S.; Kornhaaß, C.; Kapdi, A. R. *Org. Lett.* **2011**, *13*, 3082–3085. (b) Ackermann, L.; Kapdi, A. R.; Schulzke, C. *Org. Lett*. **2010**, *12*, 2298–2301.

33 Hilliard, C.; Gladysz, J. A.; Blümel, J. *Chem. Mater*. **2013**, *in preparation*.

34 Rauhut, M. M.; Currier, H. A. *J. Org. Chem.* **1961**, *26*, 4626–4628.

35 (a) Peng, W.; Shreeve, J. M. *J. Fluorine Chem.* **2005**, *126*, 1054–1056. (b) Macikenas, D.; Skrzypczak-Jankun, E.; Protasiewicz, J. D. *J. Am. Chem. Soc.* **1999**, *121*, 7164–7165. (c) Porcel, S.; Bouhadir, G.; Saffon, N.; Maron, L.; Bourissou, D. *Angew. Chem. Int. Ed.* **2010**, *49*, 6186–6189. (d) Tucci, G. C.; Donahue, J. P.; Holm, R. H. *Inorg. Chem*. **1998**, *37*, 1602–1608. (e) Berg, J. M.; Holm, R. H. *J. Am. Chem. Soc*. **1985**, *107*, 925–932.

36 (a) Duncan, T. M. *A Compilation of Chemical Shift Anisotropies*; Farragut Press: Chicago, IL, **1990**. (b) Fyfe, C. A. *Solid-State NMR for Chemists*; C.F.C. Press:

Guelph, Canada, **1983**. (c) Duer, M. J. *Introduction to Solid-State NMR Spectroscopy*; Blackwell Publishing: Oxford, **2004**. (d) Reinhard, S.; Blümel, J. *Magn. Reson. Chem*. **2003**, *41*, 406–416. (e) Mason, J., Ed., *Multinuclear NMR*; Plenum Press: New York, London, **1987**.

37 Blümel, J.; Herker, M.; Hiller, W.; Köhler, F. H. *Organometallics* **1996**, *15*, 3474–3476.

38 (a) Bemi, L.; Clark, H. C.; Davies, J. A.; Fyfe, C. A.; Wasylishen, R. E. *J. Am. Chem. Soc*. **1982**, *104*, 438–445. (b) Clayden, N. J.; Dobson, C. M.; Lian, L.-Y.; Smith, D. J. *J. Magn. Reson.* **1986**, *69*, 476–487. (c) Robert, J. B.; Wiesenfeld, L. *Mol. Phys*. **1981**, *44*, 319–327.

39 (a) Spek, A. L. *Acta Crystallogr., Sect. C: Cryst. Struct. Commun.* **1987**, *C43*, 1233–1235. (b) Brock, C. P.; Schweizer, W. B.; Dunitz, J. D. *J. Am. Chem. Soc.* **1985**, *107*, 6964–6970.

40 Bogza, M.; Oeser, T.; Blümel, J. *J. Organomet. Chem*. **2005**, *690*, 3383–3389.

41 Alekseev, V. I.; Gatilov, Yu. V.; Polyanskaya, T. M.; Bakakin, V. V.; Dyadin, Yu. A.; Gaponenko, L. A. *Zh. Strukt. Khim*. **1982**, *23*, 86–91.

42 Davies, J. A.; Dutremez, S.; Pinkerton, A. A. *Inorg. Chem*. **1991**, *30*, 2380–2387.

43 Mantina, M.; Chamberlin, A. C.; Valero, R.; Cramer, C. J.; Truhlar, D. G. *J. Phys. Chem. A.* **2009**, *113*, 5806–5812.

44 Busing, W. R.; Levy, H. A. *J. Chem. Phys.* **1965**, *42*, 3054–3059.

45 Larkin, P. *Infrared and Raman Spectroscopy, Principles and Spectral Interpretation*; Academic Press, Elsevier, **2011**.

46 (a) Daasch, L. W.; Smith, D. C. *J. Chem. Phys.* **1951**, *19*, 22–25. (b) Aksnes, G.; Brudvik, L. J. *Acta Chem. Scand.* **1963**, *17*, 1616–1622. (c) Schneider, W.; Thiel, W.; Komornicki, A. *J. Phys. Chem.* **1988**, *92*, 5611–5619.

47 Howell, G. V.; Williams, R. L. *J. Chem. Soc. A* **1968**, 117–118.

48 Hasnat, M. A.; Rahman, M. M.; Borhanuddin, S. M.; Siddiqua, A.; Bhadur, N. M.; Karim, M. R. *Catal. Commun*. **2010**, *12*, 286–291.

49 (a) Iler, R. K. *The Chemistry of Silica*; John Wiley: New York, NY **1979**. (b) Scott, R. P. W. *Silica Gel and Bonded Phases*; John Wiley and Sons: New York, NY **1993**.

50 Burg, A. B.; McKee, W. E. *J. Am. Chem. Soc.* **1951**, *73*, 4590–4591.

51 Kudryavtseva, L. I. *Zh. Obs. Khim.* **1990**, *60*, 74–79.

52 Feshchenko, N. G.; Mazepa, I. K.; Gorbatenko, Zh. K.; Mackovetskii, Yu. P.; Kukhar, V. P.; Kirsanov, A. V. *Zh. Obs. Khim.* **1969**, *39*, 1219–1223.

53 Burger, A.; Dawson, N. D. *J. Chem. Soc*. **1951**, *16*, 1250–1254.

54 (a) Merckle, C.; Blümel, J. *Chem. Mater*. **2001**, *13*, 3617–3623. (b) Merckle, C.; Blümel, J. *Topics Catal*. **2005**, *34*, 5–15. (c) Reinhard, S.; Soba, P.; Rominger, F.; Blümel, J. *Adv. Synth. Catal*. **2003**, *345*, 589–602.

55 Nishimura, T.; Onoue, T.; Ohe, K.; Uemura, S. *J. Org. Chem*. **1999**, *64*, 6750–6755.

56 Fetouaki, R.; Seifert, A.; Bogza, M.; Oeser, T.; Blümel, J. *Inorg. Chim. Acta* **2006**, *359*, 4865–4873.

57 APEX2 "Program for Data Collection on Area Detectors" BRUKER AXS Inc., 5465 East Cheryl Parkway, Madison, WI 53711-5373 USA.

58 SADABS, Sheldrick, G.M. "Program for Absorption Correction of Area Detector Frames", BRUKER AXS Inc., 5465 East Cheryl Parkway, Madison, WI 53711-5373 USA.

59 Sheldrick, G. M. *Acta Cryst.* **2008**, *A64*, 112–122.

60 Gao, W.; Dickinson, L.; Grozinger, C.; Morin, F. G.; Reven, L. *Langmuir* **1996**, *12*, 6429–6435.

61 Cluff, K. J.; Schnellbach, M.; Hilliard, C. R.; Blümel, J. *J. Organomet. Chem.* **2013**, *744*, 119–124.

62 Hazut, O.; Agarwala, A.; Amit, I.; Subramani, T.; Zaidiner, S.; Rosenwaks, Y.; Yerushalmi, R. *ACS Nano* **2012**, *6*, 10311–10318.

63 Hilliard, C. R.; Bhuvanesh, N.; Gladysz, J. A.; Blümel, J. *Dalton Trans.* **2012**, *41*, 1742–1754.

64 Alvarez, S. *Dalton Trans.* **2013**, *42*, 8617–8636.

65 Engelhardt, L. M.; Raston, C. L.; Whitaker, C. R.; White, A. H. *Aust. J. Chem.* **1986**, *39*, 2151–2154.

66 Dearie, C. M.; Dyson, R. M.; Hambley, T. W.; Lawrance, G. A.; Maeder, M.; Tannock, G. A. *Aust. J. Chem.* **1993**, *46*, 577–582.

67 Bandoli, G.; Bortolozzo, G.; Clemente, D. A.; Croatto, U.; Panattoni, C. *J. Chem. Soc. A* **1970**, 2778–2780.

68 Guenther, J.; Wong, M.; Sue, H.-J.; Bremner, T.; Blümel, J. *J. Appl. Polym. Sci.* **2013**, *128*, 4395–4404.

69 Diesveld, J. W.; Menger, E. M.; Edzes, H. T.; Veeman, W. S. *J. Am. Chem. Soc.* **1980**, *102*, 7935–7936.

70 Koole, N. J.; de Koning, A. J.; de Bie, M. J. A. *J. Magn. Reson.* **1977**, *25*, 375–378.

71 Keiter, R. L.; Keiter, E. A.; Hecker, K. H.; Boecker, C. A. *Organometallics* **1988**, *7*, 2466–2469. [66]

72 (a) Brunet, J. -J.; Kindela, F. B.; Neibecker, D.; Wander, S. A.; Darensbourg, M. Y. *trans*-Tricarbonylbis(phosphine)iron(0) Complexes: One-Pot Syntheses from

Pentacarbonyliron. In *Inorganic Syntheses*; Grimes, R. N., Ed.; John Wiley & Sons, Inc.: Hoboken, NJ, 2007; Vol. 29, pp 151–156. (b) Therien, M. J.; Trogler, W. C.; Silva, R.; Darensbourg, M. Y. Bis (Phosphine) Derivatives of Iron Pentacarbonyl and Tetracarbonyl (Tri-tert-Butylphosphine) Iron (0). In *Inorganic Syntheses*; Allcock, H. R., Ed.; John Wiley & Sons, Inc.: Hoboken, NJ, 1990; Vol. 28, pp 173–179.

73 Thompson, D. T. *J. Organomet. Chem.* **1965**, *4*, 74–81.

74 Blanch, S. W.; Bond, A. M.; Colton, R. *Inorg. Chem.* **1981**, *20*, 755–761.

75 Sowa, Jr. J. R.; Zanotti, V.; Facchin, G.; Angelici, R. J. *J. Am. Chem. Soc.* **1991**, *113*, 9185–9192.

76 Li, T.; Lough, A. J.; Morris, R. H. *Chem. Eur. J.* **2007**, *13*, 3796–3803.

77 Luo, L.; Nolan, S. P. *Inorg. Chem.* **1993**, *32*, 2410–2415.

78 Tolman, C. A. *Chem. Rev.* **1977**, *77*, 313–348.

79 Hersh, W. H. *J. Chem. Educ.* **1997**, *74*, 1485–1488.

80 Battino, R.; Rettich, T. R.; Tominaga, T. *J. Phys. Chem. Ref. Data* **1983**, *12*, 163–178.

81 Olah, G. A.; McFarland, C. W. *J. Org. Chem.* **1969**, *34*, 1832–1834.

82 Tan, K. L.; Park, S.; Bergman, R. G.; Ellman, J. A. *J. Org. Chem.* **2004**, *69*, 7329–7335.

83 (a) Reinhard, S.; Behringer, K. D.; Blümel, J. *New J. Chem.* **2003**, *27*, 776–778. (b) Cluff, K.; Blümel, J. *Inorg. Chem.* **2013**, *in preparation*.

84 Howell, J. A. S.; Johnson, B. F. G.; Josty, P. L.; Lewis, J. *J. Organomet. Chem.* **1972**, *39*, 329–333.

85 Kharel, S. *Research Report*, Texas A&M University, **2013**.

APPENDIX A

CRYSTALLOGRAPHIC DATA

X-ray structure of $OPBu_3$ (3)

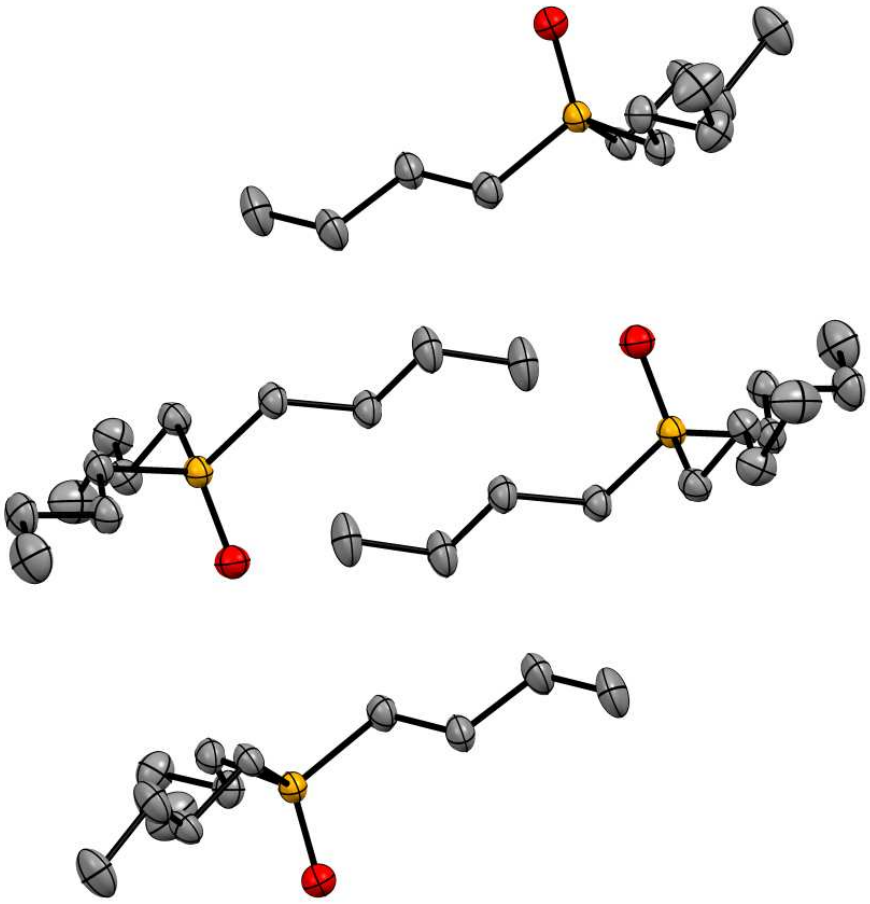

Side view

Table A-1. Crystal data and structure refinement $OPBu_3$ (**3**).

Empirical formula	$C_{12}H_{27}OP$
Formula weight	218.31
T / K	150(2)
Wavelength / Å	0.71073
Diffractometer	Bruker APEX 2
Crystal system	Monoclinic
Space group	P2(1)/c
Unit cell dimensions:	
a / Å	9.326(6)
b / Å	15.281(10)
c / Å	10.136(7)
α (°)	90
β (°)	100.548(15)
γ (°)	90
V / $Å^3$	1420.1(16)
Z	4
ρ / Mg/m^3	1.021
μ / mm^{-1}	0.168
F(000)	488
Crystal size / mm	0.15 x 0.10 x 0.07
θ range	2.22 to 27.61°
Index ranges (*h*,*k*,*l*)	–12,12; –19,19; –13,13
Reflections collected	15057
Independent reflections	3264 [R(int) = 0.0594]
Completeness to theta = 27.50°	99.6 %
Absorption correction	Semi-empirical from equivalents
Max. and min. transmission	0.9883 and 0.9752
Refinement method	Full-matrix least-squares on F^2
Data / restraints / parameters	3264 / 0 / 130
Goodness-of-fit on F^2	1.062
Final R indices [$I2\sigma(I)$]	R_1 = 0.0595, wR_2 = 0.1490
R indices (all data)	R_1 = 0.0885, wR_2 = 0.1788
Largest diff. peak / hole / e $Å^{-3}$	0.652 and –0.586

Table A-2. Bond lengths [Å] and angles [°] for $OPBu_3$ (**3**).

P(1)-O(1)	1.489(2)
P(1)-C(1)	1.797(3)
P(1)-C(5)	1.798(2)
P(1)-C(9)	1.798(2)
C(1)-C(2)	1.520(3)
C(1)-H(1A)	0.9900
C(1)-H(1B)	0.9900
C(2)-C(3)	1.518(3)
C(2)-H(2A)	0.9900
C(2)-H(2B)	0.9900
C(3)-C(4)	1.514(4)
C(3)-H(3A)	0.9900
C(3)-H(3B)	0.9900
C(4)-H(4A)	0.9800
C(4)-H(4B)	0.9800
C(4)-H(4C)	0.9800
C(5)-C(6)	1.518(3)
C(5)-H(5A)	0.9900
C(5)-H(5B)	0.9900
C(6)-C(7)	1.516(3)
C(6)-H(6A)	0.9900
C(6)-H(6B)	0.9900
C(7)-C(8)	1.506(4)
C(7)-H(7A)	0.9900
C(7)-H(7B)	0.9900
C(8)-H(8A)	0.9800
C(8)-H(8B)	0.9800
C(8)-H(8C)	0.9800
C(9)-C(10)	1.522(3)
C(9)-H(9A)	0.9900
C(9)-H(9B)	0.9900
C(10)-C(11)	1.509(3)
C(10)-H(10A)	0.9900

C(10)-H(10B)	0.9900
C(11)-C(12)	1.519(3)
C(11)-H(11A)	0.9900
C(11)-H(11B)	0.9900
C(12)-H(12A)	0.9800
C(12)-H(12B)	0.9800
C(12)-H(12C)	0.9800

O(1)-P(1)-C(1)	113.10(10)
O(1)-P(1)-C(5)	112.90(10)
C(1)-P(1)-C(5)	105.98(11)
O(1)-P(1)-C(9)	113.11(10)
C(1)-P(1)-C(9)	105.46(11)
C(5)-P(1)-C(9)	105.61(11)
C(2)-C(1)-P(1)	112.94(16)
C(2)-C(1)-H(1A)	109.0
P(1)-C(1)-H(1A)	109.0
C(2)-C(1)-H(1B)	109.0
P(1)-C(1)-H(1B)	109.0
H(1A)-C(1)-H(1B)	107.8
C(3)-C(2)-C(1)	114.0(2)
C(3)-C(2)-H(2A)	108.8
C(1)-C(2)-H(2A)	108.8
C(3)-C(2)-H(2B)	108.8
C(1)-C(2)-H(2B)	108.8
H(2A)-C(2)-H(2B)	107.7
C(4)-C(3)-C(2)	112.0(2)
C(4)-C(3)-H(3A)	109.2
C(2)-C(3)-H(3A)	109.2
C(4)-C(3)-H(3B)	109.2
C(2)-C(3)-H(3B)	109.2
H(3A)-C(3)-H(3B)	107.9
C(3)-C(4)-H(4A)	109.5
C(3)-C(4)-H(4B)	109.5

H(4A)-C(4)-H(4B)	109.5
C(3)-C(4)-H(4C)	109.5
H(4A)-C(4)-H(4C)	109.5
H(4B)-C(4)-H(4C)	109.5
C(6)-C(5)-P(1)	113.11(16)
C(6)-C(5)-H(5A)	109.0
P(1)-C(5)-H(5A)	109.0
C(6)-C(5)-H(5B)	109.0
P(1)-C(5)-H(5B)	109.0
H(5A)-C(5)-H(5B)	107.8
C(7)-C(6)-C(5)	113.9(2)
C(7)-C(6)-H(6A)	108.8
C(5)-C(6)-H(6A)	108.8
C(7)-C(6)-H(6B)	108.8
C(5)-C(6)-H(6B)	108.8
H(6A)-C(6)-H(6B)	107.7
C(8)-C(7)-C(6)	112.6(2)
C(8)-C(7)-H(7A)	109.1
C(6)-C(7)-H(7A)	109.1
C(8)-C(7)-H(7B)	109.1
C(6)-C(7)-H(7B)	109.1
H(7A)-C(7)-H(7B)	107.8
C(7)-C(8)-H(8A)	109.5
C(7)-C(8)-H(8B)	109.5
H(8A)-C(8)-H(8B)	109.5
C(7)-C(8)-H(8C)	109.5
H(8A)-C(8)-H(8C)	109.5
H(8B)-C(8)-H(8C)	109.5
C(10)-C(9)-P(1)	114.40(16)
C(10)-C(9)-H(9A)	108.7
P(1)-C(9)-H(9A)	108.7
C(10)-C(9)-H(9B)	108.7
P(1)-C(9)-H(9B)	108.7
H(9A)-C(9)-H(9B)	107.6

C(11)-C(10)-C(9)	112.47(19)
C(11)-C(10)-H(10A)	109.1
C(9)-C(10)-H(10A)	109.1
C(11)-C(10)-H(10B)	109.1
C(9)-C(10)-H(10B)	109.1
H(10A)-C(10)-H(10B)	107.8
C(10)-C(11)-C(12)	113.3(2)
C(10)-C(11)-H(11A)	108.9
C(12)-C(11)-H(11A)	108.9
C(10)-C(11)-H(11B)	108.9
C(12)-C(11)-H(11B)	108.9
H(11A)-C(11)-H(11B)	107.7
C(11)-C(12)-H(12A)	109.5
C(11)-C(12)-H(12B)	109.5
H(12A)-C(12)-H(12B)	109.5
C(11)-C(12)-H(12C)	109.5
H(12A)-C(12)-H(12C)	109.5
H(12B)-C(12)-H(12C)	109.5

X-ray structure of $(Cy_3P{=}O{\cdot}H_2O_2)_2$ (5a)

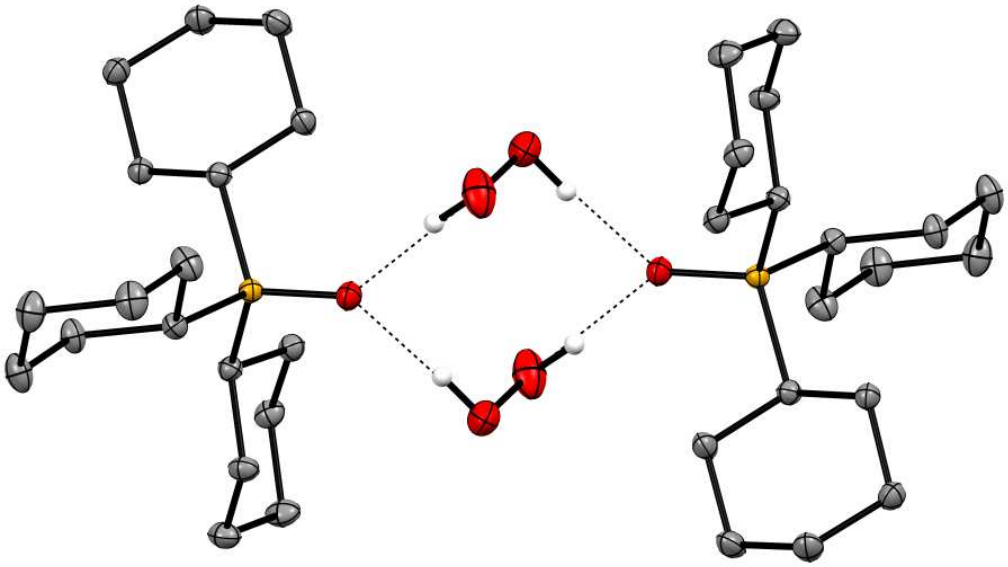

Side view

Table A-3. Crystal data and structure refinement for $(OPCy_3 \cdot H_2O_2)_2$ (**5a**).

Empirical formula	$C_{18}H_{35}O_3P$
Formula weight	330.45
T / K	110(2)
Wavelength / Å	0.71073
Diffractometer	Bruker APEX 2
Crystal system	Triclinic
Space group	*P-1*
Unit cell dimensions:	
a / Å	8.579(2)
b / Å	9.584(3)
c / Å	12.260(3)
α (°)	95.445(3)
β (°)	97.065(3)
γ (°)	112.824(3)
V / Å^3	910.8(4)
Z	2
ρ calcd / Mg/m^3	1.205
μ / mm^{-1}	0.162
F(000)	364
Crystal size / mm	0.31 x 0.18 x 0.17
θ range	1.69 to 27.48
Index ranges (h, k, l)	–11,11; –12,12; –15,15
Reflections collected	10409
Independent reflections	4067 [R(int) = 0.0169]
Completeness to theta = 27.48°	97.6 %
Absorption correction	Semi-empirical from equivalents
Max. and min. transmission	0.9730 and 0.9516
Refinement method	Full-matrix least-squares on F^2
Data / restraints / parameters	4067 / 0 / 199
Goodness-of-fit on F^2	1.044
Final R indices [I2σ(I)]	R_1 = 0.0327, wR_2 = 0.0843
R indices (all data)	R_1 = 0.0376, wR_2 = 0.0880
Largest diff. peak / hole / e Å^{-3}	0.386 and –0.195

Table A-4. Bond lengths [Å] and angles [°] for $(OPCy_3 \cdot H_2O_2)_2$ (5a).

P(1)-O(1)	1.5045(9)
P(1)-C(1)	1.8190(12)
P(1)-C(7)	1.8209(12)
P(1)-C(13)	1.8258(12)
O(20)-O(21)	1.4504(15)
O(20)-H(20)	0.8961
O(21)-H(21)	0.8952
C(1)-C(2)	1.5383(15)
C(1)-C(6)	1.5415(15)
C(1)-H(1)	1.0000
C(2)-C(3)	1.5250(16)
C(2)-H(2A)	0.9900
C(2)-H(2B)	0.9900
C(3)-C(4)	1.5235(16)
C(3)-H(3A)	0.9900
C(3)-H(3B)	0.9900
C(4)-C(5)	1.5229(16)
C(4)-H(4A)	0.9900
C(4)-H(4B)	0.9900
C(5)-C(6)	1.5283(16)
C(5)-H(5A)	0.9900
C(5)-H(5B)	0.9900
C(6)-H(6A)	0.9900
C(6)-H(6B)	0.9900
C(7)-C(12)	1.5336(15)
C(7)-C(8)	1.5370(16)
C(7)-H(7)	1.0000
C(8)-C(9)	1.5279(16)
C(8)-H(8A)	0.9900
C(8)-H(8B)	0.9900
C(9)-C(10)	1.5195(17)
C(9)-H(9A)	0.9900
C(9)-H(9B)	0.9900

C(10)-C(11)	1.5253(18)
C(10)-H(10A)	0.9900
C(10)-H(10B)	0.9900
C(11)-C(12)	1.5297(16)
C(11)-H(11A)	0.9900
C(11)-H(11B)	0.9900
C(12)-H(12A)	0.9900
C(12)-H(12B)	0.9900
C(13)-C(18)	1.5378(15)
C(13)-C(14)	1.5401(15)
C(13)-H(13)	1.0000
C(14)-C(15)	1.5280(16)
C(14)-H(14A)	0.9900
C(14)-H(14B)	0.9900
C(15)-C(16)	1.5212(17)
C(15)-H(15A)	0.9900
C(15)-H(15B)	0.9900
C(16)-C(17)	1.5250(16)
C(16)-H(16A)	0.9900
C(16)-H(16B)	0.9900
C(17)-C(18)	1.5292(15)
C(17)-H(17A)	0.9900
C(17)-H(17B)	0.9900
C(18)-H(18A)	0.9900
C(18)-H(18B)	0.9900

O(1)-P(1)-C(1)	111.03(5)
O(1)-P(1)-C(7)	109.92(5)
C(1)-P(1)-C(7)	106.76(5)
O(1)-P(1)-C(13)	112.04(5)
C(1)-P(1)-C(13)	108.68(5)
C(7)-P(1)-C(13)	108.24(5)
O(21)-O(20)-H(20)	103.2
O(20)-O(21)-H(21)	100.4

C(2)-C(1)-C(6)	109.92(9)
C(2)-C(1)-P(1)	110.59(7)
C(6)-C(1)-P(1)	112.44(8)
C(2)-C(1)-H(1)	107.9
C(6)-C(1)-H(1)	107.9
P(1)-C(1)-H(1)	107.9
C(3)-C(2)-C(1)	111.25(9)
C(3)-C(2)-H(2A)	109.4
C(1)-C(2)-H(2A)	109.4
C(3)-C(2)-H(2B)	109.4
C(1)-C(2)-H(2B)	109.4
H(2A)-C(2)-H(2B)	108.0
C(4)-C(3)-C(2)	111.37(10)
C(4)-C(3)-H(3A)	109.4
C(2)-C(3)-H(3A)	109.4
C(4)-C(3)-H(3B)	109.4
C(2)-C(3)-H(3B)	109.4
H(3A)-C(3)-H(3B)	108.0
C(5)-C(4)-C(3)	111.09(10)
C(5)-C(4)-H(4A)	109.4
C(3)-C(4)-H(4A)	109.4
C(5)-C(4)-H(4B)	109.4
C(3)-C(4)-H(4B)	109.4
H(4A)-C(4)-H(4B)	108.0
C(4)-C(5)-C(6)	111.02(9)
C(4)-C(5)-H(5A)	109.4
C(6)-C(5)-H(5A)	109.4
C(4)-C(5)-H(5B)	109.4
C(6)-C(5)-H(5B)	109.4
H(5A)-C(5)-H(5B)	108.0
C(5)-C(6)-C(1)	110.01(9)
C(5)-C(6)-H(6A)	109.7
C(1)-C(6)-H(6A)	109.7
C(5)-C(6)-H(6B)	109.7

C(1)-C(6)-H(6B)	109.7
H(6A)-C(6)-H(6B)	108.2
C(12)-C(7)-C(8)	110.55(9)
C(12)-C(7)-P(1)	116.48(8)
C(8)-C(7)-P(1)	110.95(8)
C(12)-C(7)-H(7)	106.0
C(8)-C(7)-H(7)	106.0
P(1)-C(7)-H(7)	106.0
C(9)-C(8)-C(7)	110.60(10)
C(9)-C(8)-H(8A)	109.5
C(7)-C(8)-H(8A)	109.5
C(9)-C(8)-H(8B)	109.5
C(7)-C(8)-H(8B)	109.5
H(8A)-C(8)-H(8B)	108.1
C(10)-C(9)-C(8)	111.57(10)
C(10)-C(9)-H(9A)	109.3
C(8)-C(9)-H(9A)	109.3
C(10)-C(9)-H(9B)	109.3
C(8)-C(9)-H(9B)	109.3
H(9A)-C(9)-H(9B)	108.0
C(9)-C(10)-C(11)	111.04(10)
C(9)-C(10)-H(10A)	109.4
C(11)-C(10)-H(10A)	109.4
C(9)-C(10)-H(10B)	109.4
C(11)-C(10)-H(10B)	109.4
H(10A)-C(10)-H(10B)	108.0
C(10)-C(11)-C(12)	110.97(10)
C(10)-C(11)-H(11A)	109.4
C(12)-C(11)-H(11A)	109.4
C(10)-C(11)-H(11B)	109.4
C(12)-C(11)-H(11B)	109.4
H(11A)-C(11)-H(11B)	108.0
C(11)-C(12)-C(7)	110.77(9)
C(11)-C(12)-H(12A)	109.5

C(7)-C(12)-H(12A)	109.5
C(11)-C(12)-H(12B)	109.5
C(7)-C(12)-H(12B)	109.5
H(12A)-C(12)-H(12B)	108.1
C(18)-C(13)-C(14)	110.87(9)
C(18)-C(13)-P(1)	114.44(7)
C(14)-C(13)-P(1)	110.80(8)
C(18)-C(13)-H(13)	106.8
C(14)-C(13)-H(13)	106.8
P(1)-C(13)-H(13)	106.8
C(15)-C(14)-C(13)	110.55(10)
C(15)-C(14)-H(14A)	109.5
C(13)-C(14)-H(14A)	109.5
C(15)-C(14)-H(14B)	109.5
C(13)-C(14)-H(14B)	109.5
H(14A)-C(14)-H(14B)	108.1
C(16)-C(15)-C(14)	111.59(10)
C(16)-C(15)-H(15A)	109.3
C(14)-C(15)-H(15A)	109.3
C(16)-C(15)-H(15B)	109.3
C(14)-C(15)-H(15B)	109.3
H(15A)-C(15)-H(15B)	108.0
C(15)-C(16)-C(17)	110.32(10)
C(15)-C(16)-H(16A)	109.6
C(17)-C(16)-H(16A)	109.6
C(15)-C(16)-H(16B)	109.6
C(17)-C(16)-H(16B)	109.6
H(16A)-C(16)-H(16B)	108.1
C(16)-C(17)-C(18)	110.71(9)
C(16)-C(17)-H(17A)	109.5
C(18)-C(17)-H(17A)	109.5
C(16)-C(17)-H(17B)	109.5
C(18)-C(17)-H(17B)	109.5
H(17A)-C(17)-H(17B)	108.1

C(17)-C(18)-C(13)	110.79(9)
C(17)-C(18)-H(18A)	109.5
C(13)-C(18)-H(18A)	109.5
C(17)-C(18)-H(18B)	109.5
C(13)-C(18)-H(18B)	109.5
H(18A)-C(18)-H(18B)	108.1

APPENDIX B

NMR SPECTROSCOPY DATA

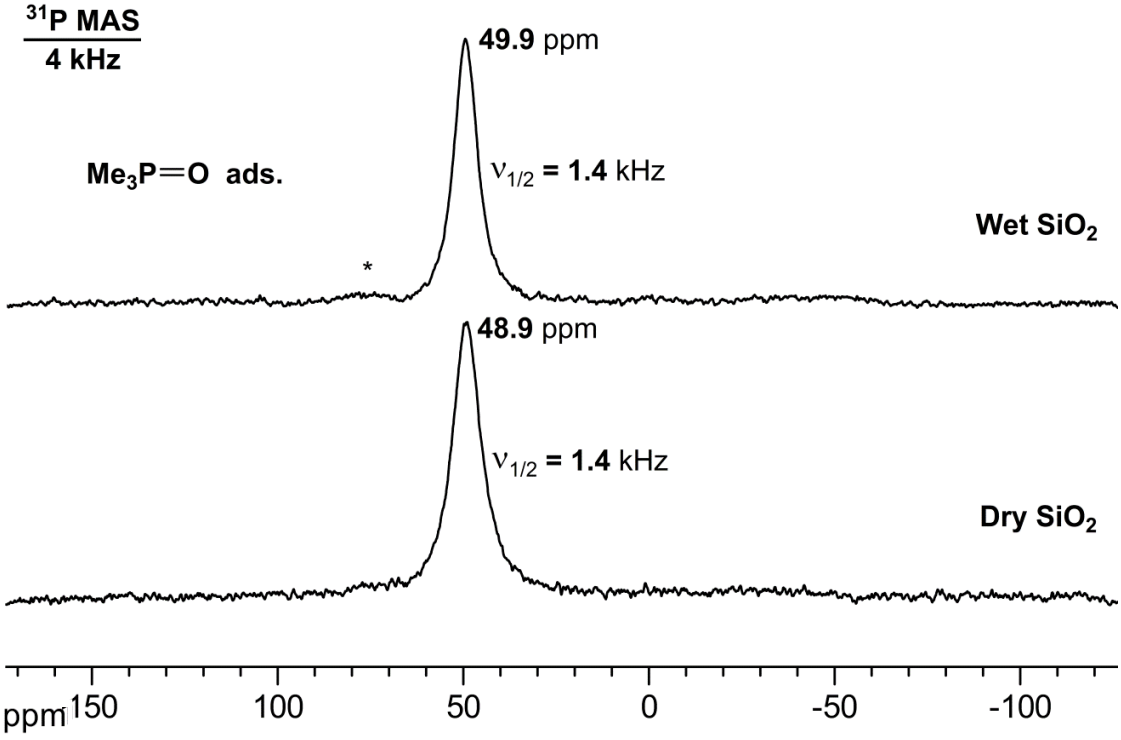

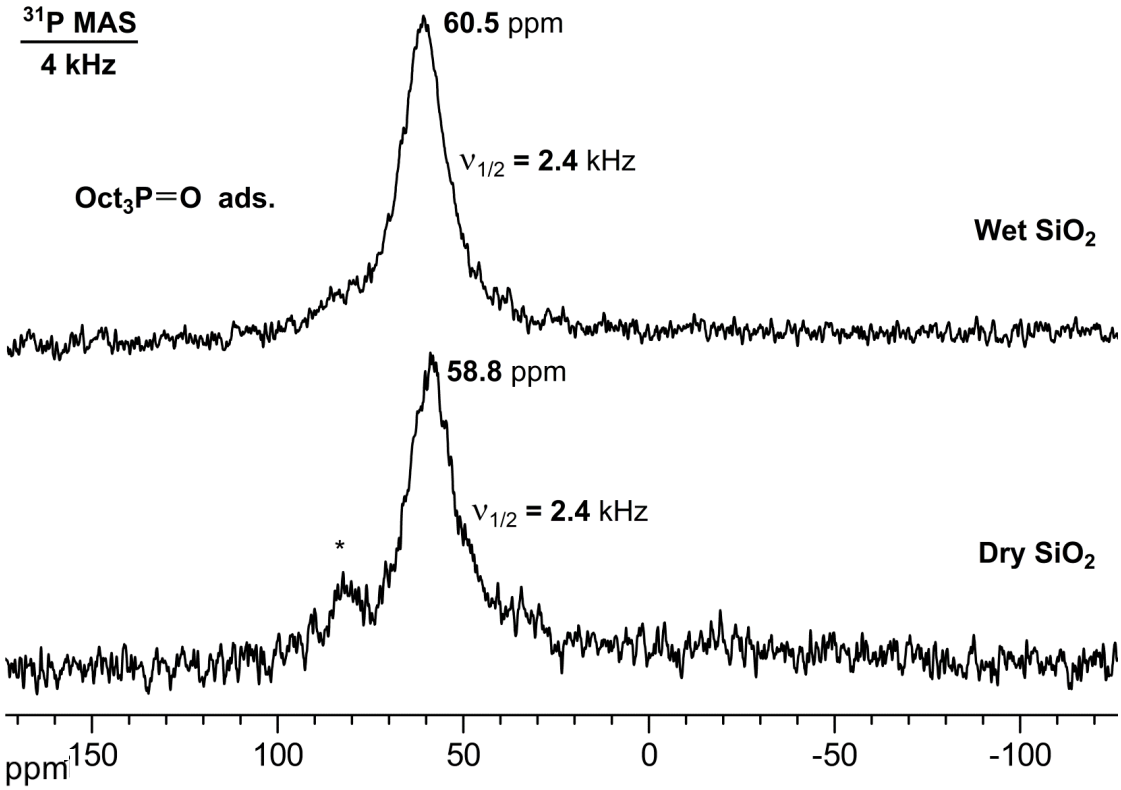
31P MAS
4 kHz
60.5 ppm
ν1/2 = 2.4 kHz
Oct3P=O ads.
Wet SiO2
58.8 ppm
ν1/2 = 2.4 kHz
*
Dry SiO2
ppm
150
100
50
0
-50
-100

$OPMe_3$ on wet SiO_2 (2_{ads}):

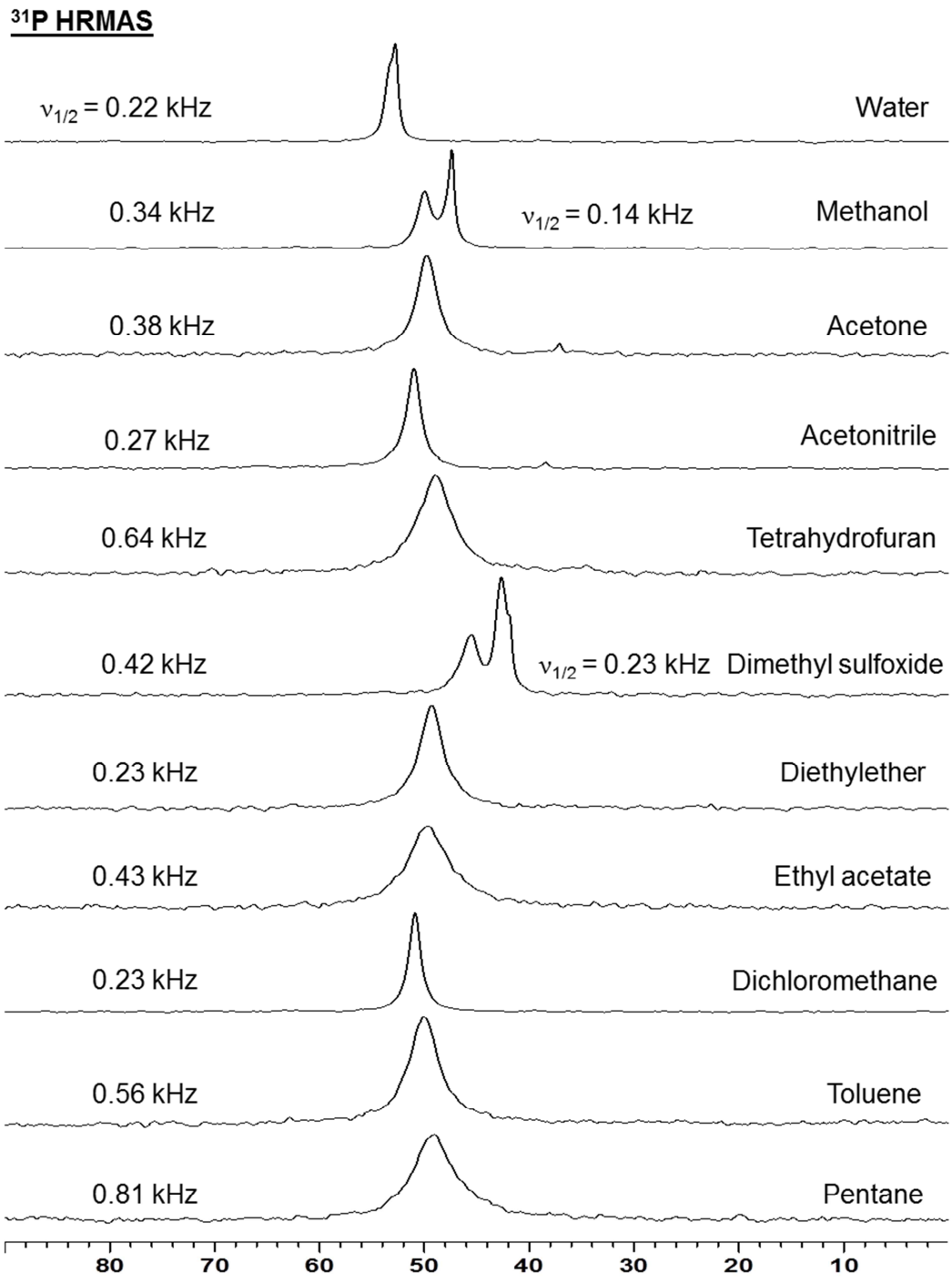

$OPOct_3$ on wet SiO_2 (4_{ads}):

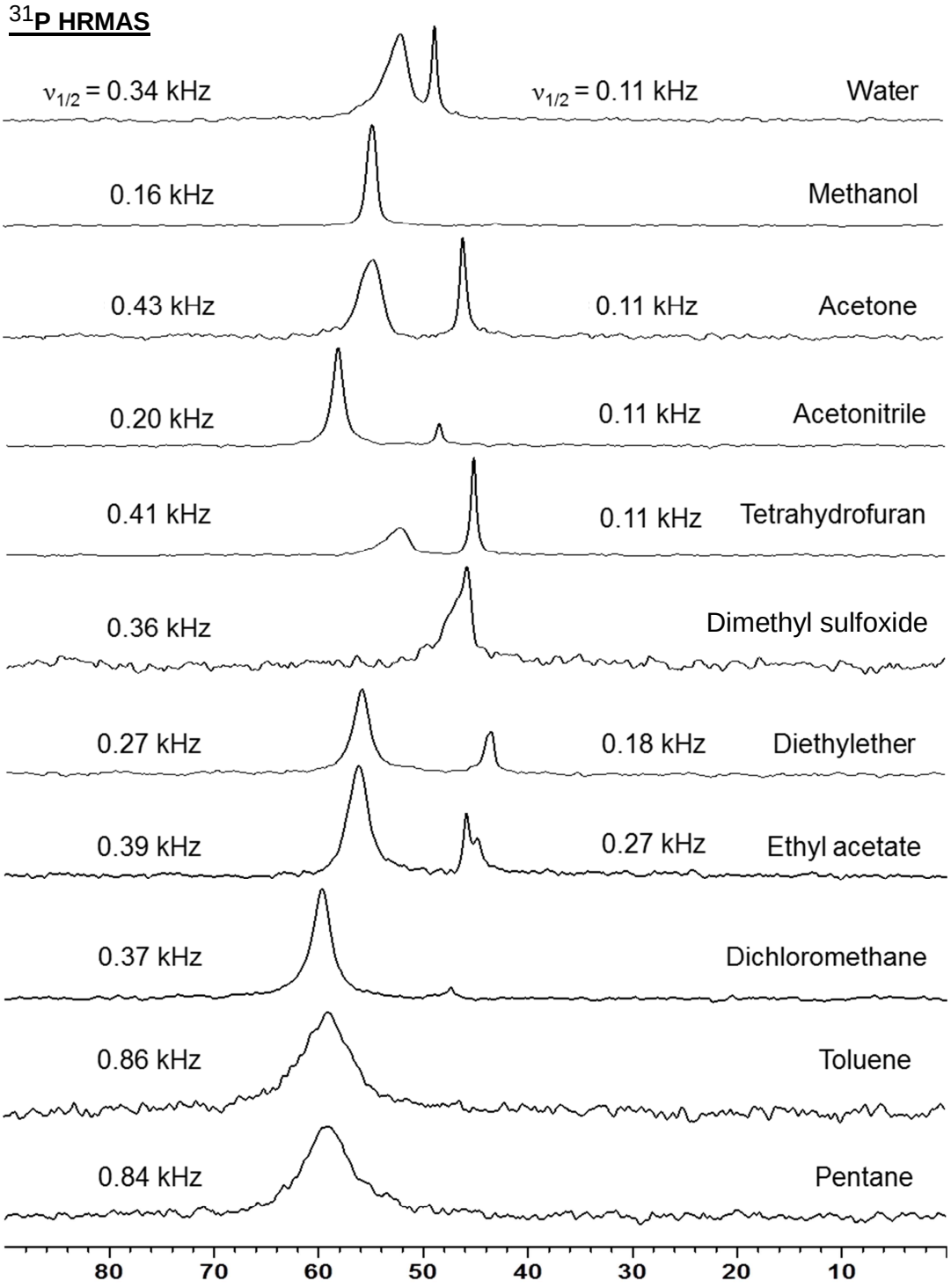

$OPCy_3$ on wet SiO_2 (5_{ads}):

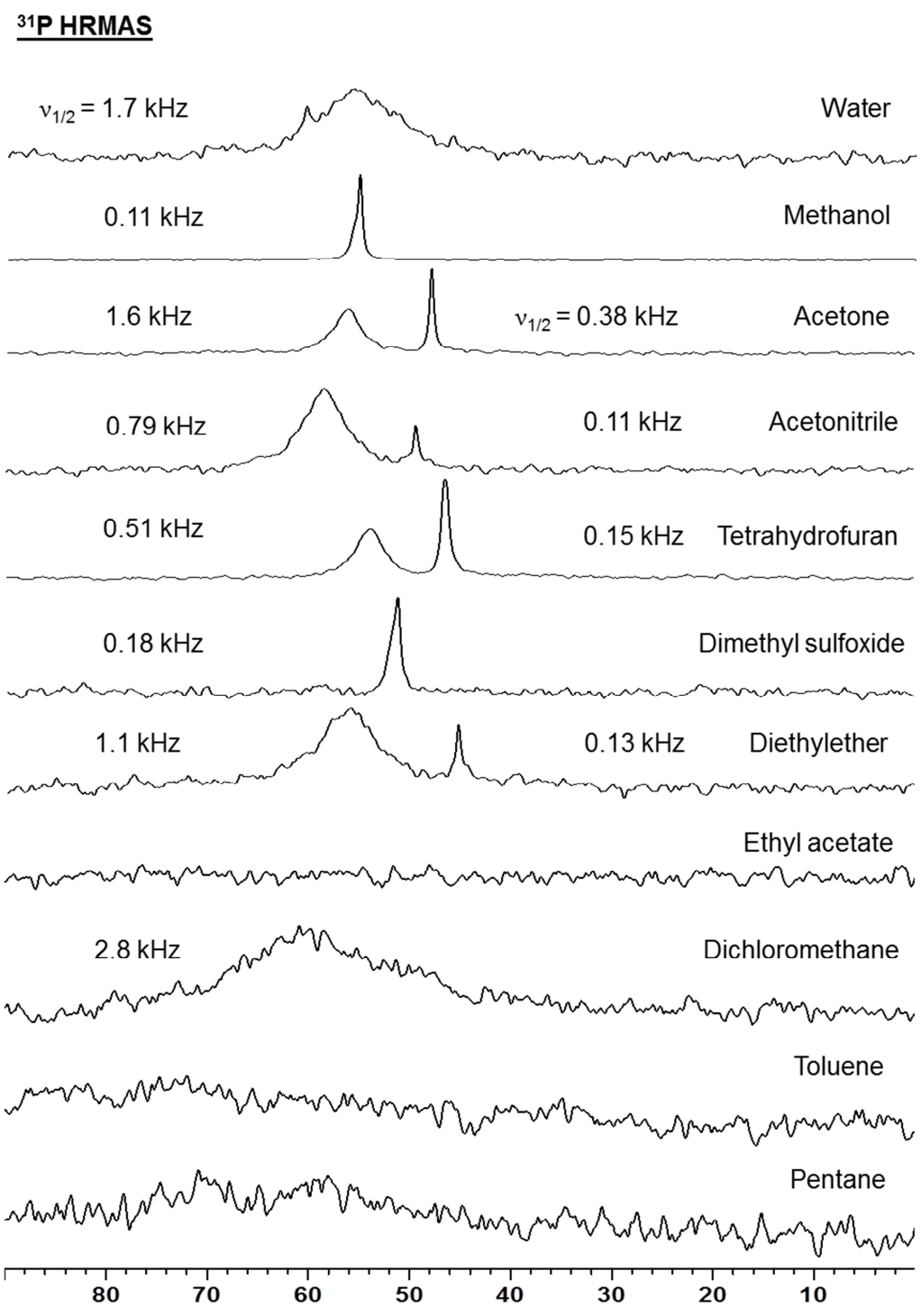

$OPPh_3$ on wet SiO_2 (6_{ads}):

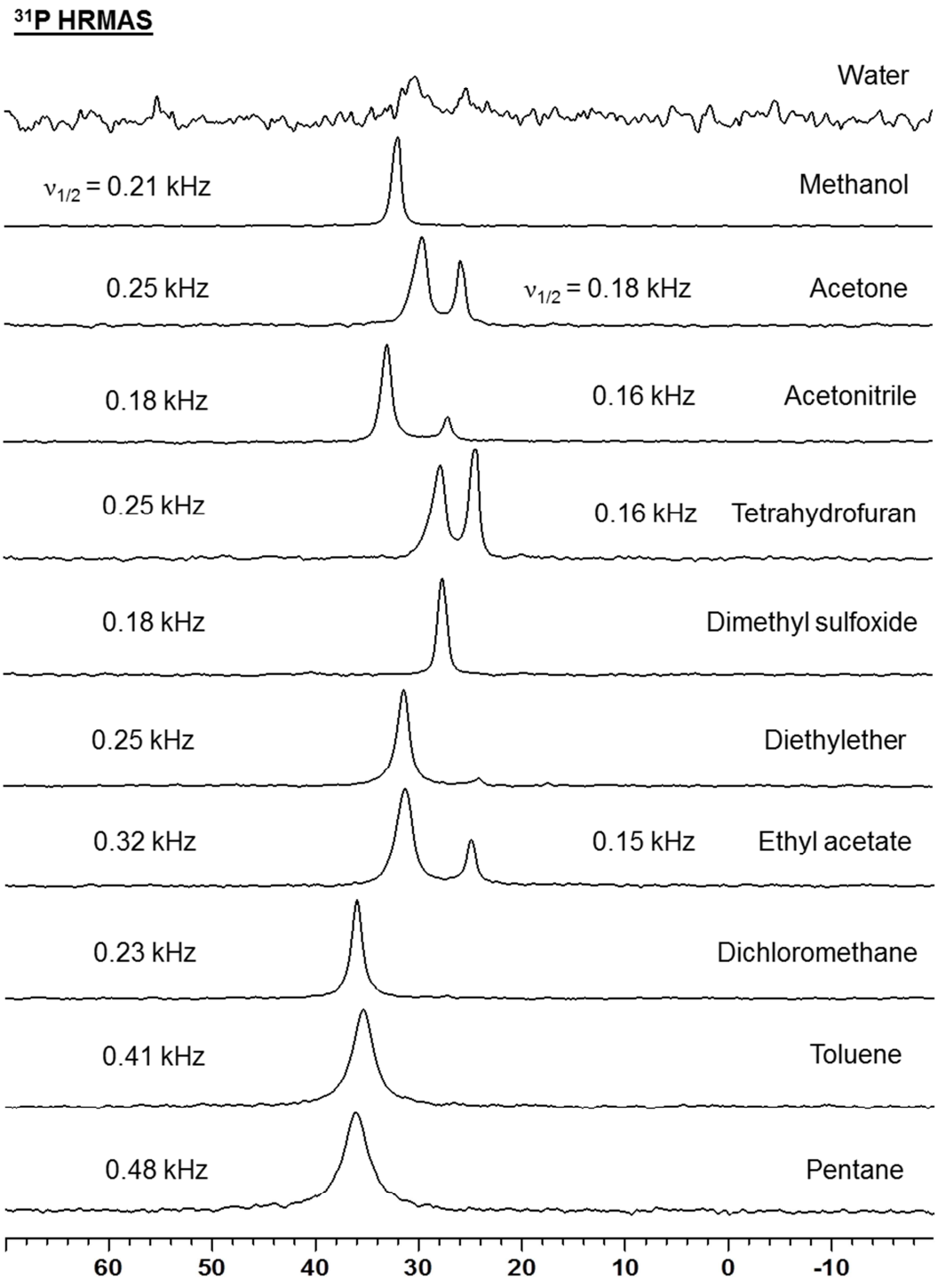

$OPCy_3$ (5) ground with dry SiO_2:

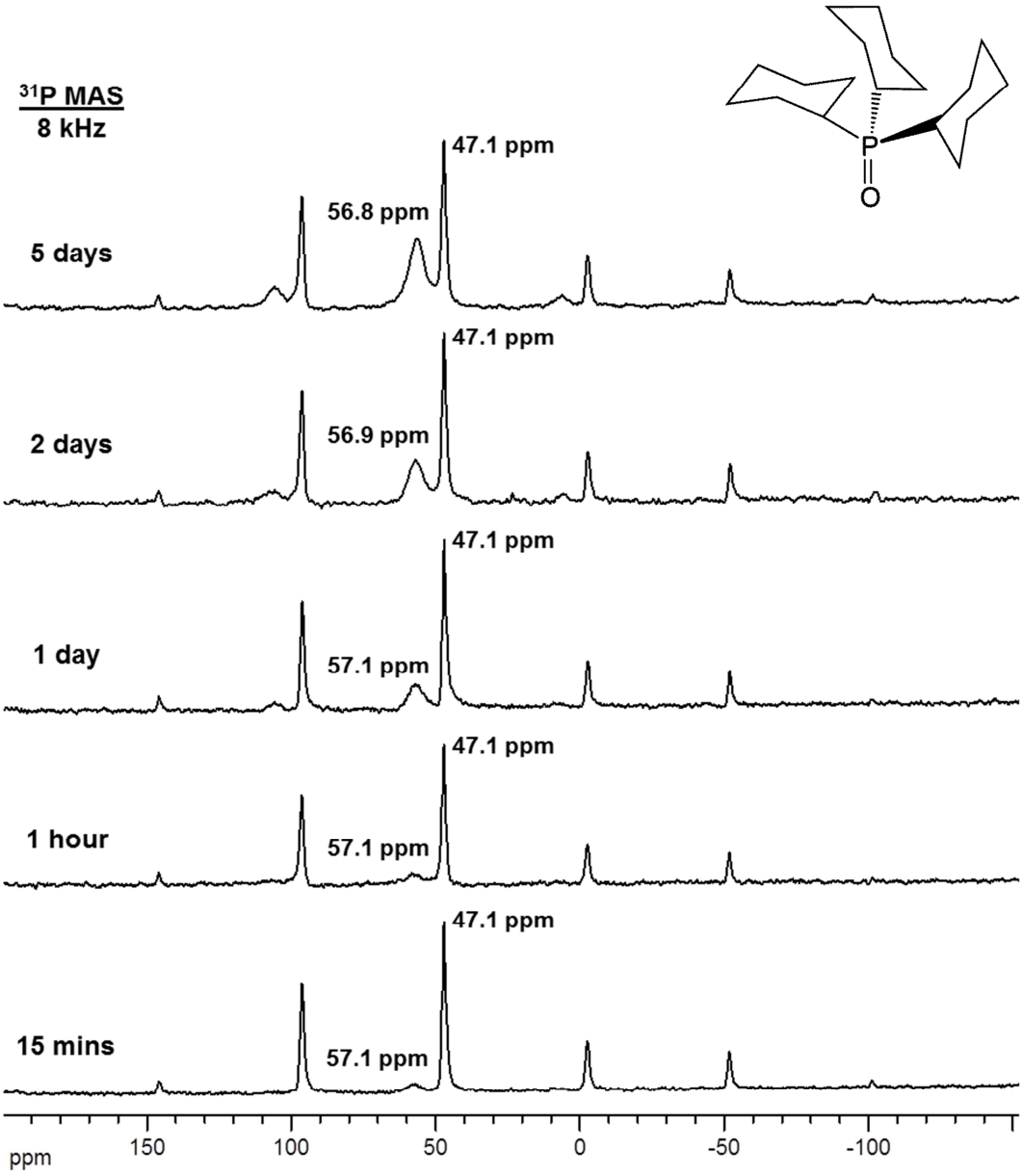

$OPPh_3$ (6) ground with dry SiO_2:

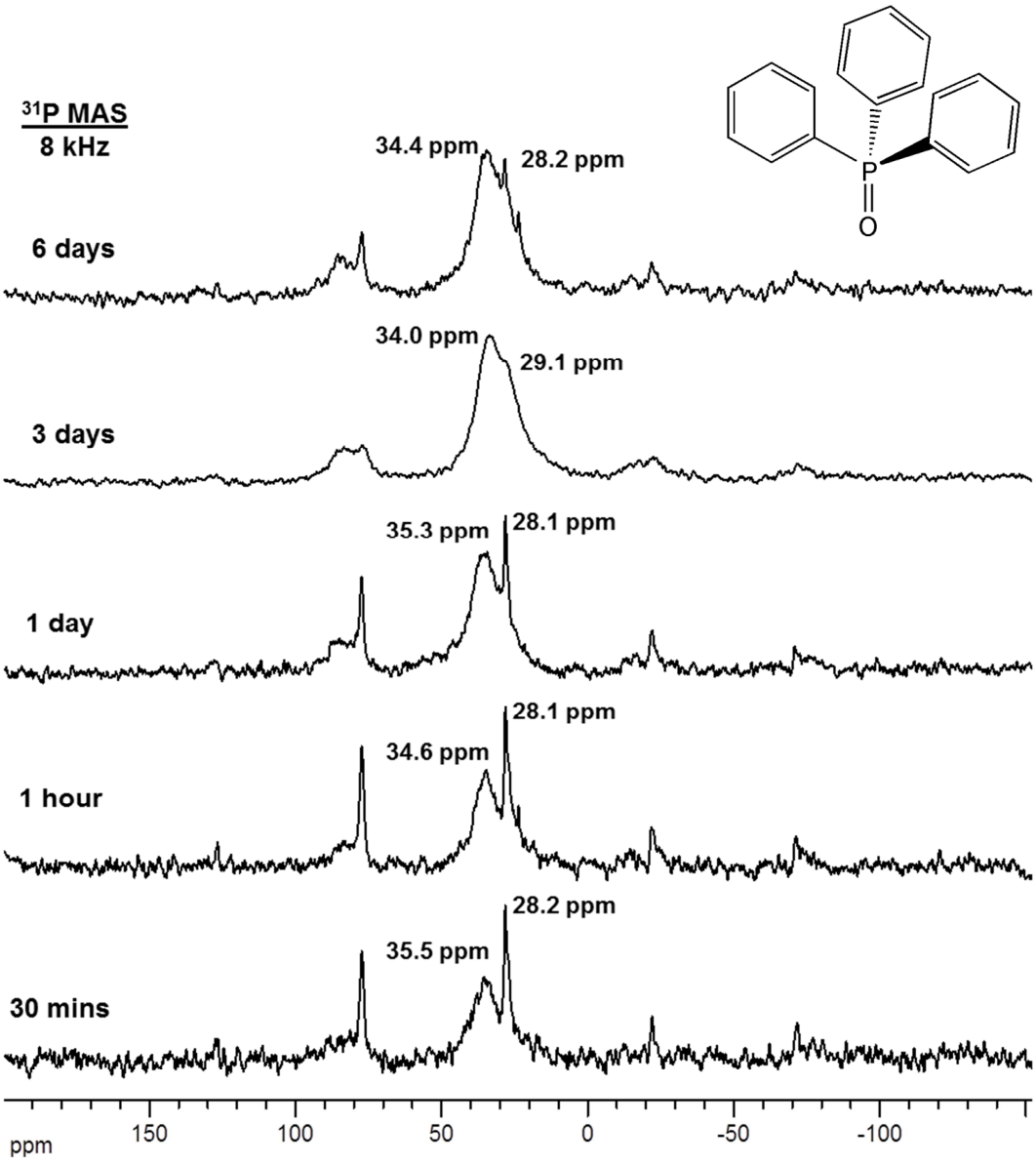

C tetraphosphine oxide adsorbed on wet silica (9_{ads}):

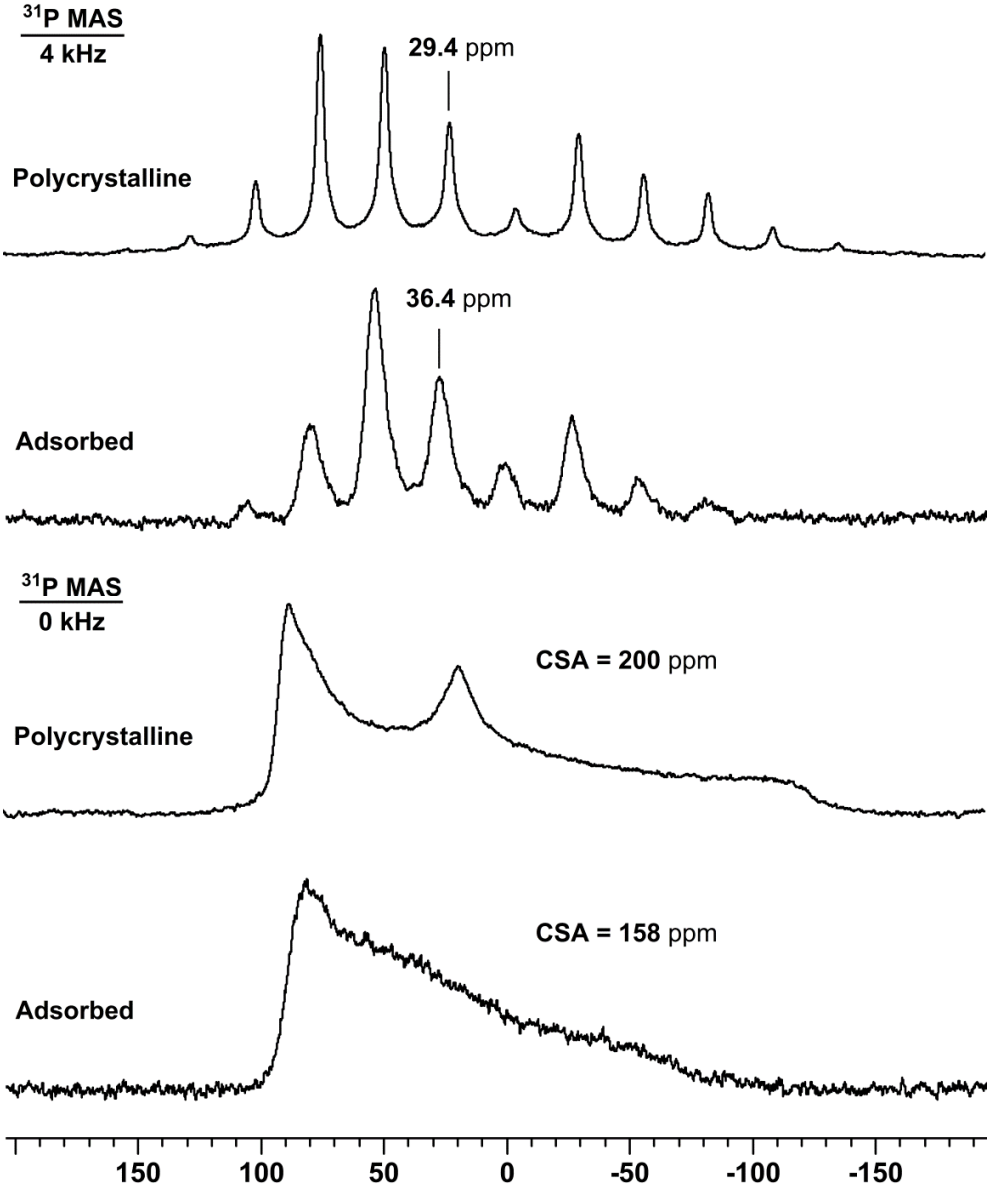

C tetraphosphine oxide adsorbed on wet silica (9_{ads}):

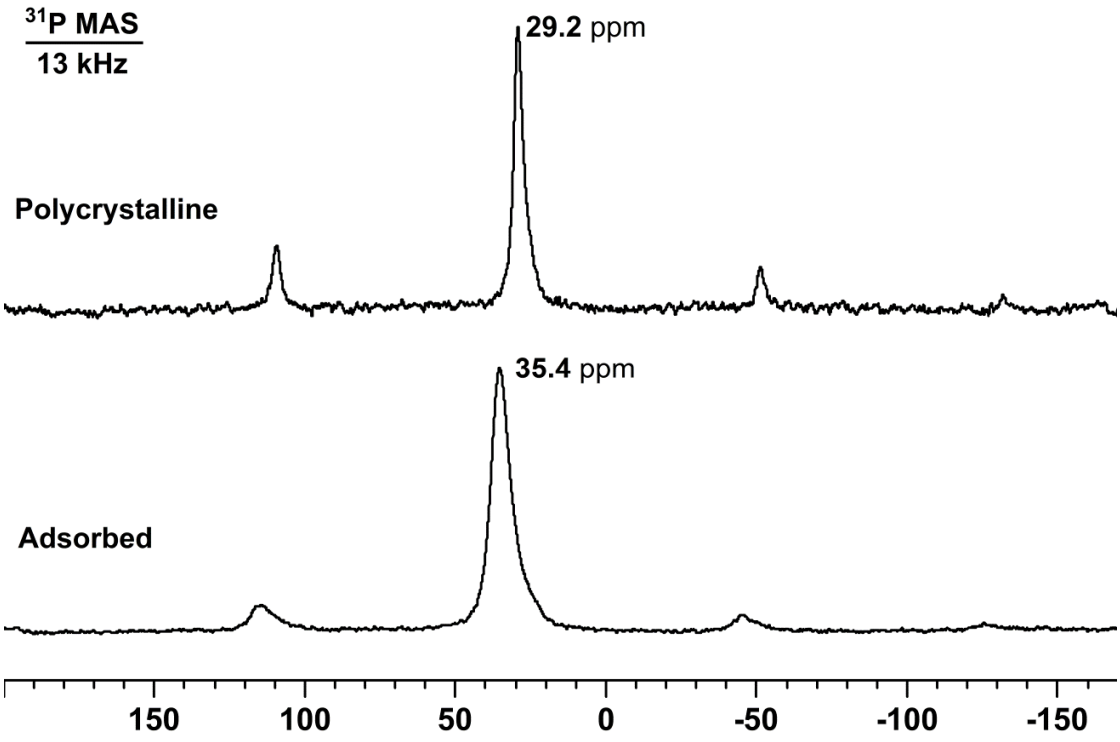

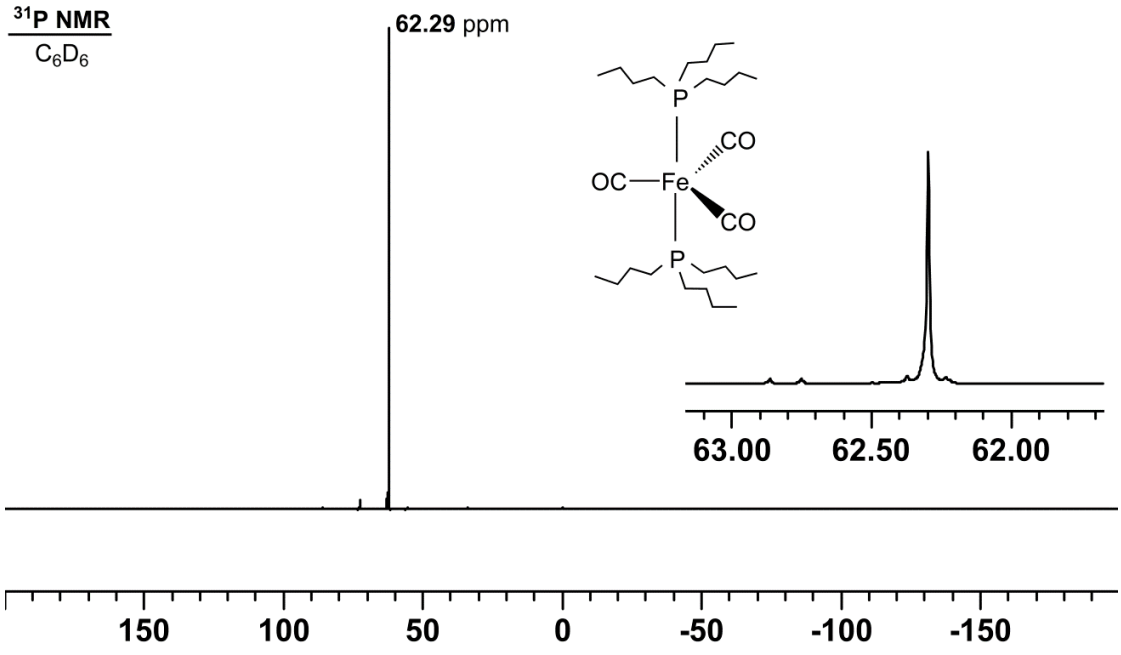
31P NMR
C6D6
62.29 ppm
P
CO
OC
Fe
CO
P
63.00
62.50
62.00
150
100
50
0
-50
-100
-150

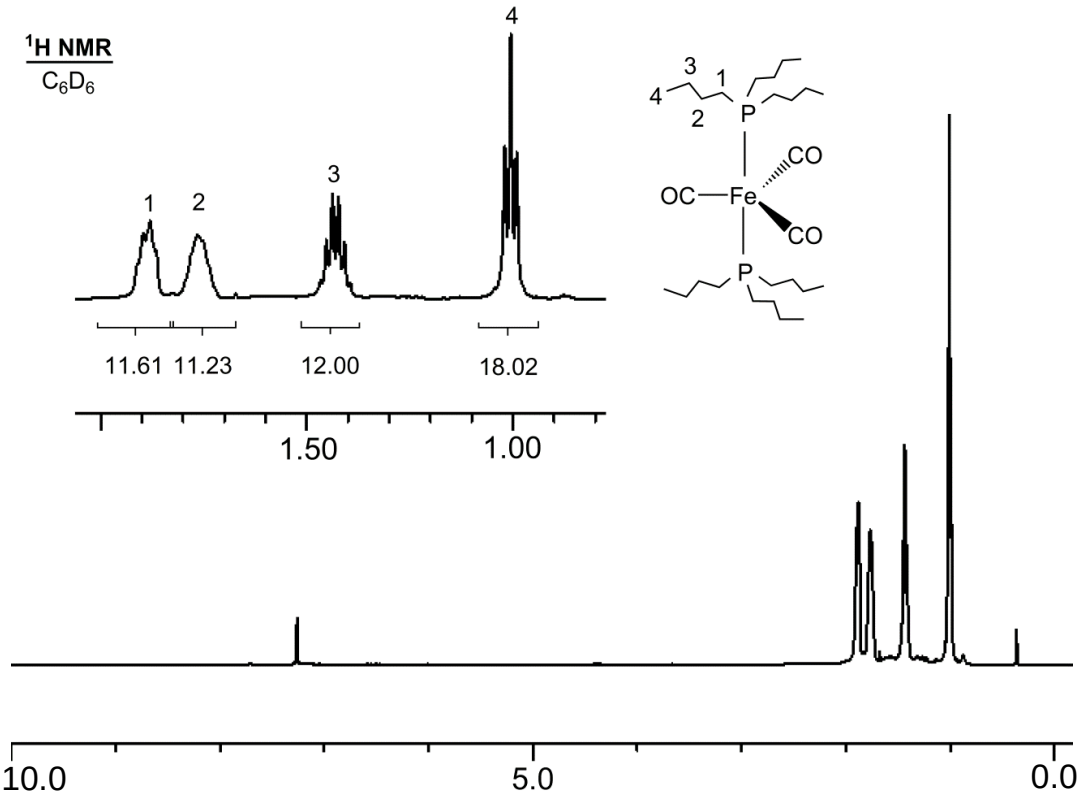
1H NMR
C6D6
1
2
3
4
11.61
11.23
12.00
18.02
1.50
1.00
OC
Fe
CO
CO
P
P
10.0
5.0
0.0

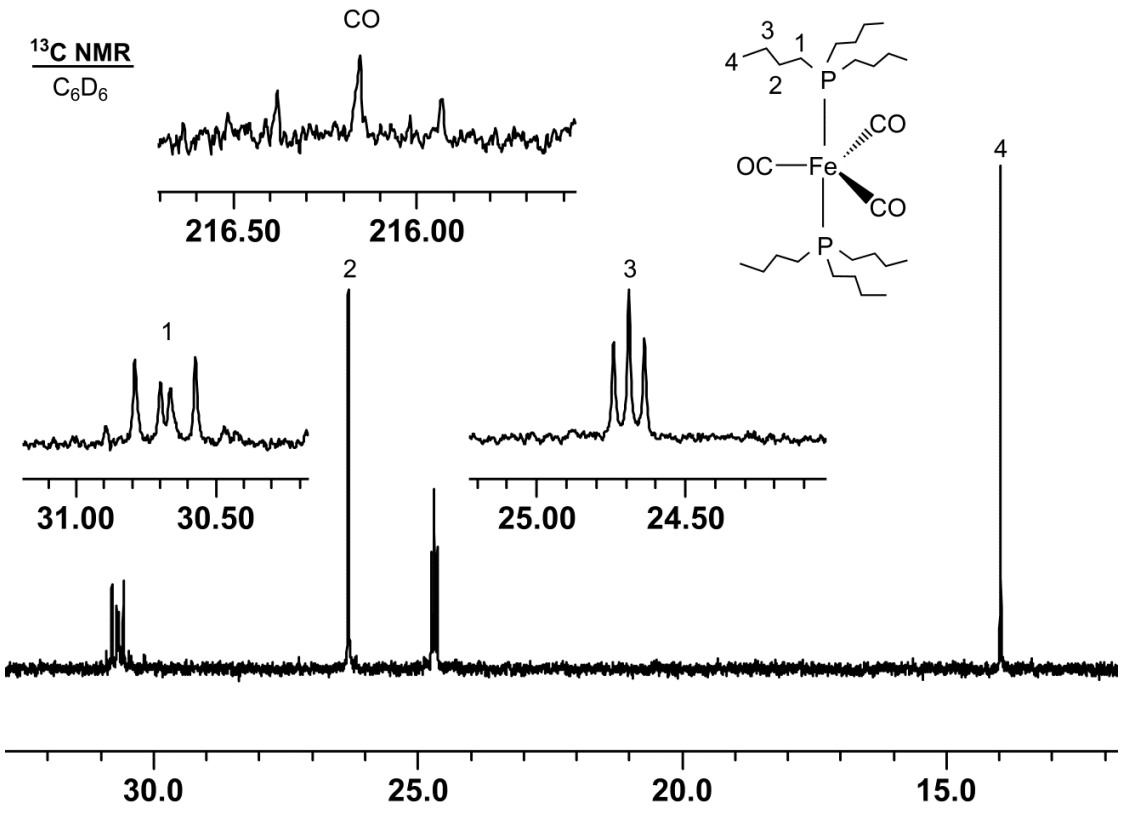
13C NMR
C6D6
CO
216.50
216.00
1
2
3
4
31.00
30.50
25.00
24.50
30.0
25.0
20.0
15.0
OC
Fe
CO
CO
P
P

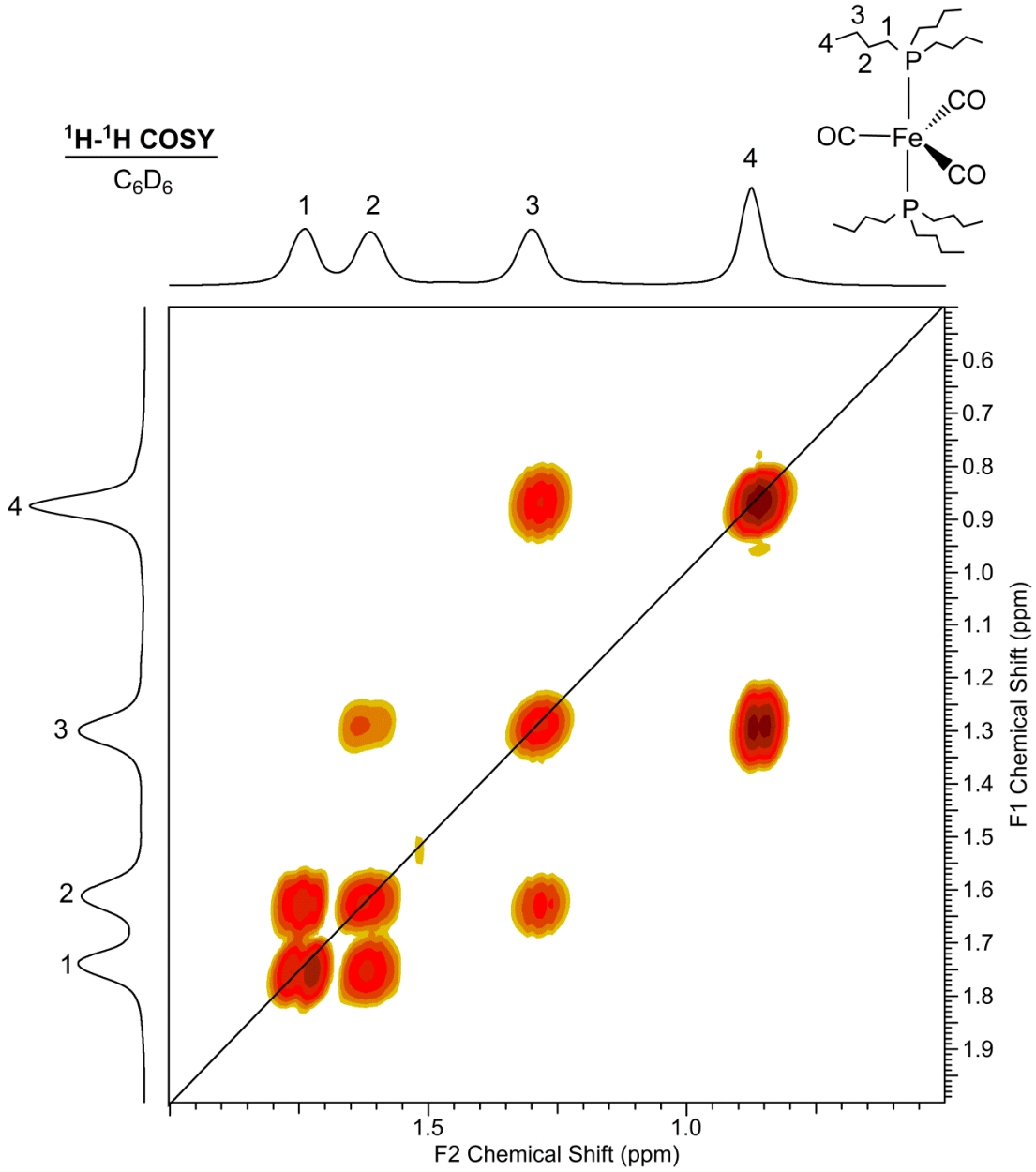
^{1}H-^{1}H COSY
C_6D_6
1
2
3
4
OC
Fe
CO
CO
P
P
F1 Chemical Shift (ppm)
F2 Chemical Shift (ppm)
0.6
0.7
0.8
0.9
1.0
1.1
1.2
1.3
1.4
1.5
1.6
1.7
1.8
1.9
1.5
1.0

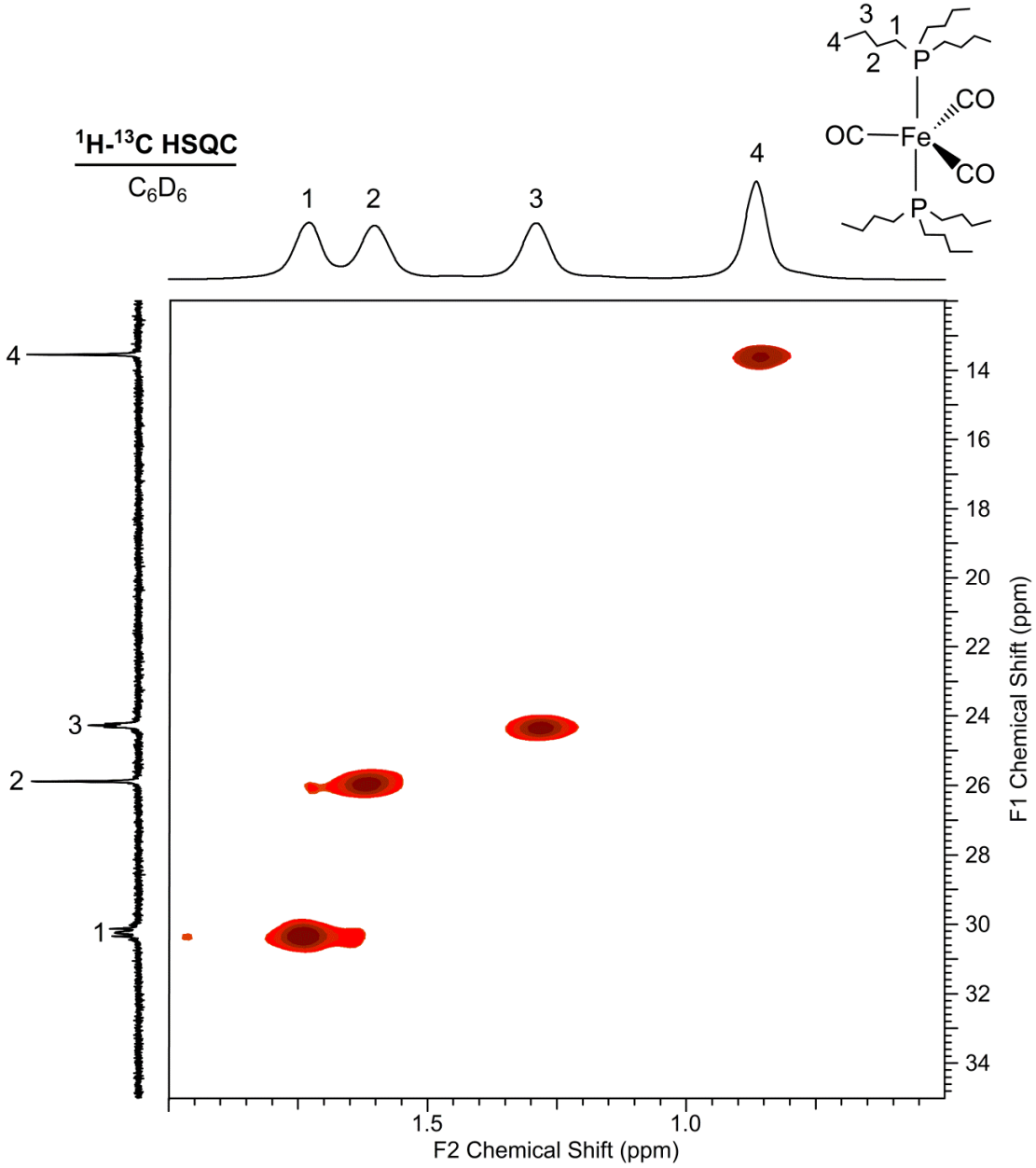
1H-13C HSQC
C6D6
1
2
3
4
CO
OC
Fe
CO
P
P
F1 Chemical Shift (ppm)
F2 Chemical Shift (ppm)
1.5
1.0
14
16
18
20
22
24
26
28
30
32
34

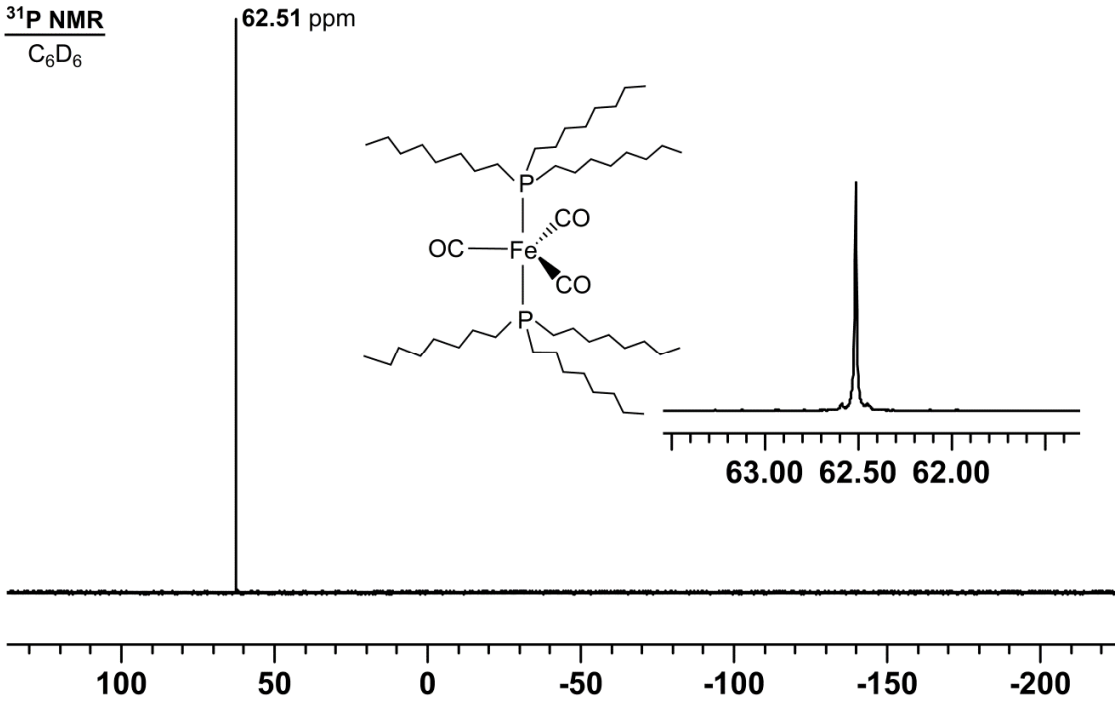
31P NMR
C6D6
62.51 ppm
P
CO
OC
Fe
CO
P
63.00 62.50 62.00
100 50 0 -50 -100 -150 -200

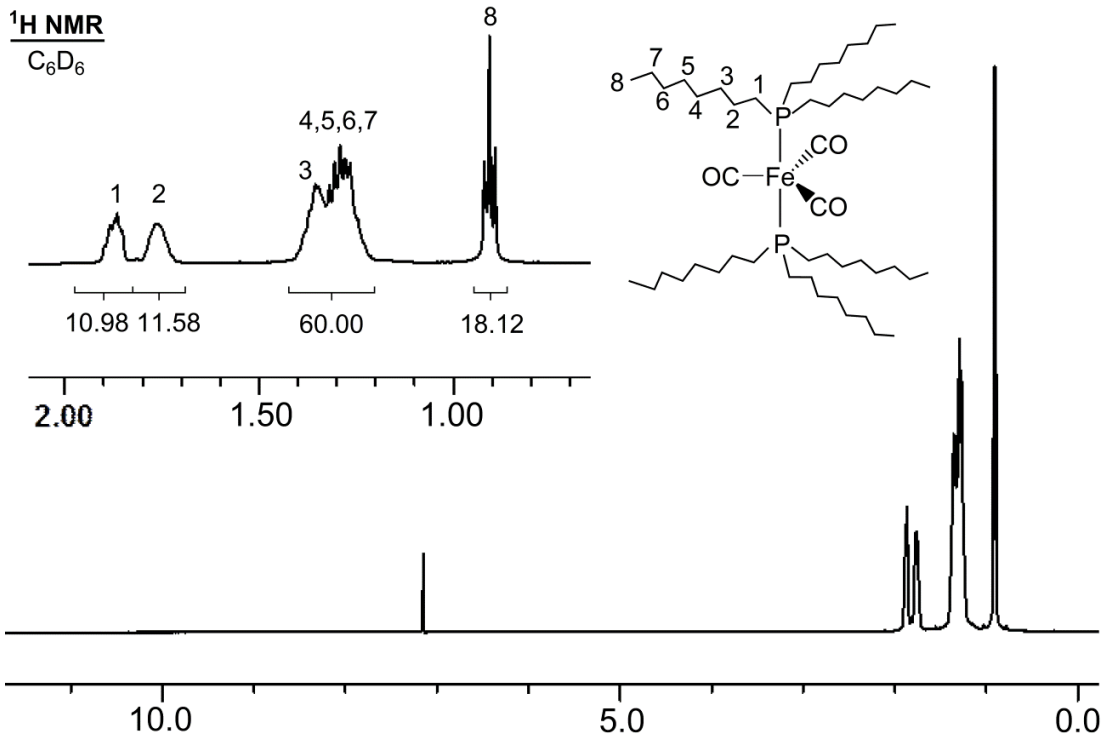
1H NMR
C6D6
8
4,5,6,7
3
1 2
10.98 11.58
60.00
18.12
2.00
1.50
1.00
7
5
3
1
8
6
4
2
P
CO
OC—Fe
CO
P
10.0
5.0
0.0

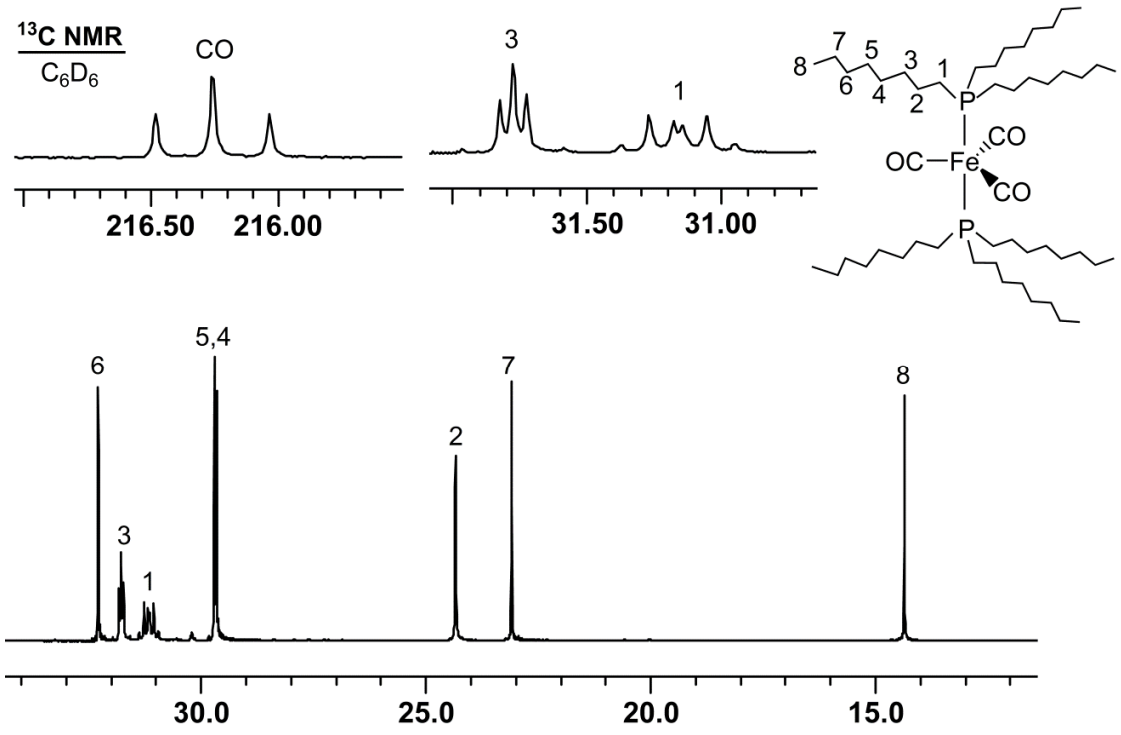
13C NMR
C6D6
CO
3
1
216.50
216.00
31.50
31.00
7
5
3
1
8
6
4
2
P
CO
OC—Fe
CO
P
6
5,4
7
8
2
3
1
30.0
25.0
20.0
15.0

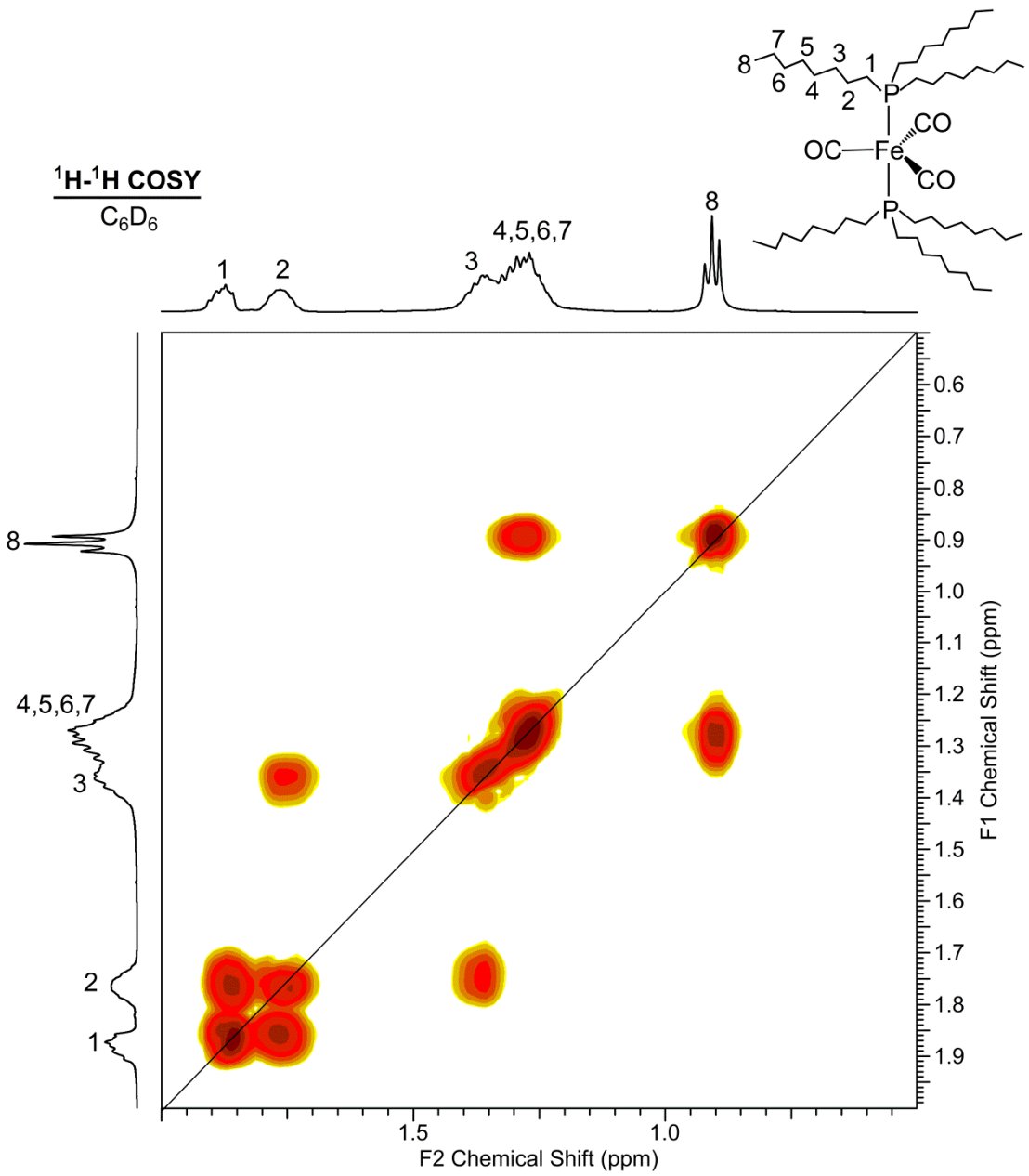
^{1}H-^{1}H COSY
C_6D_6
1
2
3
4,5,6,7
8
F2 Chemical Shift (ppm)
F1 Chemical Shift (ppm)
1.5
1.0
0.6
0.7
0.8
0.9
1.0
1.1
1.2
1.3
1.4
1.5
1.6
1.7
1.8
1.9
CO
OC
Fe
P

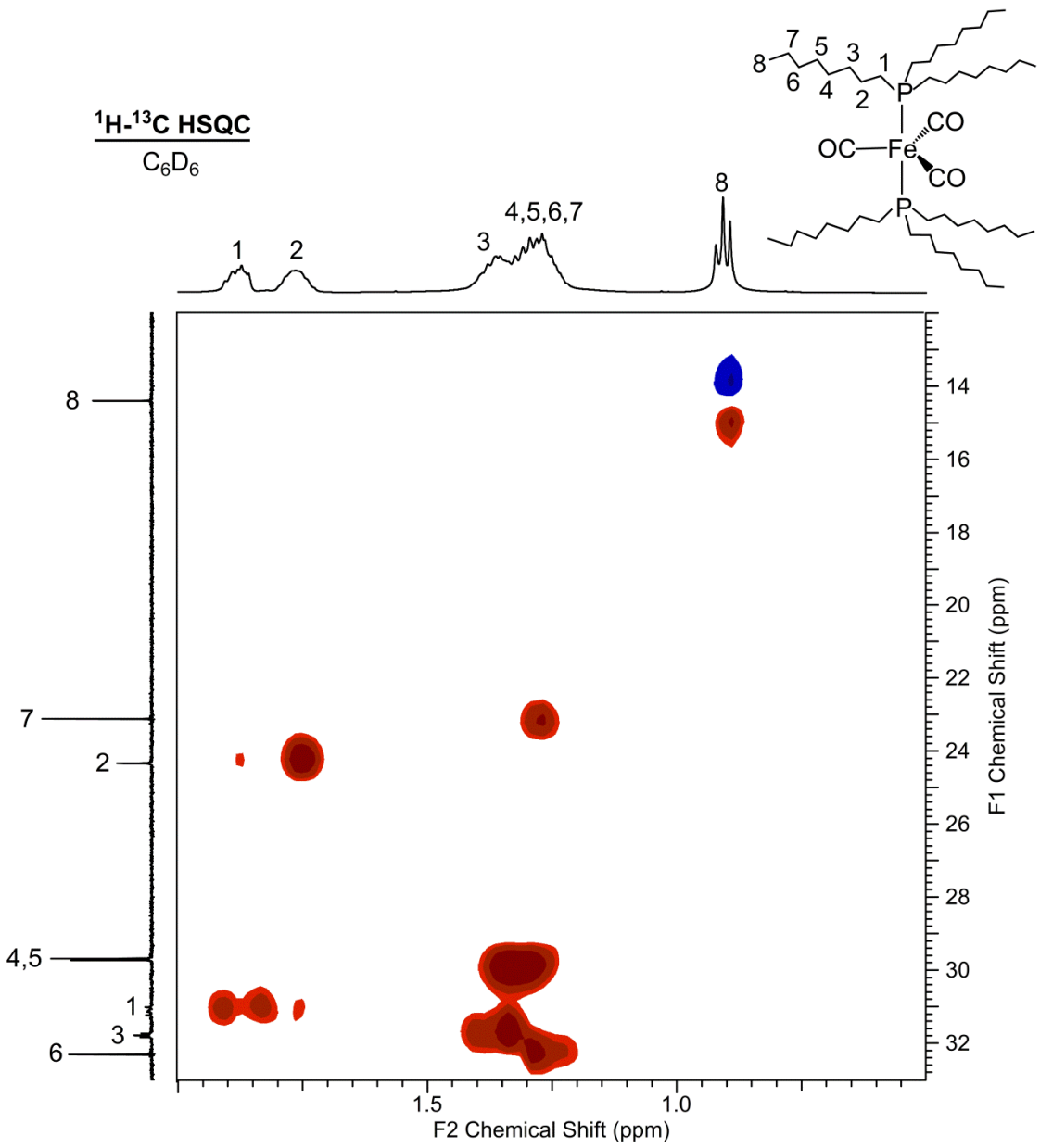
1H-13C HSQC
C6D6
1
2
3
4,5,6,7
8
8
7
2
4,5
1
3
6
1.5
1.0
F2 Chemical Shift (ppm)
F1 Chemical Shift (ppm)
14
16
18
20
22
24
26
28
30
32
CO
OC
Fe
CO
P
P

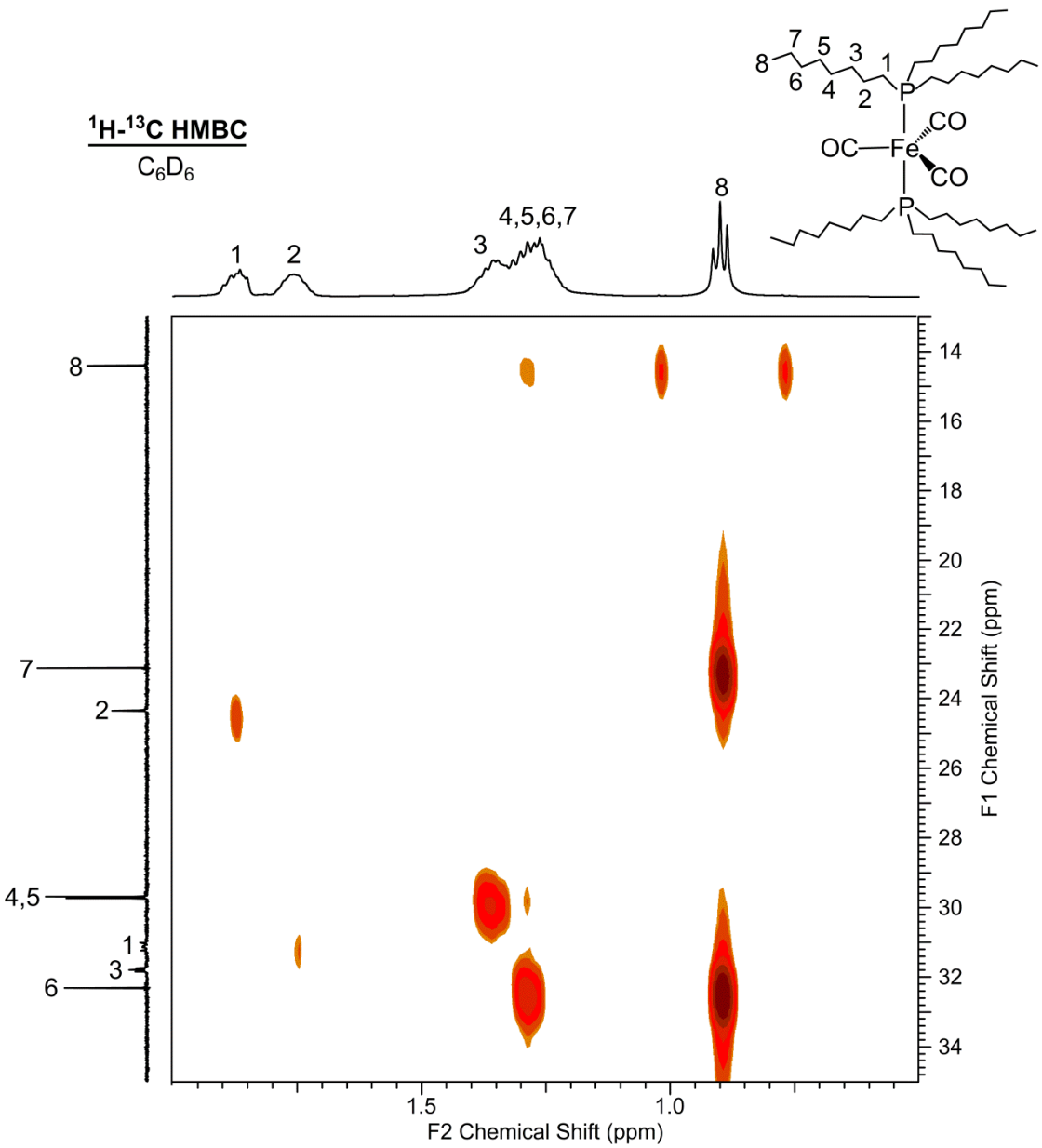
^{1}H-^{13}C HMBC
C_6D_6
1
2
3
4,5,6,7
8
8
7
2
4,5
1
3
6
1.5
1.0
F2 Chemical Shift (ppm)
F1 Chemical Shift (ppm)
14
16
18
20
22
24
26
28
30
32
34
CO
OC
Fe
CO
P
P

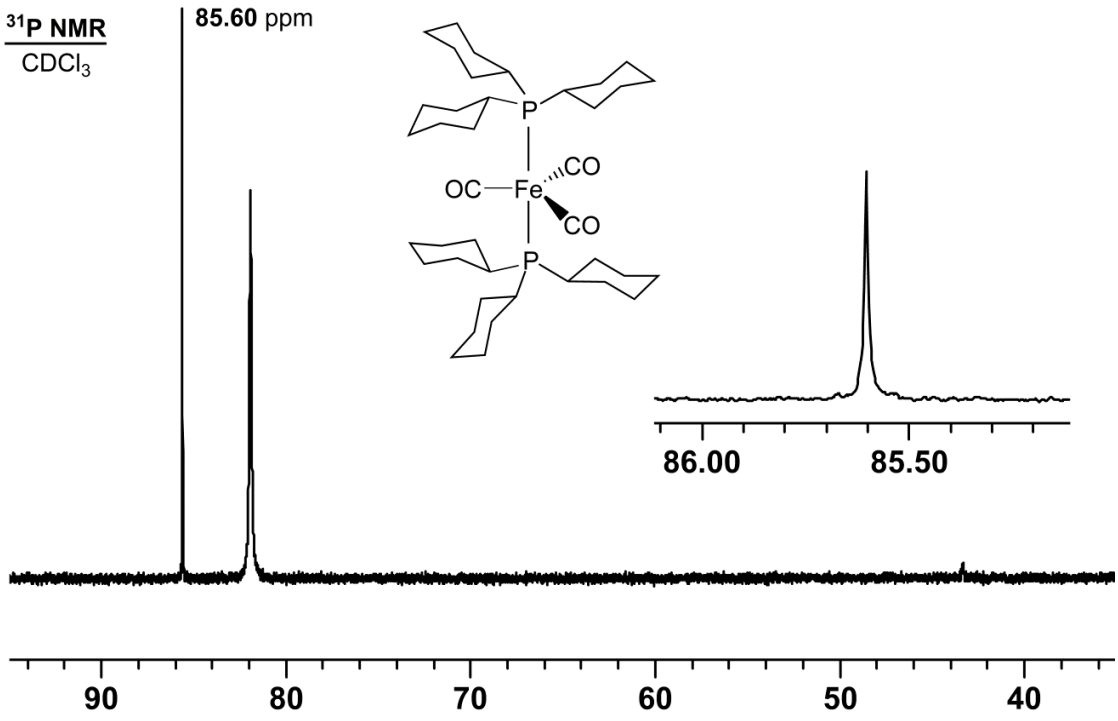
31P NMR
CDCl3
85.60 ppm
P
OC
Fe
CO
CO
P
86.00
85.50
90
80
70
60
50
40

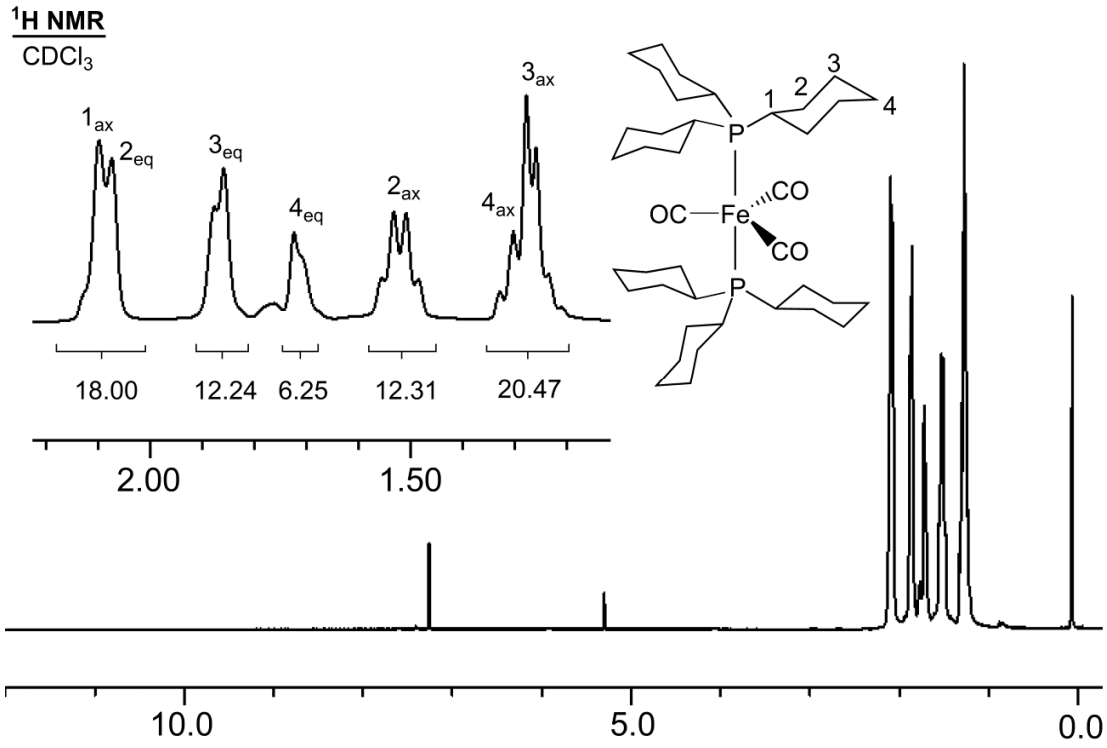
1H NMR
CDCl3
1ax
2eq
3eq
4eq
2ax
4ax
3ax
18.00
12.24
6.25
12.31
20.47
2.00
1.50
1
2
3
4
P
OC
Fe
CO
CO
P
10.0
5.0
0.0

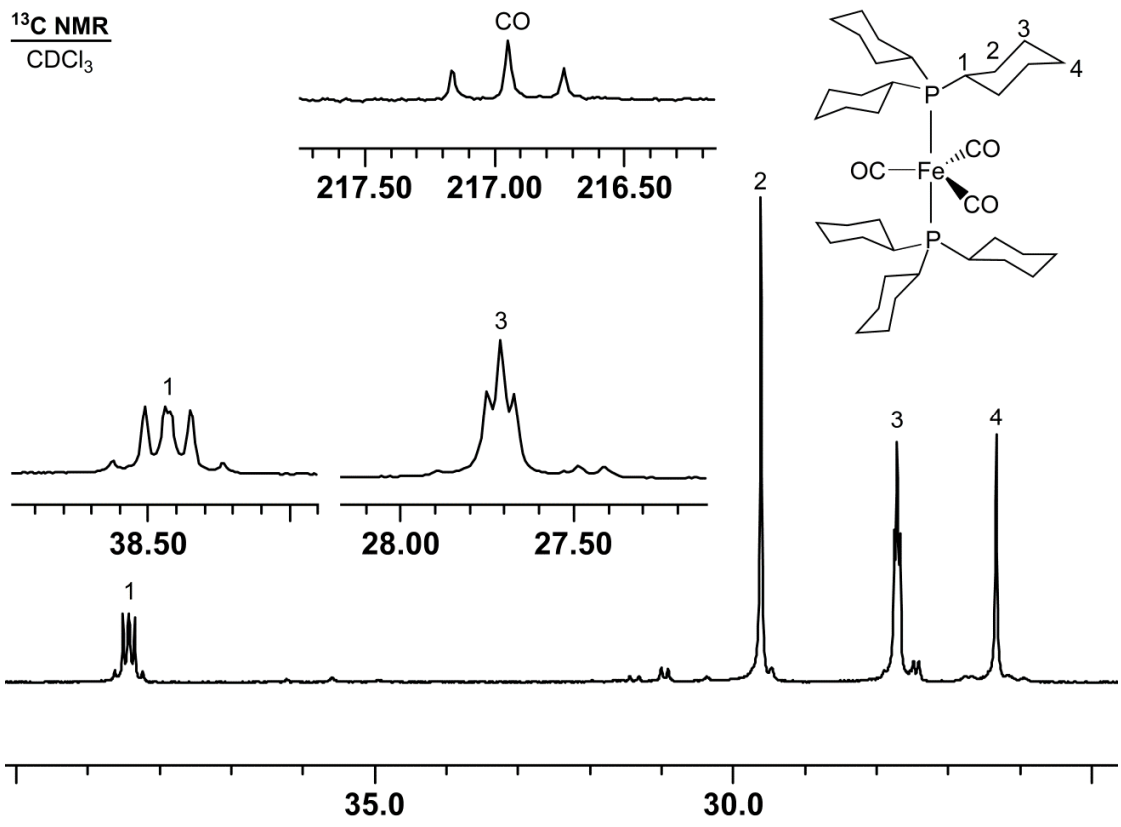
13C NMR
CDCl3
CO
217.50
217.00
216.50
1
2
3
4
P
OC
Fe
CO
CO
P
1
3
38.50
28.00
27.50
1
2
3
4
35.0
30.0

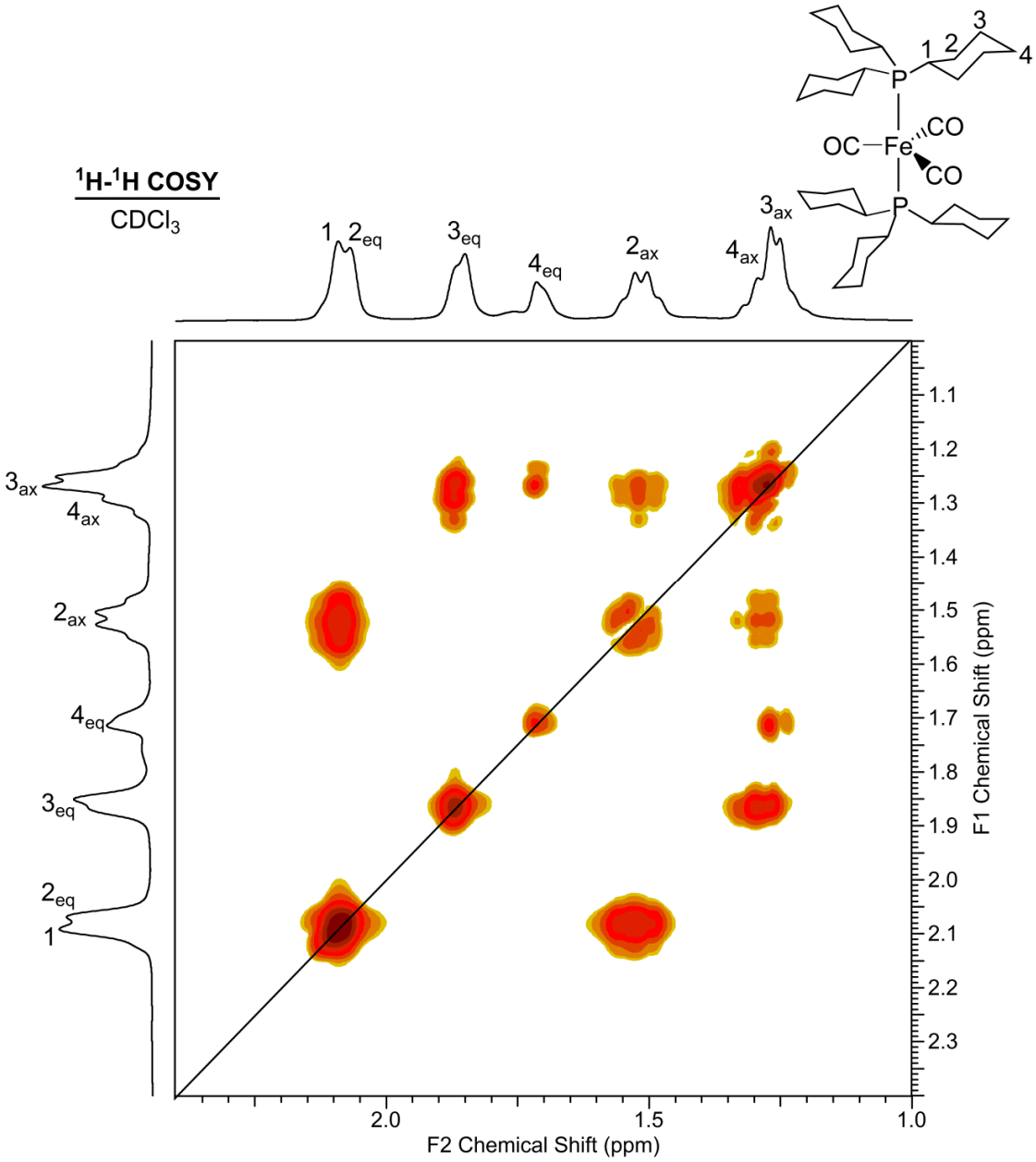
1H-1H COSY
CDCl3
1
2eq
3eq
4eq
2ax
4ax
3ax
OC—Fe—CO
CO
P
P
1
2
3
4
F1 Chemical Shift (ppm)
F2 Chemical Shift (ppm)
2.0
1.5
1.0
1.1
1.2
1.3
1.4
1.5
1.6
1.7
1.8
1.9
2.0
2.1
2.2
2.3

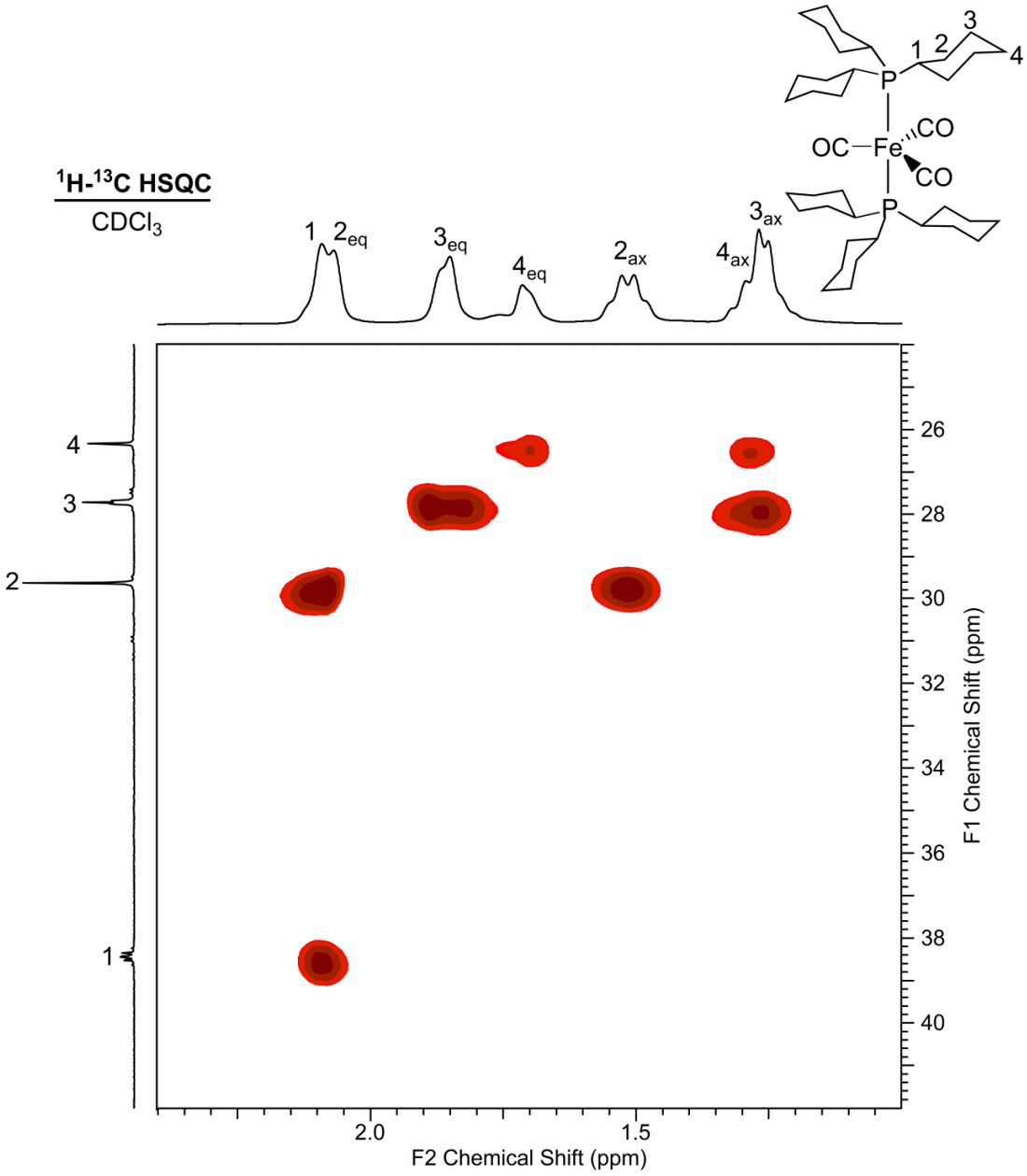
1H-13C HSQC
CDCl3
1
2eq
3eq
4eq
2ax
4ax
3ax
4
3
2
1
2.0
1.5
F2 Chemical Shift (ppm)
26
28
30
32
34
36
38
40
F1 Chemical Shift (ppm)
P
OC
Fe
CO
CO
P
1
2
3
4

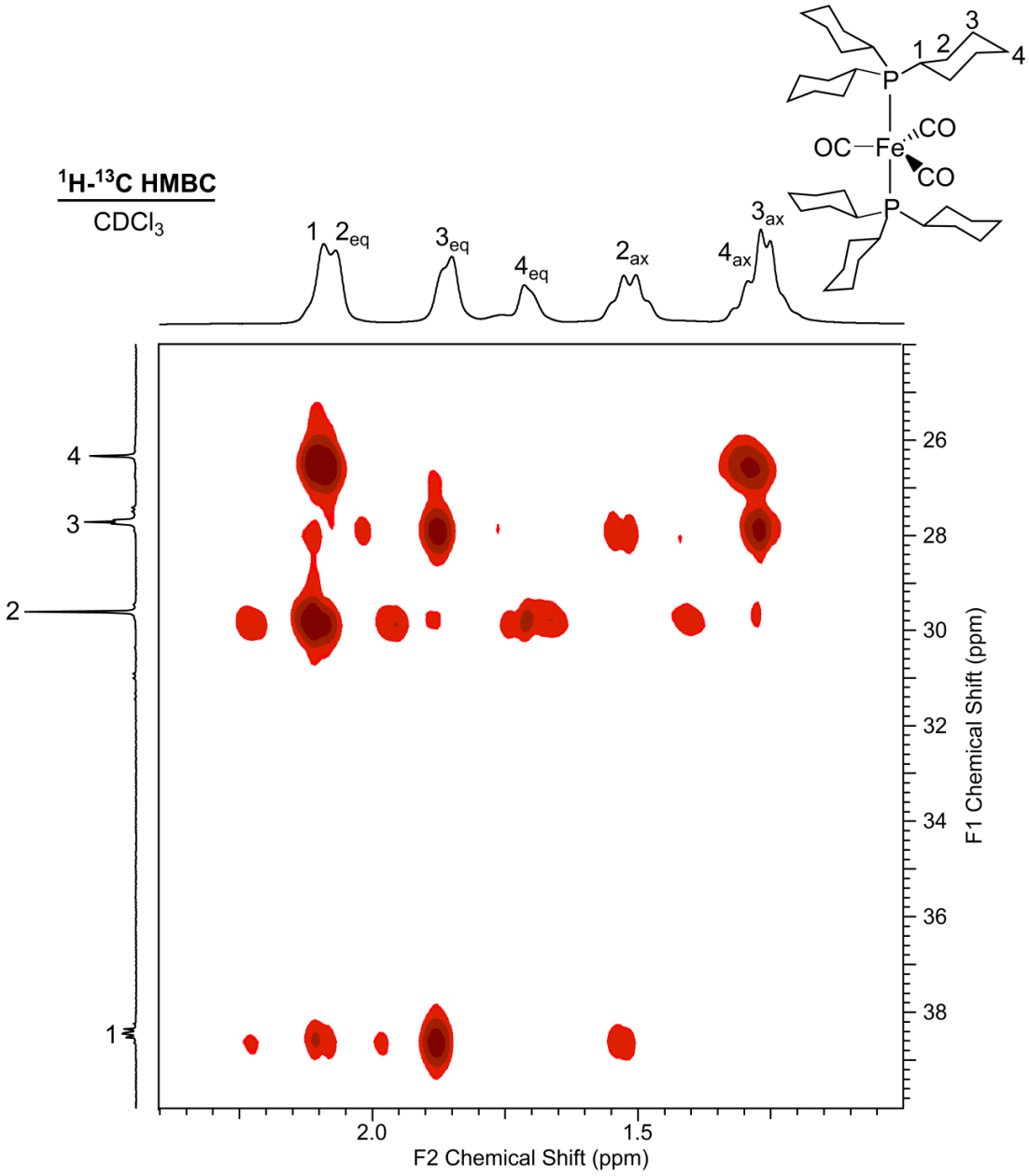
1H-13C HMBC
CDCl3
1
2eq
3eq
4eq
2ax
4ax
3ax
4
3
2
1
2.0
1.5
F2 Chemical Shift (ppm)
26
28
30
32
34
36
38
F1 Chemical Shift (ppm)
P
OC
Fe
CO
CO
P

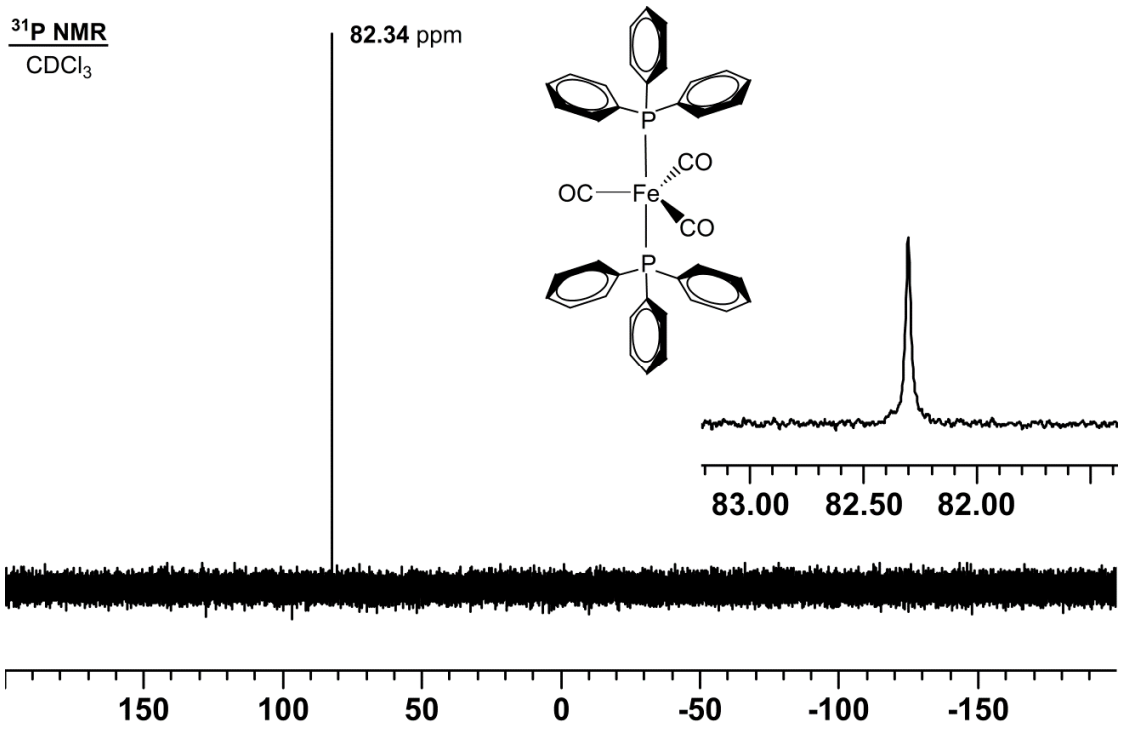
31P NMR
CDCl3
82.34 ppm
P
CO
OC
Fe
CO
P
83.00
82.50
82.00
150
100
50
0
-50
-100
-150

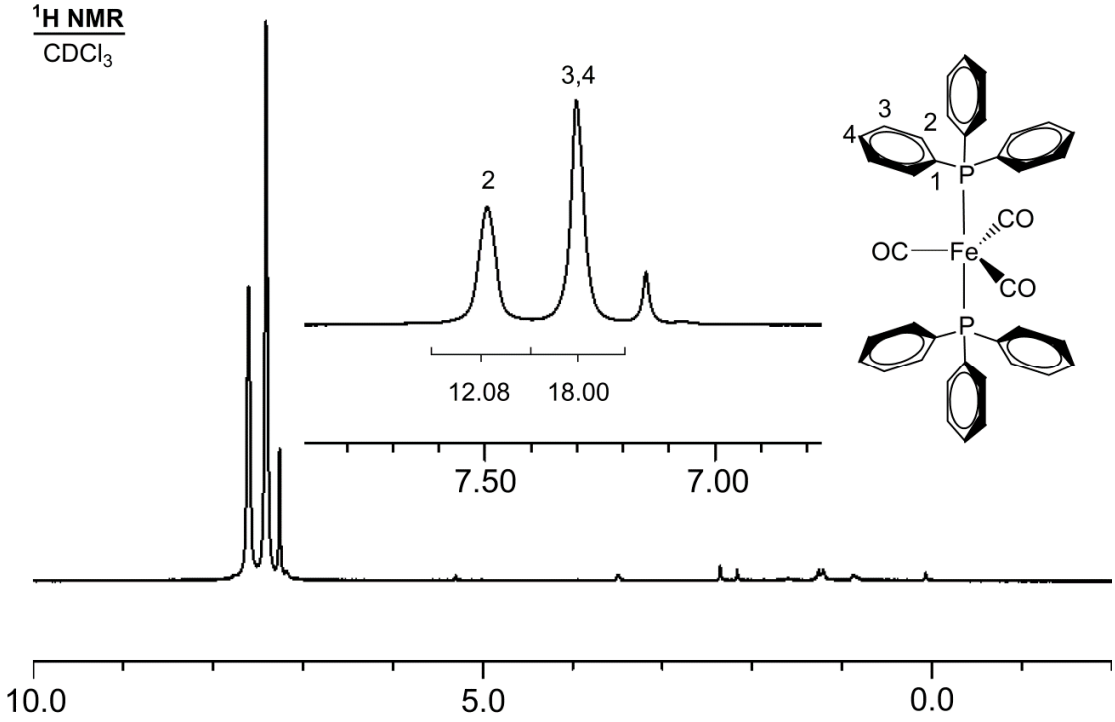
1H NMR
CDCl3
3,4
2
12.08
18.00
7.50
7.00
3
2
4
1
P
CO
OC
Fe
CO
P
10.0
5.0
0.0

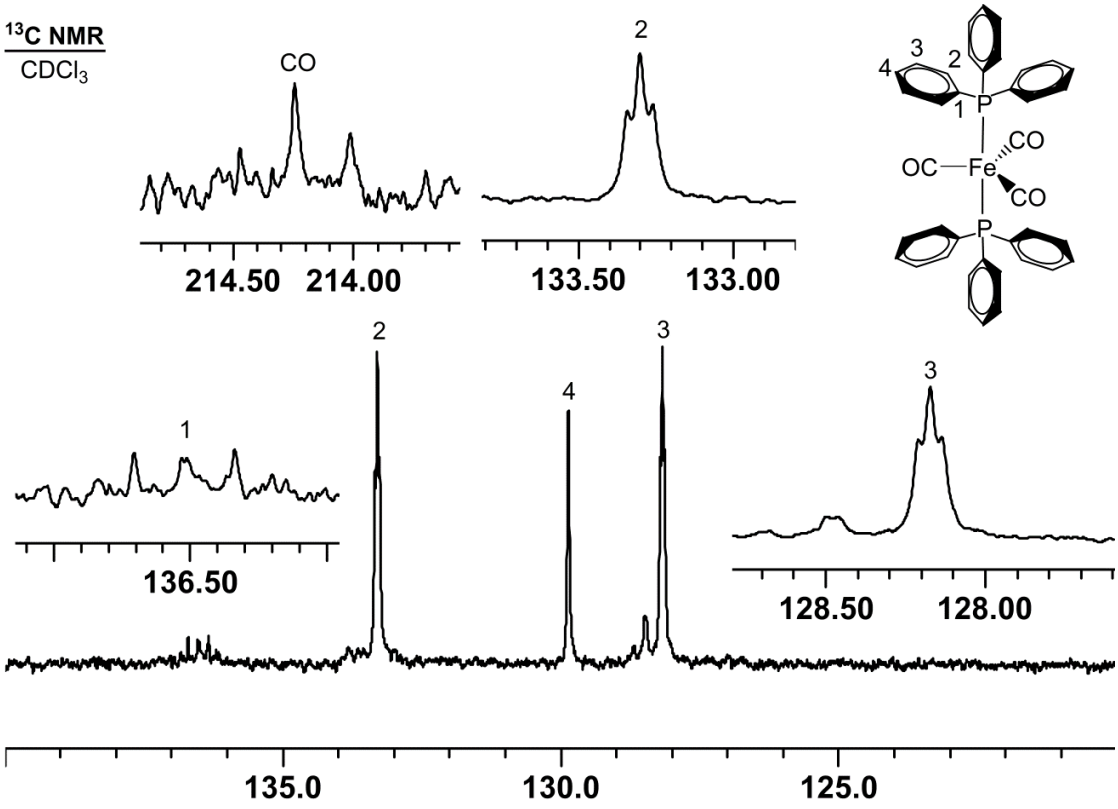
13C NMR
CDCl3
CO
2
214.50
214.00
133.50
133.00
4
3
2
1
P
CO
OC
Fe
CO
P
1
2
4
3
3
136.50
128.50
128.00
135.0
130.0
125.0

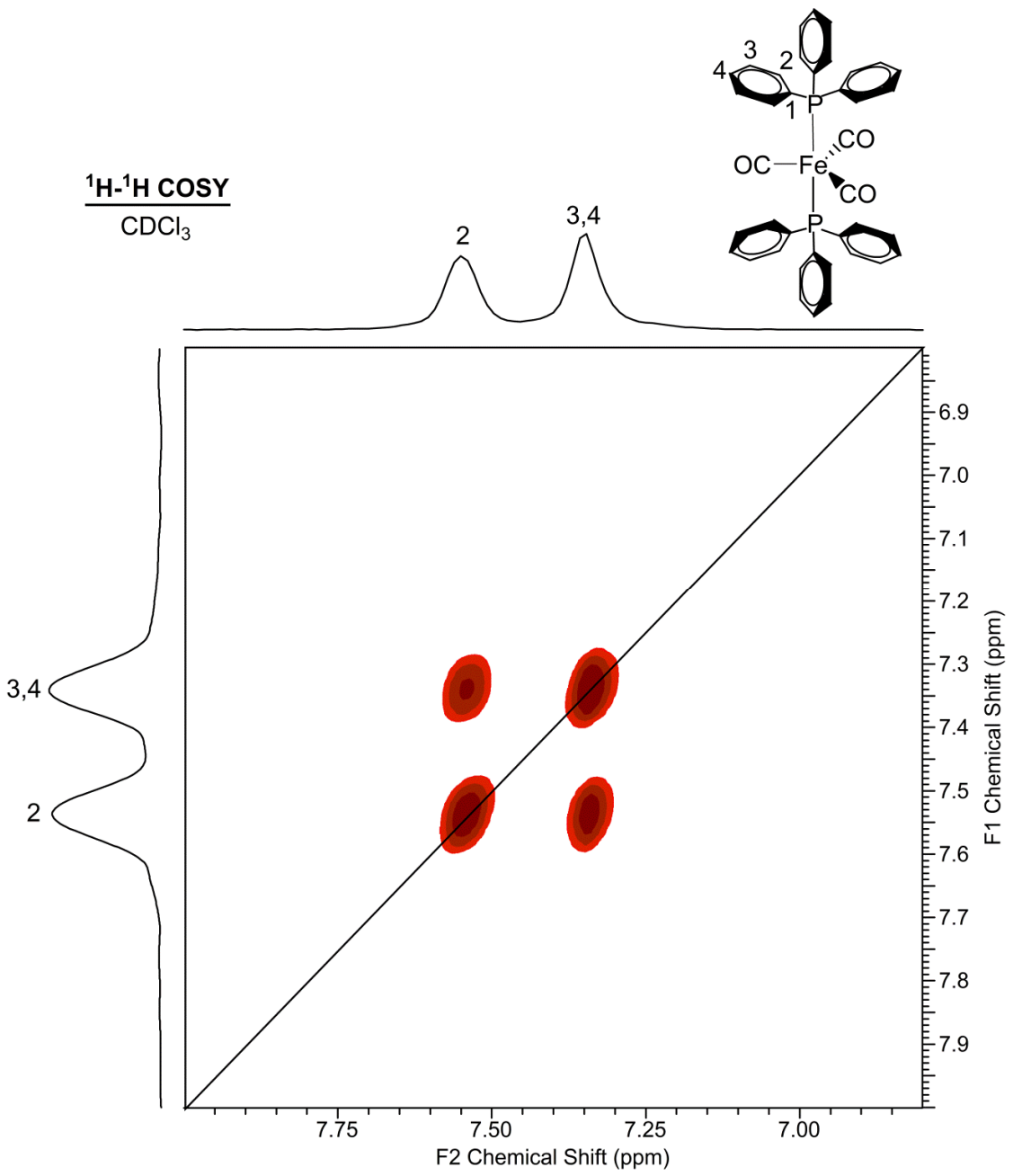
^{1}H-^{1}H COSY
$CDCl_3$
2
3,4
4
3
2
1
P
CO
OC—Fe
CO
P
3,4
2
6.9
7.0
7.1
7.2
7.3
7.4
7.5
7.6
7.7
7.8
7.9
F1 Chemical Shift (ppm)
7.75
7.50
7.25
7.00
F2 Chemical Shift (ppm)

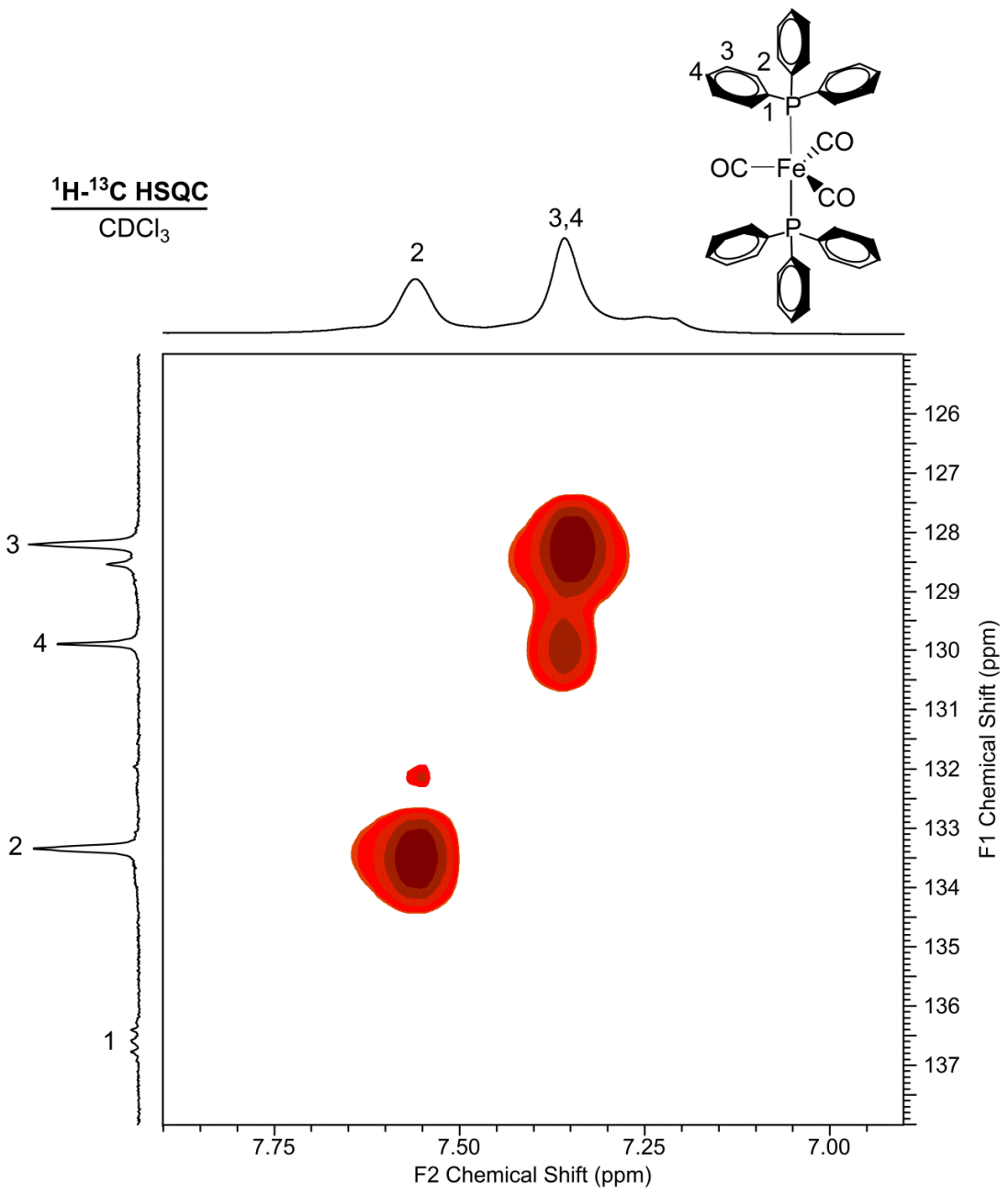
^{1}H-^{13}C HSQC
$CDCl_3$
2
3,4
3
2
4
1
P
CO
OC
Fe
CO
P
3
4
2
1
126
127
128
129
130
131
132
133
134
135
136
137
F1 Chemical Shift (ppm)
7.75
7.50
7.25
7.00
F2 Chemical Shift (ppm)

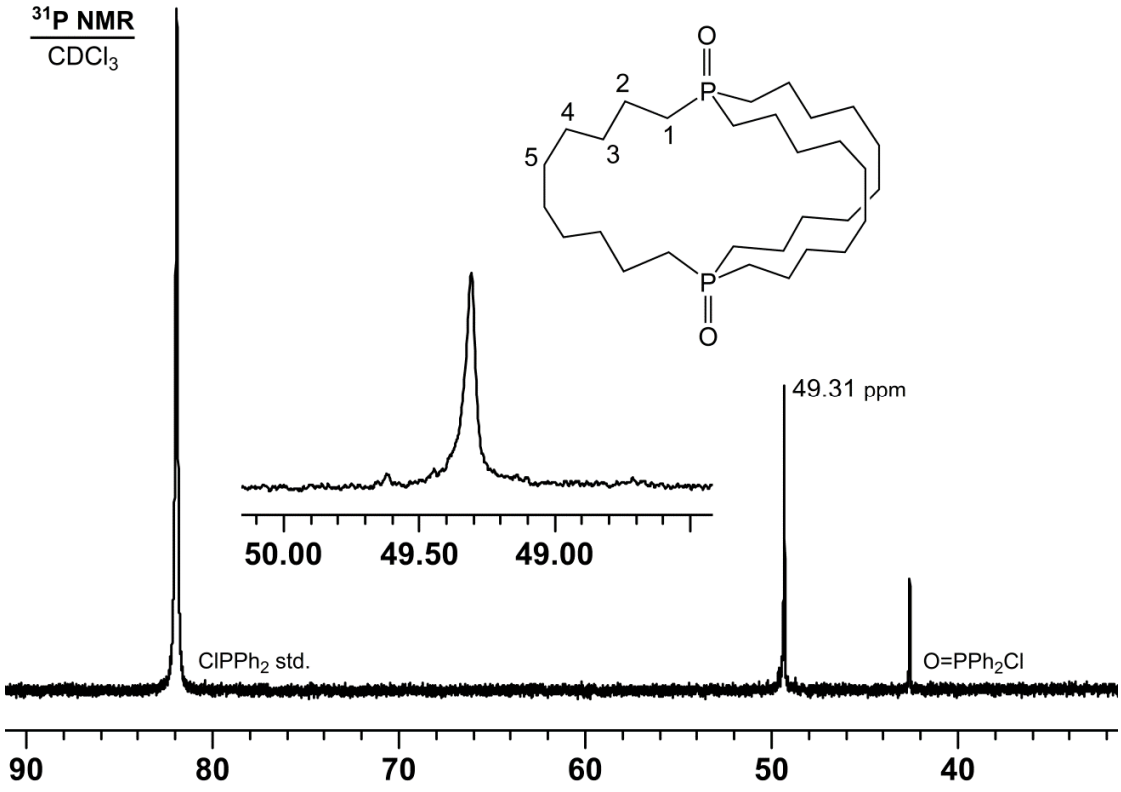
31P NMR
CDCl3
O
P
1
2
3
4
5
P
O
49.31 ppm
50.00
49.50
49.00
ClPPh2 std.
O=PPh2Cl
90
80
70
60
50
40

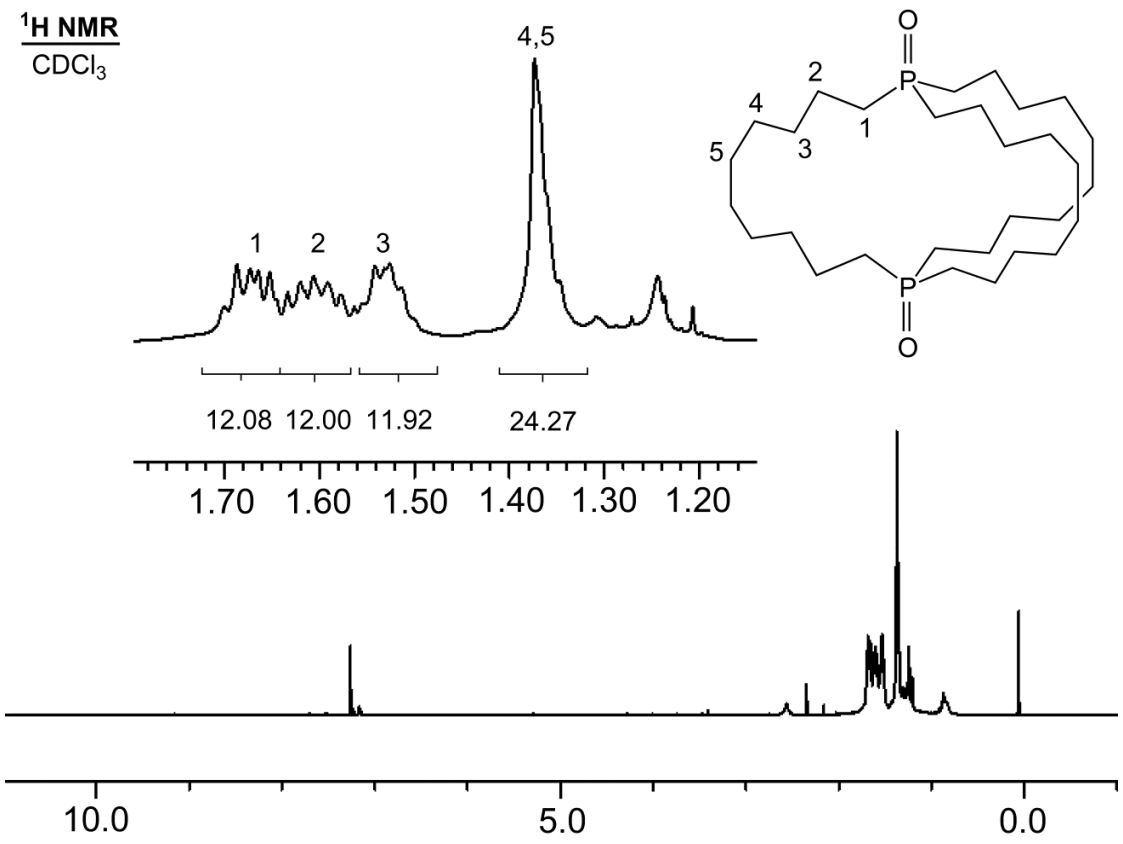
1H NMR
CDCl3
4,5
1
2
3
12.08
12.00
11.92
24.27
1.70
1.60
1.50
1.40
1.30
1.20
10.0
5.0
0.0
O
P
2
4
1
5
3
P
O

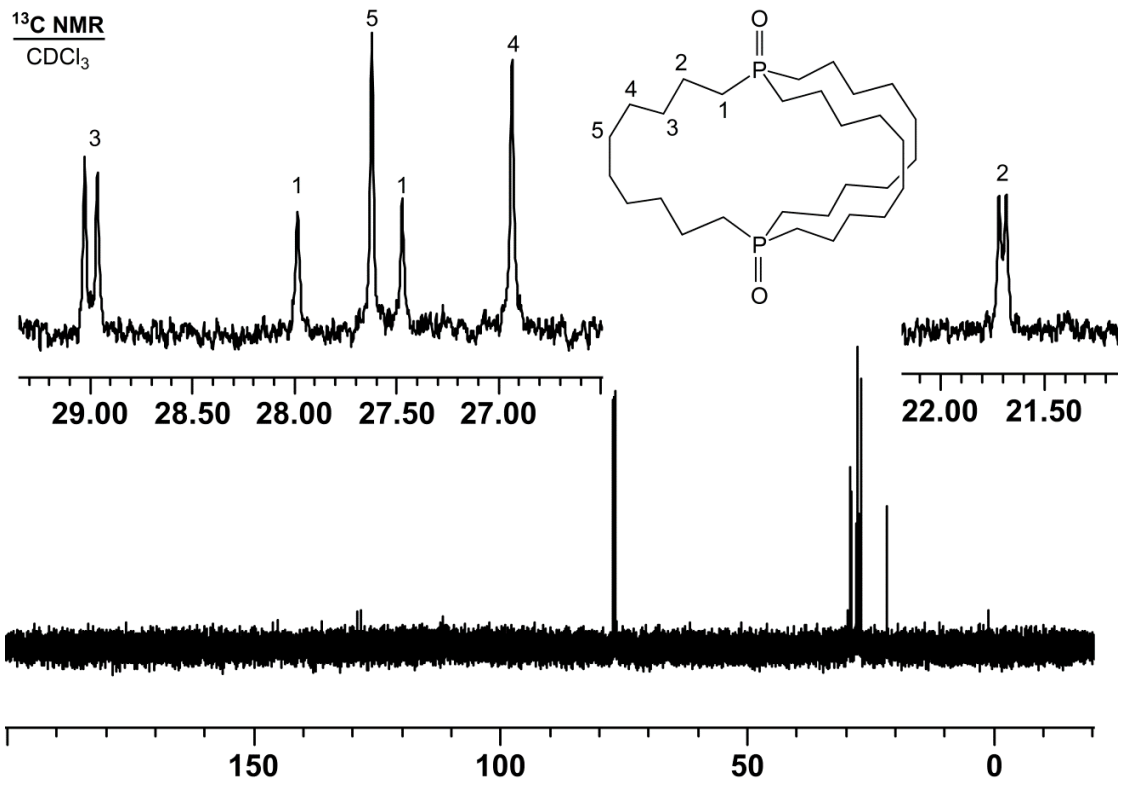
13C NMR
CDCl3
3
1
5
1
4
2
4
3
5
1
O
P
P
O
2
29.00
28.50
28.00
27.50
27.00
22.00
21.50
150
100
50
0

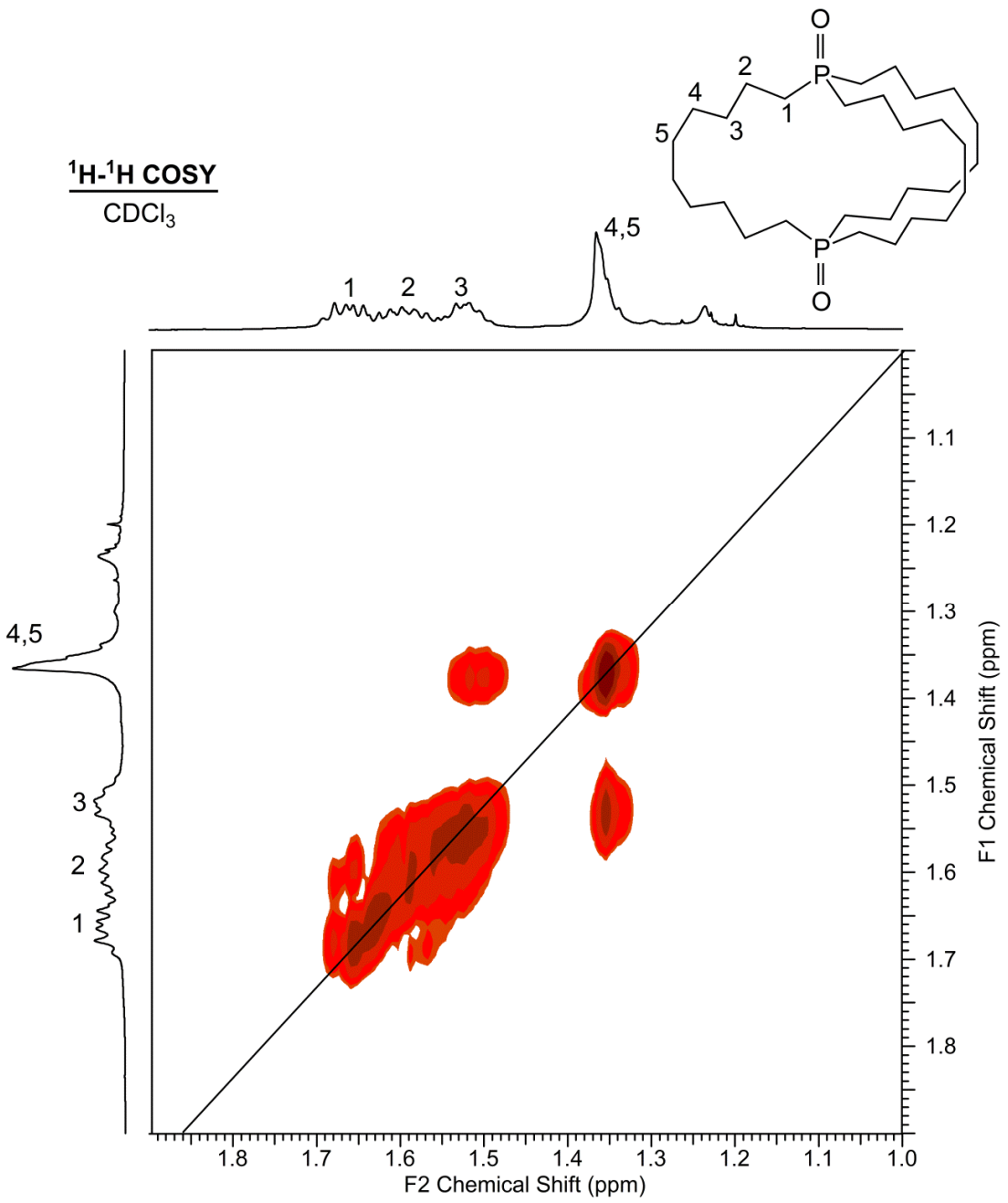
^{1}H-^{1}H COSY
$CDCl_3$
O
P
2
4
1
5
3
P
O
4,5
1
2
3
4,5
3
2
1
1.1
1.2
1.3
1.4
1.5
1.6
1.7
1.8
F1 Chemical Shift (ppm)
1.8
1.7
1.6
1.5
1.4
1.3
1.2
1.1
1.0
F2 Chemical Shift (ppm)

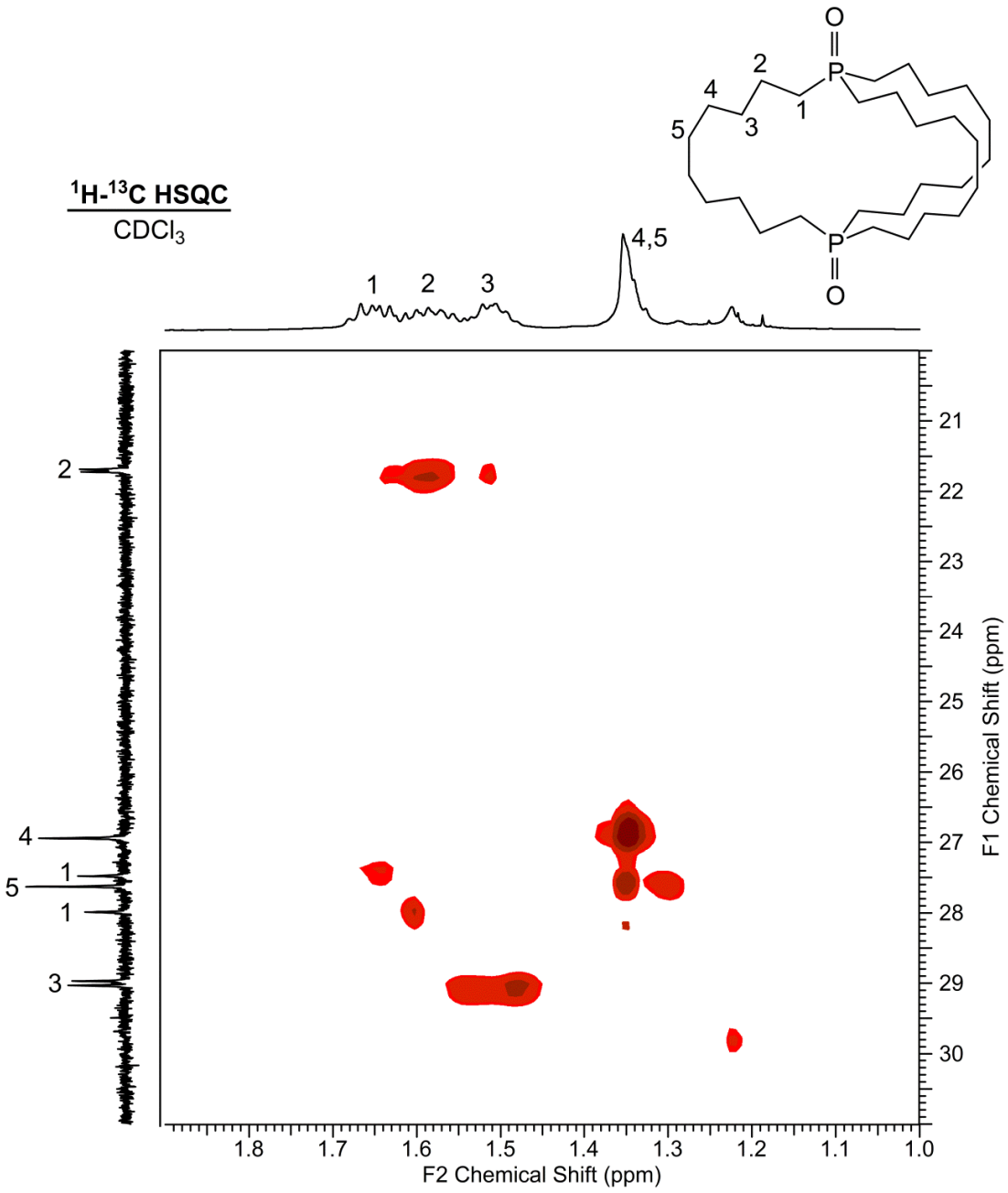
^{1}H-^{13}C HSQC
$CDCl_3$
O
P
2
4
1
5
3
P
O
1
2
3
4,5
2
4
1
5
1
3
21
22
23
24
25
26
27
28
29
30
F1 Chemical Shift (ppm)
1.8
1.7
1.6
1.5
1.4
1.3
1.2
1.1
1.0
F2 Chemical Shift (ppm)

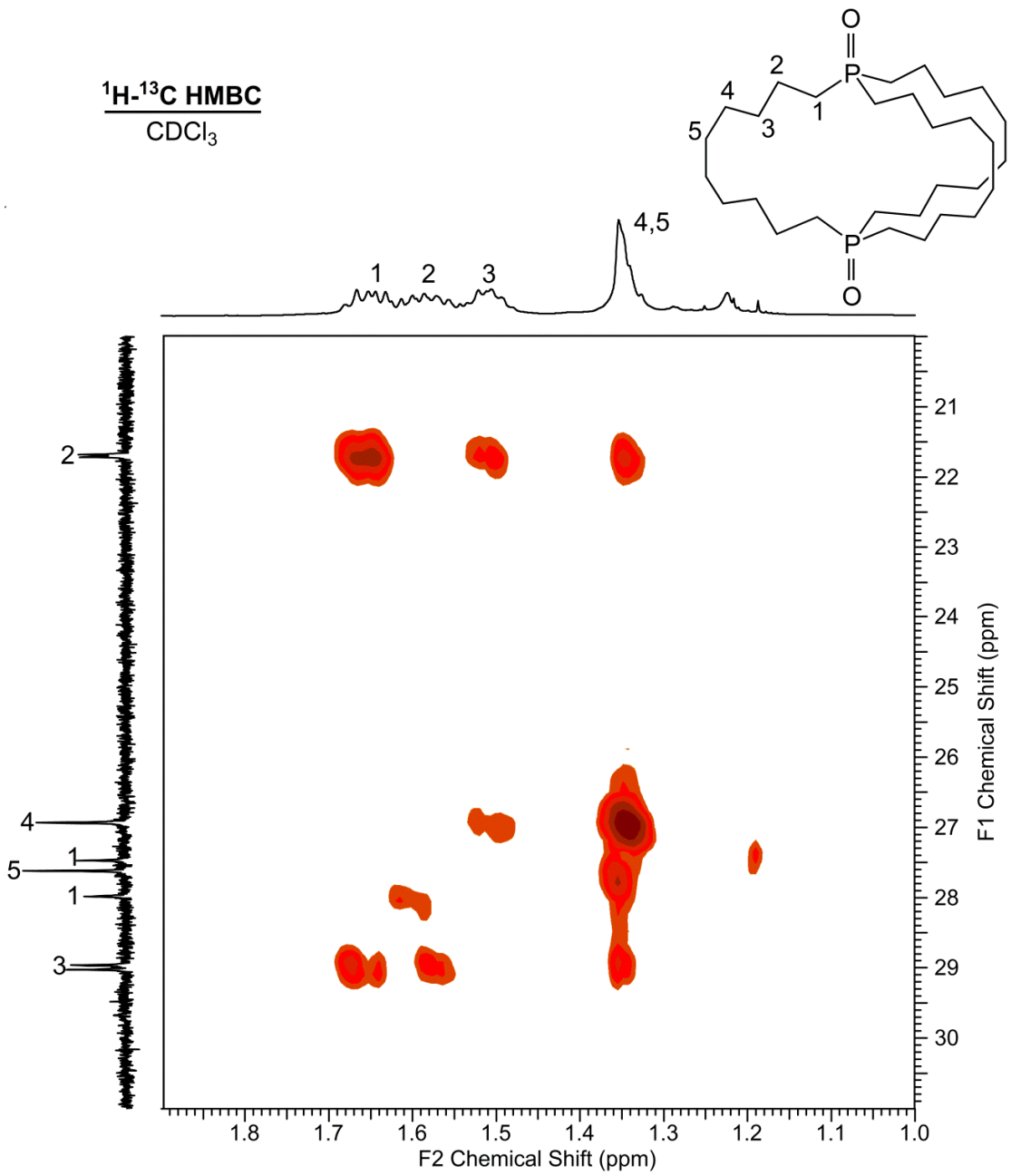
^{1}H-^{13}C HMBC
CDCl$_3$
O
P
P
O
1
2
3
4
5
1
2
3
4,5
2
4
1
5
1
3
1.8
1.7
1.6
1.5
1.4
1.3
1.2
1.1
1.0
F2 Chemical Shift (ppm)
21
22
23
24
25
26
27
28
29
30
F1 Chemical Shift (ppm)

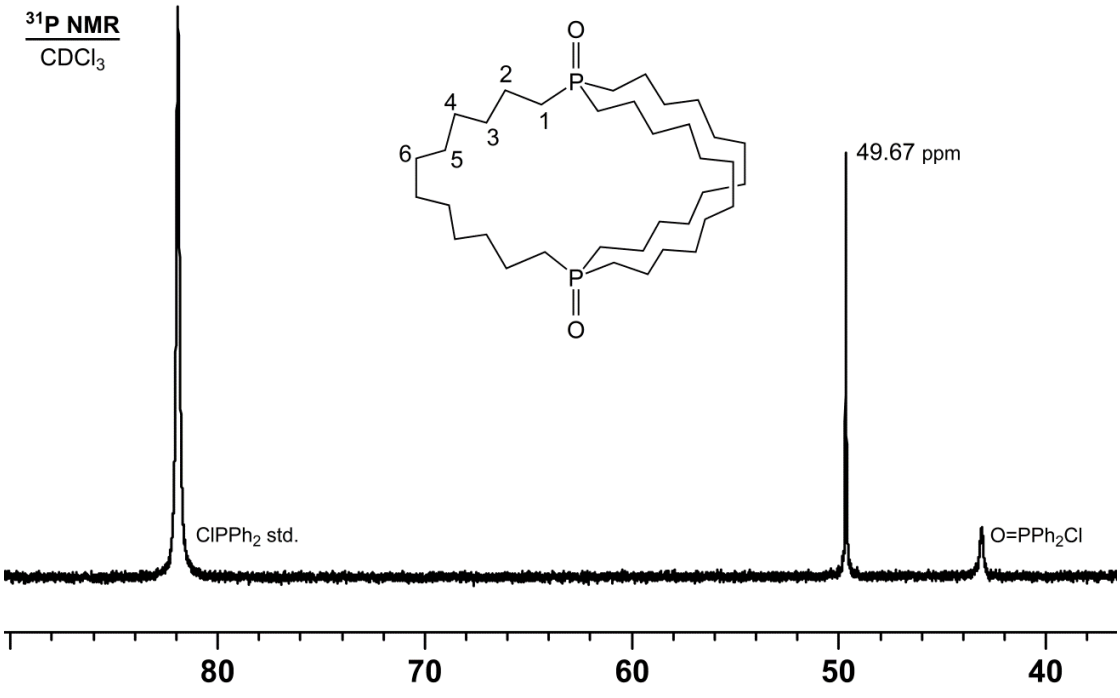
31P NMR
CDCl3
O
P
1
2
3
4
5
6
P
O
49.67 ppm
ClPPh2 std.
O=PPh2Cl
80
70
60
50
40

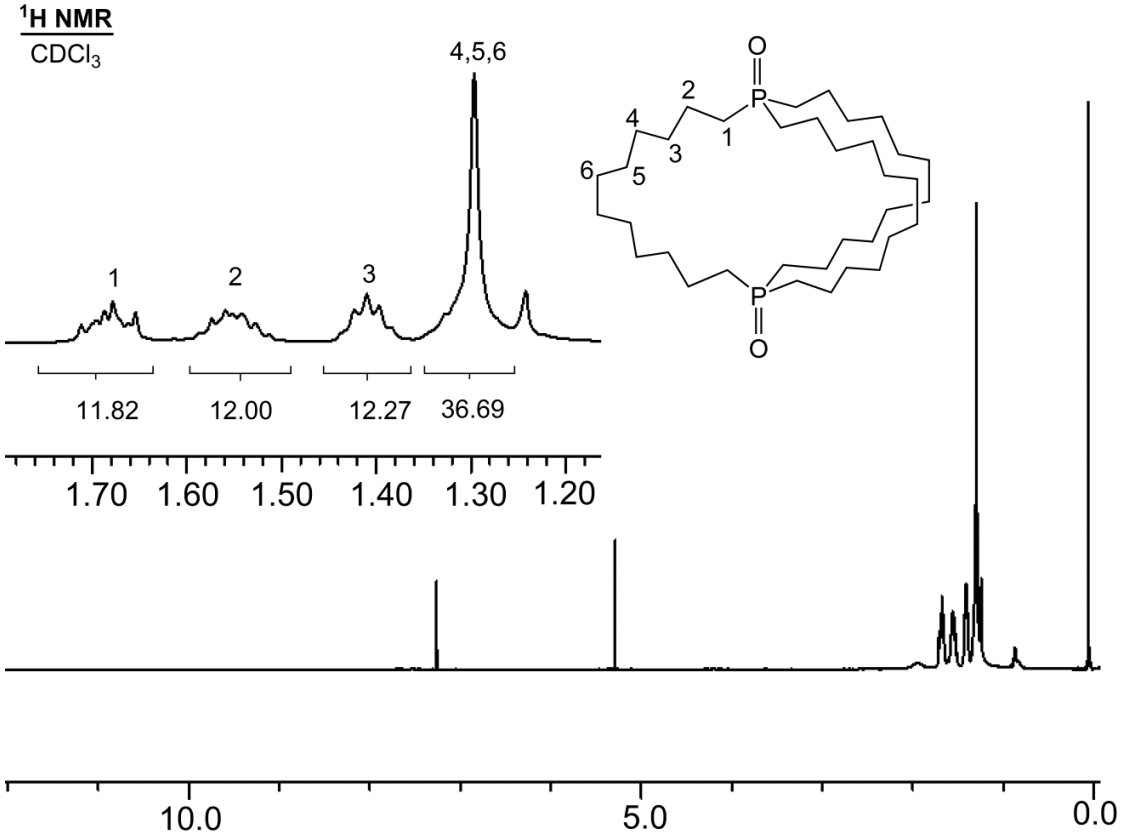
1H NMR
CDCl3
4,5,6
1
2
3
11.82
12.00
12.27
36.69
1.70
1.60
1.50
1.40
1.30
1.20
O
P
O
P
1
2
3
4
5
6
10.0
5.0
0.0

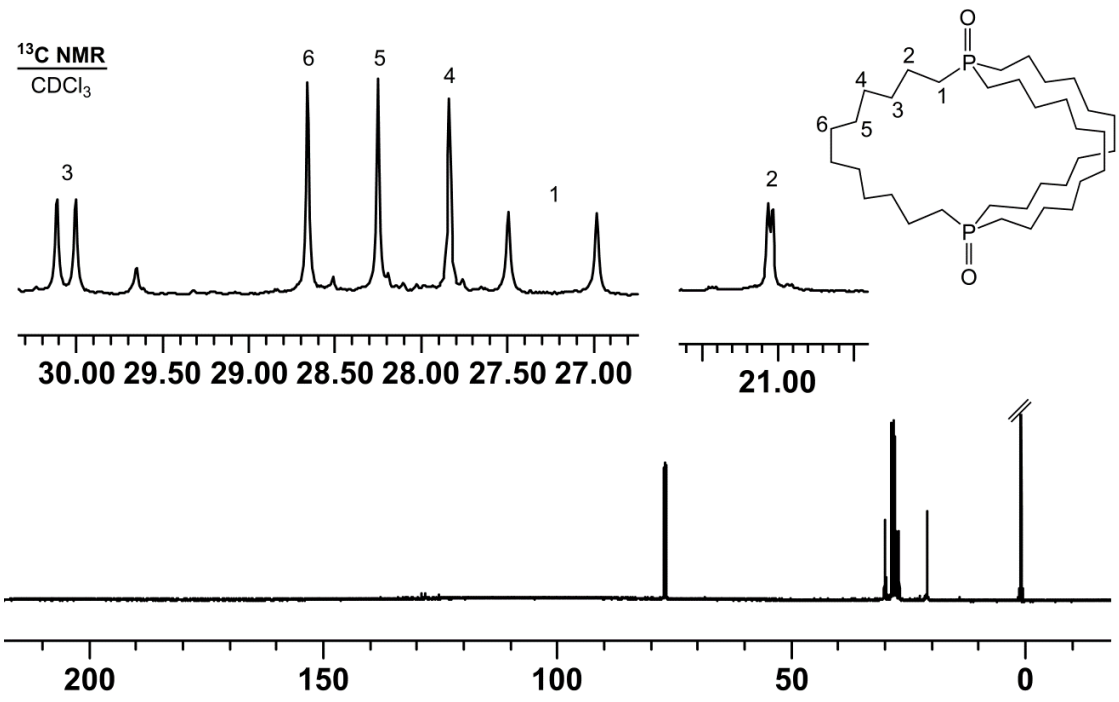
13C NMR
CDCl3
6
5
4
3
1
2
O
P
O
P
30.00 29.50 29.00 28.50 28.00 27.50 27.00
21.00
200
150
100
50
0

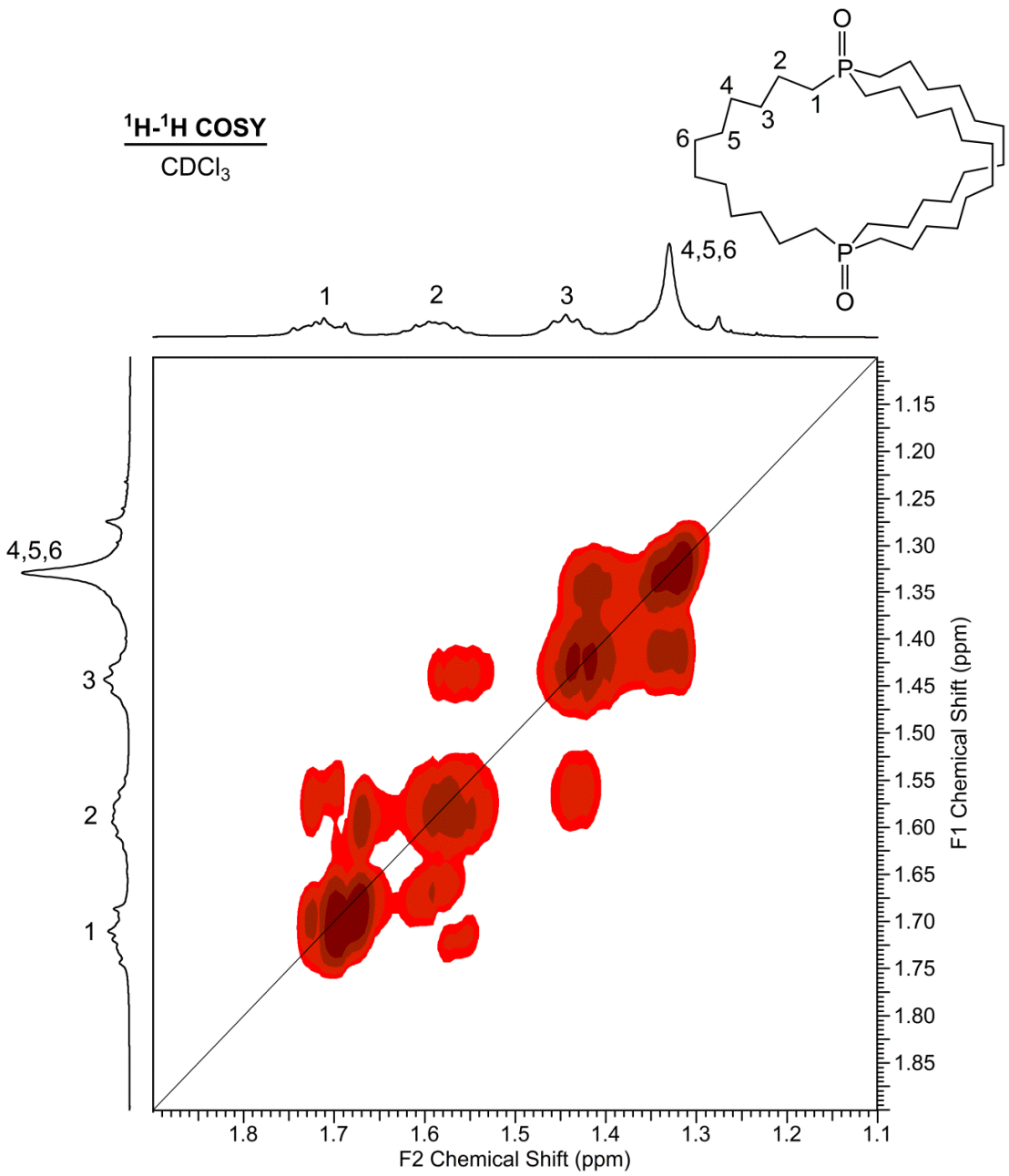
^{1}H-^{1}H COSY
$CDCl_3$
O
P
1
2
3
4
5
6
P
O
4,5,6
1
2
3
4,5,6
3
2
1
1.15
1.20
1.25
1.30
1.35
1.40
1.45
1.50
1.55
1.60
1.65
1.70
1.75
1.80
1.85
F1 Chemical Shift (ppm)
1.8
1.7
1.6
1.5
1.4
1.3
1.2
1.1
F2 Chemical Shift (ppm)

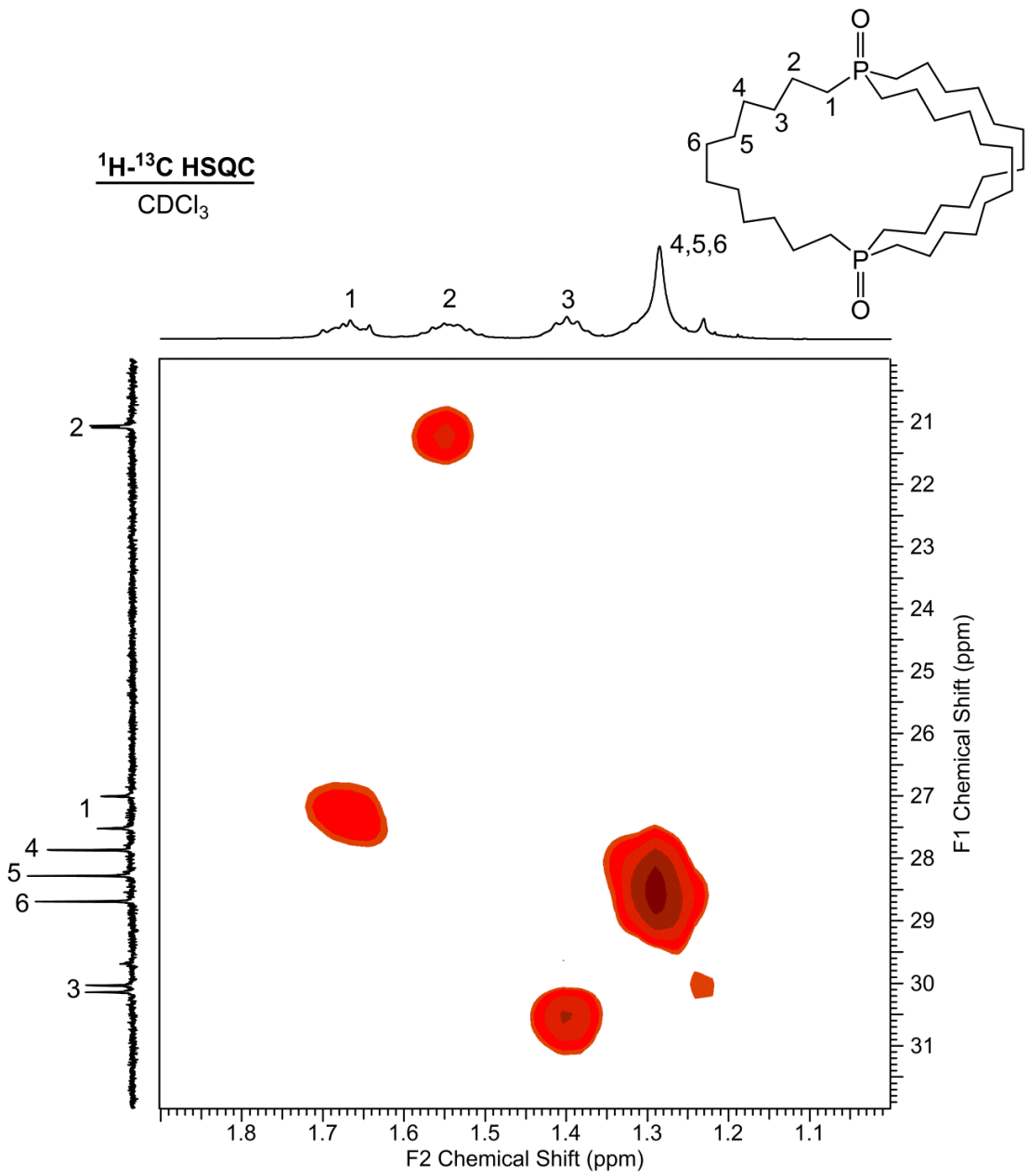
^{1}H-^{13}C HSQC
$CDCl_3$
O
P
1
2
3
4
5
6
P
O
4,5,6
1
2
3
2
1
4
5
6
3
21
22
23
24
25
26
27
28
29
30
31
F1 Chemical Shift (ppm)
1.8
1.7
1.6
1.5
1.4
1.3
1.2
1.1
F2 Chemical Shift (ppm)

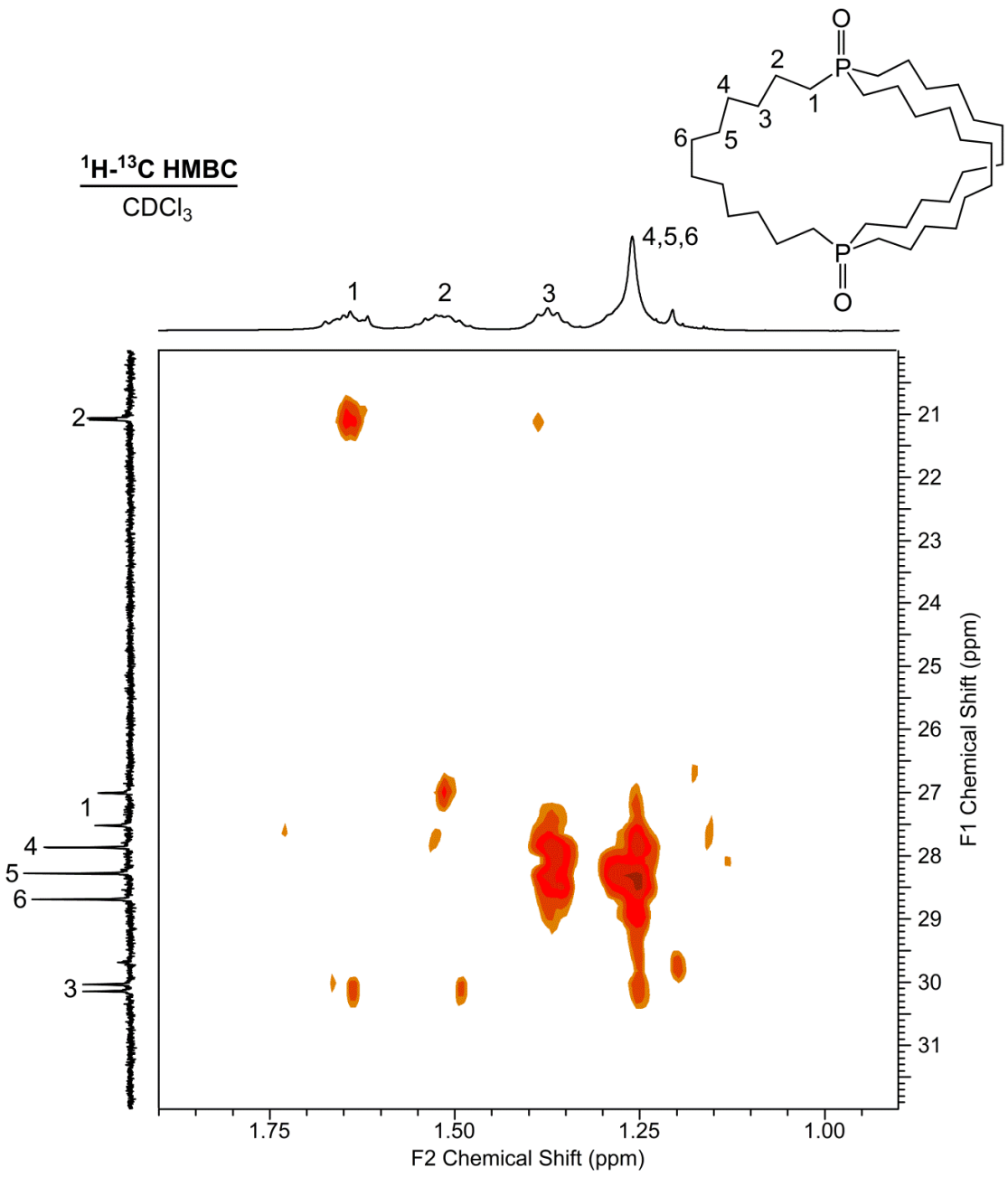
^{1}H-^{13}C HMBC
$CDCl_3$
O
P
1
2
3
4
5
6
4,5,6
1
2
3
2
1
4
5
6
3
21
22
23
24
25
26
27
28
29
30
31
F1 Chemical Shift (ppm)
1.75
1.50
1.25
1.00
F2 Chemical Shift (ppm)

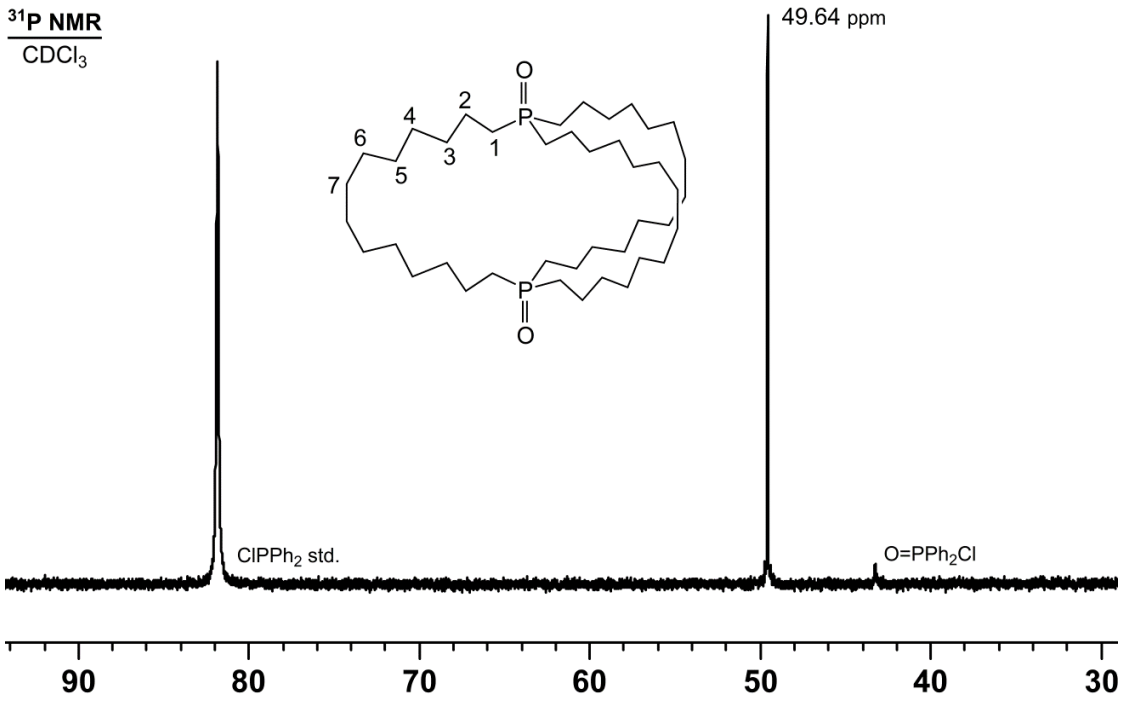
31P NMR
CDCl3
49.64 ppm
ClPPh2 std.
O=PPh2Cl
90
80
70
60
50
40
30

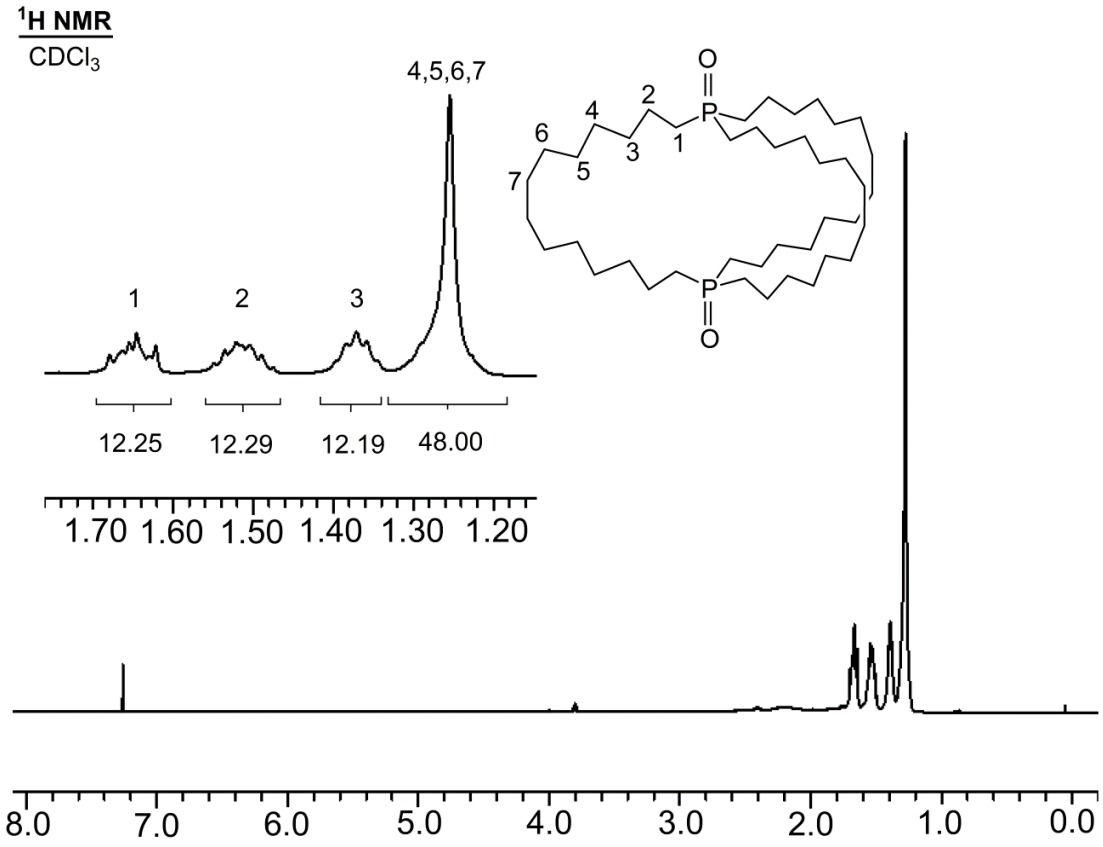
1H NMR
CDCl3
4,5,6,7
1
2
3
12.25
12.29
12.19
48.00
1.70 1.60 1.50 1.40 1.30 1.20
8.0 7.0 6.0 5.0 4.0 3.0 2.0 1.0 0.0
O
P
O
P
1
2
3
4
5
6
7

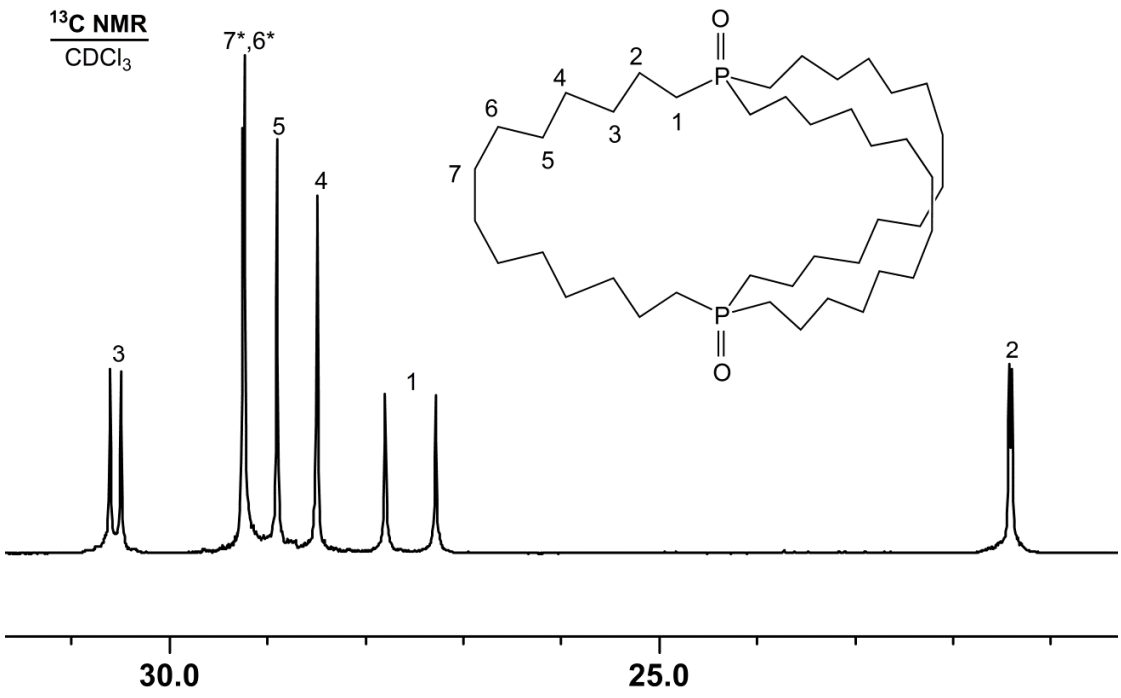
13C NMR
CDCl3
7*,6*
5
4
3
1
2
O
P
O
P
1
2
3
4
5
6
7
30.0
25.0

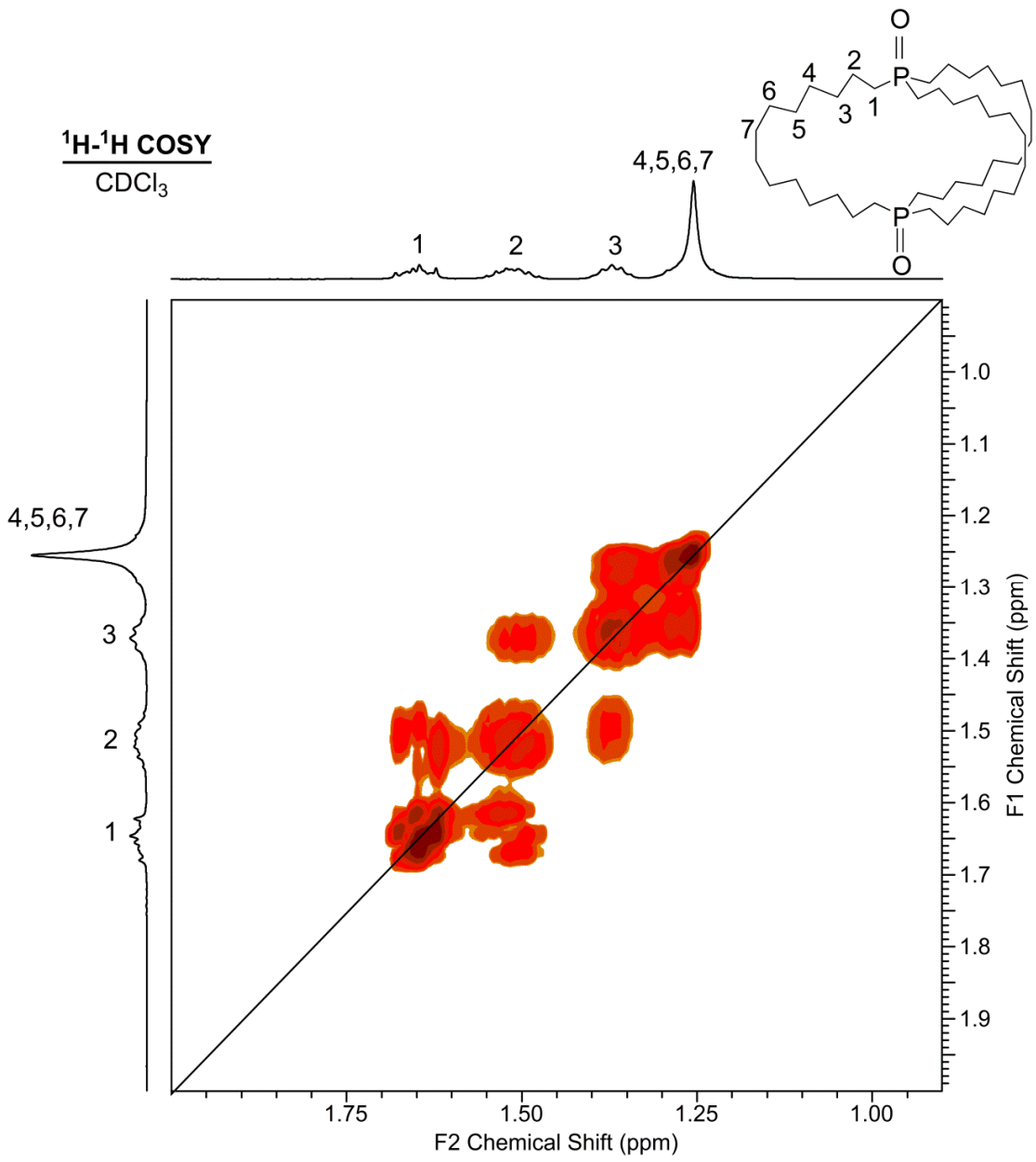
^{1}H-^{1}H COSY
$CDCl_3$
4,5,6,7
1
2
3
O
P
P
O
1
2
3
4
5
6
7
4,5,6,7
3
2
1
1.75
1.50
1.25
1.00
F2 Chemical Shift (ppm)
1.0
1.1
1.2
1.3
1.4
1.5
1.6
1.7
1.8
1.9
F1 Chemical Shift (ppm)

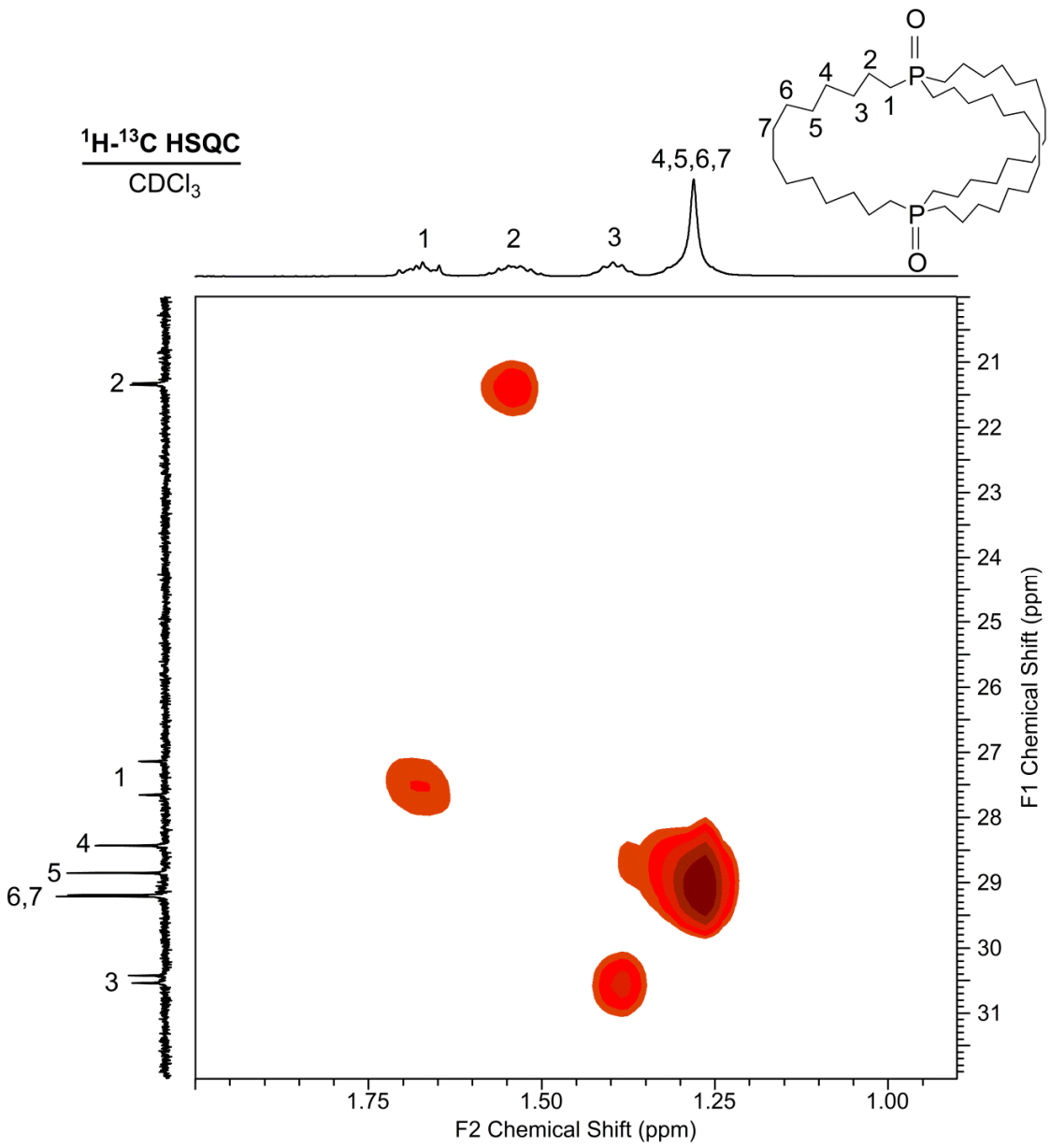
^{1}H-^{13}C HSQC
$CDCl_3$
4,5,6,7
1
2
3
O
P
P
O
1
2
3
4
5
6
7
2
1
4
5
6,7
3
21
22
23
24
25
26
27
28
29
30
31
F1 Chemical Shift (ppm)
1.75
1.50
1.25
1.00
F2 Chemical Shift (ppm)

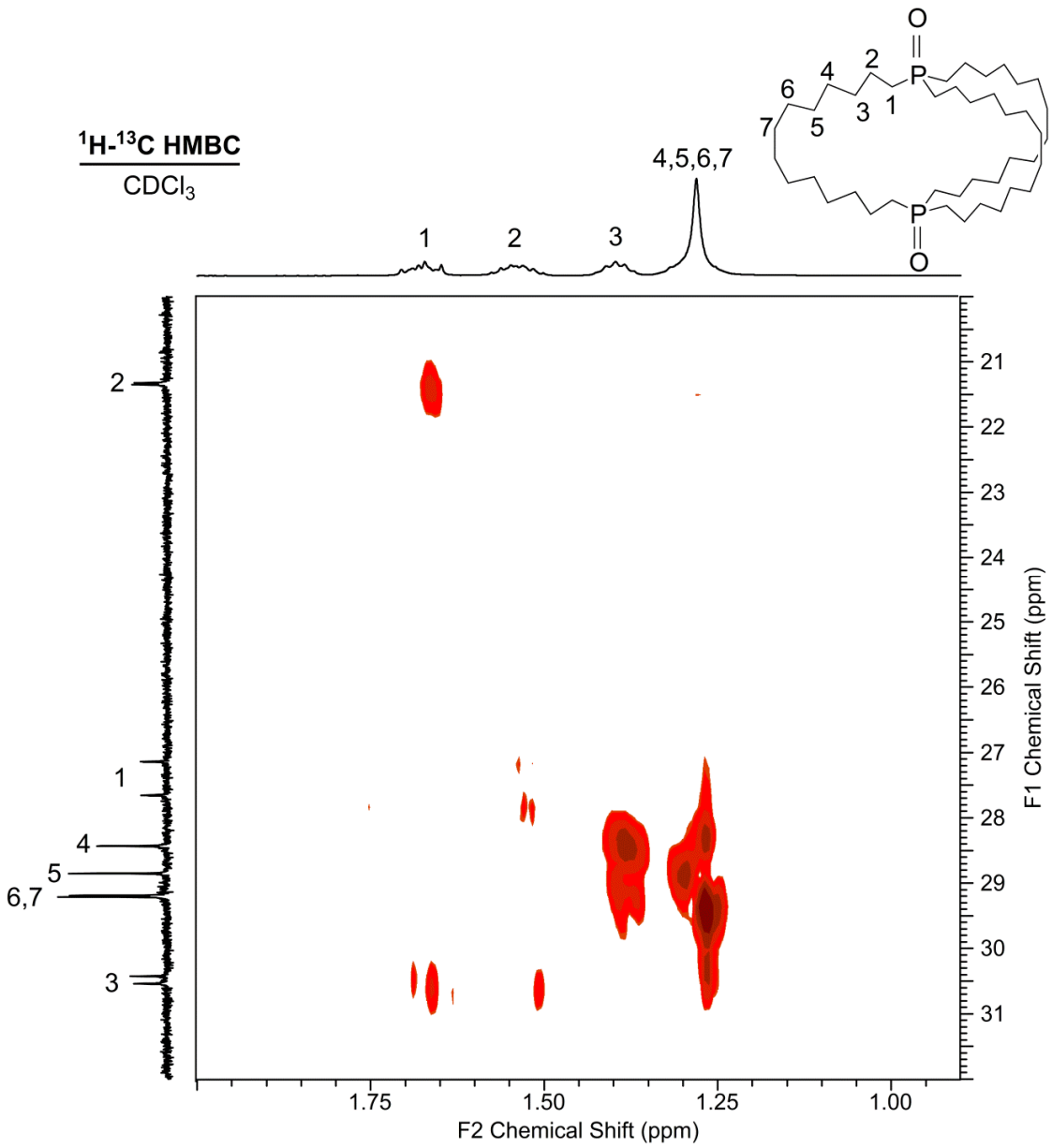
^{1}H-^{13}C HMBC
CDCl$_3$
4,5,6,7
1
2
3
O
P
P
O
2
1
4
5
6,7
3
21
22
23
24
25
26
27
28
29
30
31
F1 Chemical Shift (ppm)
1.75
1.50
1.25
1.00
F2 Chemical Shift (ppm)

APPENDIX C

MASS SPECTROMETRY DATA

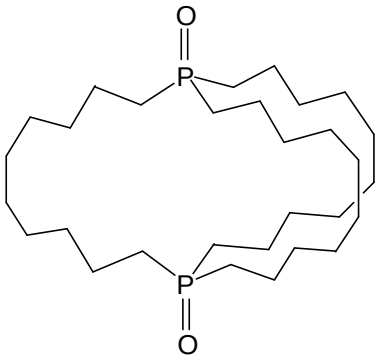

$C_{30}H_{60}O_2P_2$

Monoisotopic mass of 31: 514.41 g/mol

Monoisotopic mass of $[31+H]^+$: 515.41g/mol

Isotope pattern of $[31+H]^+$: 515 (100%), 516 (34.4%), 517 (6.1%) [Simulation]

Experimental totals: 515 (100%), 516 (80.6%), 517 (12.1%), 518 (1.2%)

100% $[31+H]^+$: 515 (100%), 516 (34.4%), 517 (6.1%)

46% impurity: 516 (46.2%), 517 (6.0%), 518 (1.2%)

➔ MS (positive ESI): 515 ([**31**+H]$^+$, 100%), 516 (impurity, 46%).[b]

[b] In contrast to cages **32** and **33**, the smallest dioxide cage **31** showed an impurity in about 46% in the isotope envelope at 516 m/z. Although the peak would correspond to [**31**+2H]$^+$, this would be expected to be a dication that would appear at 258 m/z, which is not observed in the spectrum.

Simulation:

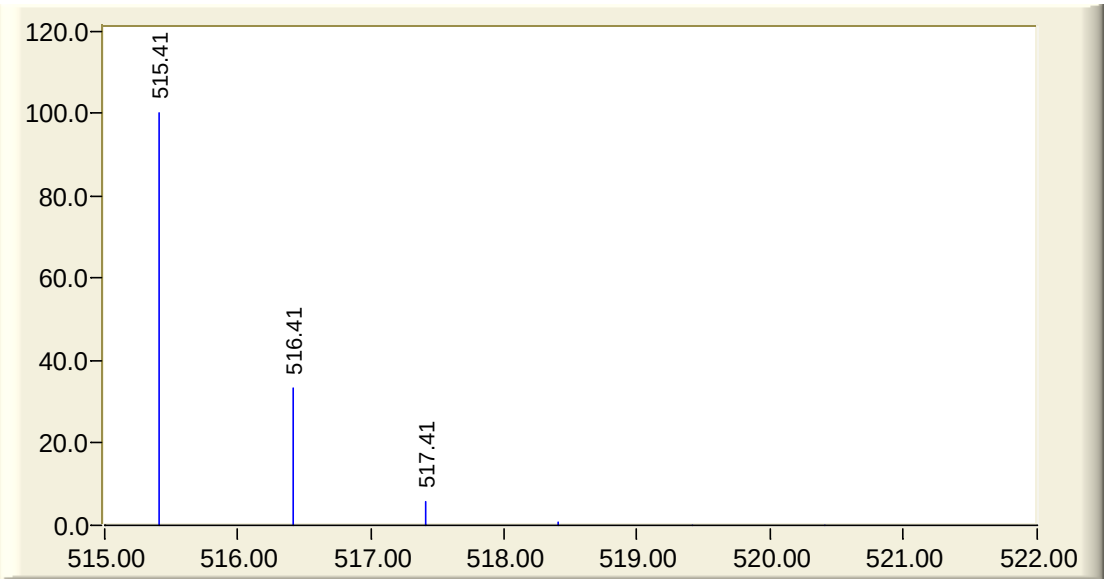

Simulation performed by the Molecular Weight Calculator provided by Pacific Northwest National Laboratory under the U.S. Department of Energy. The total percentage values for each peak are summarized above.

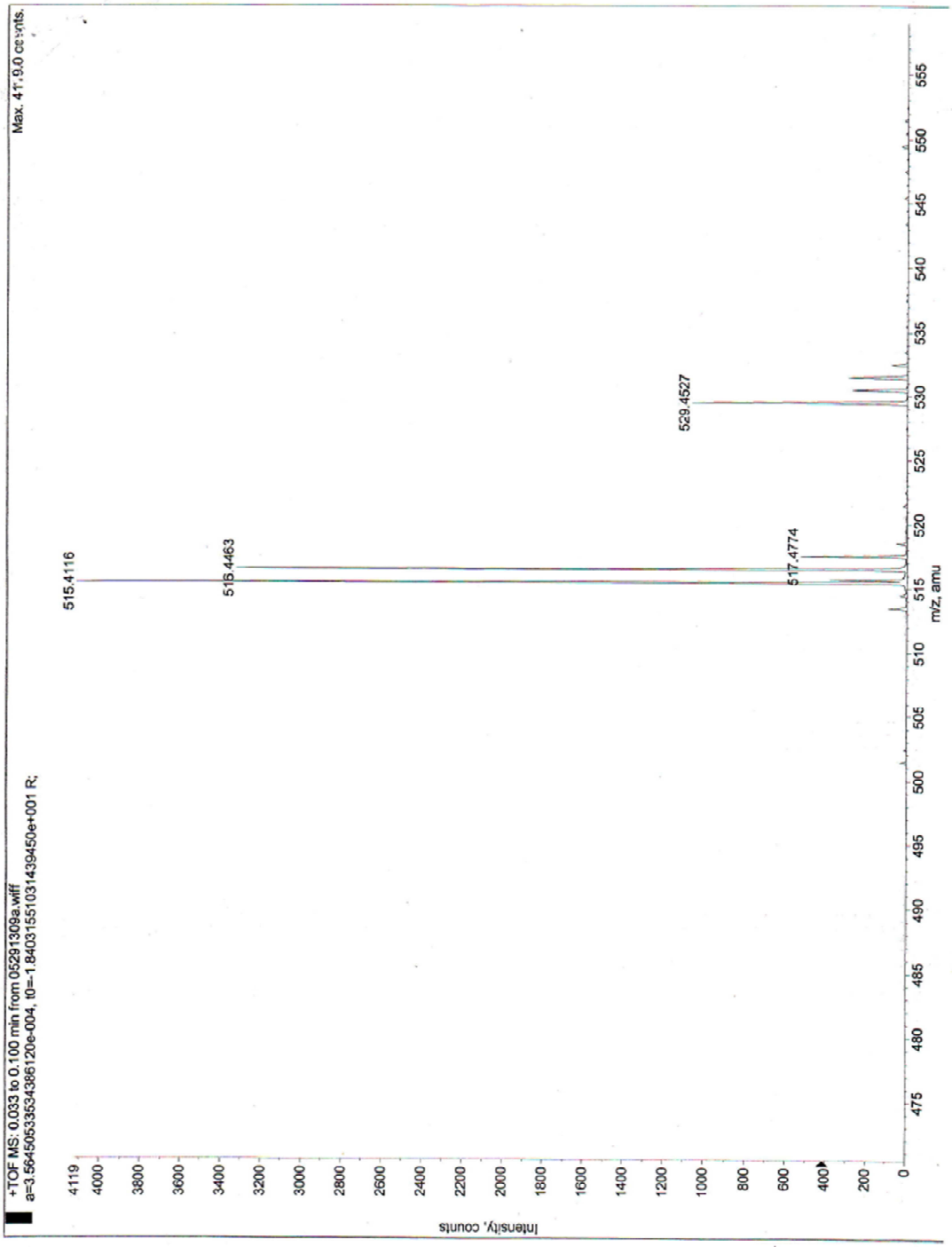
+TOF MS: 0.033 to 0.100 min from 05291309a.wiff
a=3.56450633534386120e-004, t0=-1.84031551031439450e+001 R;
Max. 41,9.0 counts.
515.4116
516.4463
517.4774
529.4527
Intensity, counts
m/z, amu

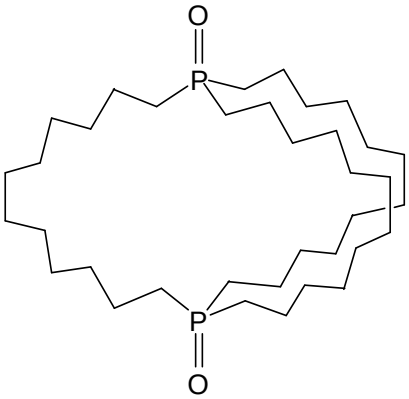

$C_{36}H_{72}O_2P_2$

Monoisotopic mass of 32: 598.51 g/mol

Monoisotopic mass of $[32+H]^+$: 599.51g/mol

Isotope pattern of $[32+H]^+$: 600 (100%), 601 (40.1%), 602 (8.3%) [Simulation]

Experimental totals: 600 (100%), 601 (39.3%), 601 (8.9%)

➔ MS (positive ESI): 600 ([**32**+H]$^+$, 100%).

Simulation:

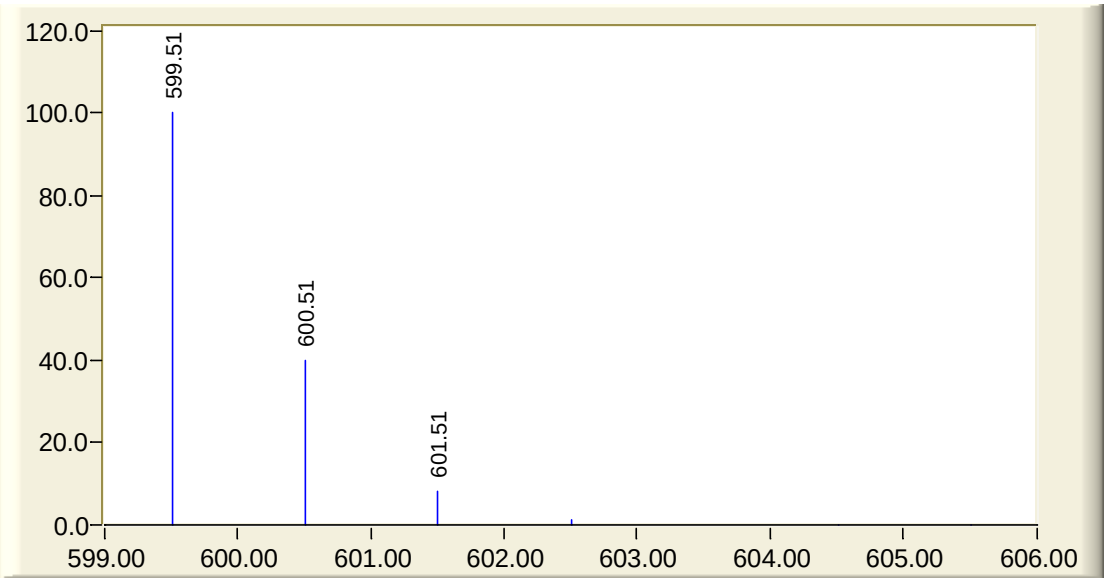

Simulation performed by the Molecular Weight Calculator provided by Pacific Northwest National Laboratory under the U.S. Department of Energy. The total percentage values for each peak are summarized above.

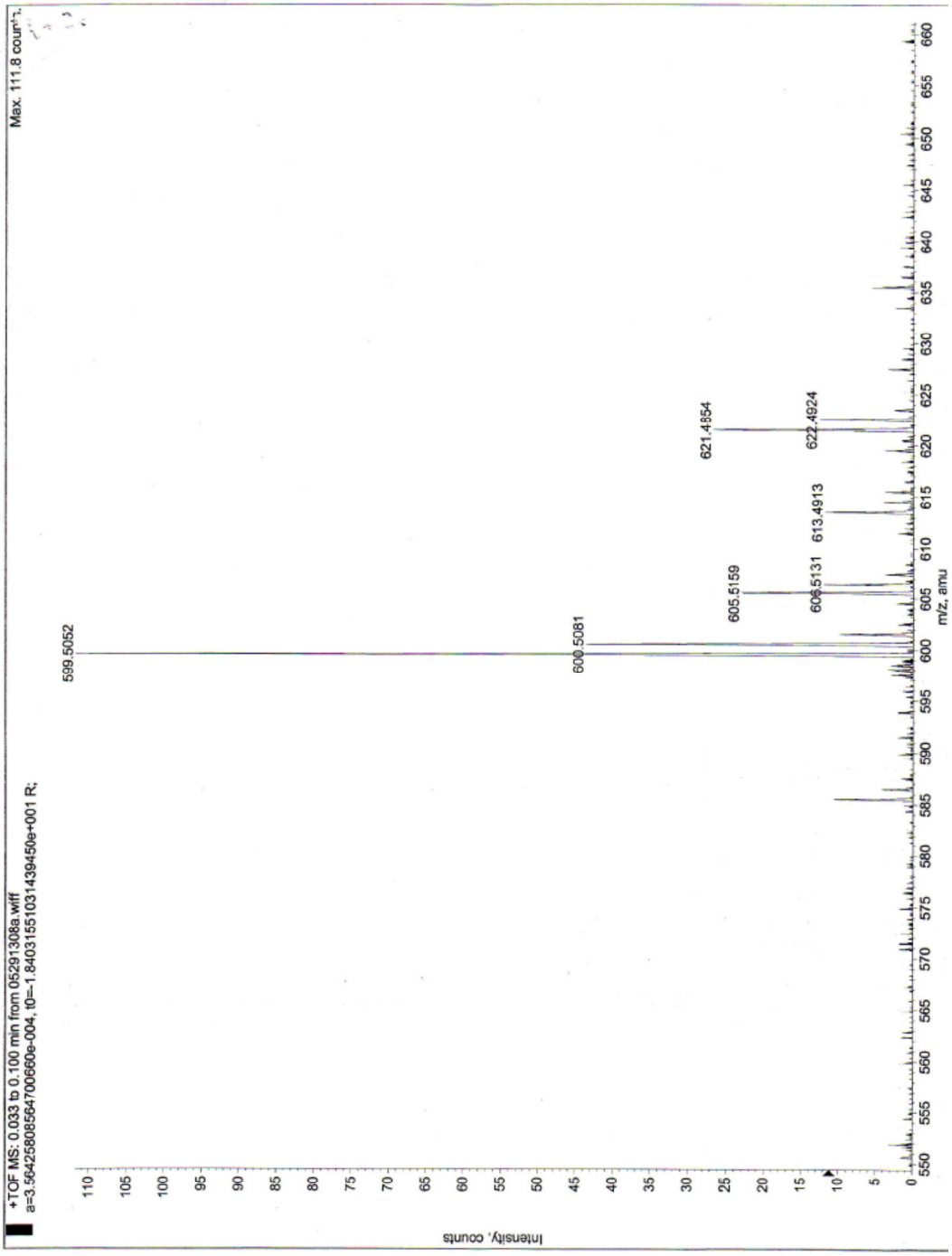
+TOF MS: 0.033 to 0.100 min from 05291308a.wiff
a=3.56425808564700660e-004, t0=-1.84031551031439450e+001 R:
Max. 111.8 coun
599.5052
600.5081
605.5159
606.5131
613.4913
621.4854
622.4924
Intensity, counts
m/z, amu

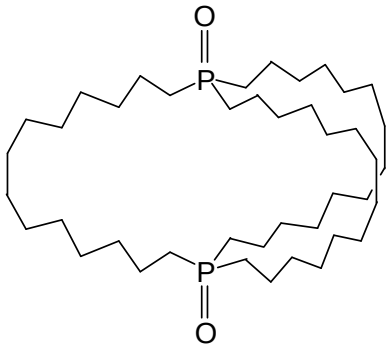

$C_{42}H_{84}O_2P_2$

Monoisotopic mass of 33: 683.07 g/mol

Monoisotopic mass of $[33+H]^+$: 684.07 g/mol

Isotope pattern of $[33+H]^+$: 684 (100%), 685 (46.8%), 686 (11.1%) [Simulation]

Experimental totals: 684 (100%), 685 (43.8%), 686 (10.1%)

➔ MS (positive ESI): 684 ([**33**+H]$^+$, 100%).

Simulation:

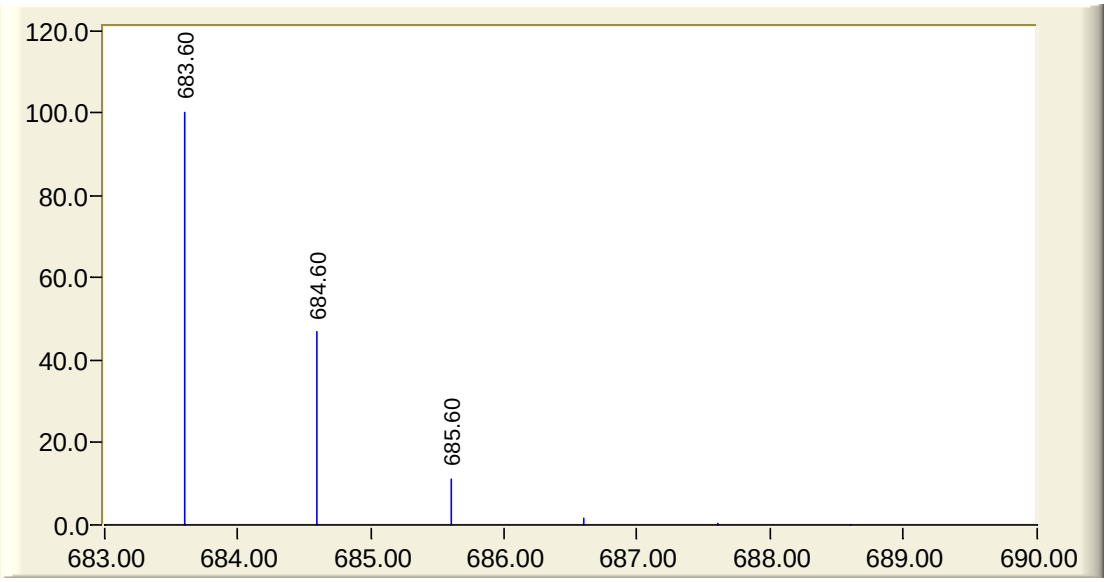

Simulation performed by the Molecular Weight Calculator provided by Pacific Northwest National Laboratory under the U.S. Department of Energy. The total percentage values for each peak are summarized above.

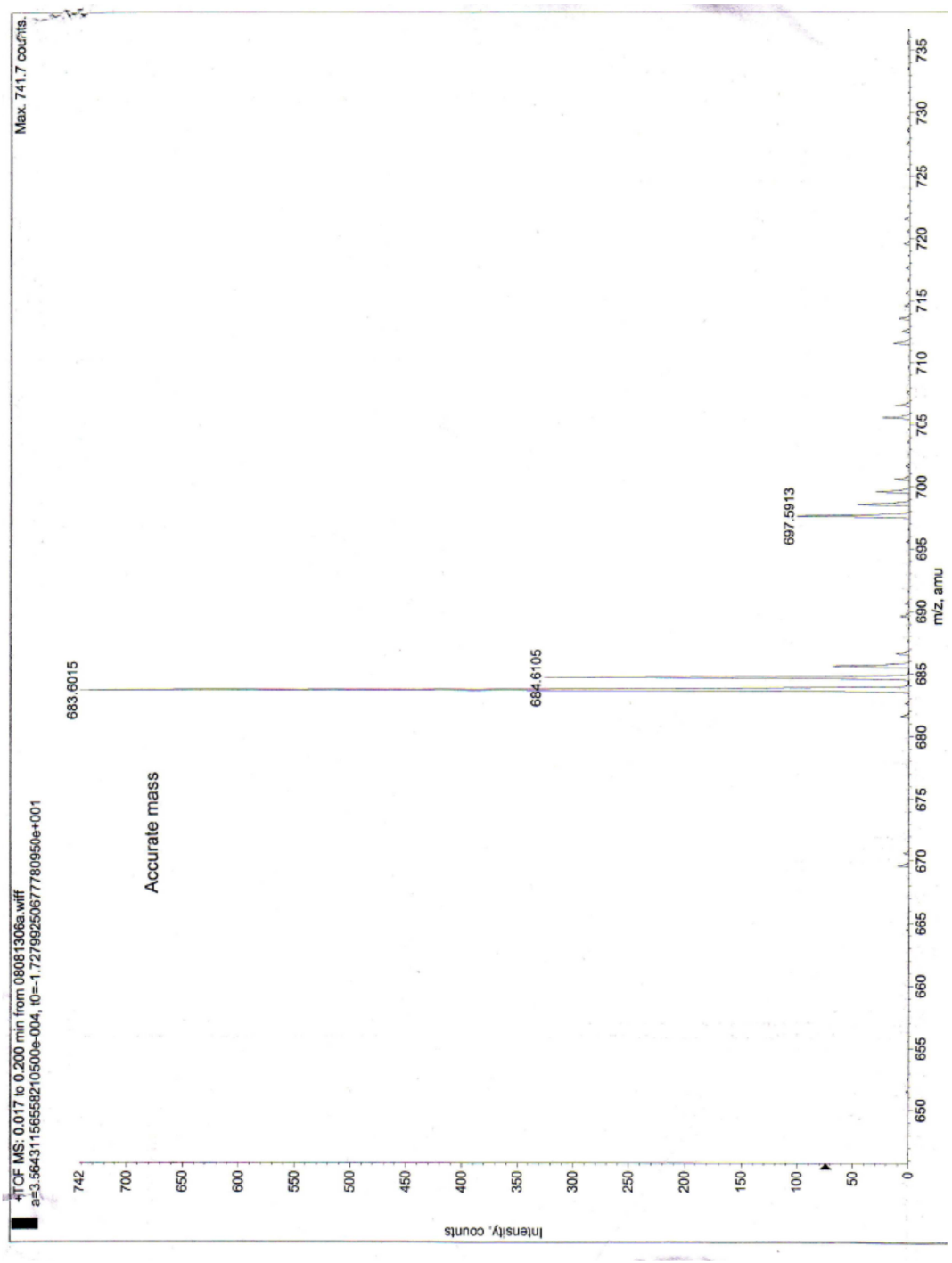
+TOF MS: 0.017 to 0.200 min from 08081306a.wiff
a=3.56431156558210500e-004, t0=-1.72799250677780950e+001
Max. 741.7 counts.
Accurate mass
683.6015
684.6105
697.5913
Intensity, counts
m/z, amu

APPENDIX D

COMPOUND CATALOG

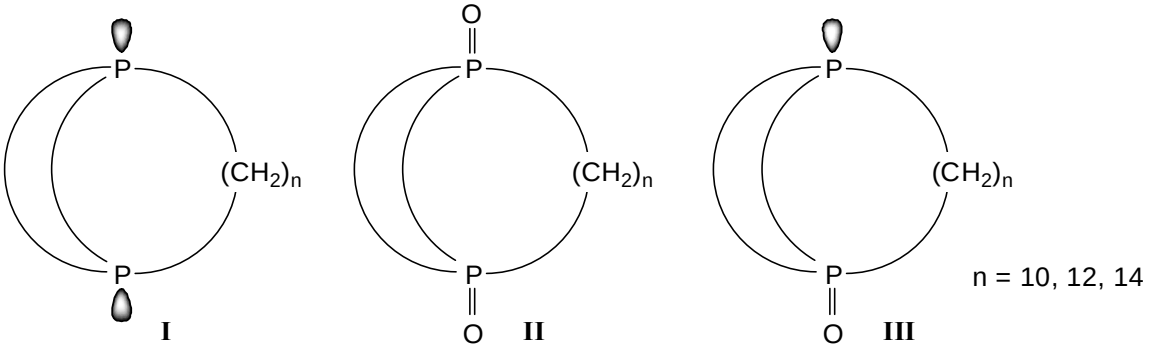

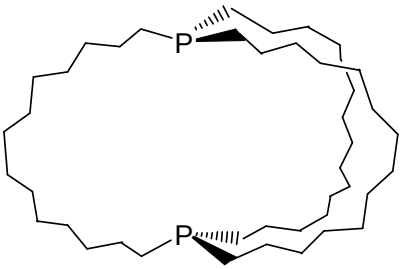

1

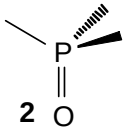

2

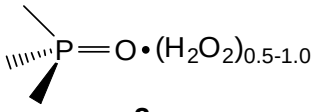

2a

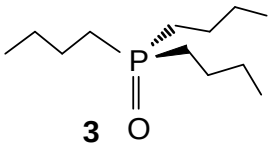

3

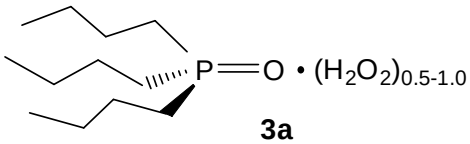

3a

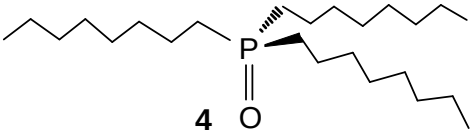

4

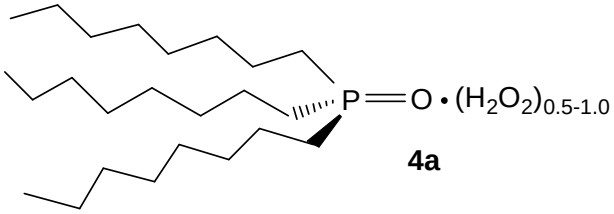

4a

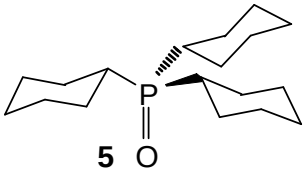

5

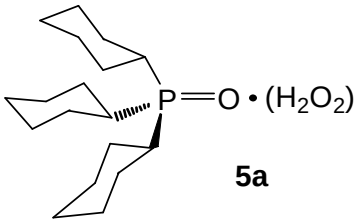

5a

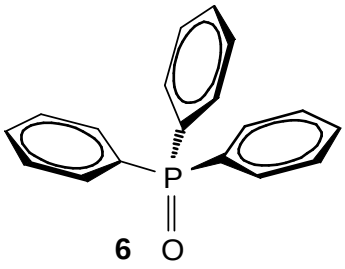

6

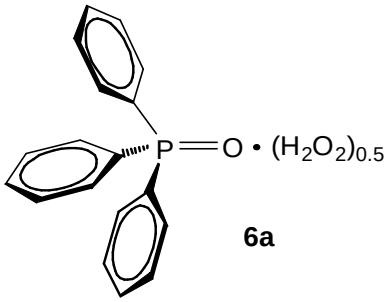

6a

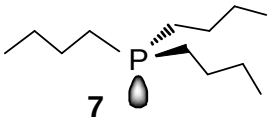

7

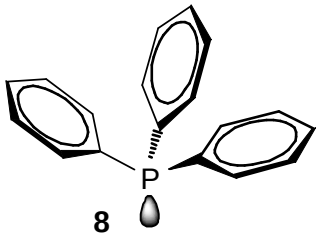

8

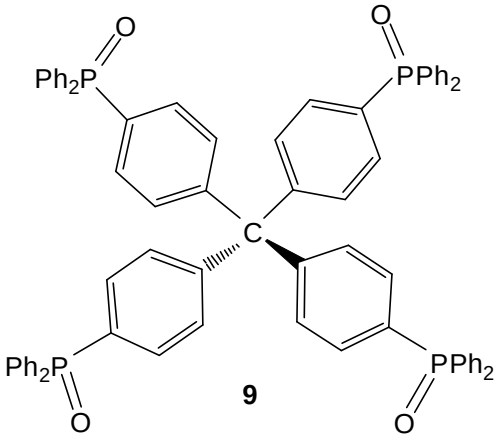

9

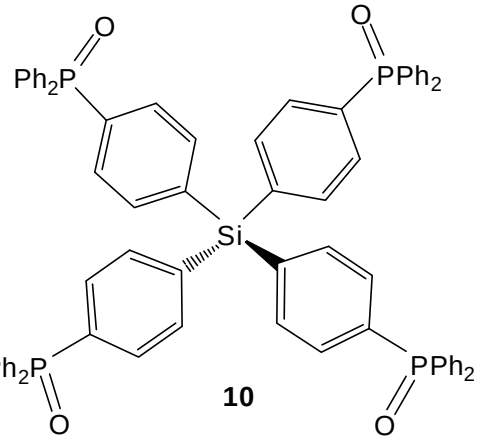

10

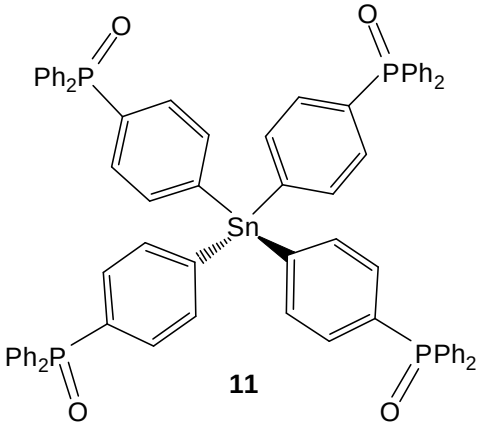

11

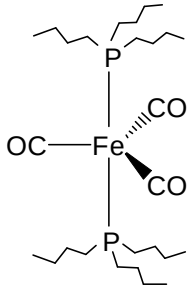

12

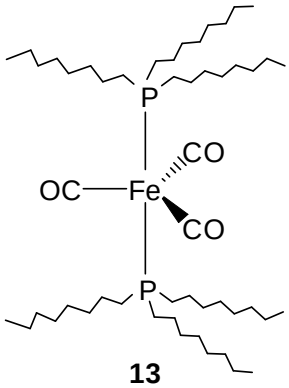

13

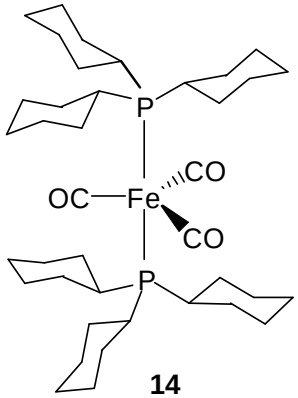

14

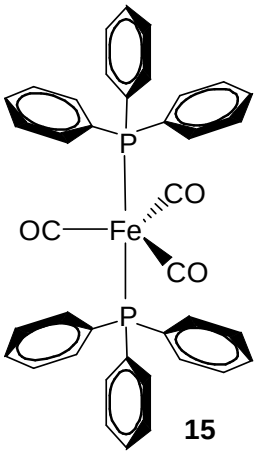

15

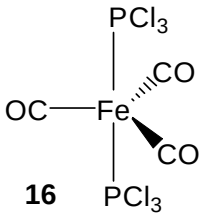

16

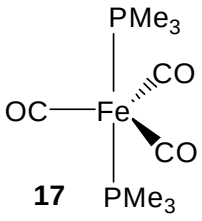

17

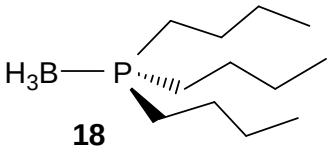

18

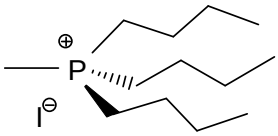

19

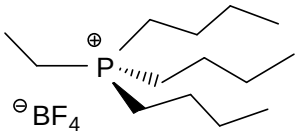

20

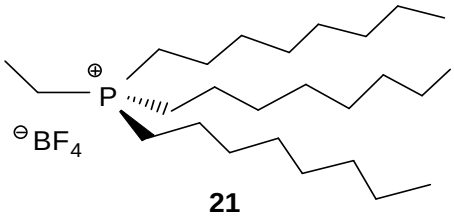

21

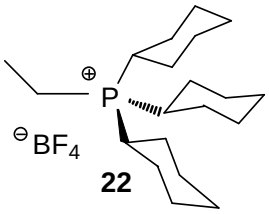

22

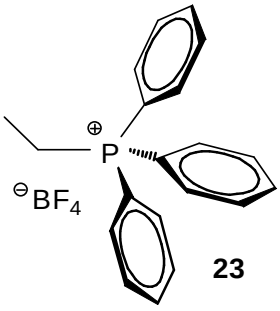

23

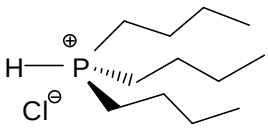

24

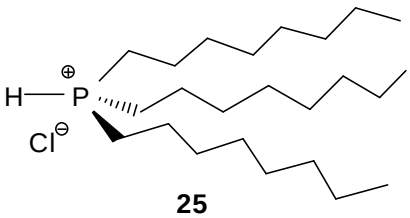

25

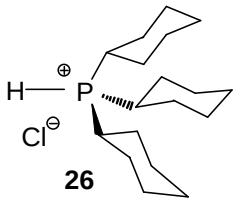

26

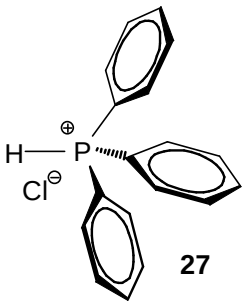

27

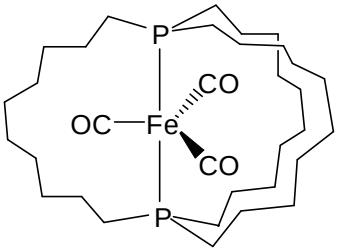

28

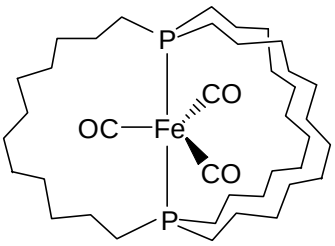

29

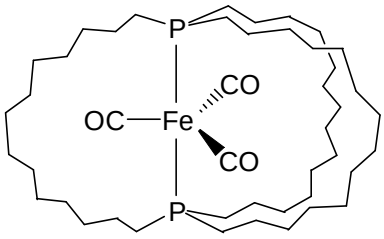

30

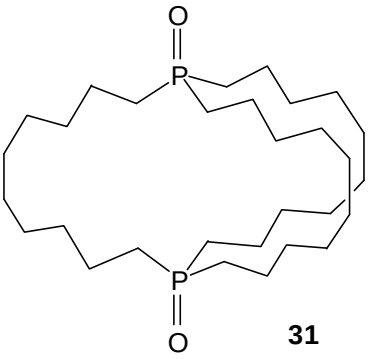

31

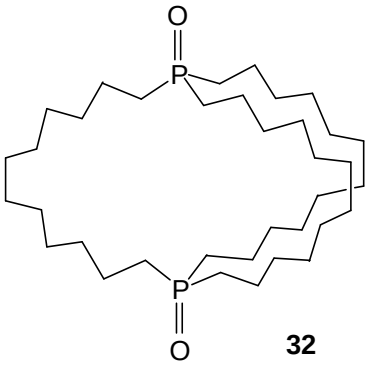

32

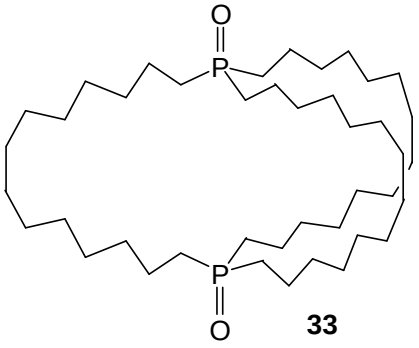

33